To the Graduate Council:
I am submitting herewith a dissertation written by Diego Venegas Vargas entitled "Final Spectral Shape and Sterile Neutrino Oscillation Analyses from the PROSPECT-I Experiment." I have examined the final electronic copy of this dissertation for form and content and recommend that it be accepted in partial fulfillment of the requirements for the degree of Doctor of Philosophy, with a major in Physics.

Alfredo Galindo-Uribarri, Major Professor

We have read this dissertation
and recommend its acceptance:

Anthony Mezzacappa

Sherwood Richers

Thomas Papenbrock

Karsten Heeger

Accepted for the Council:

Dixie L. Thompson

Vice Provost and Dean of the Graduate School

(Original signatures are on file with official student records.)

Final Spectral Shape and Sterile Neutrino Oscillation Analyses from the PROSPECT-I Experiment

A Dissertation Presented for the

Doctor of Philosophy

Degree

The University of Tennessee, Knoxville

Diego Venegas Vargas

December 2024

© by Diego Venegas Vargas, 2024
All Rights Reserved.

Así como la celebración de este logro, mi vida ha estado colmada de afecto y cariño insaciable, proveniente de diversas entidades. Es por eso que, en los momentos en que algo maravilloso me ocurre, no me considero dueño de mi felicidad, sino más bien un simple mensajero para todos aquellos cuyo apoyo y amor se traducen en mis razones. En lo que concierne a la efeméride, de la etapa que hoy culmina, quiero dedicar este trabajo a mis pilares eternos : Gloria, Timi, Meli y Hugo, por quienes soy quien soy y con quienes camino siempre de la mano.

Acknowledgements

I want to begin by thanking the people who I was honored to have as part of my doctoral committee—Alfredo Galindo-Uribarri, Karsten Heeger, Anthony Mezzacappa, Thomas Papenbrock, and Sherwood Richers—for their time and support in the revision and supervision of this work. Before mentioning all the people who have shaped my life and contributed to the successful completion of this work, I want to acknowledge the immense role that my supervisor, Alfredo Galindo-Uribarri, has had in my personal and professional development. Beyond his kindness, patience, unconditional support, and the many different roles he took while guiding me all these years, I want to thank him for believing in me and allowing me to pursue my graduate studies. In addition, I want to thank Bryce Littlejohn, whom I have considered my co-advisor throughout these past five years. His guidance, empathy, patience, and exceptional approach to scientific research have significantly shaped my perspective and are one of the main reasons I aspire to continue in academia.

Completing my doctorate is the result of a long series of events in which many people contributed in one way or another. As I reflect on how to begin this extensive list of acknowledgments, I recognize that I may inevitably leave some people out. My best attempt to capture those who have supported me comes in the form of a chronological description of the events that have brought me to this point.

I have been fortunate to have exceptional mentors and a loving, supportive community throughout my life. Whether in academia or sports, these individuals have kept me grounded and motivated at every stage. As a high school student, I had

the privilege of meeting William Hernandez, one of the first people to inspire me to pursue higher education. I credit him with sparking my passion for philosophy and literature.

During those same years, most of my time outside school was spent at the local tennis courts in my hometown of Tunja. There, I was surrounded by wonderful friends and mentors who always wanted the best for me. I am particularly grateful to Jose Niño, Gustavo Rivera, Carlos Espejo, and Juan Manuel Uscategui, all of whom have supported me from the very beginning. Finally, I want to express my deep gratitude to my dear childhood friends, Andrea Bohórquez and Cristian Uricochea, for their constant support throughout the years.

Moving to the US was probably one of the best decisions I have ever made, even though, at times, it seemed like a very scary, rushed, and complicated choice. I firmly believe that I would never have transitioned and adapted to this new reality as quickly as I did without the guidance and support of my dear friends in Pittsburgh. My time in Pittsburgh completely changed my life; not only did I learn a new language, choose a major, get into college, and become part of a community, but I also met people who, to this day, I consider family. I want to thank three people who encouraged me to pursue my dreams and went above and beyond to help me, expecting nothing in return: Jose Mieres, Mario Fratangelo, and David Vichitthavong.

My time at Ohio Wesleyan University was filled with eye-opening experiences. Although I had always enjoyed physics and mathematics, it wasn't until my last two years of undergraduate studies that I decided to pursue a career in physics. I attribute this decision primarily to the influence of Robert Haring-Kaye and Bradley Trees, who inspired me not only to continue in academia but also to become an educator. They shaped my life in ways they may not fully realize. To Dr. Haring-Kaye, who placed his unfailing trust in me, I owe my passion for experimental physics. To this day, I consider him a dear friend. In addition to my academic journey, OWU provided a fantastic outlet for me to continue pursuing the sport I love while forming lifelong friendships. Some of my best memories come from being on the road with

the tennis team under the guidance of Robert Postma, who always supported me and made me feel at home. For that, I will forever be grateful. I left OWU with many cherished friendships, particularly with Jack Hibbard, Dan Gilbert, Shouta Fukamachi, Mustapha Habib, and Alec Martin.

Writing about my time in Knoxville is deeply emotional for me. After five years as a graduate student, it feels much like leaving home for the first time in 2014. This city and its community have carved out a special place in my heart, and a part of me never wants to leave because of the wonderful connections I have made here. First, I want to thank Anthony Mezzacappa, Cristian Batista, and Elbio Dagotto for their mentorship, stimulating conversations, and reinforcing my dream of becoming a professor. I owe a special mention to my dearest friend, Di'Arra Mostella, who stood by me through the most challenging parts of graduate school. His support and friendship have been indispensable in helping me navigate the hurdles of the past five years. I am delighted to know that he and his beautiful family will be nearby for my new adventure.

I am also grateful to the incredible people I worked with at ORNL: Blaine Heffron, Jeremy Lu, Jason Newby, Rosa Luz Zamora Peinado, Andrea Delgado, and our past summer interns. My dear friend Andrea, in particular, provided me with uncompromising support and guidance, for which I am deeply thankful. I am excited about the prospect of continuing to collaborate with her. Additionally, I want to thank the PROSPECT collaboration for the significant impact this experiment has had on me. It has been a transformative experience, allowing me to learn and grow through exposure to so many brilliant individuals from diverse backgrounds. In particular, I extend my gratitude to Nathaniel Bowden, Michael Mendenhall, Xianyi Zhang, Cristian Roca, Manoa Andriamirado, Paige Kunkle, and Ohana Benevidez. Special thanks go to my friends Cristian, Manoa, and Paige for their patience and support while working alongside me, as well as for taking the time to review large portions of this work.

In addition to my graduate studies, Knoxville provided me with a wonderful tennis community. I want to thank Dave and Maeve Thornton, Kata Szekely, Derek Stultz (along with all the KRC and CBRC folks), and Zac Jumper (and all the Jumper Tennis guys) for giving me a space to escape the stresses of research. They made me feel at home and continued to fuel my passion for this sport. I leave Knoxville with countless fantastic memories and amazing people. A very special thank you goes to Morgan Ewing, who provided me with a loving and peaceful environment during the most stressful time of my life.

Finally, I wish to express my deepest gratitude to the remarkable individuals who have stood by my side throughout the years. They welcomed me into their lives with open arms, offering unwavering support without expecting anything in return. Their generosity has been instrumental in my journey, and I owe much of this accomplishment to them. I will forever cherish the kindness and encouragement of Hannah Rawlings, Israel Romero, Felipe Duarte, Omar Santiagonuñez, Felipe Bautista, Daniel Silva, Marco Kraus, Anna Nau, Viviana Herrera, Vass Mewes, and the ever-beautiful Idris.

"Como todas las cosas buenas que les ocurrieron en su larga vida, aquella fortuna desmandada tuvo origen en la casualidad." - Gabriel García Márquez.

Abstract

The discovery of the neutrino stands as a pivotal milestone in the annals of modern physics. Following the initial detection of neutrinos, a diverse array of experiments employing both natural and artificial sources of neutrinos have played a crucial role in shedding light on the elusive nature of these particles, including their intriguing behavior, such as neutrino oscillations. PROSPECT is a reactor antineutrino experiment consisting of a 4-ton liquid scintillator antineutrino detector divided into an 11x14 array of optically separated segments. The detector was designed to probe the existence of sterile neutrino oscillations and precisely measure the antineutrino spectrum resulting from ^{235}U fission. Data was taken in 2018 and 2019 with a first-generation detector called PROSPECT-I located on the Earth's surface roughly 7 m from the 85 MW, compact, highly-enriched High Flux Isotope Reactor at Oak Ridge National Laboratory. This dataset has already had a substantial impact by placing stringent limits on sterile neutrino oscillations at the eV scale, setting new direct limits on boosted dark matter models, providing a precision ^{235}U spectral measurement, and demonstrating unique neutrino detection capabilities. A new analysis of the PROSPECT-I data has been performed, incorporating innovative event selection tools, resulting in a multi-period dataset marked by a significant enhancement in statistical power and improved signal-to-background ratios. This work reports the conclusive findings regarding the measurement of the antineutrino energy spectrum from the fission of ^{235}U, as well as the search for eV scale sterile neutrino oscillations using the final PROSPECT-I multi-period data set.

Table of Contents

1 Introduction **1**

2 Historical and theoretical overview of neutrinos **4**

2.1 Historical context 4

2.2 Neutrinos in the Standard Model 9

2.2.1 Gauge symmetry 10

2.2.2 Neutrino interactions 12

2.3 Neutrino sources 12

2.4 Neutrino oscillations 15

2.4.1 Neutrino mass in the SM 15

2.4.2 Generalised neutrino oscillation formalism 16

2.4.3 Two neutrino mixing 18

2.4.4 Averaged transition probability 19

2.5 Neutrino oscillation experiments 20

2.5.1 Solar neutrino experiments 22

2.5.2 Atmospheric neutrino experiments 23

2.5.3 Accelerator experiments 25

2.6 Consolidating the 3-neutrino oscillation picture 26

2.6.1 Why three neutrinos? 26

2.6.2 Putting experimental results into context 28

2.7 Experimental Anomalies 29

2.7.1 Sterile neutrinos (3+1 formalism) . . . 31
2.8 Chapter summary . . . 33

3 Reactor Neutrino Physics **34**
3.1 Nuclear reactors as a neutrino factory . . . 34
3.1.1 Reactor-based oscillation experiments . . . 36
3.2 Modeling antineutrino emissions from nuclear reactors . . . 41
3.2.1 Summation method . . . 41
3.2.2 Conversion method . . . 43
3.2.3 Combined models . . . 43
3.3 Reactor-based anomalies . . . 46
3.3.1 Spectral shape anomaly, 'The Bump' . . . 46
3.3.2 Reactor Antineutrino Anomaly (RAA) . . . 47
3.4 Chapter summary . . . 48

4 The PROSPECT experiment **50**
4.1 Introduction . . . 50
4.2 Experimental Facility . . . 50
4.2.1 Experiment room, detector location, and shielding strategies . 52
4.2.2 Modelling HFIR reactor neutrinos . . . 55
4.3 Detector Design . . . 56
4.3.1 Description of inner detector . . . 56
4.3.2 ^{6}Li-Doped Liquid Scintillator . . . 58
4.3.3 Low mass optical grid . . . 59
4.3.4 Photo Multiplier Tube (PMT) modules and segment supports 65
4.4 Calibration methods . . . 67
4.4.1 Optical calibration system . . . 69
4.4.2 Radioactive source system . . . 71
4.4.3 Intrinsic radioactive sources . . . 73
4.5 Detector Monitoring . . . 74

4.6 Data acquisition system . . . 74
4.6.1 DAQ hardware . . . 75
4.6.2 DAQ triggering . . . 76
4.6.3 Data transfer and data rates . . . 78
4.6.4 Clock signal distribution . . . 78
4.7 Chapter summary . . . 80

5 PROSPECT Data processing, event reconstruction and detector response simulation 81
5.1 Introduction . . . 81
5.2 Low-level signal processing . . . 82
5.2.1 Raw waveforms, unpacked data . . . 82
5.2.2 Pulse analysis, pairing and clustering . . . 82
5.2.3 Timing calibration . . . 84
5.2.4 Position calibration . . . 86
5.2.5 Position-dependent combined PSD metric . . . 88
5.2.6 Visible energy calibration . . . 89
5.2.7 Cluster-based event reconstruction . . . 91
5.2.8 Performance of calibrated physics metrics . . . 94
5.3 Antineutrino energy response simulation . . . 97
5.3.1 PROSPECT Monte Carlo strategy . . . 97
5.3.2 Simulated waveforms . . . 99
5.3.3 Determining absolute energy response . . . 100
5.3.4 Energy resolution . . . 104
5.3.5 Determination of position-dependent energy response variation 104
5.4 Chapter summary . . . 105

6 Antineutrino detection 108
6.1 Description of datasets . . . 108
6.2 IBD detection strategy in PROSPECT . . . 109

6.2.1 IBD cuts . . . 111
6.2.2 Background vetoes . . . 112
6.2.3 Implementation of IBD selection criteria . . . 114
6.3 IBD backgrounds . . . 119
6.3.1 Accidental backgrounds . . . 120
6.3.2 Time-correlated cosmic ray induced backgrounds . . . 122
6.4 Measured IBD signal . . . 124
6.5 Simulating IBD interactions and efficiencies . . . 128
6.5.1 Determination of relative IBD efficiency . . . 131
6.6 Validation of IBD signal . . . 133
6.7 Multi-Period Analysis . . . 139
6.7.1 Single Ended Event Reconstruction . . . 141
6.7.2 Re-Optimization with SEER variables . . . 145
6.7.3 Data Splitting . . . 151
6.7.4 Results of DS+SEER . . . 155
6.8 Chapter summary . . . 161

7 Multi-Period Spectral Shape Analysis 162
7.1 Description of previous results . . . 163
7.2 Description of datasets . . . 167
7.2.1 Data inputs . . . 167
7.2.2 Statistical uncertainty . . . 170
7.2.3 Systematic uncertainties . . . 170
7.3 Unfolding strategy . . . 173
7.3.1 Unfolding PROSPECT Data . . . 174
7.3.2 Optimizing the Wiener filter . . . 176
7.4 Spectral shape comparison . . . 178
7.5 Hypothesis testing . . . 180
7.5.1 Gaussian excess fit - procedure . . . 181

7.5.2 Gaussian excess fit - results . . . 182
7.6 PROSPECT in the global context . . . 183
7.7 Chapter summary . . . 185

8 Multi-Period Sterile Neutrino Oscillation Analysis 187
8.1 Description of previous analysis . . . 188
8.1.1 Motivation shift since last oscillation result . . . 189
8.2 Description of datasets . . . 193
8.2.1 Data inputs . . . 194
8.3 Generating predictions of un-oscillated and oscillated spectra . . . 201
8.3.1 Visualizing data in L/$E_{\bar{\nu}}$ space . . . 211
8.4 Strategy for sterile neutrino search . . . 220
8.4.1 Statistical uncertainties . . . 221
8.4.2 Systematic uncertainties . . . 223
8.4.3 χ^2 Grid search . . . 225
8.4.4 Sensitivity and exclusion contours . . . 227
8.4.5 Results . . . 228
8.5 PROSPECT in the global context . . . 233
8.6 Chapter summary . . . 236

9 Joint Oscillation Analysis 239
9.1 Introduction . . . 239
9.2 Motivation and strategy . . . 241
9.3 Daya Bay . . . 243
9.3.1 Experimental description . . . 243
9.3.2 Inputs for DPS analysis . . . 245
9.4 STEREO . . . 247
9.4.1 Experimental description . . . 247
9.4.2 Inputs for DPS analysis . . . 248
9.4.3 Reproducing STEREO results . . . 254

9.5 Expected combined median sensitivity . . . 254
9.5.1 Incorporating Daya Bay's ^{235}U model uncertainty . . . 257
9.5.2 Current Results . . . 260
9.6 Chapter Summary . . . 260

10 Conclusion **263**

Bibliography **265**

A Statistical Methods **294**
A.1 Covariance matrix formalism . . . 294
A.1.1 Covariance matrix generation . . . 297
A.1.2 Toy generation with covariance matrices . . . 298
A.2 Wiener-SVD unfolding technique . . . 299
A.2.1 Traditional Regularization Approach . . . 302
A.2.2 Wiener-SVD Approach . . . 303
A.3 Combined Neyman-Pearson χ^2 test . . . 305
A.4 Gaussian CLs method . . . 307
A.5 Feldman-Cousins method . . . 308
A.5.1 Example: Determining the Mixing Angle in a Neutrino Oscillation Experiment . . . 310

Vita **313**

Chapter 1

Introduction

Neutrinos are among the most fundamental particles in the universe, yet they remain some of the most elusive. Despite being the second most abundant particle, detecting neutrinos is extraordinarily challenging due to their extremely weak interactions with matter, earning them the nickname 'ghost particles.'

The unearthing of the neutrino stands as an epochal achievement in the annals of modern physics. Originally proposed as a purely theoretical construct to reconcile apparent violations of momentum-energy conservation laws within the beta-decay spectrum, the neutrino's cryptic nature presented a formidable experimental challenge to physicists. Despite the daunting hurdles in its detection, the inaugural observation of a neutrino materialized in 1956, 26 years after Wolfgang Pauli postulated its existence. This monumental endeavor, spearheaded by Reines and Cowan [104], marked the inception of an exceptional journey of discovery, one that continues to unveil remarkable insights into the enigmatic properties of this particle, which is crucial in testing the Standard Model (SM) of particle physics and look for possible extensions of it. The current picture of the SM contains three types of neutrinos (one for each lepton flavor), all of which are massless neutral fermions.

Nuclear reactors have become indispensable in neutrino research, serving as powerful, controlled sources of antineutrinos. Over the past two decades, more

than 20 reactor-based experiments have provided precise measurements of neutrino properties, including the mixing angle θ_{13}, and have refined our understanding of neutrino oscillation phenomena. Despite these advances, reactor-based experiments have reported anomalies in the expected antineutrino flux and energy spectrum shape, most notably the observed flux deficit known as the reactor neutrino anomaly (RAA). This anomaly has driven the search for new physics beyond the Standard Model, such as the existence of a light sterile neutrino.

Models involving light sterile neutrinos suggest a mass-splitting around 1 eV^2, indicating the possibility of meter-scale, short-baseline oscillations. The PROSPECT experiment, explicitly designed to test this hypothesis, commenced in 2016 and conducted both spectral shape and sterile neutrino oscillation analyses from 2018 to 2024. This dissertation presents the definitive findings from the PROSPECT experiment, which set world-leading limits on the search for eV-scale sterile neutrinos and provides the most precise measurement to date of the antineutrino energy spectrum from ^{235}U fission. The structure of this work is as follows:

- **Chapter 1** introduction.
- **Chapter 2** provides a historical overview of neutrino physics, detailing the current understanding of neutrinos within the Standard Model, the formalism of neutrino oscillations, and a description of main oscillation experiments and sterile neutrino formalism.
- **Chapter 3** reviews reactor-based antineutrino studies, highlighting the discovery of the reactor antineutrino anomaly (RAA), which motivated the development of the PROSPECT experiment.
- **Chapter 4** describes the design and instrumentation of the PROSPECT detector, focusing on its technical aspects and operational capabilities.

- **Chapter 5** discusses the data acquisition and calibration processes, detailing the extraction of physical quantities necessary for identifying antineutrino events from raw waveforms.

- **Chapter 6** outlines the inverse beta decay (IBD) event selection criteria used in both the initial single-period analysis and the optimized multi-period analysis, leading to an enhanced dataset with improved statistics.

- **Chapter 7** presents the final spectral shape analysis using the new multi-period dataset from the PROSPECT-I experiment.

- **Chapter 8** details the final sterile neutrino oscillation analysis based on the new multi-period dataset from the PROSPECT-I experiment.

- **Chapter 9** discusses the current status of the joint oscillation analysis involving the Daya Bay, PROSPECT, and STEREO collaborations.

- **Chapter 10** conclusions.

Chapter 2

Historical and theoretical overview of neutrinos

This chapter provides a historical and theoretical overview of neutrino physics, primarily focused on the phenomena of neutrino oscillations. It also presents an overview of the primary neutrino sources, experiments, and oscillation results and describes the long-standing experimental anomalies motivating the sterile neutrino hypothesis. Lastly, the formalism of 3+1 sterile neutrino oscillations is briefly described.

2.1 Historical context

The first evidence for the existence of neutrinos emerged from studies of nuclear beta decay in the 1920s. At the time, beta decay was known as a type of radioactivity in which a nucleus (A, Z) transforms into a lighter nucleus with the same mass number but a different charge by one unit, accompanied by the emission of an electron (or positron) and no other visible particles:

$$(A, Z) \rightarrow (A, Z \pm 1) + e^{\mp} + (\text{nothing else visible}) \tag{2.1}$$

A well-known example of β-decay is the transformation of a free neutron into a proton and an electron, with a lifetime of about 886.7 seconds. If no additional invisible particles were involved, the emitted electron or positron ($e^{\mp}$) should have a specific energy, $E_e \simeq Q \equiv M_i - M_f$. Contrary to this expectation, early experiments revealed a continuous energy spectrum for the electron, extending from its rest mass m_e up to the maximum allowed energy Q as illustrated in Fig. 2.1 [115].

To explain this unexpected result, several hypotheses were proposed, including Niels Bohr's suggestion that energy-momentum conservation might not hold in these cases. However, in December 1930, Wolfgang Pauli proposed the existence of an undetected particle emitted during the decay process [180]. This hypothetical particle needed to be electrically neutral (to conserve charge), extremely light (as $E_{e,\max} \simeq Q$), and possess spin-$\frac{1}{2}$ (to satisfy both angular momentum conservation and the Pauli exclusion principle).

Today, these beta decay processes are understood as:

$$\begin{aligned} n &\to p + e^- + \bar{\nu}_e \\ A(Z,N) &\to A(Z+1, N-1) + e^- + \bar{\nu}_e \\ A(Z,N) &\to A(Z-1, N+1) + e^+ + \nu_e \end{aligned} \tag{2.2}$$

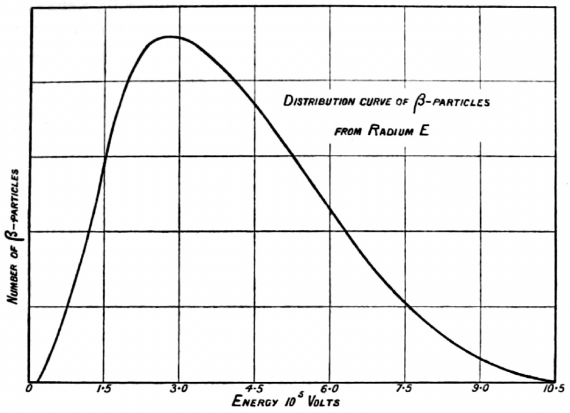


Figure 2.1: Distribution curve of β-particles measured from the beta decay of a radium source showing a continuous energy spectrum. Source [115].

Soon after Pauli's proposal, Enrico Fermi [208] introduced a model of β-decay (and weak interactions in general). This model described the process as the product of two weak 'currents': one connecting the initial and final state nucleons and the other connecting the final state electron and antineutrino. The coupling constant G_F characterized the strength of the interaction. In Fermi's theory, the two currents connected at the same space-time point, assuming the interaction was short-ranged. In modern language, the Fermi constant G_F can be understood as the effect of the exchange of a virtual but massive heavy 'photon,' that is, the gauge boson $W^{\pm}$ with a mass $M_W \simeq 80\text{GeV}$. The weakness of the weak interaction can be understood as the effect of the large mass (and corresponding short range) of the W boson with $G_F \simeq e^2/M_W^2$, or more exactly:

$$\frac{G_F}{\sqrt{2}} = \frac{1}{8}\left(\frac{e}{\sin\theta_W}\right)^2 \frac{1}{M_W^2} \tag{2.3}$$

(where θ_W is the Weinberg angle). Fermi's theory could successfully describe the observed spectra of electrons and positrons emitted in beta decays. At the same time, it could predict the existence of other processes involving 'weak currents,' in particular the existence of the 'inverse β-decay' processes such as:

$$\begin{aligned} \bar{\nu}_e + p &\to e^+ + n \\ \nu_e + n &\to e^- + p \end{aligned} \tag{2.4}$$

The cross-section for these processes is approximately given by

$$\sigma < \frac{\hbar^3}{m^3 c^4 t}, \tag{2.5}$$

where t is the lifetime of a β-radiating nucleus emitting neutrinos. Here, $\frac{\hbar}{mc^2}$ is the Compton time, and $\frac{\hbar}{mc}$ is the Compton wavelength. This yields a cross-section of $\sigma < 10^{-44}\,\text{cm}^2$ for a neutrino energy of $2 \cdot 3 \times 10^6\,\text{eV}$ and a lifetime t of 3 minutes.

Given this cross-section, the corresponding penetrating power is approximately 10^{16} km in solid matter. Based on this, Bethe and Peierls [92] concluded that observing neutrino interactions involving creation and annihilation would be 'absolutely impossible'. While σ increases linearly with neutrino energy, the interaction cross-section remains so small that it was considered highly unlikely for σ to become large enough to be observable, even at cosmic ray energies, suggesting that no practically feasible method existed for detecting neutrinos.

The detection of neutrinos remained elusive for over 20 years until 1951 when Fred Reines recognized the potential of the large flux of neutrinos generated by nuclear reactors through the decay of fission products during chain reactions. In these reactors, each fission event results in an average of six beta-decay processes, each emitting a neutrino.

This realization led to an experiment by Reines and Cowan in 1956, known as Project Poltergeist [104]. They used the nuclear reactor at Savannah River in South Carolina as an antineutrino source and designed a detector filled with water containing dissolved cadmium chloride. The detection method relied on the coincident observation, with a delay of a few microseconds, of a positron emitted in the inverse beta decay reaction, $\bar{\nu}_e + n \rightarrow e^+ + n$, followed by a photon emitted during the de-excitation of cadmium after neutron capture: $n + {}^{112}\mathrm{Cd} \rightarrow {}^{113}\mathrm{Cd} + \gamma$.

Reines and Cowan positioned two 200-liter water tanks with cadmium chloride dissolved as a neutron absorber 13 meters from the reactor core, as shown in Fig. 2.2 [164]. More than 10^{13} neutrinos traveled through the detector per second per cm^2, with two neutrinos detected per hour, resulting in a measured cross-section consistent with Fermi's theory. Detecting the 'poltergeist' confirmed, for the first time, the free neutrino's existence and conclusively resolved the apparent lack of energy-momentum conservation in beta decay.

In addition to the discovery of the electron neutrino, ν_e, two other types of neutrinos — the muon neutrino (ν_μ) and the tau neutrino (ν_τ) — were later

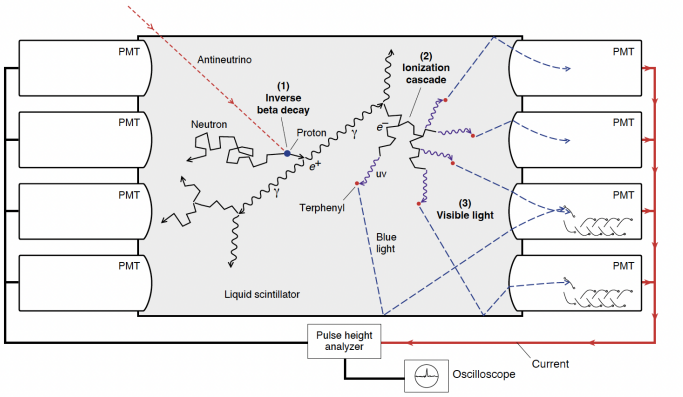


Figure 2.2: Liquid scintillation counter used to detect the inverse beta decay positron in the Reines-Cowan experiment. Source: [115].

discovered. Muon neutrinos and antineutrinos are produced during pion and muon decays, such as:

$$\begin{aligned} \pi^+ &\to \mu^+ + \nu_\mu, \\ \mu^+ &\to e^+ + \nu_e + \bar{\nu}_\mu. \end{aligned} \tag{2.6}$$

When the decay $\pi^\pm \to \mu^\pm + \nu$ was first observed, it raised the question of whether the undetected particles produced in this decay were the same as the neutrinos involved in β-decay. This question was experimentally answered in 1962 by L. Lederman, M. Schwartz, and J. Steinberger [106], who conducted the first experiment using accelerator-produced neutrinos. They bombarded a beryllium target with a 15 GeV primary proton beam to create a beam of pions, which decayed and produced a neutrino beam. They then studied the interactions of these neutrinos with nucleons, looking for the reactions $\nu_\mu + N \to \mu^- + X$ and $\nu_\mu + N \to e^- + X$. They found only the first interaction type, demonstrating that ν_e and ν_μ are distinct particles.

The tau neutrino, ν_τ, is associated with the third charged lepton, the tau (τ^-), which was discovered in 1975 at Stanford. Tau neutrinos and anti-neutrinos are expected to be produced in $\tau^\pm$ decays:

$$\begin{aligned}\tau^- &\to \nu_\tau + W^-, \\ &\to \nu_\tau + e^- + \bar{\nu}_e, \\ &\to \nu_\tau + \mu^- + \bar{\nu}_\mu, \\ &\to \nu_\tau + [\bar{u}s'].\end{aligned} \tag{2.7}$$

the ν_τ was finally observed in 2000 by the DONUT collaboration [156]. These three kinds of neutrinos constitute the current neutrino picture in the SM.

2.2 Neutrinos in the Standard Model

The Standard Model (SM) of particle physics is a theoretical framework describing the electromagnetic (EM), weak, and strong interactions of fundamental particles. While it successfully predicts many phenomena with high precision and is well-supported by experiments, the SM is incomplete. It does not explain neutrino masses and oscillations, and it relies on numerous particles and parameters (like masses and coupling constants) that do not reflect the simpler symmetries physicists favor. Extending the SM with new particles, symmetries, and interactions is necessary to account for beyond Standard Model (BSM) anomalies observed experimentally.

The SM categorizes elementary particles into fermions (matter particles) and bosons (force carriers). Fermions have half-integer spin and include quarks, which interact via the strong force, and leptons, which interact via the EM and weak forces. The EM and weak forces unify at high energies into the electroweak (EW) force.

Quarks come in six flavors, grouped into three generations, and possess a color charge, which causes them to bind into hadrons due to the strong force. They cannot exist in isolation because color confinement allows only color-neutral combinations. Leptons, which do not carry color charge, can exist individually. Both quarks and leptons have antiparticles and are organized into three generations. Each generation consists of two quark flavors (one up-type with a charge of $+\frac{2}{3}e$, and one down-type

with a charge of $-\frac{1}{3}e$) and two lepton flavors (one charged lepton and one neutral neutrino):

$$\begin{pmatrix} u & \nu_e \\ d' & e^- \end{pmatrix}, \quad \begin{pmatrix} c & \nu_\mu \\ s' & \mu^- \end{pmatrix}, \quad \begin{pmatrix} t & \nu_\tau \\ b' & \tau^- \end{pmatrix}, \tag{2.8}$$

where the neutral lepton is the neutrino of the corresponding flavor to the charged lepton, bosons have integer spin and serve as force carriers. Photons mediate electromagnetic (EM) interactions between charged particles, the $W^\pm$ and Z bosons mediate the weak force in processes like beta decay and neutrino interactions, and gluons mediate the strong force that binds quarks into hadrons. The Higgs boson is a scalar boson associated with the Higgs field, which gives mass to other elementary particles through electroweak (EW) symmetry breaking. Photons, $W^\pm$ and Z bosons, and gluons are spin-1, while the Higgs boson has spin 0 [197].

2.2.1 Gauge symmetry

The SM is a gauge theory built on the symmetry group $SU(3)_C \otimes SU(2)_L \otimes U(1)_Y$, which represents color symmetry for strong interactions, weak isospin symmetry for weak interactions, and weak hypercharge symmetry for EW interactions. In this framework, particle interactions are described through the exchange of spin-1 gauge bosons, which are the force carriers associated with each symmetry group.

The $SU(3)$ color symmetry group includes eight gauge bosons, known as gluons (g_i for $i = 1, 2, \ldots, 8$), corresponding to the generators of the color charge. The $SU(2)$ weak isospin symmetry involves three gauge bosons (W_i for $i = 1, 2, 3$), including the $W^\pm$ and Z^0 bosons. The $U(1)$ weak hypercharge symmetry involves a gauge boson B, associated with the photon γ. Both gluons and photons are massless due to the local gauge invariance that preserves the $SU(3)$ and $U(1)$ symmetries [197].

In addition to these gauge bosons, the SM describes particles as fermion fields ψ_α that transform according to the gauge symmetries. These fields are chiral, allowing

a distinction between left-handed and right-handed components using projection operators:

$$P_L = \frac{1}{2}\left(1 - \gamma^5\right), \quad P_R = \frac{1}{2}\left(1 + \gamma^5\right), \tag{2.9}$$

where the chirality operator γ^5 is defined in terms of the Dirac matrices: $\gamma^5 = i\gamma^0\gamma^1\gamma^2\gamma^3$. Chirality refers to a particle's intrinsic 'handedness', determined by how its wavefunction transforms under Lorentz transformations. It is a property of the particle's field, not its spin, independent of its motion or the observer's frame of reference. For massless particles, chirality is equivalent to helicity, corresponding to the projection of the particle's spin onto the direction of its momentum [197]. Thus, the left-handed and right-handed fermion fields are:

$$\psi_L = P_L\psi, \quad \psi_R = P_R\psi. \tag{2.10}$$

Under weak isospin, left-handed fermions form doublets, while right-handed fermions are singlets and do not participate in weak interactions. Since the weak interaction eigenstates of quarks are different from their mass eigenstates, there is a mixing between quark flavors, resulting in flavor-changing interactions. This mixing is described by the Cabibbo-Kobayashi-Maskawa (CKM) matrix [155], which is a unitary matrix that relates weak eigenstates to mass eigenstates:

$$\begin{pmatrix} d' \\ s' \\ b' \end{pmatrix} = \begin{pmatrix} V_{ud} & V_{us} & V_{ub} \\ V_{cd} & V_{cs} & V_{cb} \\ V_{td} & V_{ts} & V_{tb} \end{pmatrix} \begin{pmatrix} d \\ s \\ b \end{pmatrix}, \tag{2.11}$$

where V_{ij} represents the probability amplitude for a quark of flavor i to transition into a quark of flavor j via the weak interaction. The unitarity of the CKM matrix ensures the conservation of probability. The left-handed quark doublet $(u_\alpha, d'_\alpha)_L$ under $SU(2)$ is paired with the left-handed lepton doublet $(\nu_\alpha, l_\alpha)_L$, while right-handed fermions do not transform under $SU(2)$. This chiral asymmetry arises from the nature of gauge interactions in the SM, where only left-handed fermions are

involved in weak interactions. The SM Lagrangian is constructed to be invariant under gauge transformations, ensuring that physical predictions remain consistent under local gauge changes.

2.2.2 Neutrino interactions

Because neutrinos are neutral leptons, they do not interact with the strong or EM forces. They interact via the gravitational and weak forces, where they undergo weak charged current (CC) and neutral current (NC) interactions. For each charged lepton $l = e, \mu, \tau$ the SM includes one active neutrino ν_e, ν_μ, ν_τ. Like other fermions each active neutrino has an associated antiparticle $\bar{\nu}_e, \bar{\nu}_\mu, \bar{\nu}_\tau$. The corresponding CC and NC interaction Lagrangians are of the form:

$$\begin{aligned} \mathcal{L}_{CC} &= -\frac{g}{\sqrt{2}} \sum_{\alpha} \bar{\nu}_{\alpha L} \gamma^{\mu} l_L^- W_{\mu}^+ + \text{h.c.} \\ \mathcal{L}_{NC} &= -\frac{g}{2\cos\theta_W} \sum_{\alpha} \bar{\nu}_{\alpha L} \gamma^{\mu} \nu_{\alpha L} Z_{\mu}^0 \end{aligned} \tag{2.12}$$

where g is the weak isospin coupling constant and θ_W is the Weinberg angle. These equations describe all neutrino interactions in the SM [131]. CC interactions involve the annihilation of a neutrino and the creation of a quark or lepton of the same flavor as the neutrino in the final state (or vice versa) via the exchange of a $W^{\pm}$boson. In contrast, NC interactions involve neutrino scattering via the exchange of a Z^0 boson, as shown in Fig. 2.3.

Weak CC interactions are fundamental in producing neutrinos in accordance with Fermi's theory of beta decay.

2.3 Neutrino sources

From being completely unknown and once considered impossible to detect, neutrinos are now recognized as the second most abundant particles in the visible universe,

after photons. Despite the challenge in detecting them, neutrinos are produced by various natural and artificial processes, each providing valuable insights into their fundamental properties.

Solar neutrinos are produced in the core of the Sun through nuclear fusion reactions that convert hydrogen into helium. These reactions predominantly generate electron neutrinos. Detecting solar neutrinos has been crucial in understanding the Sun's fusion processes.

Atmospheric neutrinos are created when cosmic rays—high-energy particles originating from outer space—collide with atomic nuclei in the Earth's atmosphere. This interaction produces a shower of secondary particles, including pions and muons, which decay into neutrinos. Atmospheric neutrinos include both electron neutrinos and muon neutrinos, and a small fraction of tau neutrinos.

Reactor neutrinos are produced in nuclear reactors through beta decay of neutron-rich fission fragments from isotopes such as ^{235}U, ^{238}U, ^{239}Pu, and ^{241}Pu. These decays emit electron antineutrinos.

Geoneutrinos are emitted from radioactive decay of isotopes such as ^{238}U, ^{232}Th, and ^{40}K within the Earth's mantle and crust. These are electron antineutrinos. The study of geoneutrinos provides insights into the Earth's internal heat production and geological processes, offering a unique window into the planet's interior.

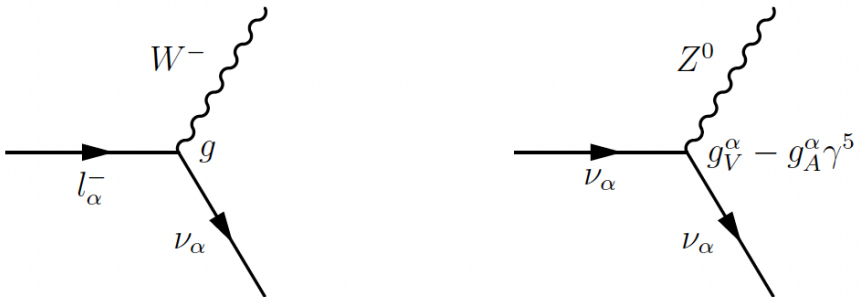


Figure 2.3: Neutrino weak CC interaction vertex with W boson exchange (left) and NC interaction vertex with Z boson exchange (right). Source: [115].

Supernova neutrinos are produced in vast numbers during a supernova explosion, which occurs when a massive star exhausts its nuclear fuel and undergoes a catastrophic collapse. These explosions emit all three types of neutrinos (electron, muon, and tau) and their antineutrinos. The detection of supernova neutrinos provides valuable information about the explosion mechanism and neutron star formation.

Accelerator neutrinos are generated in particle accelerators where high-energy protons collide with a target to produce mesons (like pions and kaons), which decay into neutrinos. These experiments primarily produce muon neutrinos and muon antineutrinos, with smaller fractions of electron neutrinos and antineutrinos.

Neutrinos from the Big Bang, also known as the Cosmic Neutrino Background, were produced shortly after the Big Bang, around one second after the universe began. These neutrinos, which are expected to include all flavors (electron, muon, and tau neutrinos and antineutrinos), carry information about the early conditions of the universe. They are analogous to the cosmic microwave background but are much harder to detect due to their low energy.

Neutrinos from dark matter annihilation or decay are a hypothetical type of neutrinos produced from the annihilation or decay of dark matter particles. The types of neutrinos generated depend on the nature of the dark matter interactions. Detecting such neutrinos could provide crucial insights into the nature of dark matter and its role in the universe.

Artificial neutrino sources are used in calibration experiments, where the radioactive decay of specific isotopes produces neutrinos. These sources, which emit electron neutrinos or antineutrinos depending on the decay process, help researchers understand detector responses and calibrate neutrino experiments accurately.

Each source provides distinct opportunities to investigate various facets of neutrino properties and their potential connections to BSM physics. Figure 2.4 illustrates a diverse array of natural and artificial neutrino sources and their fluxes across energy

scales, underscoring the extensive range of sources available for exploration in neutrino physics.

2.4 Neutrino oscillations

2.4.1 Neutrino mass in the SM

Generating neutrino masses differs fundamentally from the process of mass generation for other fermions in the SM. The Higgs mechanism [148] would require the existence of a right-handed neutrino, which does not carry any SM gauge quantum number. However, this approach struggled to account for the anomalies observed in neutrino experiments.

In 1968, Raymond Davis began data collection for the Homestake experiment in Lead, South Dakota, aiming to detect solar neutrinos produced by fusion reactions in the Sun [102]. He compared the observed neutrino flux with the rate predicted by John Bahcall. To detect the neutrinos, a 380 m^3 tank of perchloroethylene was placed about 1,500 meters underground in the Homestake gold mine to reduce background noise from cosmic rays. When an electron neutrino interacted with a ^{37}Cl atom in the perchloroethylene, it converted it into ^{37}Ar through the reaction:

$$\nu_e + {}^{37}\mathrm{Cl} \rightarrow {}^{37}\mathrm{Ar} + e^-. \tag{2.13}$$

Davis extracted and counted the resulting argon atoms to determine the number of neutrinos interacting with the detector [102]. The measured electron neutrino rate was consistently only one-third of the value predicted by Bahcall using Standard Model-based calculations [107]. This discrepancy between the observed and predicted neutrino flux became known as the 'solar neutrino problem' (SNP).

In 1969, Vladimir Gribov and Bruno Pontecorvo [94], along with Ziro Maki, Masami Nakagawa, and Shoichi Sakata [168], proposed that neutrinos could change their flavor as they traveled from the Sun to the Earth. This phenomenon, known as

neutrino oscillation, would imply that neutrinos have nonzero masses and can switch between different flavor states. If this were the case, the Homestake experiment, designed to detect only solar electron neutrinos, would miss the other neutrino flavors into which the neutrinos had oscillated, thereby explaining the observed deficit.

2.4.2 Generalised neutrino oscillation formalism

The formal theory of neutrino oscillations was developed in 1975-76 by Eliezer and Swift [114], Fritzsch and Minkowski [122], and Pontecorvo and Bilenky [95]. The theory is based on the idea that a neutrino produced in a weak interaction exists as a quantum superposition of mass eigenstates. The following derivation of the neutrino oscillation amplitude, assuming k mass eigenstates, follows the treatment presented in [129].

In this context, natural units are used, where the speed of light, the mass of the electron, the reduced Planck constant, and the vacuum permittivity are all set to 1. A neutrino with flavor α and momentum $\vec{p}$, produced via a CCW interaction, is represented by the flavor state:

$$|\nu_\alpha\rangle = \sum_k U^*_{\alpha k} |\nu_k\rangle , \quad \alpha \in \{e, \mu, \tau\}, \tag{2.14}$$

where U is the Pontecorvo-Maki-Nakagawa-Sakata (PMNS) [168] mixing matrix, which is unitary and generally complex. The matrix elements $U_{\alpha k}$ denote the probability amplitudes for a neutrino of flavor α to be found in a mass eigenstate ν_k.

The massive neutrino states are assumed to be orthonormal, satisfying $\langle \nu_k | \nu_j \rangle = \delta_{kj}$, and the flavor states are also orthonormal due to the unitary nature of the mixing matrix U, such that $\langle \nu_\alpha | \nu_\beta \rangle = \delta_{\alpha\beta}$. Since the massive states are eigenstates of the Hamiltonian, they propagate through the vacuum as plane waves:

$$|\nu_k(t)\rangle = e^{-iE_k t} |\nu_k\rangle . \tag{2.15}$$

The time evolution of a flavor state $|\nu_\alpha(t)\rangle$ at time t is then given by:

$$|\nu_\alpha(t)\rangle = \sum_k U^*_{\alpha k} e^{-iE_k t} |\nu_k\rangle \,. \tag{2.16}$$

Using the unitarity of U, equation (2.14) can be inverted to express the mass eigenstates in terms of the flavor eigenstates:

$$|\nu_k\rangle = \sum_\alpha U_{\alpha k} |\nu_\alpha\rangle \,. \tag{2.17}$$

Substituting equation (2.17) into equation (2.16) yields:

$$|\nu_\alpha(t)\rangle = \sum_{\beta\in\{e,\mu,\tau\}} \left(\sum_k U^*_{\alpha k} e^{-iE_k t} U_{\beta k} \right) |\nu_\beta\rangle \,. \tag{2.18}$$

Therefore, the amplitude for a transition from a neutrino of flavor α at time $t = 0$ to a neutrino of flavor β at time t is:

$$A_{\nu_\alpha \to \nu_\beta}(t) = \sum_k U^*_{\alpha k} U_{\beta k} e^{-iE_k t}. \tag{2.19}$$

The corresponding probability for this transition is:

$$P_{\nu_\alpha \to \nu_\beta}(t) = \left| A_{\nu_\alpha \to \nu_\beta}(t) \right|^2 = \sum_{k,j} U^*_{\alpha k} U_{\beta k} U_{\alpha j} U^*_{\beta j} e^{-i(E_k - E_j)t}. \tag{2.20}$$

Neutrinos detected in experiments have a lower energy threshold of around 100 keV. Since the neutrino mass is less than 1 eV, as indicated by the current upper bounds set by the KATRIN experiment [37], it is a reasonable approximation to treat neutrinos as traveling at nearly the speed of light. Therefore, the energy for a mass state k can be approximated as $E_k \approx E + \frac{m_k^2}{2E}$, where $E = |\vec{p}|$. The energy difference between two mass states can then be approximated as:

$$E_k - E_j \approx \frac{\Delta m^2_{kj}}{2E}, \tag{2.21}$$

where $\Delta m^2_{kj} \equiv m^2_k - m^2_j$.

Substituting Eq. 2.21 into Eq 2.20, and considering that neutrinos propagate very close to the speed of light, so that $t = L$, where L is the distance from the source to the detector, yields:

$$P_{\nu_\alpha \to \nu_\beta}(L, E) = \sum_{k,j} U^*_{\alpha k} U_{\beta k} U_{\alpha j} U^*_{\beta j} \exp\left(-i \frac{\Delta m^2_{kj} L}{2E}\right). \tag{2.22}$$

Thus, the oscillation phase depends on the squared-mass differences between the mass states and the distance-to-energy ratio, L/E. In contrast, the oscillation amplitude depends only on the elements of the mixing matrix U. Separating the real and imaginary components of this probability expression is useful. By applying the unitarity of the matrix U, the oscillation probability can be rewritten as:

$$\begin{aligned} P_{\nu_\alpha \to \nu_\beta}(L, E) = \delta_{\alpha\beta} &- 4 \sum_{k>j} \mathfrak{Re}\left[U^*_{\alpha k} U_{\beta k} U_{\alpha j} U^*_{\beta j}\right] \sin^2\left(\frac{\Delta m^2_{kj} L}{4E}\right) \\ &+ 2 \sum_{k>j} \mathfrak{Im}\left[U^*_{\alpha k} U_{\beta k} U_{\alpha j} U^*_{\beta j}\right] \sin\left(\frac{\Delta m^2_{kj} L}{2E}\right). \end{aligned} \tag{2.23}$$

2.4.3 Two neutrino mixing

It is often beneficial to consider the case of two-neutrino mixing to simplify the oscillation formalism for practical use in experiments. This approach reduces the number of relevant parameters and is effective because most experiments are primarily sensitive to mixing between two specific neutrino flavors within the L/E range they probe.

Consider two flavor states, α, β, which may correspond to any pair among $\{e, \mu\}, \{\mu, \tau\}, \{e, \tau\}$, or a linear combination of two flavor states (e.g., $\nu_\beta = c_\mu \nu_\mu + c_\tau \nu_\tau$, with $c^2_\mu + c^2_\tau = 1$). For two mass states, ν_1 and ν_2, the effective two-neutrino mixing matrix is:

$$U = \begin{pmatrix} \cos\theta & \sin\theta \\ -\sin\theta & \cos\theta \end{pmatrix}, \tag{2.24}$$

where $0 \leq \theta \leq \pi/2$. The mass-squared difference in the two-neutrino case is defined as $\Delta m^2 \equiv \Delta m^2_{21} = m^2_2 - m^2_1$, with ν_1 being the lighter of the two mass states, ensuring that $\Delta m^2 > 0$.

By substituting the mixing matrix from Eq. 2.24 into the general oscillation probability formula $P_{\nu_\alpha \to \nu_\beta}$ given in Eq. 2.22, the two-neutrino oscillation probability simplifies to:

$$\begin{aligned} P_{\nu_\alpha \to \nu_\beta}(L, E) &= \frac{1}{2} \sin^2 2\theta \left[1 - \cos\left(\frac{\Delta m^2 L}{2E} \right) \right] \\ &= \sin^2 2\theta \sin^2 \left(\frac{\Delta m^2 L}{4E} \right), \quad (\alpha \neq \beta). \end{aligned} \tag{2.25}$$

The corresponding survival probability for the same flavor, due to unitarity, is:

$$P_{\nu_\alpha \to \nu_\alpha}(L, E) = 1 - \sin^2 2\theta \sin^2 \left(\frac{\Delta m^2 L}{4E} \right). \tag{2.26}$$

To express the oscillation probability in units commonly used in experiments—where source-detector distances are measured in meters (m) or kilometers (km), and neutrino energies are given in mega-electron volts (MeV) or giga-electron volts (GeV)—the formula becomes:

$$P_{\nu_\alpha \to \nu_\beta}(L, E) = \sin^2 2\theta \sin^2 \left(1.27 \frac{\Delta m^2\, L}{E} \right), \quad (\alpha \neq \beta). \tag{2.27}$$

2.4.4 Averaged transition probability

Due to the finite spatial and energy resolution of detectors and the neutrino source's finite size and energy distribution, the transition probability must be averaged over

the distribution of the L/E ratio. Given a distribution $\phi(L/E)$ that incorporates these effects, the measured average transition probability is given by:

$$\langle P_{\nu_\alpha \to \nu_\beta}(L,E) \rangle = \frac{1}{2} \sin^2 2\theta \left[1 - \left\langle \cos\left(\frac{\Delta m^2 L}{2E} \right) \right\rangle \right], \quad (\alpha \neq \beta), \tag{2.28}$$

where the average is obtained by integrating over the distribution $f(L/E)$. A common example is a Gaussian distribution f with standard deviation $\sigma_{L/E}$ resulting in an average cosine term of the form:

$$\left\langle \cos\left(\frac{\Delta m^2 L}{2E} \right) \right\rangle = \cos\left(\frac{\Delta m^2}{2} \left\langle \frac{L}{E} \right\rangle \right) \exp\left[-\frac{1}{2} \left(\frac{\Delta m^2}{2} \sigma_{L/E} \right)^2 \right]. \tag{2.29}$$

2.5 Neutrino oscillation experiments

Neutrino oscillation experiments can be categorized into seven main types: solar, reactor long-baseline (LBL), reactor short-baseline (SBL), atmospheric, accelerator disappearance, and accelerator appearance. Solar experiments measure the neutrino flux produced in the Sun's fusion processes, while atmospheric experiments detect neutrinos produced by cosmic ray interactions in the Earth's atmosphere.

On the other hand, accelerator experiments measure neutrinos generated by particle beams interacting with targets in particle accelerators. These are further divided into short-baseline meter-scale experiments and long-baseline kilometer-scale experiments. Lastly, reactor experiments observe antineutrinos emitted from nuclear fission reactors at different distances. Reactor-based experiments are discussed explicitly in Section 3.1.1.

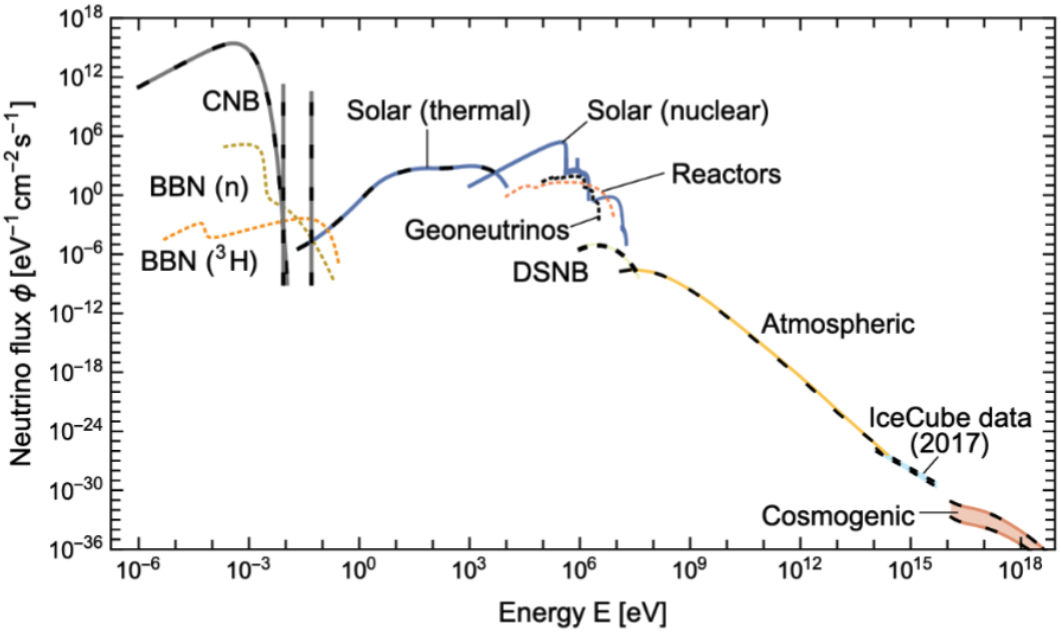


Figure 2.4: Neutrino energies and fluxes from natural and artificial sources. Source [200].

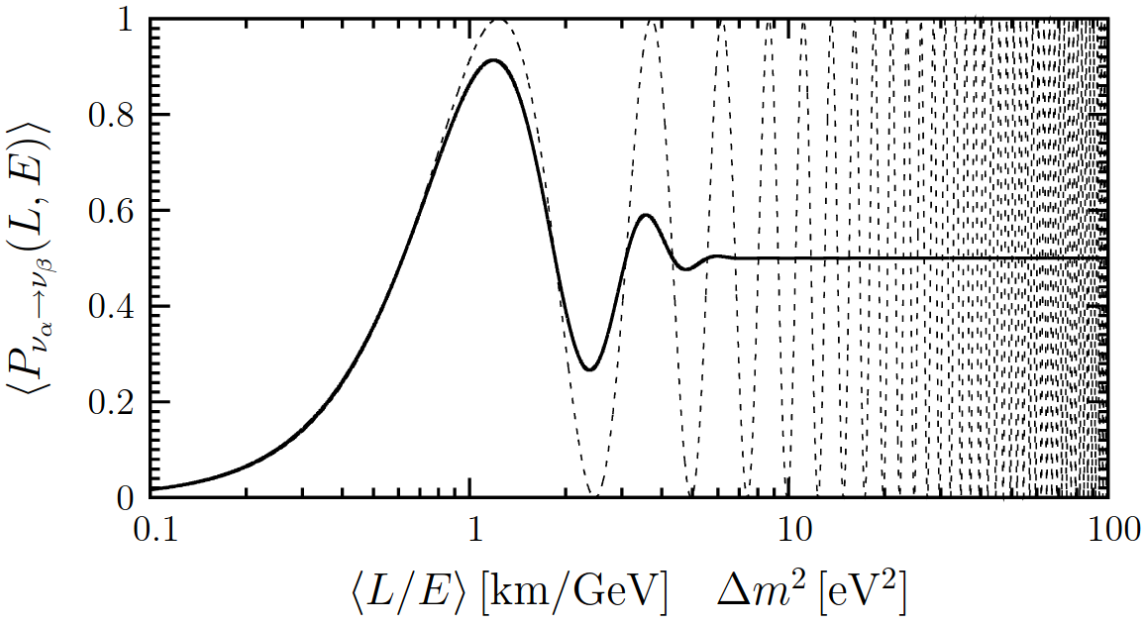


Figure 2.5: The $\nu_\alpha \to \nu_\beta$ transition probability as a function of $\frac{L}{E}\Delta m^2$, assuming $\sin^2 2\theta = 1$. The dashed line shows the transition probability, while the solid line represents the transition probability averaged over a Gaussian L/E distribution with $\sigma_{L/E} = 0.2 \left\langle \frac{L}{E} \right\rangle$. Source: [129].

2.5.1 Solar neutrino experiments

Aside from the Homestake experiment, various other experiments have aimed at detecting neutrinos generated during fusion processes in the Sun. Similar to the Homestake experiment, the Gallium experiments GALLEX [199], GNO [50], and SAGE [7] are radiochemical experiments that utilized the IBD reaction:

$$^{71}\mathrm{Ga} + \nu_e \rightarrow ^{71}\mathrm{Ge} + e^-, \tag{2.30}$$

which has a lower energy threshold of 0.233 MeV compared to the process employed by Homestake, making it more sensitive to the *pp* reaction and the electron capture ^{7}Be reaction. These reactions contribute 54% and 27% of the predicted IBD event rate within the detector, respectively.

Another type of solar neutrino experiment is the water Cherenkov-type detector. Water Cherenkov detectors identify neutrinos by detecting Cherenkov radiation produced by ultrarelativistic leptons traveling through water, resulting from neutrino interactions. The Cherenkov light is emitted with an energy spectrum of the form:

$$\frac{\mathrm{d}N}{\mathrm{d}\lambda\,\mathrm{d}x} = 2\pi\alpha\left[1 - \left(\frac{1}{nv}\right)^2\right]\lambda^{-2}, \tag{2.31}$$

for a charged particle traveling along coordinate x with velocity v and wavelength λ in a medium of refractive index n, where α is the fine structure constant [152].

In water, Cherenkov radiation consists of about 340 photons per centimeter with wavelengths from 300 to 600 nm [129], emitted in a cone with a half-angle of $\theta \approx 41°$ [113]. An array of photomultiplier tubes (PMTs) surrounding the target volume detects this radiation, enabling particle track reconstruction. A PMT coverage of at least 20% is needed for accurate neutrino identification.

Kamiokande [159] was the first to use Cherenkov radiation for neutrino detection, designed initially to detect nucleon decays, and was later adapted to detect ^{8}B neutrinos by reducing background noise and adding a shielding volume of water.

Kamiokande-II [179], a modified version, had an inner volume of 13.1 m in height and 14.4 m in diameter, containing 2142 tons of water with 948 PMTs covering 20% of the surface. Super-Kamiokande [8] expanded on this by differentiating between electron and muon neutrinos using the Cherenkov light topology, with a larger inner volume (42 m height, 39.3 m diameter) and increased PMT coverage to 40%.

The Sudbury Neutrino Observatory (SNO) [33, 34, 66] detected tau neutrinos using a heavy water Cherenkov detector. It used 1000 tons of D_2O to detect neutrinos via three channels: charged current (CC), neutral current (NC), and elastic scattering (ES). The CC interaction is:

$$\nu_e + d \rightarrow p + p + e^-, \tag{2.32}$$

with a threshold of 1.442 MeV. SNO primarily detected ^{8}B neutrinos with sensitivity above 6.9 MeV. The NC interaction:

$$\nu_\alpha + d \rightarrow p + n + \nu_\alpha, \tag{2.33}$$

has a 2.224 MeV threshold and allows detection of all three neutrino flavors, providing a model-independent measure of the total solar neutrino flux. In its second phase, SNO added NaCl to improve NC detection by enhancing neutron capture on ^{35}Cl, yielding 8.57 MeV gamma rays, which allowed better background discrimination. The third phase used ^{3}He proportional counters to increase neutron detection efficiency. SNO conclusively resolved neutrino oscillations by measuring the solar neutrino flux across multiple flavors and confirmed Bahcall's calculations from 40 years prior [66].

2.5.2 Atmospheric neutrino experiments

Cosmic rays, primarily composed of high-energy protons and some heavier nuclei, interact with the Earth's atmosphere to produce neutrinos. The primary production

of atmospheric neutrinos comes from the decay of pions created in these interactions [129]:

$$\pi^+ \to \mu^+ + \nu_\mu, \qquad \pi^- \to \mu^- + \bar{\nu}_\mu. \tag{2.34}$$

Muons from pion decay can further decay into electron neutrinos:

$$\mu^+ \to e^+ + \nu_e + \bar{\nu}_\mu, \qquad \mu^- \to e^- + \bar{\nu}_e + \nu_\mu. \tag{2.35}$$

these neutrinos cover a wide energy range, from hundreds of MeV up to the TeV scale, and underground detectors can detect those between 100 MeV and 100 GeV.

The first detections of atmospheric neutrinos were made at the East Rand Proprietary Gold Mine in South Africa [184] and the Kolar Gold Field Mine in India [16], using liquid scintillators to observe muons from ν_μ interactions. Later, the Kamiokande experiment [123] detected ν_μ and ν_e neutrinos, followed by the IMB detector [140, 100, 90, 141] and the MACRO experiment [89], both using water Cherenkov and scintillator techniques to observe these neutrinos underground.

The Soudan-2 experiment [46] used an iron tracking calorimeter to detect neutrinos via interactions in a honeycomb-structured iron target, operating from 1989 to 2001 with a fiducial exposure of 5.90 kton-years. The Frejus [2] and NUSEX [26] experiments also used tracking calorimeters for muon neutrino detection.

The IceCube Neutrino Observatory at the South Pole [3], the largest neutrino detector in operation, investigates neutrino astronomy and particle physics across a wide energy range. It uses a cubic kilometer of ice equipped with digital-optical modules to detect Cherenkov radiation from particles produced by neutrino interactions. Its DeepCore sub-array measures atmospheric neutrinos, providing some of the most stringent constraints on Δm^2 [65]. Together, IceCube-DeepCore and Super-Kamiokande [123] offer the best statistics on atmospheric ν_μ flux, crucial for global neutrino oscillation studies.

These experiments detected a deficit in the muon neutrino flux compared to the predicted electron neutrino flux, suggesting that neutrino oscillations could account for the observed discrepancies [163, 87, 147]. Analysis within the two-neutrino framework indicated that the best fit to the atmospheric data corresponds to maximal mixing, with $\sin^2 2\theta = 1.0$ and $\Delta m^2 = 2.1 \times 10^{-3}\,\mathrm{eV}^2$. These values were derived from the Super-Kamiokande (SuperK) experiment [123], which provided the most precise measurements of the atmospheric neutrino flux.

2.5.3 Accelerator experiments

Short baseline

SBL accelerator experiments are designed to measure neutrinos produced from pion decays in flight, muon decays at rest, and beam dump experiments. These experiments detect neutrinos primarily through the ν_μ channel, resulting from pion or muon decay, allowing for both appearance and disappearance studies (as summarized in Table 2.1).

Pion decay in flight (DIF) experiments focus on detecting neutrinos generated from the decay of pions and kaons, which produce either neutrinos or antineutrinos depending on the magnetic horn's polarity. The neutrino energies in these experiments are typically around 1 GeV but can reach much higher values depending on the proton beam energy. The source-detector distance is usually about 1 km, and energies above 3.5 GeV are required to produce tau neutrinos (ν_τ).

Muon decay at rest (DAR) experiments, in contrast, use lower-energy proton beams to produce antineutrinos ($\bar{\nu}_\mu$) with energies in the tens of MeV range. In these setups, most π^- mesons are absorbed by the target nuclei, so neutrino production primarily comes from π^+ decay. The typical distance between the source and detector is on the order of tens of meters.

Lastly, beam dump experiments utilize proton beams with energies in the hundreds of GeV. A thick target stops the proton beam, producing heavy hadrons that decay

into muons and electrons. This process generates neutrinos (ν_μ and ν_e) with energies around 100 GeV, and the detectors are typically placed about 1 km from the source.

Long baseline

Long-baseline accelerator experiments are defined by having source-to-detector distances of over 100 km. In these experiments, neutrinos are generated through the decay of pions and kaons in flight. Prominent examples of such experiments include K2K [173], MINOS [171], OPERA [22], T2K [126], and NOνA [45]. Looking ahead, future experiments in this category include Hyper-Kamiokande (Hyper-K) [137], which will employ a water Cherenkov detector, and the Deep Underground Neutrino Experiment (DUNE) [13], which plans to use a liquid argon time projection chamber.

2.6 Consolidating the 3-neutrino oscillation picture

2.6.1 Why three neutrinos?

The number of light neutrino species that interact via the standard electroweak interactions can be determined by studying the process:

$$Z^0 \to \nu_\alpha + \bar{\nu}_\alpha. \tag{2.36}$$

The partial width of this decay, $\Gamma_{\nu\bar{\nu}}$, is precisely calculable within the Standard Model:

$$\Gamma_{\nu\bar{\nu}} = 166.9\,\text{MeV}. \tag{2.37}$$

Thus, the Z boson will have a branching ratio into invisible final states that is proportional to the number of light neutrino species:

$$\Gamma_{\text{invisible}} = N_\nu\,\Gamma_{\nu\bar{\nu}}. \tag{2.38}$$

Table 2.1: Short Baseline Accelerator experiments and the oscillation channel tested. Source [5].

Experiment	**Process**	**Type**
LSND [28]	$\overline{\nu}_\mu \to \overline{\nu}_e$	Muon DAR
KARMEN [73]	$\overline{\nu}_\mu \to \overline{\nu}_e$	Muon DAR
LAMPF [121]	$\overline{\nu}_\mu \to \overline{\nu}_e$	Muon DAR
BNB-MiniBooNE [30, 31]	$\nu_\mu \to \nu_e$	Pion DIF
BNB-MiniBooNE [29, 32]	$\overline{\nu}_\mu \to \overline{\nu}_e$	Pion DIF
NumI-MB [17]	$\nu_\mu \to \nu_e$	Pion DIF
SciBooNE [167]	$\nu_\mu \to \nu_\mu$	Pion DIF
SciBooNE [101]	$\overline{\nu}_\mu \to \overline{\nu}_\mu$	Pion DIF
NOMAD [85]	$\nu_\mu \to \nu_e$	Pion DIF
CCFR [192]	$\nu_\mu \to \nu_\mu$	Pion DIF
CDHS [111]	$\nu_\mu \to \nu_\mu$	Pion DIF
FNAL-E531 [198]	$\nu_\mu \to \nu_\tau$	Pion DIF
BEBC [193]	$\nu_\mu \to \nu_e$	Beam Dump
CHARM [91]	$\nu_\mu \to \nu_\tau$	Pion DIF
CHARM [110]	$\nu_\mu \to \nu_\mu$	Beam Dump
CHORUS [116]	$\nu_\mu \to \nu_\tau$	Pion DIF
NOMAD [84]	$\nu_\mu \to \nu_\tau$	Pion DIF
CHORUS [116]	$\nu_e \to \nu_\tau$	Pion DIF
NOMAD [84]	$\nu_e \to \nu_\tau$	Pion DIF
CCFR [169]	$\overline{\nu}_\mu \to \overline{\nu}_\tau$	Pion DIF
CCFR [174]	$\overline{\nu}_e \to \overline{\nu}_\tau$	Pion DIF

The invisible width can be obtained experimentally by subtracting the contributions of all visible channels from the measured total width:

$$\Gamma_{\text{invisible}} = \Gamma_{\text{tot}} - \Gamma_{\text{vis}} = 498 \pm 4.2\,\text{MeV}. \tag{2.39}$$

This result can be interpreted [134] as indicating that the number of light, active neutrino species is:

$$N_\nu = \frac{\Gamma_{\text{invisible}}}{\Gamma_{\nu\bar{\nu}}} = 2.994 \pm 0.012. \tag{2.40}$$

2.6.2 Putting experimental results into context

In the three-neutrino framework of the SM, the oscillation probability given in Eq. 2.23 with $k = 3$ can be expressed using the PMNS matrix:

$$U_{\text{PMNS}} = \begin{pmatrix} c_{12}c_{13} & s_{12}c_{13} & s_{13}e^{-i\delta_{CP}} \\ -s_{12}c_{23} - c_{12}s_{23}s_{13}e^{i\delta_{CP}} & c_{12}c_{23} - s_{12}s_{23}s_{13}e^{i\delta_{CP}} & s_{23}c_{13} \\ s_{12}s_{23} - c_{12}c_{23}s_{13}e^{i\delta_{CP}} & -c_{12}s_{23} - s_{12}c_{23}s_{13}e^{i\delta_{CP}} & c_{23}c_{13} \end{pmatrix}, \tag{2.41}$$

where $c_{ab} = \cos\theta_{ab}$ and $s_{ab} = \sin\theta_{ab}$. This framework is characterized by three mixing angles—θ_{12}, θ_{13}, and θ_{23}—and a CP-violating phase, δ_{CP}. Suppose neutrinos are Majorana particles, meaning they are their own antiparticles. In that case, there are two additional phases (often labeled α and β), which only appear in processes that violate lepton number conservation and do not affect neutrino oscillations.

Table 2.2 summarizes these standard oscillation parameters and the primary methods and neutrino sources used to measure them. A key question in neutrino physics is whether the mass state predominantly consisting of the first-generation electron neutrino is the heaviest or the lightest. This open question is referred to as the 'mass ordering', which can be either normal or inverted. In the standard terminology, a normal mass ordering corresponds to $m_3 > m_2 > m_1$ (with $\Delta m^2_{31} > 0$),

while an inverted mass ordering corresponds to $m_2 > m_1 > m_3$ (with $\Delta m^2_{31} < 0$). The terms 'normal' and 'inverted' compare this situation with the quark sector, where the mass state primarily composed of the first-generation up quark is the lightest.

While the three-neutrino model has successfully explained solar and atmospheric anomalies and observed oscillations in long-baseline reactor and beam experiments, recent indications suggest deviations from the three-neutrino paradigm. Many of these anomalies share a common feature: they are observed primarily in association with electron neutrino detections—whether from electron or muon neutrino sources—using either Cherenkov or scintillator detectors and at relatively short baselines from the neutrino sources.

2.7 Experimental Anomalies

Over the last decade, four long-standing anomalies in the neutrino sector have served as primary drivers in developing a vibrant short-baseline neutrino program. These are:

- **The Reactor Antineutrino Anomaly (RAA)**: refers to a discrepancy observed in the measured flux of electron antineutrinos from nuclear reactors compared to theoretical predictions. Around 2011, several experiments reported detecting 5–7% fewer antineutrinos than expected over baselines of about 10-100 meters. This anomaly raised the possibility that some electron antineutrinos were 'disappearing' due to oscillation into a new type of neutrino that does not interact via the weak force — a sterile neutrino. The RAA remains an area of active research, with ongoing debates about whether the anomaly is due to new physics or uncertainties in modeling antineutrino production in reactors [170]. See more details in Section 3.3.

- **Gallium Anomaly**: The Gallium Anomaly arises from experiments designed to detect neutrinos using gallium-based detectors, such as the GALLEX and

Table 2.2: Standard neutrino parameters, the main method(s) to determine them, the most important source(s) for the determination, and the current status. Except for the phases α and β (for the case of Majorana neutrinos), all unknown parameters are expected to be determined within the next 20 years. Source [5].

Parameter	**Main method(s)**	**Source(s)**	**Status**
θ_{12}	Oscillations	solar, reactor	known
θ_{23}	Oscillations	atmospheric, accelerator	known
θ_{13}	Oscillations	reactor, accelerator	known
δ_{CP}	Oscillations	accelerator	hints
α, β	Rare processes	double beta decay	unknown
Δm^2_{21}	Oscillations	reactor, solar	known
$\lvert\Delta m^2_{31}\rvert$	Oscillations	reactor, accelerator, atmospheric	known
Ordering (sgn Δm^2_{31})	Oscillations	reactor, accelerator, atmospheric	hints
$m_{1,2,3}$	Kinematics	β decay, cosmology	limits

Table 2.3: Best fit three neutrino oscillation parameters from 2021 NuFit analysis [132]. For normal ordering (NO), $l = 1$, for inverted ordering (IO), $l = 2$.

Parameter	**NO best fit $\pm1\sigma$**	**IO best fit $\pm1\sigma$**
$\sin^2\theta_{12}$	$0.304^{+0.012}_{-0.012}$	$0.304^{+0.013}_{-0.012}$
$\sin^2\theta_{23}$	$0.405^{+0.019}_{-0.016}$	$0.570^{+0.016}_{-0.022}$
$\sin^2\theta_{13}$	$0.02246^{+0.00062}_{-0.00062}$	$0.02241^{+0.00074}_{-0.00062}$
$\delta_{CP}/^\circ$	230^{+36}_{-25}	278^{+22}_{-30}
$\frac{\Delta m^2_{21}}{10^{-5}\mathrm{eV}^2}$	$7.42^{+0.21}_{-0.20}$	$7.42^{+0.21}_{-0.20}$
$\frac{\Delta m^2_{3l}}{10^{-3}\mathrm{eV}^2}$	$+2.510^{+0.027}_{-0.027}$	$-2.490^{+0.026}_{-0.028}$

SAGE experiments, initially conducted in the 1990s to study solar neutrinos. These experiments also used intense artificial radioactive sources to calibrate the detectors. When calibrating with known neutrino sources, the detected number of electron neutrinos was consistently lower than predicted — by about 10-20%. This deficit could indicate the oscillation of electron neutrinos into sterile neutrinos over short baselines (of a few meters) [50, 7].

- **LSND and MiniBooNE Anomalies**: The Liquid Scintillator Neutrino Detector (LSND) experiment at Los Alamos National Laboratory (conducted in the 1990s) and the MiniBooNE experiment at Fermilab (operational since the early 2000s) both reported evidence for anomalous neutrino behavior over short baselines. LSND observed an excess of electron antineutrinos in a beam of muon antineutrinos, suggesting possible oscillations from $\bar{\nu}_\mu$ to $\bar{\nu}_e$ that the three-neutrino framework could not explain. MiniBooNE, a follow-up experiment designed to test this result, also reported an excess of electron neutrinos and antineutrinos over short baselines consistent with the LSND signal. These findings suggest that additional neutrino oscillation channels might exist, potentially involving sterile neutrinos with mass differences on the order of 1 eV^2. However, this interpretation remains controversial, and some physicists argue that other, less exotic explanations (such as unaccounted-for backgrounds or detector effects) could account for the observed anomalies [28, 30].

2.7.1 Sterile neutrinos (3+1 formalism)

The leading hypothesis to explain the short-baseline anomalies is the existence of sterile neutrinos. Unlike the three known 'active' neutrinos (electron, muon, and tau neutrinos), sterile neutrinos do not interact via the weak nuclear force, making them undetectable except through gravitational effects or via mixing with active neutrinos.

If sterile neutrinos exist, they could cause active neutrinos to oscillate into sterile states over short distances, effectively making some neutrinos 'disappear.' This would

account for the observed deficits in SBL neutrino experiments. In the simplest 3+1 model, the standard neutrino sector is extended by an additional neutrino flavor, ν_s, a gauge singlet that does not participate in weak interactions. The three active neutrino flavors and the sterile neutrino are linear combinations of four mass eigenstates, where the mass m_4 is assumed to be of the order of ~ 1 eV, as motivated by the LSND anomaly.

To describe this mixing, the 3×3 PMNS matrix shown in Eq. 2.41 is extended to a 4×4 matrix, $U_{\alpha i}$, with $\alpha = e, \mu, \tau, s$ and $i = 1, \ldots, 4$. To avoid dependence on parametrization, it is often useful to work directly with the mixing matrix elements U_{e4}, $U_{\mu 4}$, and $U_{\tau 4}$ as described in [5]. In this framework, the fourth mass eigenstate is assumed to be predominantly sterile and significantly heavier than the others, such that $\Delta m^2_{41} \gg |\Delta m^2_{31}|, \Delta m^2_{21}$. This approximation allows Δm^2_{31} and Δm^2_{21} to be considered nearly degenerate and close to zero. The large mass splitting Δm^2_{41} enables short-baseline neutrino oscillations.

In the limit where oscillations due to Δm^2_{31} and Δm^2_{21} are negligible, short-baseline oscillations can be approximated by:

$$P(\nu_e \to \nu_e) \simeq 1 - 4|U_{e4}|^2(1 - |U_{e4}|^2)\sin^2\left(\frac{\Delta m^2_{41} L}{4E_\nu}\right) \equiv 1 - \sin^2(2\theta_{ee})\sin^2\left(\frac{\Delta m^2_{41} L}{4E_\nu}\right), \tag{2.42}$$

$$P(\nu_\mu \to \nu_\mu) \simeq 1 - 4|U_{\mu 4}|^2(1 - |U_{\mu 4}|^2)\sin^2\left(\frac{\Delta m^2_{41} L}{4E_\nu}\right) \equiv 1 - \sin^2(2\theta_{\mu\mu})\sin^2\left(\frac{\Delta m^2_{41} L}{4E_\nu}\right), \tag{2.43}$$

$$P(\nu_\mu \to \nu_e) \simeq 4|U_{\mu 4}|^2|U_{e4}|^2\sin^2\left(\frac{\Delta m^2_{41} L}{4E_\nu}\right) \equiv \sin^2(2\theta_{\mu e})\sin^2\left(\frac{\Delta m^2_{41} L}{4E_\nu}\right). \tag{2.44}$$

These equations do not make explicit assumptions about $U_{\tau 4}$ (or, consequently, U_{s4}). However, unitarity requires that:

$$|U_{e4}|^2 + |U_{\mu 4}|^2 + |U_{\tau 4}|^2 + |U_{s4}|^2 = 1. \tag{2.45}$$

The focus is placed on electron and muon neutrino flavors because these are the channels most extensively studied and where short-baseline anomalies have been observed. In this scenario, oscillations are significant for $L/E_\nu \approx$ m/MeV or km/GeV if $\Delta m^2_{41} \approx 1$ eV^2. Crucially, the relationships among Eqs. 2.42–2.44 imply that if both $|U_{e4}|^2$ and $|U_{\mu 4}|^2$ are nonzero, then electron neutrino disappearance, muon neutrino disappearance, and muon-to-electron neutrino appearance must all occur at the same L/E_ν. The oscillation amplitudes for appearance and disappearance are related by:

$$\sin^2(2\theta_{\mu e}) \leq \frac{1}{4}\sin^2(2\theta_{\mu\mu})\sin^2(2\theta_{ee}).$$

This relation allows combinations of experiments to over-constrain the 3+1 model, a key feature exploited by global fits when performing combined analyses of neutrino appearance and disappearance data. The possible resolution of a sterile neutrino oscillation at meter-scale baseline with MeV-scale neutrinos motivates a reactor-based short baseline antineutrino experiment such as PROSPECT.

2.8 Chapter summary

This chapter provided an overview of the history and theory of neutrino oscillation physics, establishing the foundation for the reactor measurements discussed in the subsequent chapters. Additionally, it introduced the sterile neutrino hypothesis, a leading theory proposed to explain various anomalies observed in reactor and beam-based neutrino experiments.

Chapter 3

Reactor Neutrino Physics

3.1 Nuclear reactors as a neutrino factory

Nuclear reactors are an exceptionally potent and plentiful reservoir of MeV-scale antineutrinos, offering a distinct flavor purity. Within reactors, electron antineutrinos emerge as a result of the beta decay reactions of unstable, neutron-rich byproducts generated during nuclear fission [206]

$$ {}^{A}_{Z}B \rightarrow {}^{A}_{Z+1}C_{N-1} + e^{+} + \bar{\nu}_{e} \tag{3.1} $$

as illustrated in Fig. 3.1. On average, each fission of one of the fissionable isotopes yields two fission fragments and some free neutrons. The fragments typically undergo six beta decays, each of which produces one $\bar{\nu}_e$ as show in in Fig. 3.2.

The energy spectrum of $\bar{\nu}_e$ emitted from an active reactor core reflects the decay schemes inherent in decaying isotopes. These schemes span a broad energy range, from sub-MeV to approximately 10 MeV. Additionally, the composition of the energy spectrum is intricately influenced by the relative abundance of these isotopes within the nuclear fuel [39].

Roughly speaking, nuclear reactors can be categorized based on the isotopic composition of their fuel. For example, research reactors utilize highly isotopically

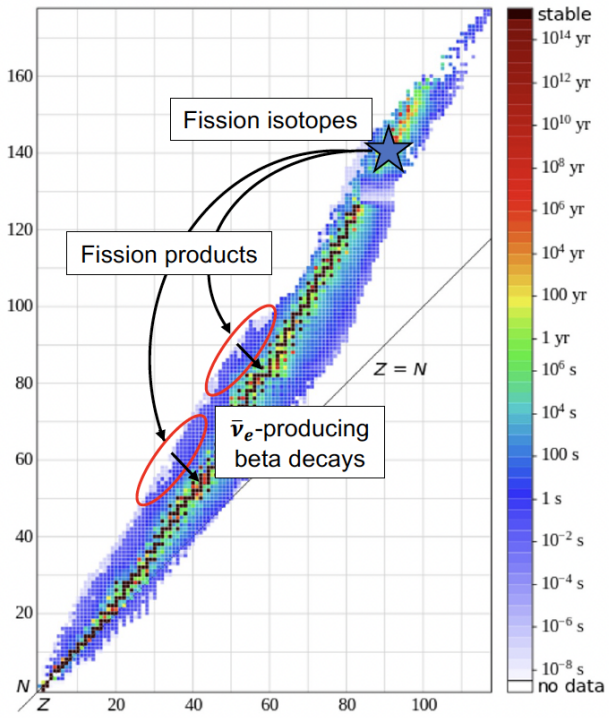


Figure 3.1: Chart of nuclides (Z vs. N) displaying the transition from fission isotopes to fission products where subsequent beta decays produce electron antineutrinos. Source [207].

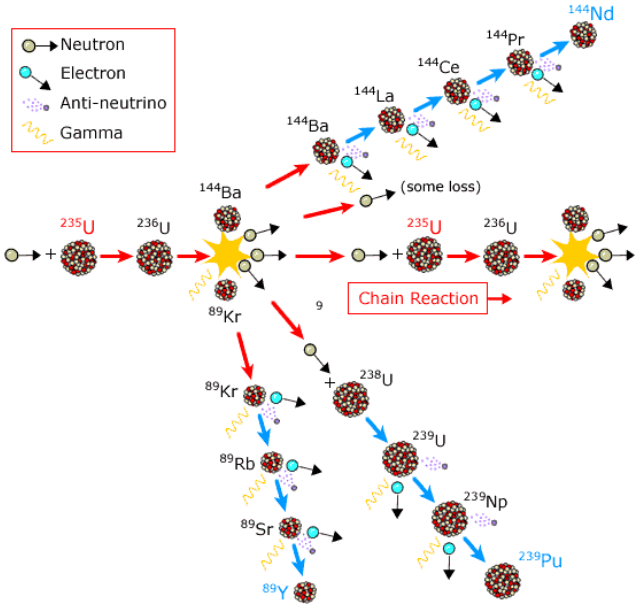


Figure 3.2: Schematic of the fission process taking place in the core of a nuclear reactor. Source [196].

enriched (HEU) cores that burn only ^{235}U, while the core of commercial reactor facilities burns an evolving mixture of all fissile isotopes (LEU). Electron antineutrinos produced at nuclear reactors can be detected via multiple detection channels, IBD on protons or other nuclei, neutral current inelastic nuclear scattering, neutrino-electron elastic scattering, and coherent elastic neutrino-nucleus scattering [183].

In recent decades, various experiments at both research and commercial reactor facilities have ushered in a precision era for reactor antineutrino measurements [63, 47]. Most of these experiments implemented liquid scintillator (LS) technologies and utilized the IBD interaction as the primary mechanism for antineutrino detection. In this process, an $\overline{\nu}_e$ interacts with a proton in the LS, producing a positron and a neutron. As a result, IBD candidates are reconstructed by taking advantage of the spatial-temporal correlation of a prompt electromagnetic deposition (e^+ ionization and annihilation) and a delayed neutron capture on either hydrogen or on a dopant mixed with the LS such as lithium (Li) or gadolinium (Gd). These experimental efforts spanning baselines from 7-2000 m from the reactor cores have enabled an assessment of antineutrino energy spectra and flux originating from the main fissile isotopes (^{235}U, ^{238}U, ^{239}Pu, and ^{241}Pu).

Locations of current and recent past experiments are illustrated in Fig. 3.3. Most of these have been at commercial power reactors, which operate in the $\sim$GW$_{\text{th}}$ regime and burn fuel with a relatively low-level of ^{235}U enrichment (low enriched, or LEU).

3.1.1 Reactor-based oscillation experiments

Considering the 3-neutrino oscillation formalism described in Section 2.6, Eq.2.23 for k=3 can provide the electron-disappearance probability of the form

$$
\begin{aligned}
P_{\bar{\nu}_e \to \bar{\nu}_e} &= 1 - 4|U_{e1}^2||U_{e3}^2| \sin^2 \Delta_{31} - 4|U_{e2}^2||U_{e3}^2| \sin^2 \Delta_{32} - 4|U_{e1}^2||U_{e2}^2| \sin^2 \Delta_{21} \\
&= 1 - \sin^2 2\theta_{13}(\cos^2 \theta_{12} \sin^2 \Delta_{31} + \sin^2 \theta_{12} \sin^2 \Delta_{32}) - \cos^4 \theta_{13} \sin^2 2\theta_{12} \sin^2 \Delta_{21},
\end{aligned}
\tag{3.2}
$$

where it can be observed that reactor antineutrino disappearance offers a clean experimental channel that depends solely on the oscillation parameters θ_{12}, θ_{13}, Δm^2_{21}, Δm^2_{31}, and the neutrino mass ordering. This makes it an ideal approach for precision measurements of these parameters.

Fig. 3.4 shows the survival probability as a function of the travel distance L for a typical 4 MeV reactor $\bar{\nu}_e$. The large disappearance at ~60 kilometers is driven by the solar-mixing mass scale Δm^2_{21} and its corresponding large mixing angle θ_{12}, while the smaller disappearance at ~2 kilometers is caused by the atmospheric-mixing mass scale $\Delta m^2_{31} \sim \Delta m^2_{32}$ and the small mixing angle θ_{13}. The two very different Δm^2 scales benefit designs of reactor antineutrino oscillation experiments, which can isolate the parameters of interest and improve the precision of their determination by placing detectors at strategic baselines.

Much like accelerator-based experiments, reactor antineutrino experiments can be categorized between long and short baseline. Long-baseline experiments have usually occurred at LEU reactors, while short-baseline experiments have favored research HEU reactors.

Long baseline

The KamLAND experiment [10], constructed in the early 2000s in Japan, was the first reactor antineutrino experiment to provide evidence of neutrino oscillations. Located in central Japan, KamLAND is surrounded by 55 nuclear reactor cores, with a flux-weighted average baseline of approximately 180 kilometers. As shown in Fig. 3.4, this baseline makes KamLAND particularly sensitive to the solar mixing parameters

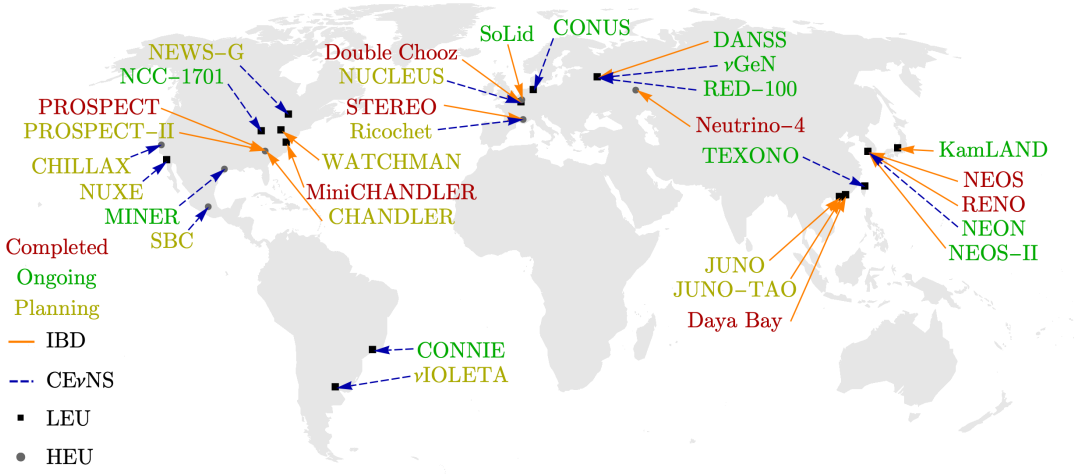


Figure 3.3: Map of planned, current, and completed reactor antineutrino experiments. The text color indicates experimental status, while the arrow indicates the interaction channel used by the experiment. Only completed experiments taking data after 2010 are included. Source [39]

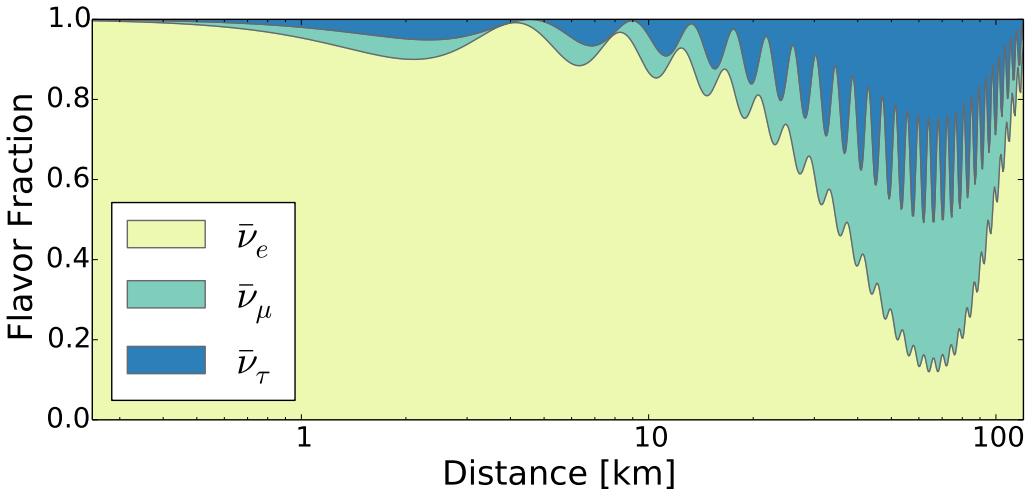


Figure 3.4: Expected flavor composition of the reactor antineutrino flux as a function of distance to a reactor core for neutrinos of 4 MeV energy. The light yellow region corresponds to the survival probability of $\bar{\nu}_e$ that reactor antineutrino experiments can measure by placing their detectors at different baselines. Source [203].

Δm^2_{21} and θ_{12}. It allows it to benefit from a well-understood neutrino source and a more straightforward vacuum oscillation formula than solar neutrino experiments.

The KamLAND detector consists of a one-kiloton liquid scintillator target within a 13-meter-diameter transparent balloon and surrounded by a region of mineral oil with 1,879 PMTs. In 2008, KamLAND observed 1,609 events over a 2.9 kton-year exposure, which was only about 60% of the expected signal in the absence of oscillations [10]. The measured survival probability exhibited a distinct oscillatory pattern as a function of L/E_ν, providing strong evidence for neutrino oscillations. These results were in excellent agreement with solar neutrino experiments, and, when combined with data from the SNO experiment [33, 34, 66], yielded the most precise measurements to date of $\tan^2\theta_{12} = 0.47^{+0.06}_{-0.05}$ and $\Delta m^2_{21} = 7.59^{+0.21}_{-0.21} \times 10^{-5}$ eV^2 [10]. Earlier reactor experiments, such as CHOOZ [72] and Palo Verde [97], did not observe $\bar{\nu}_e$ disappearance and set only an upper limit of $\sin^2 2\theta_{13} < 0.10$ at the 90% confidence level. In the 2000s, a new generation of experiments — Daya Bay [53], Double Chooz [109], and RENO [35] — was launched to measure the small mixing angle θ_{13} more precisely.

For reactor antineutrino experiments targeting the mass-squared difference Δm^2_{31} suggested by atmospheric neutrino experiments, the optimal baseline is approximately 1–2 kilometers, as indicated in Fig. 3.4. All three experiments utilized a relative measurement strategy with near and far detectors that are functionally identical, significantly reducing reactor and detector-related systematic uncertainties. After initial hints in 2011 [9, 18], clear evidence of $\bar{\nu}_e$ disappearance was reported by all three experiments in 2012, after just a few months of data collection [11, 60, 35]. Results from Double Chooz, Daya Bay, and RENO show a consistent deficit in the number of detected neutrino events compared to the no-oscillation model indicative of the presence of neutrino oscillations as illustrated in Fig. 3.5. Among them, the Daya Bay experiment (described in Section 9.3) was the most sensitive, excluding $\theta_{13} = 0$ with a significance of 5.2 σ after only 55 days of data [60].

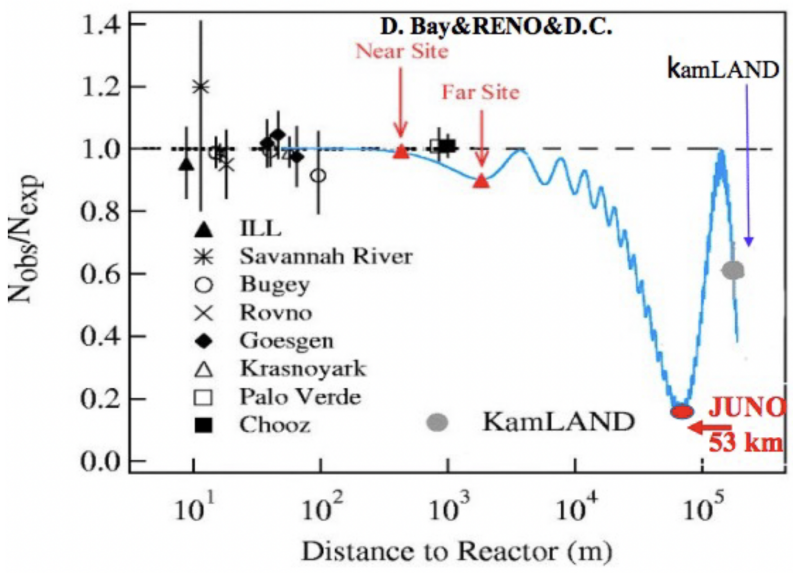


Figure 3.5: Ratio between the number of observed neutrino events and the corresponding expected value in the absence of neutrino oscillations as a function of baseline for past, present and future reactor experiments including near and far detectors for Daya Bay [53], Double Chooz [109], RENO [35], KamLAND [10] and the future JUNO [51] experiment.

Short baseline

Short-baseline reactor experiments, with source-to-detector distances of only a few meters, face unique challenges due to their proximity to reactors and locations near the Earth's surface. Unlike solar, atmospheric, and accelerator-based neutrino experiments conducted deep underground to minimize background interference, these experiments must contend with higher levels of cosmic radiation. Additionally, they face significant gamma and neutron backgrounds from reactor operations.

Examples of short-baseline reactor experiments include Savannah River [133], BUGEY [6], Krasnoyarsk [44], ILL [160], Goesgen [205], ROVNO [21], PROSPECT [70], STEREO [49], SoLid [15], NEOS [154], and Neutrino-4 [190]. A detailed description of the most relevant short-baseline reactor experiments will be provided in later chapters, focusing on the PROSPECT experiment and its new results that contribute to the global understanding of SBL reactor experiments.

3.2 Modeling antineutrino emissions from nuclear reactors

A crucial part of studying reactor-produced antineutrinos is accurately modeling their production via fission. Two main approaches have been used to predict the flux of $\bar{\nu}_e$ and the spectra per fission.

3.2.1 Summation method

The first approach, known as the 'summation' or '*ab initio*' method, relies on available nuclear data to calculate the antineutrino flux and spectrum [172, 119, 191]. This method determines the $\bar{\nu}_e$ flux and spectrum by summing the theoretical beta spectra of hundreds of fission products and thousands of beta decay branches. This approach uses theoretical models of nuclear structure and decay processes based on quantum mechanics to predict the behavior of isotopes in the reactor core. Fig. 3.6 illustrates the beta decay scheme of ^{90}Sr, a fission fragment produced from the fission of heavy nuclei such as ^{235}U and ^{239}Pu, which undergoes beta decay to form ^{90}Y and subsequently ^{90}Zr.

In a uranium fuel cycle, over 99% of the nuclear power is produced by the fission of four dominant isotopes. The cycle begins with fissions primarily in uranium isotopes, while plutonium is gradually produced through neutron capture on ^{238}U. As the reactor burn-up progresses, more than six thousand beta decay branches contribute to the neutrinos emitted by each isotope. However, the specific details of each beta decay are not always fully known [204]. For isotopes with unknown beta branches, general properties of nuclear decay, such as nuclear matrix elements and the available phase space for decay products, are used to estimate decay rates.

The absolute neutrino flux from a reactor, $\phi(E)$, can be expressed as:

$$\phi(E) = \sum_i S_i(E) f_i, \tag{3.3}$$

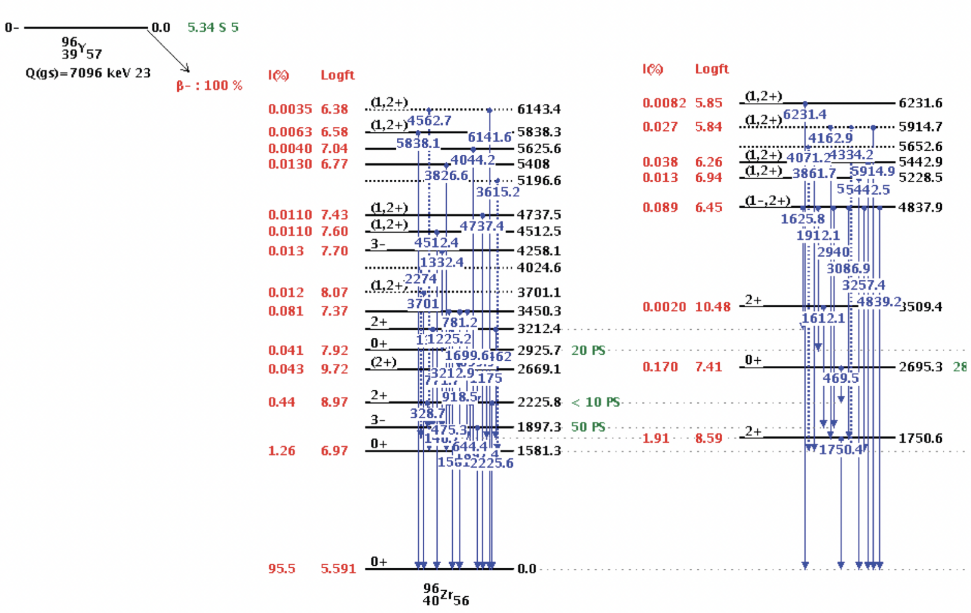


Figure 3.6: Beta decay scheme (blue) of ^{90}Sr to ^{90}Y and ^{90}Zr, showing the energy levels of the nuclei and transitions between levels [124].

where $S_i(E)$ is the neutrino yield and f_i is the fission rate of isotope i. The neutrino yield for each isotope is determined by the neutrino spectra $\nu_k(E)$ and the cumulative fission yield Y_k^i for each fission fragment k, allowing for the calculation of contributions from each of the four main fissionable isotopes:

$$S_i(E) = \sum_k \nu_k(E) Y_k^i, \tag{3.4}$$

where k represents approximately 1,800 isotopes on average [150]. The overall neutrino energy spectrum is obtained by summing the contributions from all relevant isotopes in the reactor core while considering their predicted decay rates and branching fractions. Finally, integrating over neutrino energies provides the total neutrino flux.

3.2.2 Conversion method

Beta conversion calculations of neutrino energy spectra and flux are based on empirical data obtained from direct measurements of beta spectra from fission products [149]. Thousands of beta spectra from the dominant fission isotopes are measured and fitted with individual representative beta spectra. These are converted kinematically into antineutrino energy spectra, as illustrated in Fig. 3.7. By multiplying the converted spectra by the IBD interaction cross-section and integrating over all neutrino energies, the expected absolute flux can be calculated. Beta spectrum conversions using accurate nuclear data should predict the reactor neutrino flux with an uncertainty of about 2% [150].

3.2.3 Combined models

Different fissile neutrino spectrum models combine the '*ab initio*' and beta conversion methodologies to predict reactor antineutrino flux and spectra. However, these flux prediction methods are inherently flawed. Without knowledge of the neutrino spectrum of specific fission fragments, '*ab initio*' calculations rely on information regarding the beta spectrum of thousands of decays, which is often inaccurate,

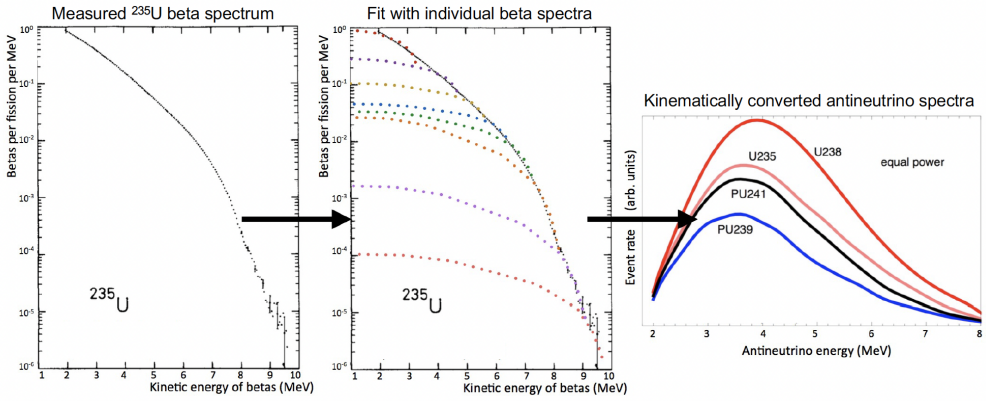


Figure 3.7: Cumulative beta spectra produced by ^{235}U, ^{238}U, ^{239}Pu, and ^{241}Pu are directly measured (left) [188], fitted with individual beta spectra (middle), and then kinematically converted into antineutrino spectra (right) [149].

incomplete, or completely unknown. Meanwhile, beta spectrum conversion is susceptible to uncertainties arising from forbidden decays in the neutrino emission spectrum which depend on unknown information about underlying nuclear structure and can contribute up to 40% of all neutrinos in specific energy ranges. Consequently, models made using these calculation procedures are not fully robust and may contribute to discrepancies between predicted and observed antineutrino spectra and fluxes.

ILL-Vogel

The ILL-Vogel reactor neutrino production model combines theoretical calculations with experimental beta spectra measurements from the Institut Laue-Langevin (ILL) reactor in Grenoble, France. In 1980, physicists at ILL measured the total beta spectra produced by the fission of ^{235}U, ^{239}Pu, and ^{241}Pu by inserting foils of these isotopes into the reactor and observing their beta decays under a thermal neutron flux using a magnetic spectrometer. These measurements, combined with the inferred neutrino yields and the evolving fuel composition, were used to predict the expected neutrino spectrum [188, 204, 139].

In 1981, Petr Vogel calculated the neutrino spectrum from ^{238}U using the summation method (Eqs. 3.3 and 3.4), which utilized cumulative fission yields from the Evaluated Nuclear Data File (ENDF/B-V) and considered the effects of fission, beta decay, and neutron capture by fission fragments under a neutron flux. The combination of ILL's experimental model for ^{235}U, ^{239}Pu, and ^{241}Pu with Vogel's theoretical model for ^{238}U created the first comprehensive reactor neutrino production model, providing a reference spectrum that laid the groundwork for future improvements.

Huber-Mueller

In 2011, Patrick Huber reanalyzed the neutrino production model for ^{235}U, ^{239}Pu, and ^{241}Pu initially developed by the ILL, while Thiago Mueller revised Vogel's model for ^{238}U. Their updated predictions of reactor neutrino energy spectra and flux incorporated new experimental data and corrected for systematic uncertainties found in the original ILL measurements [149].

Several theoretical corrections were introduced to account for transitions between nuclear energy levels, known as forbidden decays, which deviate from the standard beta decay rules and significantly affect the shape of the energy spectrum. Additional modifications were made to account for nuclear structure effects, which impact beta decay rates, and the finite size of fissile nuclei, which influences the distribution of beta decay energies [172]. The resulting Huber-Mueller (HM) reactor neutrino production model improved the accuracy and reduced the systematic uncertainties of the earlier ILL-Vogel model, making it the standard reference for reactor neutrino experiments today.

Kopeikin

In 2021 Vladimir Kopeikin reanalyzed reactor neutrino energy spectra based on new relative measurements of the ratio between cumulative beta spectra from ^{235}U and ^{239}Pu performed at a research reactor in National Research Centre Kurchatov Institute (KI) in Moscow, Russia [157]. The ^{235}U, ^{239}Pu, and ^{241}Pu neutrino spectra were predicted by using a set of 30 allowed beta transitions to fit the measured ILL cumulative beta spectra [188, 204, 139]. The corresponding $\bar{\nu}_e$ spectra of the individual transitions were summed to derive the total $\bar{\nu}_e$ spectrum [157].

KI physicists incorporated their updated measurements and compared them with ILL results to identify and correct discrepancies in the spectra normalization. The ^{235}U spectrum was found to be lower than previously estimated by the HM model, which aligns with updated results from Daya Bay and RENO. Kopeikin retained

the HM beta spectrum conversion methodology to derive the ^{235}U spectrum while correcting for the overestimated normalization [157].

A separate beta spectrum study for fast neutron fissions of ^{238}U was performed at the neutron source Forschungsreaktor München II (FRM II) in Garching, Germany [135]. The experiment used an empirical beta conversion method based on the similarity of the cumulative beta and $\bar{\nu}_e$ spectra to predict the final ^{238}U neutrino spectrum. Because the original spectrum was normalized using ^{235}U data corrections were made to the ^{238}U model to account for the changes in the ^{235}U prediction which resulted in a more accurate ^{238}U spectrum model below 3 MeV [157].

3.3 Reactor-based anomalies

3.3.1 Spectral shape anomaly, 'The Bump'

Recent measurements of antineutrino energy spectra made at both LEU and HEU reactors reported notable inconsistencies compared to theoretical predictions [143]. Illustrated in Fig. 3.8, an excess of events is observed between 5-7 MeV when comparing measured antineutrino spectra against model predictions. This observation, often called the 'bump,' has attracted substantial attention from the neutrino and nuclear physics communities. The widespread occurrence of this disagreement suggests a common factor influencing both prediction techniques, possibly originating from assumptions regarding the theoretical shape of the beta spectra utilized in these calculations. In contrast to the RAA, the existence of sterile neutrinos cannot be the cause of the bump. Still, instead, it is attributed to the mismodeling of the antineutrino yield from the different fissile isotopes [144].

The acquisition of new, highly accurate antineutrino measurements from reactors employing diverse fuel compositions holds promise for delving deeper into the nature of the observed 'bump.' These enhanced measurements offer a unique opportunity to refine our comprehension of antineutrino production by fission daughters. An

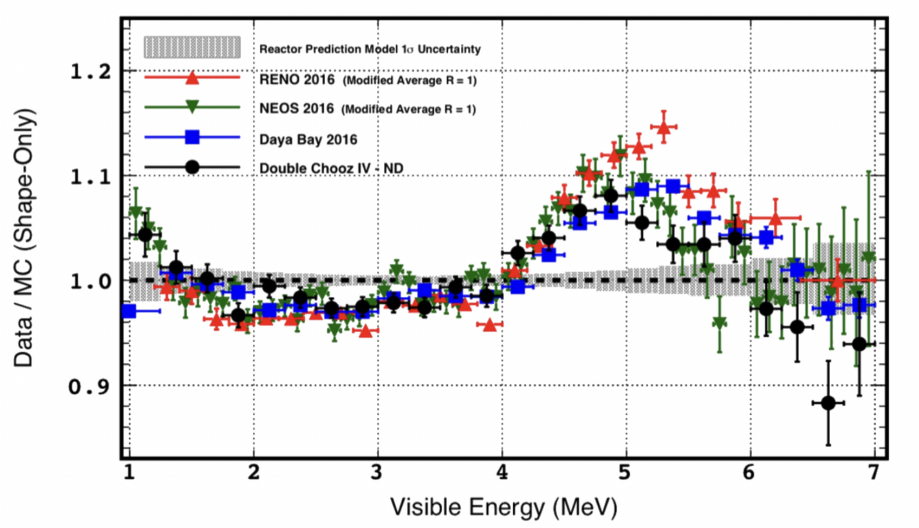


Figure 3.8: Comparisons of reactor neutrino normalized energy spectra measured by neutrino experiments deployed at commercial LEU reactor sites [108, 187].

essential aspect of this investigation involves determining whether the discrepancies in antineutrino spectrum and flux predictions extend uniformly across all four principal fission isotopes. This nuanced exploration is crucial for pinpointing specific sources of inaccuracy and advancing our overall understanding of the intricacies inherent in antineutrino behavior arising from nuclear fission processes.

3.3.2 Reactor Antineutrino Anomaly (RAA)

As observed in Fig. 3.9, a consistent deficit of approximately 6% in IBD yields compared to the predictions made by the HM has been reported by different reactor-based experiments known as the RAA [170].

As discussed in Section 2.7, a widely studied model to explain these anomalous results is the existence of an additional sterile neutrino state with an eV-scale mass difference relative to the SM neutrino flavors [127]. This scenario is commonly referred to as the '3+1' model. Prior experiments have demonstrated that reactor electron antineutrinos undergo flavor transformations during propagation from the source to the detector. If a sterile neutrino exists, this BSM physics could cause deficits in

electron antineutrino detection rates. These deficits are characterized by a modified survival probability for a two-neutrino scenario, which builds upon Eq. 2.44

$$P_{\text{dis}} \approx \sin^2 2\theta_{14} \sin^2 \left(1.27 \Delta m^2_{41}(\text{eV}^2) \frac{L(\text{m})}{E_\nu(\text{MeV})} \right), \tag{3.5}$$

where Δm^2_{41} is the mass difference squared, θ_{14} is a mixing angle describing the electron flavor content of the new mass state, and E_ν and L are the energy and travel distance (baseline) of the neutrino, respectively.

As outlined in Eq. 3.5, a mass splitting on the order of 1 eV^2 or greater leads to an observable average deficit in energy-integrated reactor antineutrino detection rates. This deficit becomes evident when comparing experimental observations with predictions for reactor experiments conducted at baselines of approximately 10 m or more [170]. To unambiguously test the hypothesis of the existence of an eV-scale sterile neutrino as the cause for the RAA, experiments must directly probe the baseline and neutrino energy dependence of reactor $\overline{\nu}_e$ signals. Any departure from the expected $1/\text{r}^2$ behavior as a function of both baseline and energy would signify the presence of an oscillation effect providing an opportunity to deduce the parameters that characterize such oscillations. Demonstration of the existence and properties of a sterile neutrino would have far-reaching implications in particle physics and cosmology.

3.4 Chapter summary

This chapter provides an overview of antineutrino production at nuclear reactors and discusses the key experiments that have significantly contributed to this field. It also outlines the models to predict reactor antineutrino flux and spectra, highlighting current discrepancies in these predictions. Additionally, the chapter addresses experimental anomalies in the reactor sector, which motivate the ongoing search for eV-scale sterile neutrino oscillations.

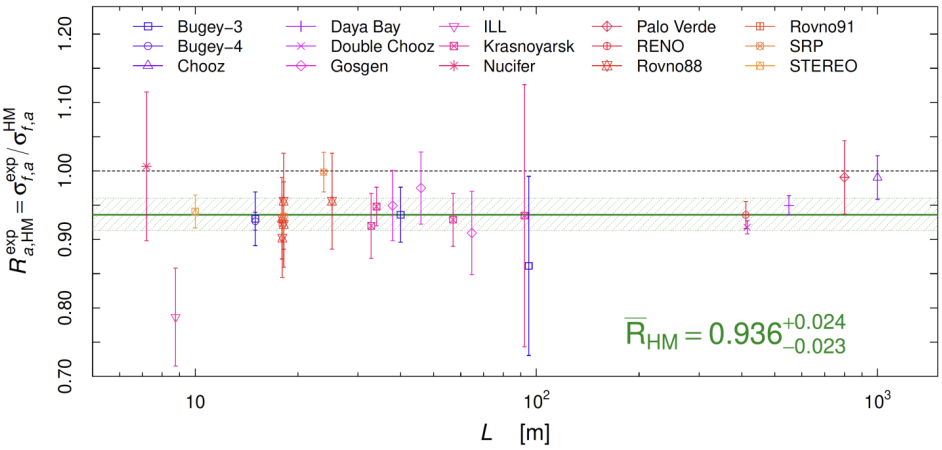


Figure 3.9: The ratio ($\mathrm{Ra}^{exp}_{a,HM}$) of the measured to predicted Inverse Beta Decay (IBD) yields is depicted as a function of baseline, with the HM model utilized for predicting IBD yields. Each data point corresponds to a specific experiment, with the error bars representing the experimental uncertainties. The green line and accompanying band illustrate the average of $\mathrm{Ra}^{exp}_{a,HM}$ and the average uncertainty, respectively [128].

Chapter 4

The PROSPECT experiment

4.1 Introduction

Previous chapters emphasized the necessity of new short-baseline reactor experiments to address experimental anomalies in the neutrino sector, specifically the RAA and the observed spectral 'bump' [170, 144]. In response to the DOE Intermediate Neutrino Research Program Funding Opportunity, the PROSPECT experiment secured funding and began construction in 2016. The Precision Reactor Oscillation and Spectrum Experiment (PROSPECT) was designed with two primary objectives: searching for eV-scale sterile neutrino oscillations and performing a precise measurement of the antineutrino energy spectrum from ^{235}U fission. Data were collected in 2018 and 2019 using the first-generation PROSPECT-I detector, deployed on the surface approximately 7-9 m from the 85 MW High Flux Isotope Reactor (HFIR) core at Oak Ridge National Laboratory. This chapter overviews the experimental site, detector design, calibration strategies, and data acquisition methodology.

4.2 Experimental Facility

A comprehensive evaluation of three potential U.S. research reactor sites was conducted to identify the most suitable location for the experiment. The reactors

assessed were located at the National Institute of Standards and Technology (NIST), Idaho National Laboratory (INL), and Oak Ridge National Laboratory (ORNL) [76]. The HFIR reactor at ORNL emerged as the ideal site due to its high power and compact core, enriched ^{235}U, availability of unoccupied near-reactor floor space[78], easy access to experiment room, and its status as a DOE user facility. HFIR supports neutron scattering, isotope production, materials irradiation, and neutron activation analysis. An aerial view of the HFIR facility at ORNL is shown in Figure 4.1.

The HFIR reactor is located approximately 250 meters above sea level within the HFIR building. Its core has a diameter of 0.435 meters and a height of 0.508 meters. It is designed with two concentric rings of ^{235}U fuel plates, achieving 93% enrichment, which are encased in an aluminum cladding and structural support system, further shielded by a robust concentric beryllium reflector. This configuration allows HFIR to reach thermal neutron flux levels exceeding 2×10^{15} n/cm^2/s within its core.

The reactor core and pressure vessel are submerged in a large water pool, with the water surface approximately eight meters above the core's midplane. Operating at a thermal power output of 85 MWth, HFIR typically runs seven cycles per year, each lasting 24 days, resulting in an operational duty cycle of about 46%. After each cycle, the entire fuel assembly is replaced. Highly enriched uranium fuel and the comprehensive core replacement every 24-day cycle ensure minimal fuel evolution,



Figure 4.1: Areal view of the HFIR facility area at ORNL. Source [162].

with over 99% of emitted electron antineutrinos originating from ^{235}U fission. Reactor-off data is crucial for accurately measuring background signals from coincidental cosmogenic sources during reactor-on periods.

4.2.1 Experiment room, detector location, and shielding strategies

The PROSPECT detector is positioned in the experiment room one floor above the HFIR core, adjacent to the pool walls, as illustrated in Fig. 4.2. This diagram also presents the inner detector, the antineutrino target, with dimensions and orientation relative to the HFIR core. The coordinate system used in this study, centered at the inner detector's core, is also depicted. Detailed in section 4.3, the PROSPECT inner detector is a rectangular prism measuring 2.045 meters in length (x-axis), 1.607 meters in height (y-axis), and 1.176 meters in width (z-axis). It is offset from the reactor core center by -1.19 meters along the z-axis and +5.09 meters along the y-axis.

The distances from the outer edges of the inner detector to the detector package vary by approximately 40 cm on the sides and bottom and about 100 cm on the top. To determine the distance from the detector to the reactor, measurements were made from a specific point on the exterior of the detector package with an estimated precision of approximately ±10 cm, using HFIR facility mechanical drawings and a measuring tape.

Given the lack of significant overburden at the HFIR facility, the PROSPECT detector faces several background challenges, necessitating effective shielding (details on IBD backgrounds are provided in section 6.3). The primary sources of background affecting antineutrino detection can be categorized into two types: single energy deposits, primarily from γ-rays entering the detector, and simultaneous energy deposits, mainly from the recoil and capture of fast neutrons. The former requires suppression to control data acquisition rates and minimize IBD backgrounds from

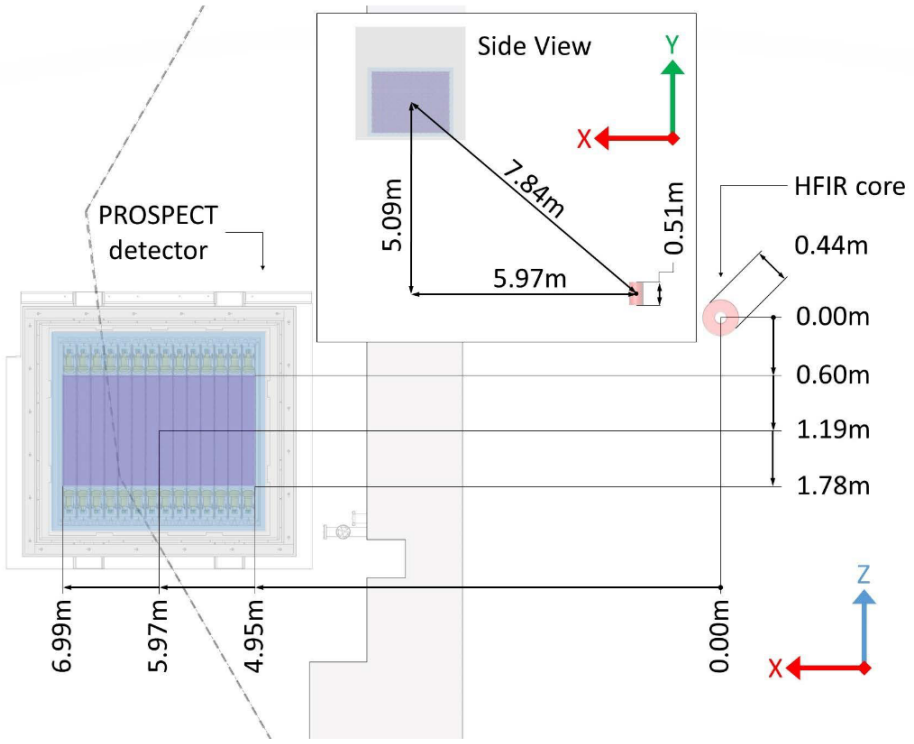


Figure 4.2: A top and side view of the PROSPECT experimental setup within the HFIR building. The illustration shows the HFIR reactor, the PROSPECT detector, the reactor pool containment wall (in gray), and the concrete monolith beneath much of the detector (indicated by a dashed line). The diagram includes horizontal and vertical distances from the reactor core center to various detector positions, as well as the coordinate axes used to define the orientation of the reactor and detector. The detector floor is aligned with the x-z plane, with the zenith pointing in the $+y$ direction. Source [70]

accidental coincidences. At the same time, the latter presents a more difficult challenge as it closely mimics the IBD signal.

Gamma-ray background measurements conducted at HFIR [80, 146, 136] identified multiple sources originating predominantly from penetrations in the shielding wall around the reactor pool. The shielding design was divided into two components to mitigate backgrounds: a fixed lead wall near the gamma-ray sources and a portable shielding package surrounding the detector volume. The local shield wall, shown in Fig. 4.3, was installed adjacent to the concrete pool wall to mitigate these background sources effectively.

The central section of the shield wall measures 3.0 meters wide and 2.1 meters high, with shorter sections on either side. Protective cages were installed around two pipes passing through the wall. The central part of the wall is made of 0.10-meter-thick lead, while the side sections use 0.05-meter-thick lead. An additional 0.10-meter-thick mini-wall was placed between the local shield wall and the EF4 opening, supported by robust steel structures for seismic safety to enhance shielding. In contrast, the passive shielding design uses a single 0.025-meter-thick lead layer surrounded by layers

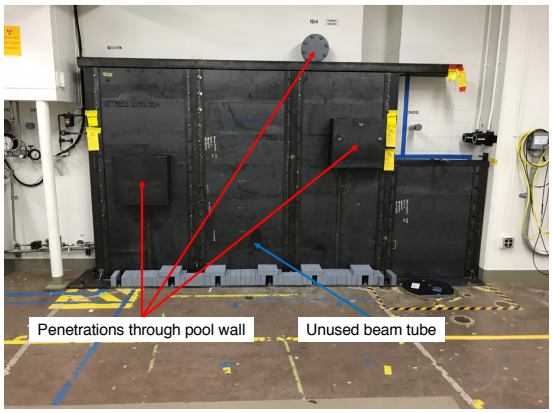


Figure 4.3: A photograph of the local shield wall, with red arrows indicating the locations of pipes penetrating the reactor pool and a blue arrow marking the position of the unused EF-4 beam line that points directly toward the reactor vessel. Source [78].

of polyethylene, borated polyethylene, and water to reduce cosmogenic background effects.

4.2.2 Modelling HFIR reactor neutrinos

More than 99% of the antineutrinos emitted by the HFIR originate from ^{235}U fission. However, neutron activation of materials surrounding the core generates a small fraction of neutrinos. The primary non-^{235}U sources of $\overline{\nu}_e$ include ^{28}Al from the fuel cladding and ^{6}He produced in the beryllium neutron reflector surrounding the core [86]. Each of these sources contributes less than 1% to the total observed $\overline{\nu}_e$ flux and predominantly affects the low-energy region of the spectrum (below 4 MeV true neutrino energy). The predicted contribution of each source to the detected spectrum is shown in Fig. 4.4.

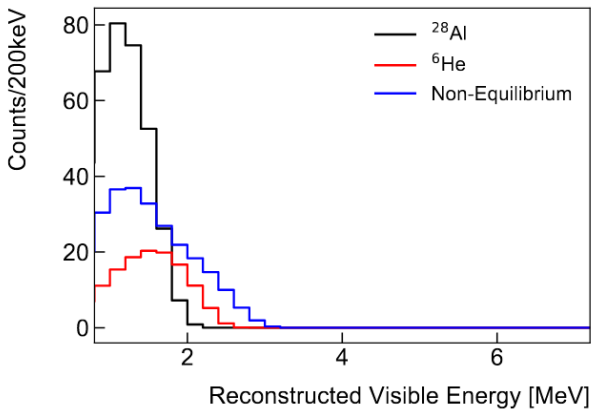


Figure 4.4: Corrections added to the predicted ^{235}U spectrum to account for non-equilibrium isotopes and neutrinos from ^{28}Al and ^{6}He. Source [86].

4.3 Detector Design

4.3.1 Description of inner detector

The PROSPECT detector, shown in Fig. 4.5, consists of an inner vessel containing four tons of pulse shape discriminating (PSD) liquid scintillator, enriched with 0.08% ^{6}Li. This vessel is surrounded by inner and outer containment tanks, shielding components, and three electronic racks for data acquisition (DAQ) and control electronics. The active scintillator volume is arranged in an 11x14 lattice, creating 154 optically isolated segments, each measuring 14.5 cm $\times$ 14.5 cm $\times$ 117.6 cm. These segments are separated by an optical grid of thin (1.18 mm) specularly reflecting panels supported by white, diffusely reflecting PLA plastic rods. Some support rods are instrumented to hold removable radioactive calibration sources, while others contain stationary optical sources, as depicted in Fig. 4.6. Non-instrumented rods are filled with square acrylic rods. The inactive materials used in the optical grid and calibration subsystems make up 3.5% of the scintillator mass within the 154 active segments. As illustrated in Fig. 4.5, the material arrangement is consistent from bottom to top, with increased shielding on the upper part of the detector to minimize cosmogenic backgrounds.

The detector segments run parallel to the north wall of the reactor pool. The end of each detector segment is enclosed by an acrylic box filled with mineral oil, housing a 5-inch PMT, a magnetic shield, a light reflector, and support structures. These PMT housings are interconnected mechanically, creating a continuous structure along the z-axis of the inner detector, outside its outermost segments. The inner detector and its support structure are housed within a rectangular acrylic vessel submerged in a water-filled aluminum tank. The inner vessel is continually purged with nitrogen cover gas to maintain inert conditions for the detector liquids.

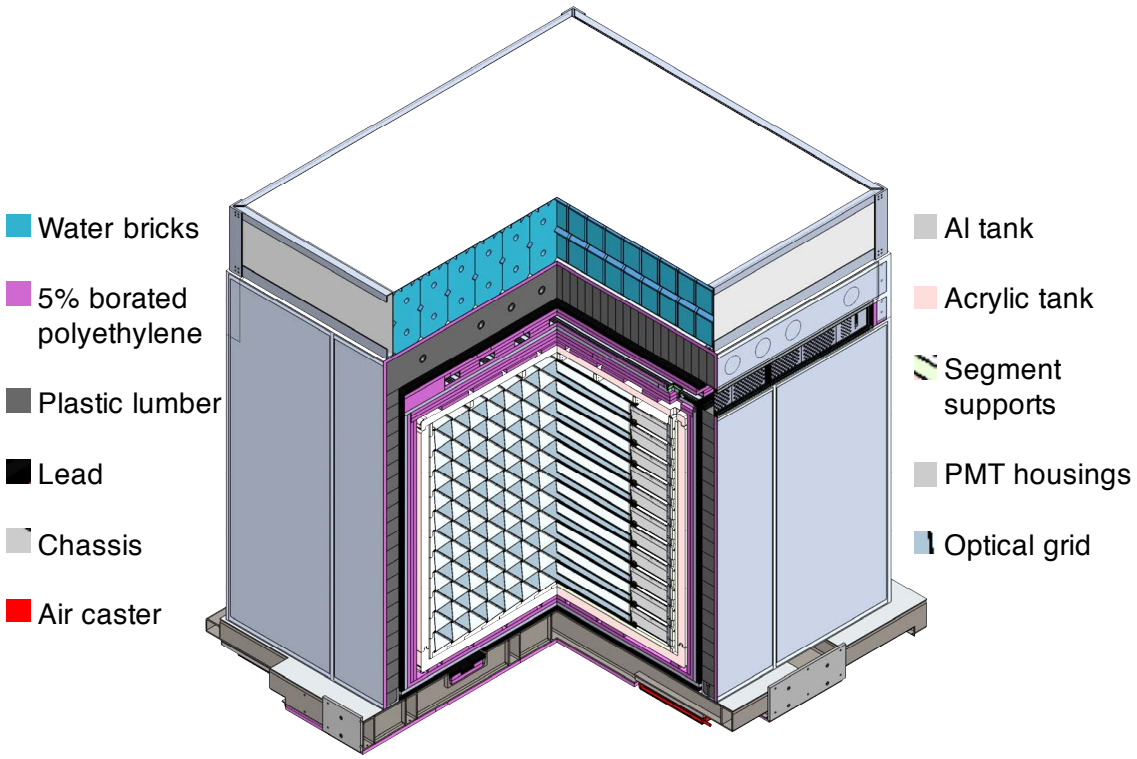


Figure 4.5: A 3D cutaway view of the detector and shielding assembly model showing the inner detector enclosed within an acrylic tank (rose), which is divided into an 11-by-14 grid by reflective optical separators. The active detector region, filled with ^{6}Li-doped liquid scintillator (LiLS), is viewed by PMT housings (beige) positioned at both ends. The grid and PMT housings are supported by acrylic segment supports (light green). Surrounding the acrylic tank are layers of borated polyethylene (purple) and a secondary aluminum tank (light gray). Source [78].

4.3.2 ^{6}Li-Doped Liquid Scintillator

While water is a cost-effective and directionally sensitive medium for monolithic neutrino detectors, liquid scinitllator is often preferred for smaller scale, surface-level detectors due to its higher light yield and increased energy resolution compared to water-based detectors. Gadolinium has been historically chosen as a dopant to enhance neutron capture signals in such detectors, emitting robust 8 MeV γ-rays [58, 12, 189]. However, in smaller, highly segmented detectors like PROSPECT, the spatial distribution of these γ-rays compromises segmentation. This issue is exacerbated as γ-rays can escape detection near the detector's edges, resulting in spatially varying detection efficiency. Moreover, given PROSPECT's location in a high γ-ray background environment, γ-rays generated by neutron capture on gadolinium could be indistinguishable from random coincidences caused by prevalent γ-ray backgrounds.

The design of the PROSPECT detector necessitated a liquid scintillator with good PSD capabilities, surpassing those of linear alkylbenzene used in previous experiments like Daya Bay [52] and RENO [35]. This requirement was crucial for rejecting backgrounds from fast neutrons and ambient γ-rays. PSD distinguishes interactions with high dE/dx, such as heavy-charged particles, from those with low dE/dx, like muons and electrons. The detector's compact volume and meter-scale segmentation required a neutron capture agent that produces only charged particles, ensuring a concise capture signature. Moreover, the scintillator had to be non-toxic, non-flammable, and easy to deploy within the HFIR reactor building. Extensive prototyping studies determined that a light yield exceeding 8000 optical photons per MeV would be necessary to achieve the desired energy resolution.

Consequently, the collaboration developed a novel lithium-doped liquid scintillator (LiLS) formulation based on EJ-309 from Eljen Technologies, renowned for its superior PSD capabilities in distinguishing electron-like recoils from nuclear recoils. This scintillator formulation also met the performance requirements, providing an

energy resolution of 4.5% RMS at 1 MeV. The reflector panels mentioned earlier were specifically designed to match the emission spectrum of this scintillator, as illustrated in Fig. 4.7.

Doping the scintillator with ^{6}Li enables neutron capture interactions characterized by the reaction:

$$n + {}^6\,\mathrm{Li} \rightarrow \alpha + t + 0.55\mathrm{MeV}ee \tag{4.1}$$

This process produces a distinct, monoenergetic signal generated by the short-range particles. The formulated LiLS with PSD capabilities effectively differentiates neutron captures from background γ-ray events, thereby minimizing the occurrence of random coincidences.

Fig. 4.8 illustrates the production process of PROSPECT's LiLS. Raw components were purified and mixed in stages within a 90-liter reaction vessel. According to [77], 10 mol/L solutions of lithium chloride were prepared in 1-liter batches. This was achieved by reacting 95.37% ^{6}Li-enriched lithium carbonate with concentrated (37% by mass) hydrochloric acid, as described by the chemical equation:

$$\mathrm{Li_2CO_3} + 2\mathrm{HCl} \rightarrow 2\mathrm{LiCl} + \mathrm{H_2O} + \mathrm{CO_2}. \tag{4.2}$$

Fig. 4.9 illustrates the susceptibility of LiLS to degrade in the air due to oxygen absorption, emphasizing the necessity of maintaining a nitrogen cover gas within the acrylic tank at all times. The final formulation of LiLS used in the PROSPECT detector contained 0.08% ^{6}Li by mass. Combustion analysis of the LiLS indicated that carbon comprised 84.34 $\pm$ 0.11% by mass and hydrogen 9.69 $\pm$ 0.21%. The density of the LiLS was measured at 0.9781 $\pm$ 0.0008 g/cc.

4.3.3 Low mass optical grid

The antineutrino target is 1.176 meters wide, 2.045 meters long, and 1.607 meters tall. As mentioned earlier, each of the 154 segments is 1.176 meters long and has a square

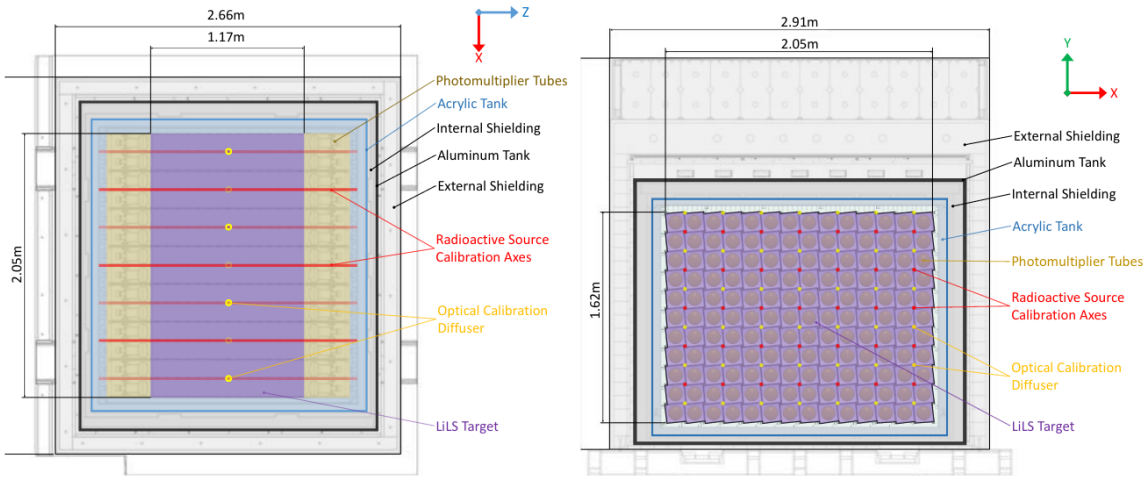


Figure 4.6: A schematic of the PROSPECT detector presented along two different orientations showing the 14 x 11 segments separated by reflector panels within the acrylic containment vessel. The detector features internal shielding made of borated polyethylene and water bricks, and external shielding composed of lead, borated polyethylene, and water. Source [78].

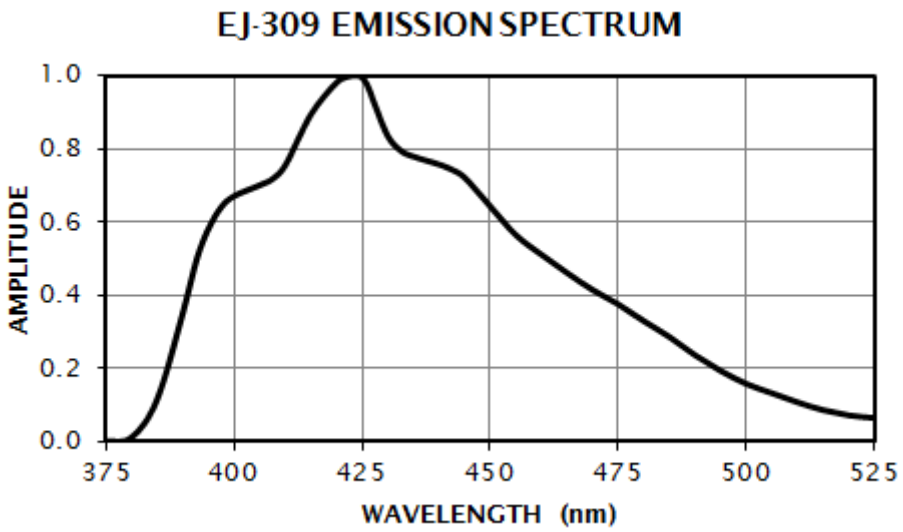


Figure 4.7: EJ-309 emission spectrum. Source [1].



Figure 4.8: LiLS production at various stages in the 90 L Chemglass reactor: raw material injection (left), mixing in progress (middle), and completion of synthesis (right). The liquid appears opaque during synthesis and turns clear once the process is finished. Source [77].

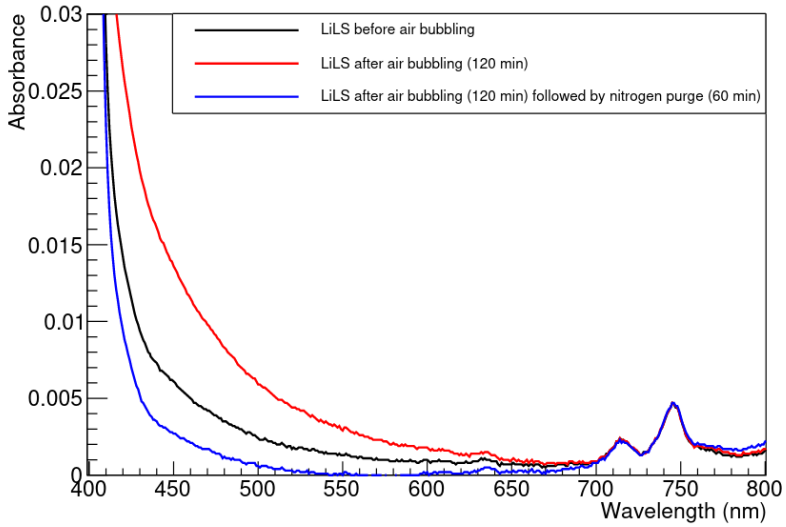


Figure 4.9: Relative absorbance of the LiLS measured after production, with curves representing conditions before exposure to air (black), after exposure to air (red), and after nitrogen sparging (blue). The data illustrate how scintillator light yield degrades over time due to oxygen contamination. Source [77].

cross-sectional area of 0.145 meters by 0.145 meters. This optical grid comprises low-mass, highly reflective optical separators secured by white 3D-printed support rods. PMT housings stabilize the grid at both ends, and acrylic supports stabilize the grid on the other four sides.

Scintillation light generated within each segment travels efficiently along the segment length with minimal cross-talk, thanks to the reflective optical separators covering about 99% of each segment's interior surface. In addition to holding the separators, the support rods contain channels running along each segment's corners, allowing for calibration source deployment throughout the detector. The combined mass of the optical grid components is less than 3% of the total target mass, reducing the energy loss of IBD positrons in non-scintillating regions. A diagram of a single detector segment's optical grid components is shown in Fig. 4.10.

To achieve the experiment's physics goals, the components of the PROSPECT optical grid must maintain high dimensional uniformity for proper detector assembly and consistent segment volumes, and they must be chemically compatible with the liquid scintillator. During assembly, dimensional checks ensured that each segment's size variation was less than 0.1%, resulting in segment volumes differing by less than 1%.

The optical separators were built with a carbon fiber backbone, covered on both sides with adhesive-backed 3M DF2000MA specularly reflecting film, an optically clear adhesive film, and a thin layer of FEP film. These layers are bonded using cold pressure lamination, and the outer FEP film layers are heat-sealed to prevent scintillator contact with the separator interior. The glossy twill carbon fiber sheet provides structural support and prevents cross-talk between optical segments. The DF2000MA polymeric film is highly reflective (>99% at normal incidence) and highly specular (>95% at normal incidence) for photons above 400 nm. Total internal reflection at the interface between the FEP layer (refractive index ∼1.33) and the PROSPECT scintillator (refractive index ∼1.56) facilitates light transport at higher incident angles. Quality assurance checks on dimensions, optical properties,

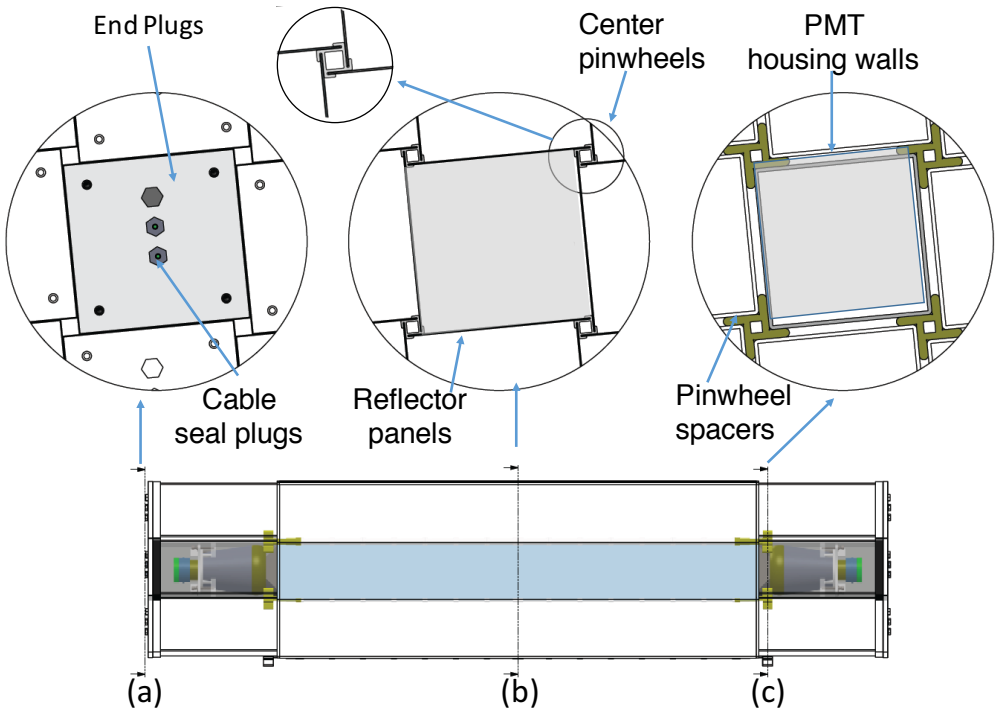


Figure 4.10: (Bottom) A depiction of a single PROSPECT segment surrounded by adjacent segments, with PMT housings inserted into the optical grid at both ends. The PMT housing is rendered transparent to reveal the PMT inside. Plane (a) shows the end plugs that secure the PMT housings. Plane (b) illustrates the center pinwheels and optical separators. The PMT housings are held in place by the end plugs and pinwheel spacers, set at an angle of 5.5°, as shown in plane (c). The detailed structure of the pinwheels can be viewed in Fig. 4.11. Source [78].

mechanical integrity, and leak-tightness were conducted on all optical separators before use.

Pinwheel support rods were made using filament-based 3D printing with a 100-micron polylactic acid filament, which is white-dyed and compatible with the scintillator. The support axes, each over 1.2 meters long, are constructed from shorter 150 mm rods of varying designs, strung onto a central Teflon tube or an extruded acrylic rod, used for calibration and un-instrumented axes, respectively. Isometric drawings of the two pinwheel designs are shown in Fig. 4.11. Each sub-rod features multiple tabs for gripping the four attached optical separators. Sub-rods closest to the PMT housings have additional thick profiles (Fig. 4.11b) that serve as the mechanical interface between the optical grid and the PMT housings or the acrylic supports on the detector's exterior.

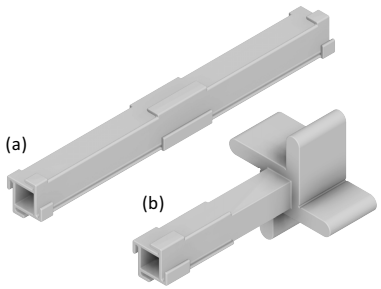


Figure 4.11: Pinwheel types: (a) Central pinwheel – features three tabs on each side to secure the optical separator. (b) End pinwheel – includes spacer arms that separate the PMT housing bodies and support the pinwheel string. Source [78].

4.3.4 Photo Multiplier Tube (PMT) modules and segment supports

PMTs with similar characteristics from two different manufacturers were selected. Specifically, 240 Hamamatsu R6594 SEL PMTs were installed in the inner segments, as shown in Fig. 4.12, while 68 ADIT Electron Tubes 9372KB (ET) PMTs were used in the outer segments. This configuration ensured that all PROSPECT segments in the fiducial region had a uniform PMT type. The main components of a PMT module are illustrated in Fig. 4.13.

The PMT housing is crafted from acrylic pieces bonded with Acrifix, forming an approximately 350 mm long rectangular shape. Slots are machined into the 144-mm-square front window and back flange to secure the 3-mm-thick white acrylic side walls. The front window, made of 13-mm-thick ultra-violet transmitting acrylic (UVT), and the back flange, made of 19-mm-thick black acrylic, feature a 130 mm diameter circular hole for PMT insertion during assembly. A 32-mm-thick clear back plug, with a cylindrical front section featuring an O-ring groove and a rear 145-mm-square section, seals the housing module once all components are installed. The module includes two cable seal plugs and a fill/test port connecting to its interior. The back plug (Fig. 4.14a) and the pinwheel spacer arms at the front support the housings. The back flange and plug design allows for rotational adjustment, ensuring the front window and back plug remain parallel. With a 132-mm-square cross-section, the sidewalls are intentionally smaller than the front window and back plug to accommodate construction variations.

A conical light guide is formed from a layer of adhesive-backed DF2000MA film and 1 mm thick acrylic. Rectangular reflector strips made from the same material are affixed to the interior walls of the housing to complete the light guide. The round PMT face is pressed into this light guide by an acrylic plate at the rear of the housing. Due to the different shapes of the Hamamatsu and ET PMT glass, different light guide shapes were required. A conical section of Hitachi Finemet surrounds the

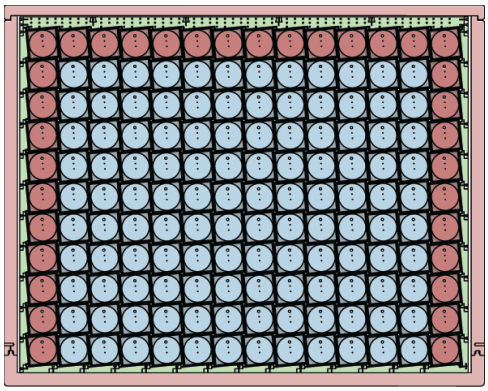


Figure 4.12: A cross-sectional view of the active PROSPECT detector illustrating 68 ET PMTs (red) placement in the outer columns and top row. The remaining segments use 240 Hamamatsu PMTs (blue). Source [78].

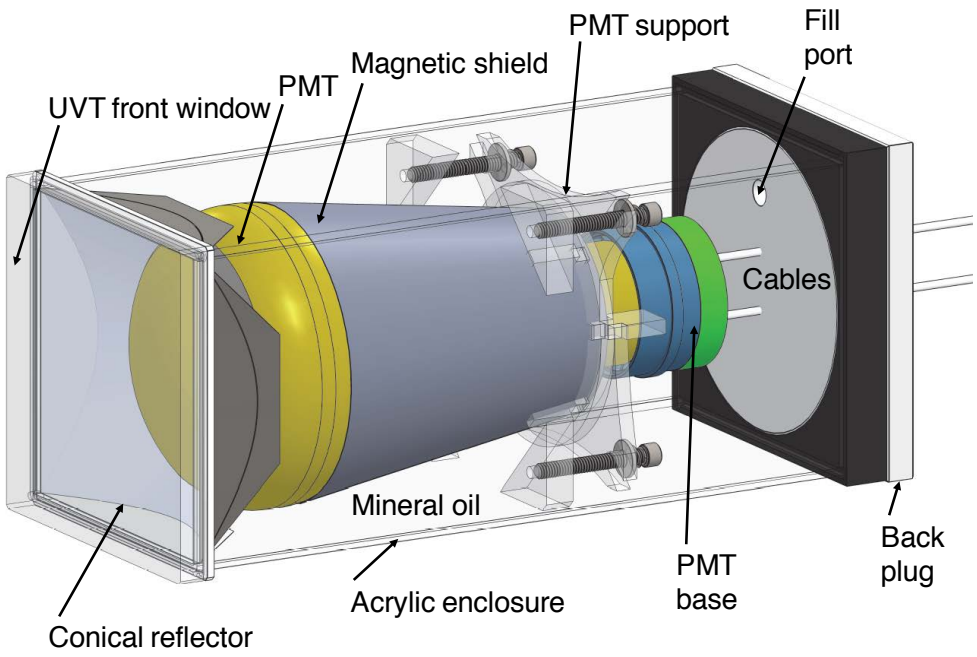


Figure 4.13: PMT housing module with all relevant components. Source [78].

PMT to shield it from stray magnetic fields. Type-specific PMT bases and sockets attach to the PMT pins and connect to signal and high voltage cables, which exit through the rear plug. Both signal and high voltage (HV) cables, made from RG188 cable, are uniformly 4.88 meters in length and terminate in bulkhead connectors that are later mounted on panels outside the aluminum tank.

After all quality control tests and PMT stability studies were completed, the housings were filled with optical-grade mineral oil. Machined acrylic segment supports beneath the bottom row of PMT housings ensure the back plug of the PMT housings was positioned at the necessary 5.5° tilt and 0.146 m pitch. These wedge-shaped acrylic planks were bolted together to form the bottom and sides of the inner detector, as depicted in Fig. 4.14a. The side supports secure the optical grid's outermost layers and determines the active volume's size.

Fig. 4.14b displays the horizontal and vertical planks that interconnect the rear sections of the PMT housings. This framework is further reinforced by machined acrylic baffles (shown in Fig. 4.14c) positioned on top of the support structure to unify all sides and secure the top reflectors in position.

4.4 Calibration methods

Each PROSPECT segment's timing and energy response is measured and tracked over time using a combination of optical reference signals, radioactive sources, and intrinsic radioactive backgrounds. Optical diffusers inside 42 center pinwheels can be pulsed at various intensities to measure timing offsets, determine single photo-electron responses, and study PMT linearity. Radioactive sources can be positioned at any desired location along the length of 35 other segments using a motor that moves a toothed drive belt attached to the source capsule [83]. The locations of the optical and radioactive sources are shown in Fig. 4.15.

Analyses of time-correlated signals in the PROSPECT data stream can cleanly identify neutron captures on ^{6}Li , ^{214}Bi $\rightarrow$ ^{214}Po+β $\rightarrow$ ^{210}Pb+α or ^{212}Bi $\rightarrow$ ^{212}Po+

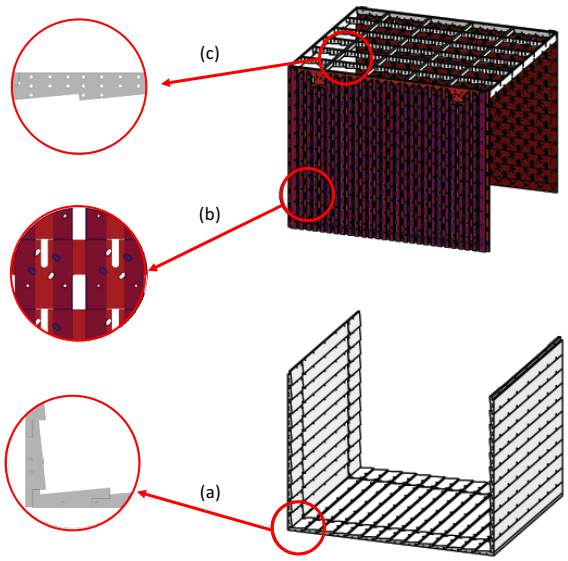


Figure 4.14: Acrylic segment support structure: (a) Wedge-shaped planks support the two walls of PMT housings at the near and far faces. These planks are joined in a shiplap style and feature slots for accurately positioning the pinwheel spacer arms. The side walls secure the outer rows of pinwheels and define the active detector volume. (b) Horizontal planks are fastened to the backs of the PMT housings, while vertical planks reinforce the structure and create pathways for cables and calibration tubes leading to the lid. (c) Baffles at the top connect the side and PMT walls, securing the top reflector layer. The baffles' performances allow the LiLS to fill the space above the top optical separator layer. Source [78].

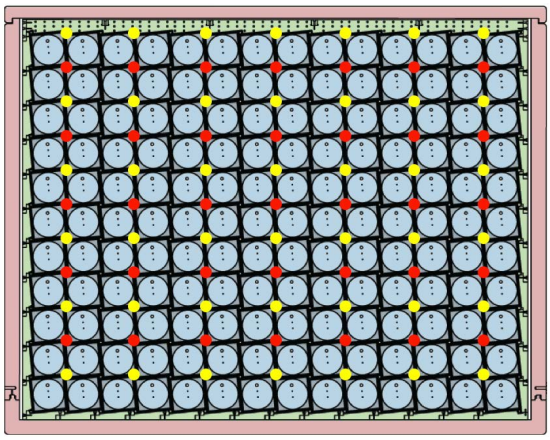


Figure 4.15: Locations of the source tube (red) and optical insert (yellow) positioned between the segments of the inner detector. Source [83].

$\beta \rightarrow {}^{208}\mathrm{Pb} + \alpha$ decays. Additionally, 0.5 Bq of ^{227}Ac was dissolved in the liquid scintillator to provide a source of $^{227}\mathrm{Ac} \rightarrow {}^{219}\mathrm{Rn} + \alpha \rightarrow {}^{215}\mathrm{Po} + \alpha \rightarrow {}^{211}\mathrm{Pb} + \alpha$ decays.

4.4.1 Optical calibration system

Timing differences between segments, the balance of PMT response across segments, and the single photon response of the PMTs are assessed using light sources integrated within the pinwheel rods. A pulsed laser beam is split and directed through 42 light guides, each covered with PTFE tubing, to reach the center of the pinwheel rods. These rods illuminate four segments simultaneously through symmetrically arranged Teflon diffusion disks embedded in the rod structure. See Fig. 4.16 for a visual representation of this setup.

The Optical Calibration System (OCS) uses a 15 mW laser emitting at 450 nm to illuminate 42 spots inside the detector, covering all 154 optical segments. The laser is powered by a high-performance driver that generates pulses up to 800 mA with less than 10 ns width and 0.5 ns rise time. The laser beam is split into 48 ports, with 42 directing light to optical diffusers inside the detector and two to monitor laser

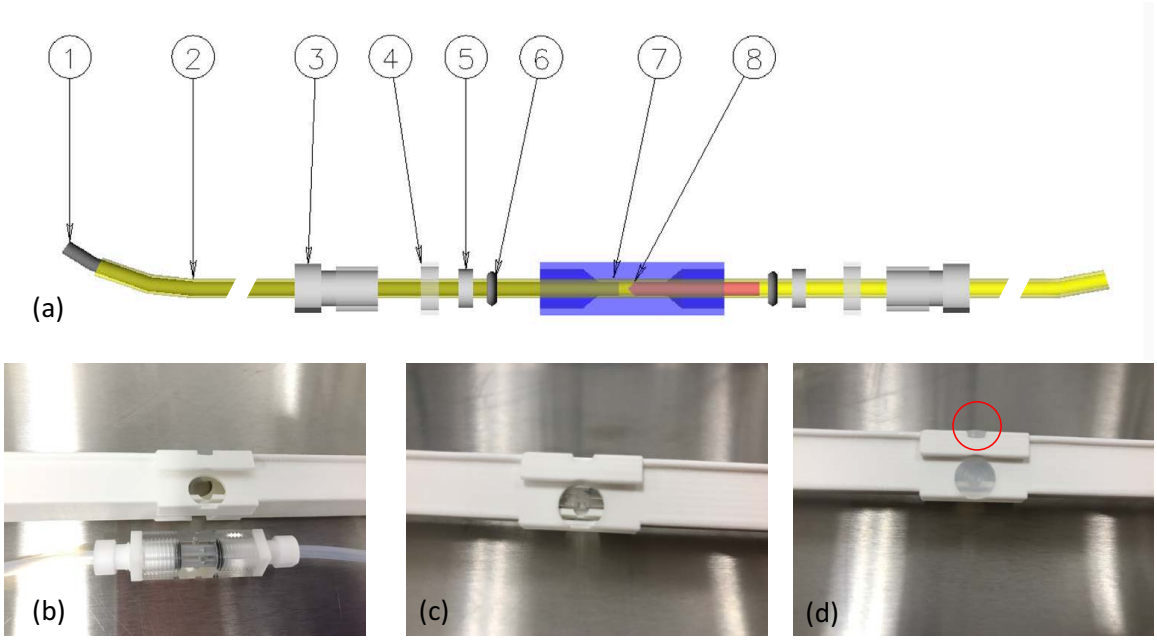


Figure 4.16: (a) Components of the fiber optic assembly: (1) Fiber optic cable, (2) PTFE tube, (3) Compression nut, (4, 5) Spacer washers, (6) O-ring, (7) Square clear acrylic body, (8) Conical reflector. The assembled fiber optic unit, shown in (b), is inserted into the square bore of the center pinwheel. In (c), the assembly is positioned within the pinwheel before being covered by a diffusive Teflon disk, as depicted in (d). Most of the disk is concealed by a reflective optical separator (not shown), leaving only a small exposed area, circled in red in (d), within the optical volume. The conical reflector directs light pulses from the fiber optic cable (1) radially (8). The light passes through the acrylic body (7) and into four Teflon diffusers embedded in the pinwheel rod, ultimately reaching the center of the segment. Each fiber optic assembly supplies light to four adjacent segments. Source [83].

intensity. Optical fibers connect the laser to the detector, ending in diffusing units that distribute light evenly across four adjacent optical segments.

The OCS adjusts light intensity by varying laser current and pulse width, enabling a range from single photoelectrons to several hundred per pulse. It calibrates PMT gain, measures relative timing offsets with 0.1 ns precision, assesses PMT non-linearity, and monitors the scintillator's attenuation length. The system typically pulses between 10 and 20 Hz for continuous monitoring, with rates exceeding 1 kHz during specific runs.

4.4.2 Radioactive source system

The PROSPECT radioactive source calibration system is designed to maneuver gamma-ray, neutron, and positron emitters through tubes extending into the detector's active volume, as illustrated in Fig. 4.17. This setup serves to measure and calibrate the detector's energy and position responses, as well as to investigate topological effects. Thirty-five source tubes are integrated with the optical array, arranged in a 5 by 7 grid. Each source can be reliably positioned to within approximately 1 mm, with an overall accuracy of about 1 cm along the length of its tube. PROSPECT employed sources including ^{137}Cs, ^{60}Co, ^{22}Na, and ^{252}Cf. Information about these sources and their uses is summarized in Table 4.1.

Each source is stored in a small aluminum cylinder sealed with a set-screw and epoxy (see Fig. 4.18). These capsules are attached to the belt using stainless steel

Table 4.1: Proposed γ-ray, positron, and neutron sources for calibration.

Source	**Decay**	**γ energies (MeV)**	**Purpose**
^{137}Cs	β^-	0.662	Segment comparison
^{22}Na	β^+	0.511, 1.274	Positron energy reconstruction
^{60}Co	β^-	1.173, 1.332	Detector energy scale
^{252}Cf	n (fission)	2.223 from nH capture	Neutron response

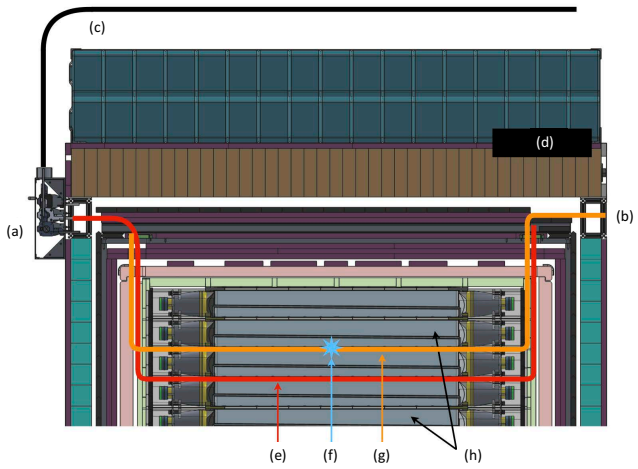


Figure 4.17: End view of the detector showing the path of a typical source deployment tube ((e) in red) and an optical insert ((g) in orange). Also depicted are: (a) source drive motors, (b) optical fiber connector panel, (c) belt storage tube, (d) shielding, (f) light injection point, and (h) detector segments. Source [83].

spring pins. Each capsule is marked with a unique ID number and later logged in the source control database. Toothed drive belts, known as timing belts, are used to smoothly move the capsules into the detector through the source tubes and retract them when necessary. Ensuring the timing belt has the correct width and stiffness is essential to prevent problems like buckling or excessive friction inside the tubes. A 3 mm wide polyurethane belt with an AT3 pitch and reinforced steel cords has proven effective.

The timing belt is operated by a custom 3D-printed pulley connected to a NEMA 23 stepper motor (Fig. 4.18). The pulley is mounted on the motor shaft to drive the belt, while a spring-loaded jockey maintains tension on the timing belt pulley. A 3D-printed belt guide keeps everything aligned, guiding the belt from the source tube to the pulley and onward to a storage tube on top of the detector. This assembly includes two micro switches: one stops the motor when the source capsule reaches the pulley, serving as a safety measure and marking the capsule's home position, and the other prevents the belt from extending past the pulley. Specifically designed for this

system, the timing belt pulleys and motor housings are 3D printed using UV-cured resin.

4.4.3 Intrinsic radioactive sources

Three radioactive sources are utilized within the liquid scintillator itself. Two of these sources are intrinsic and are known as **BiPo** decays. They result from simultaneous β-decays of ^{212}Bi and ^{214}Bi, followed by α-decays of ^{212}Po and ^{214}Po. These isotopes originate from naturally occurring ^{232}Th (with a half-life of 14 billion years) and ^{238}U (with a half-life of 4.5 billion years), respectively. A third source, ^{227}Ac (half-life of 22 years), was intentionally added to monitor efficiency-volume product for all detector segments. It was dissolved into the liquid scintillator from a commercial actinium source at about 0.5 Bq across the detector. These sources produce **RnPo** decays, simultaneous α-decays from ^{219}Rn and ^{215}Po (half-life of 1.78 milliseconds). The AcCl solution was dissolved into the scintillator before entering the detector.

Signals from these sources are triggered and recorded in the standard DAQ stream. Events are analyzed using energy thresholds, decay time distributions, and pulse shape discrimination, leveraging their decay times of 0.3-3 milliseconds.

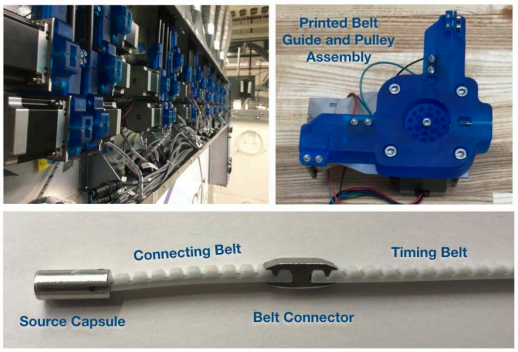


Figure 4.18: Bottom: Source capsule attached to the drive belt, with a short connecting belt linked to the source and belt connector for easier source swapping. Top right: 3D-printed belt guide and pulley. Top left: Source motors and belt assemblies. Source [83].

4.5 Detector Monitoring

Temperature is monitored using 11 resistance temperature detectors (RTDs) placed strategically throughout the detector. Another monitor between the acrylic and aluminum tanks oversees water temperature. Ultrasonic sensors on top of the tanks monitor LiLS and water levels. To prevent oxygen from entering the liquid scintillator, a layer of liquid nitrogen cover gas is maintained above it. A mass flow controller regulates nitrogen input, and another monitors nitrogen outflow through an oil-filled bubbler to prevent air ingress if nitrogen flow stops. Additionally, a sensor measures pressure, temperature, and humidity at the gas outlet to control oxygen and water content. Tubes around the LiLS volume allow nitrogen flow through the liquid as needed, enhancing control over the detector's environment.

4.6 Data acquisition system

The PROSPECT DAQ system is designed with several critical priorities in mind. As previously discussed, the system must effectively analyze PSD signals from all 308 PMTs within the LiLS to ensure robust background rejection, necessitating waveform digitization. Moreover, it requires a wide dynamic range from 0 to 14 MeV with exceptional linearity and resolution. This upper limit is specifically chosen to encompass the endpoint energy of cosmogenically produced ^{12}B, essential for precise energy calibration and linearity assessments. Operating at data rates as high as 40 kHz during HFIR operation, complete waveform digitization across all PMT channels would generate an immense data volume. Therefore, an efficient triggering mechanism is implemented to selectively transfer and record channels only when relevant data is detected.

PROSPECT utilizes commercial Waveform Digitizer Modules (WFDs) for its data acquisition system. PMT anode signals are directly fed into the WFD inputs without

prior analog preprocessing, simplifying the setup significantly. Trigger decisions rely on digital processing of the sample stream performed onboard.

The selected WFD model features a 250 MHz sample rate and 14-bit depth per sample. Evaluations using prototype detector modules [79, 81] confirmed that these digitization parameters met PROSPECT's PSD and dynamic range requirements. Tests showed that increasing the sampling rate to 500 MHz did not significantly improve PSD performance due to long optical propagation distances and resulting time dispersion within the PROSPECT segment structure. While a higher sampling rate could enhance longitudinal position reconstruction, benefits beyond the segment size (0.15 m) did not contribute significantly to physics or background rejection.

Onboard digital logic controls trigger and sample processing functions. The WFDs do not perform amplitude or PSD calculations onboard; instead, they record waveforms for subsequent offline analysis. This approach provides flexibility in optimizing the processing strategy but results in higher data rates.

4.6.1 DAQ hardware

Figure 4.20 shows the DAQ hardware setup used by PROSPECT, featuring twenty-one WFD modules managing data from 308 PMTs across two VME crates. DAQ control computers, equipped with optical fiber link cards, handle control and data retrieval from these modules. Each optical link card can support up to four optical links, connecting two or three WFD modules per link.

To efficiently manage trigger signals, a custom Logic Fan-In/Fan-Out module with 32 input and 32 output channels ensures each input signal is distributed across all outputs. Scintillation light from particle interactions is directed to PMTs, where the analog signals are digitized by CAEN V1725 250 MHz 14-bit waveform digitizer modules. The digitized waveforms reflect the scintillator's timing, photon transit time dispersion, PMT transit times, and cabling impedance.

Scintillator light emission involves processes with different exponential decay times, resulting in varied pulse shapes. Low ionization events, like electron tracks, have a 16 ns decay time, while high ionization events, such as proton recoils, exhibit a 38 ns component and a minor 225 ns tail. Averaged waveforms for electron and proton interactions in PROSPECT are illustrated in Fig. 4.19.

4.6.2 DAQ triggering

The PROSPECT detector utilizes a trigger configuration and zero-suppression strategy to effectively capture all energy depositions above approximately 200 keV, even amidst challenging background conditions. The DAQ trigger initiates when a pair of PMTs within the same segment detects a signal surpassing 50 ADC channels (approximately 5 photoelectrons) above baseline within a 16 ns timeframe. This pairwise logical AND operation is conducted for each segment, and the results are aggregated via a logical OR operation at the WFD board level, accommodating up to 8 pairs per board. Subsequently, the logical OR output from each of the 21 WFD boards is consolidated using a Phillips Scientific 757D Fan-in/Fan-out NIM module, specially configured for 32-in-to-32-out operation by the manufacturer. This combined OR operation across all segment pairs defines the global acquisition trigger for the DAQ system, which is then distributed to the acquisition trigger inputs of each WFD. The global trigger rate operates at approximately 5000 events per second when the HFIR reactor is inactive and increases to about 20,000 events per second when the reactor is active, mainly due to background γ-rays associated with the reactor's operation.

Upon receiving the global trigger signal, each WFD records a 592 ns (148-sample) data sequence for every channel, capturing approximately 200 ns of data before the trigger signal. Any subsequent events occurring within 592 ns after the initial trigger do not trigger the DAQ again. This introduces a deadtime period after each trigger, during which light pulses may be recorded in the waveform but are truncated at the

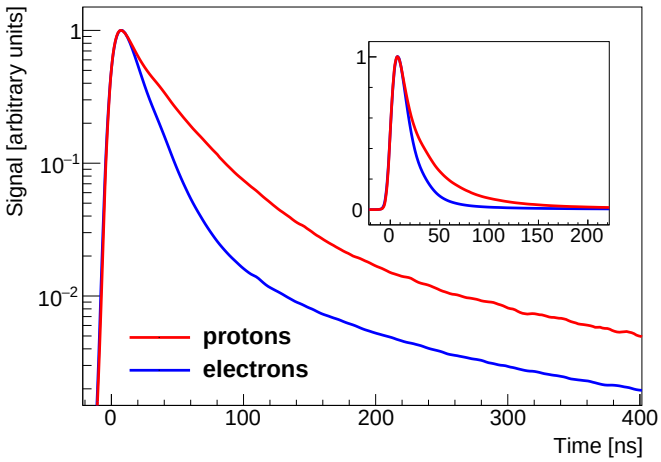


Figure 4.19: Averaged waveforms for low-energy-density (electron) tracks (lower, blue) and high-energy-density (proton recoil) tracks (upper, red). Electron-like pulse shapes remain consistent across different energies. In contrast, recoil pulses exhibit varying amounts of the longer tail component, eventually resembling the electron track shape at high energies and low ionization densities. The inset panel shows these waveforms on a linear scale. Source [78].

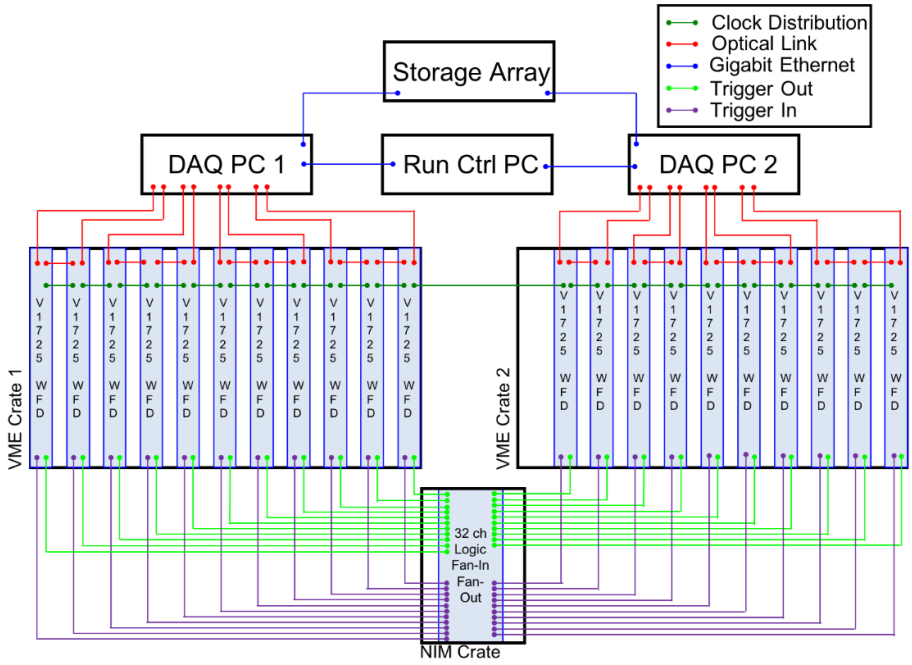


Figure 4.20: Schematic diagram of the DAQ. Source [78].

end of the sampling sequence. This deadtime effect is typically around 1%, depending on the overall trigger rate.

Events can result in light emission across one or multiple segments, typically occurring in fewer than 5% of all segments. To minimize the transferred data volume, the WFDs employ 'Zero Length Encoding' (ZLE) in their firmware to eliminate empty signals. ZLE applies a threshold of 20 ADC channels above baseline (equivalent to 2 photoelectrons) to the waveform data. Sections of the waveform that lie more than 24 samples before or 20 after the nearest above-threshold value are suppressed, potentially encompassing the entire 148-sample sequence. This reduction in stored data volume is illustrated in Fig. 4.21.

4.6.3 Data transfer and data rates

The memory within the WFD modules is structured into two buffers: as one buffer accumulates waveform data, the other stands ready for transfer to disk storage via optical links. DAQ control software, managed by two independent computers, continuously monitors the WFDs and initiates data transfers when a buffer reaches capacity. Table. 4.2 outlines specific trigger and data rates.

4.6.4 Clock signal distribution

The V1725 WFD module can use either an internal or external clock. When it receives a clock signal at the 'CLOCK IN' input, it mirrors it to the 'CLOCK OUT' output. One module is the master clock, providing a 62.5 MHz differential clock signal. This signal is passed from module to module through short cables (about 0.05 meters long), with a longer cable (about 1 meter) used between the two VME crates. Any delays in this setup are measured and corrected during data analysis.

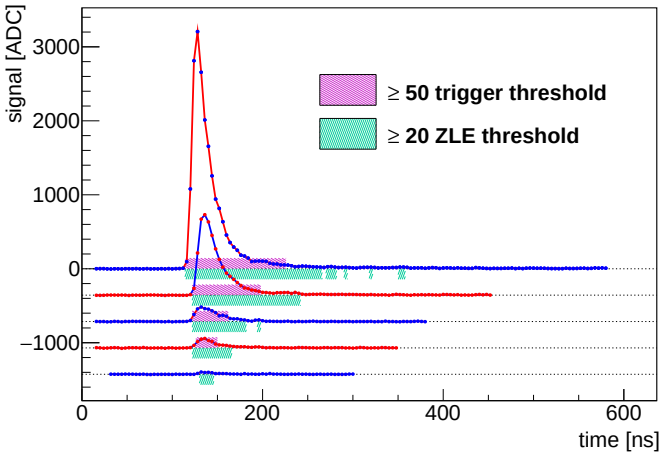


Figure 4.21: Example DAQ trigger readout (y-axis offset for clarity). The waveforms shown are inverted and baseline-subtracted from the raw DAQ output. Blue and red data points represent PMT channels at high and low z, respectively. Pink and green highlighted regions indicate waveform segments above the 50 ADC and 20 ADC trigger and ZLE thresholds. The global trigger is generated by the first segment pair coincidence above the trigger threshold (top two waveforms). All PMT channels shown would have portions of their waveforms read out. Source [70].

Table 4.2: Approximate data acquisition and transfer parameters for three typical operating conditions. The calibration case involves deploying five ^{137}Cs sources within the detector while the reactor is off. The average multiplicity is higher for the reactor-off periods because muon and other cosmic events, which have high multiplicity, make up a larger fraction of the events in this state. Source [78].

Quantity/Run Condition	**Reactor On**	**Reactor Off**	**Calibration**
Acquisition Event Rate (kHz)	28	4	35
Segment Event Rate (kHz)	115	35	190
Avg. Segment Multiplicity	4.0	7.0	5.5
Max Opt. Link Rate (MB/s)	3.0	1.0	7.2
Min Opt. Link Rate (MB/s)	1.1	0.6	2.2
Data Volume per Day (GB)	671	312	476

4.7 Chapter summary

This chapter provides an overview of the PROSPECT experiment, detailing the facility, detector, materials, and methods from construction through data collection. The following chapter will outline the data analysis process, covering steps from raw data handling and pulse analysis to the selection of IBD events. Additionally, it will include a detailed description of energy response characterization, backgrounds, and simulation.

Chapter 5

PROSPECT Data processing, event reconstruction and detector response simulation

5.1 Introduction

The previous chapter described the instrumentation of the PROSPECT experiment, including detector design and the DAQ system. This chapter focuses on the analysis strategy for converting raw digitized pulses from each PMT in the detector segments into calibrated physics quantities. These quantities are essential for identifying inverse beta decay candidates and performing the experiment's physics analyses. Additionally, the Geant4-based simulation package for the detector is introduced. This package is critical in validating calibration data from various radioactive sources, ensuring accurate energy reconstruction and detector response modeling.

5.2 Low-level signal processing

The conversion of the raw data to physics quantities is performed within the analysis framework `PROSPECT2xAnalysis (P2X)`, which also provides a plugin-based platform for high-level analyses dealing with selected IBD candidates.

5.2.1 Raw waveforms, unpacked data

The digitizers' raw waveform data is stored on disk by two DAQ computers in a proprietary CAEN format, modified to include extra header information and exclude empty data blocks. This process produces eight parallel files containing data from two or three WFDs, ensuring complete readout from the DAQ without data loss due to buffer overflows in the WFDs' onboard memory. The files are then collated and time-ordered into a ROOT [98] binary file format. Additionally, the mapping between the physical channel numbers of each PMT and their corresponding logical channel numbers is stored.

5.2.2 Pulse analysis, pairing and clustering

Unpacked ROOT files are processed into uncalibrated waveform data by identifying local maxima as well as well-separated pulses within each acquisition window. Each waveform file is examined to locate and characterize pulses, represented by sequences of 14-bit integer ADC samples at 4 ns intervals. Negative-polarity waveforms are inverted so that higher sample values indicate larger charge signals. A global maximum sample and local maxima (separated by at least 20 samples from any higher point) are identified as initial pulse candidates. The waveform baseline b is determined by averaging the median 8 samples within 5 to 30 samples before the global maximum. This baseline is subtracted from all waveform samples for subsequent analysis. Pulses are defined as the global maximum and any local maxima at least 30 ADC units above the baseline. Fig. 5.1 illustrates the main quantities for each selected pulse.

The area S of each pulse is determined by summing the samples from 3 samples before to 25 samples after its peak. The arrival time t is found by scanning backward from the peak to the first level crossing at 50% of the maximum, then linearly interpolating to the 50% point between the two threshold-crossing samples. The PSD value for each pulse is calculated as the ratio of the pulse area from 11 to 50 samples after t (pulse tail) to the area from 3 samples before to 50 samples after t (shown in Fig. 5.2), using trapezoidal interpolation. These integration windows are selected to optimize the PSD's ability to differentiate neutron captures from γ-ray interactions of similar energy. The time-ordered list of analyzed pulses, including each waveform area S, arrival time t, PSD, baseline b, and peak height h, is written to an HDF5 table format file. This data structure is known in the PROSPECT analysis chain as a `DetPulse`.

Subsequently, pulses from individual PMTs are grouped into multi-segment clusters within a 20 ns arrival time window. Paired waveforms from PMTs on opposite ends of a double-ended (DE) segment are stored and analyzed, creating a reconstructed pulse containing segment-level information. These paired pulses are

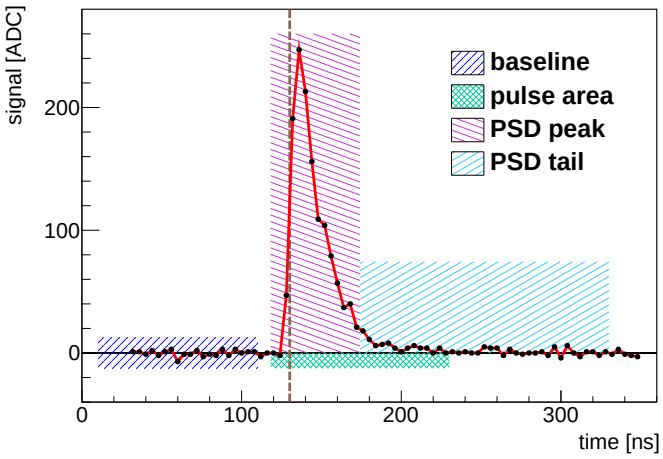


Figure 5.1: Typical electron pulse with a smaller signal. The half-height leading edge timing (dashed vertical line) defines windows for baseline subtraction, pulse area calculation, and PSD. The waveform shown is inverted and baseline-subtracted relative to the raw DAQ output. Source [70].

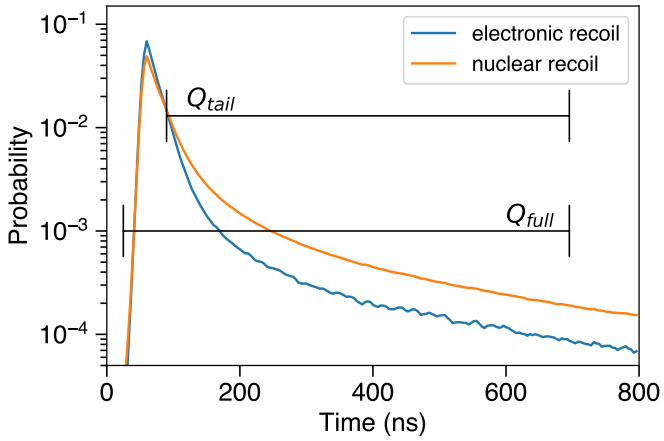


Figure 5.2: Template waveforms from the PROSPECT-50 detector illustrating the difference between electronic and nuclear recoil energy depositions from a ^{252}Cf source. The fraction of charge in the tail of the pulse relative to the total integral charge is used as a discrimination metric. Source [81].

processed and combined to produce calibrated physics quantities that describe the interaction producing the collected waveform in that segment, including time, position, visible energy deposition, and PSD, which are explained in the following subsections. Single-ended (SE) segments with only one operable PMT also have their waveform features stored and reconstructed as pulses. Nevertheless, the position dependence of scintillation light collection prevents accurate energy reconstruction. [79, 81, 47, 190].

5.2.3 Timing calibration

Segment hit time is characterized by two variables, the segment time

$$t^i = \frac{1}{2}(t_0^i + t_1^i) \tag{5.1}$$

and the time difference

$$\delta t^i = t_1^i - t_0^i \tag{5.2}$$

where t_0^i and t_1^i are the pulse arrival times for both PMTs in segment i. The time difference correlates with the position along the cell axis (z position) because the

light transit length to each end varies based on the energy deposition location. Clusters are scanned for candidate muon tracks to determine relative time offsets between PMTs due to cable lengths, PMT electronics, and WFD board clock offsets. As shown in Fig. 5.3, muon tracks generate signals across multiple segments with nearly simultaneous origin times, accounting for the muon's transit speed through the detector, providing enough statistics to extract timing offsets.

Candidate muons are identified by signals exceeding $> 10^5$ ADC counts and at least four paired segment hits. Muons traversing the entire width of a segment deposit more than 10 MeV_{ee} of energy, resulting in clipped signals due to gain settings optimized for a range up to 14 MeV_{ee}. However, signals from muons passing through the corners of the segments generate a wide range of signals within the PMTs' dynamic range. The high event rate of corner-clipping muons ensures sufficient statistics for a complete timing calibration within 5 minutes of data collection, allowing each hour-long run to provide ample data for precise timing calibration.

After sufficient muon statistics are collected, a principal component analysis [166] (PCA) is performed to determine the muon's direction and energy deposition. This PCA helps refine the selection of candidate events by excluding multi-component

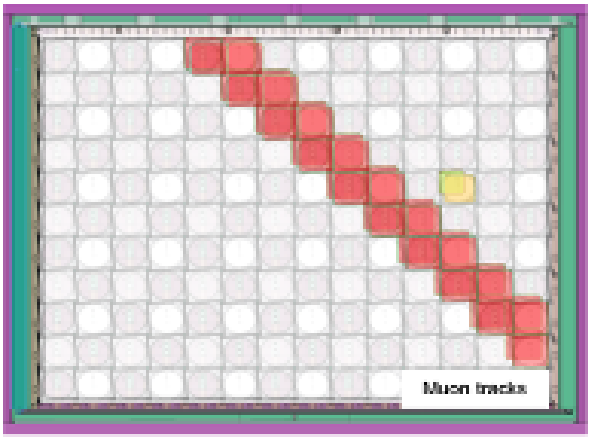


Figure 5.3: Event display for a muon track crossing the PROSPECT detector. Source [75].

electron showers resulting from cosmic ray interactions. Optimal muon candidates are identified by an RMS track width spread of 0.2 to 0.4 cell widths and a track length exceeding four cell widths. Corner-clipping hits are selected for these candidates by requiring the geometric mean of the two PMT signals to be between 4×10^3 and 5×10^4 ADC counts.

The mean and variance of the segment-to-segment timing distributions are calculated for each segment pair with corner-clipping-range signals. These values create an over-determined linear system for determining timing offsets, solved using the least-squares method. The resulting average and differential timing offsets are stored in the calibration database to adjust raw timing data, producing accurate reconstructed event times and position-dependent timing values.

Timing differences for segments and PMT pairs generally range from -10 to 10 ns. ET and Hamamatsu PMTs exhibit different timing characteristics, with ET PMTs showing more significant variance. Board offsets in 8 ns increments largely account for the remaining timing discrepancies. The timing calibration remains highly stable, with offsets changing by less than 1 ns over the data collection period and variations of less than 20 ps between runs. Fig. 5.4 shows the segment timing calibrations extracted from a typical one-hour run.

5.2.4 Position calibration

The Δt parameter provides information about the event's position within the segment. Additionally, the relative number of photoelectrons collected by each PMT provides further positional information. The position estimate of an event in a single segment is derived from both the Δt timing parameter and the logarithmic ratio of pulse areas $R \equiv \ln(S_1/S_0)$. Fig. 5.5 illustrates the distribution of Δt and R for a subset of corner-clipping muons. The distribution is uneven across the segment due to geometric selection efficiencies for this event type. However, the edges of the distribution mark the ends of the active scintillator volume. The fine-scale oscillations

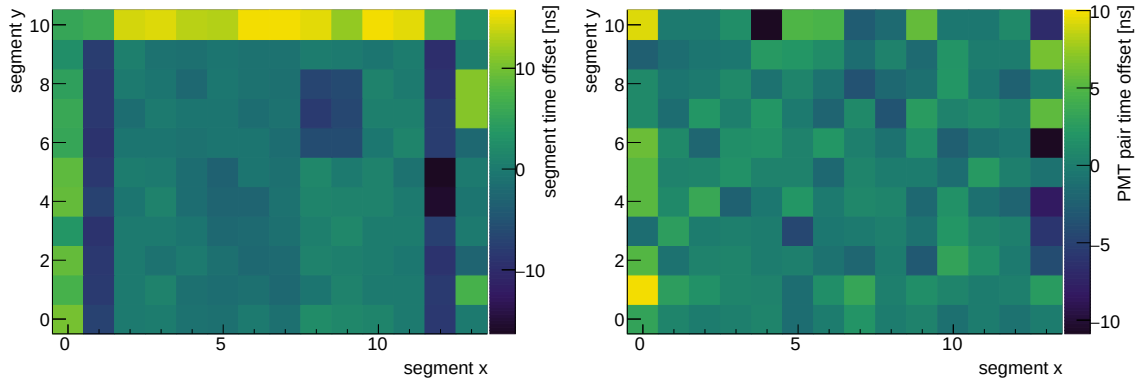


Figure 5.4: Segment timing calibration constants extracted from a March 2018 physics run, with no inactive PMT channels; note that not all channels displayed are used in the final IBD selection. Segment (0,0) is the closest to the reactor core. Left: $\bar{t}^i$ segment time offsets, highlighting large-scale features due to board clock offsets and systematic differences between ET and Hamamatsu PMT transit times. Right: $\overline{\delta t}^i$ PMT pair offsets, showing greater transit time variation between ET PMTs. Source [70].

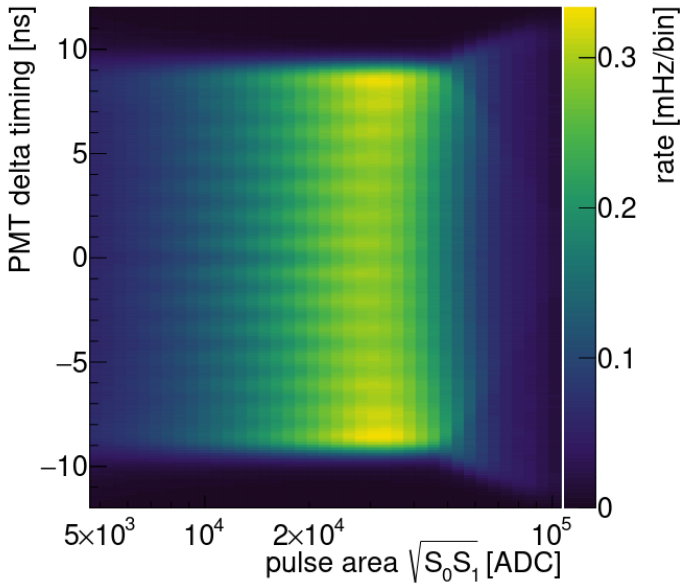


Figure 5.5: Histogram of the timing differential between PMTs within a segment and the geometric mean of pulse areas for corner-clipped muon events during a calibration run. Each position calibration run collects approximately two weeks of data to ensure sufficient statistics, especially for identifying dips in the spectra associated with pinwheel tabs. Source [70].

in Δt are caused by light transport perturbations from the diffusely reflecting plastic support rod clips that secure the edges of the specularly reflecting optical grid panels. Because corner-clipped muon events occur near these clips, this light collection effect is more pronounced than in datasets with uniformly distributed events throughout the detector.

The distributions in Fig. 5.5 can be fitted to obtain z-position estimates based on timing and signal amplitude. The timing-based z-position $z(\Delta t)$ is obtained by fitting a linear plus cubic polynomial function, $z = a\Delta t + b(\Delta t)^3$, to Δt. This method accurately reproduces the positions of radioactive sources within the calibration tubes, as detailed in Section. 5.2.8, with an accuracy of within 1 cm. Similarly, the signal-amplitude-based z-position $z(R)$ is determined using a cubic polynomial, $z = a + bR + cR^3$, achieving comparable accuracy to $z(\Delta t)$. All constants for these fits are stored in the calibration database.

Both $z(\Delta t)$ and $z(R)$ are saved in the calibration database for future numerical evaluation. The final reconstructed position z_{rec} for each pulse is calculated from a statistically weighted average of $z(\Delta t)$ and $z(R)$. Excluding the time- or amplitude-based information from z_{rec} significantly degrades the reconstructed position resolution. About two weeks of data collection is sufficient to accumulate enough corner-clipped muon statistics to resolve the fine-scale variations due to the pinwheel tabs for each segment. Therefore, the data collection period was divided into 11 distinct calibration periods for position calibration.

5.2.5 Position-dependent combined PSD metric

The PSD parameter for a single pulse varies with the location of energy deposition along the segment. This position dependence is due to photon collection effects, where more light reaches the PMT face during the tail of the pulse if the energy deposition is farther away. To account for position variations of the PSD metric, the event selection of corner-clipping muons used for timing calibration is empirically fitted as a function

of Δt for each PMT within a segment for a given data run. This fitting is performed using a three-parameter curve $p \cdot (1 + d \cdot [1 - e^{k\Delta t}])$.

Subsequently, a position-corrected PSD value is obtained for each PMT by subtracting the measured position-dependent factor $pd[1-e^{k\Delta t}]$ from the PSD of each pulse. The parameter p represents the center of the PSD distribution for electron-like energy depositions. At the same time, nuclear-like recoils have a PSD centered at a value larger than p, allowing for particle identification. The two position-corrected PSD values for the PMT signals in a given segment are then averaged, weighted by the estimated number of photoelectrons in each pulse, to yield a single PSD value.

Figure 5.6 displays a calibrated PSD distribution for pulses following candidate muon tracks, which contain a substantial population of ^{6}Li-captured spallation neutrons. The calibrated pulse PSD values are plotted against the uncalibrated signal amplitude, defined as the product of the pulse areas S_0 and S_1 for the segment's low-z and high-z PMT channels, respectively.

The long-term variations in p, d, and k are attributed to changes in the scintillator's optical properties. While the position-dependent terms d and k are calibrated out, the long-term variation in p persists, trending towards lower values as increased attenuation filters out longer light paths. Rather than calibrating out this variation, the time-varying value of p defines PSD cuts. Additionally, the center of the PSD distribution for n+^{6}Li capture events is tracked over time. This center value gradually decreases, and the neutron capture PSD acceptance bounds are adjusted to correspond with this shift. PSD cuts are described in detail in Section 6.2.1.

5.2.6 Visible energy calibration

The highly segmented design of the PROSPECT detector, combined with scintillator nonlinearity (quenching) and trigger acquisition thresholds, complicates the extraction of interaction energies on an event-by-event basis. Rather than attempting to

reconstruct the initial energy of each interaction, the energy calibration strategy for the experiment is divided into two components:

- Extracting a consistent measure of the visible energy, E_{vis}, which represents the light produced after correcting for scintillator nonlinearity but before accounting for light transport and PMT gain effects.
- Fine-tuning parameters in a Monte Carlo (MC)-based detector response model to accurately match data observables in the E_{vis} space.

To determine E_{vis}, it is crucial to understand the position-dependent light collection variation within a segment. The necessary inputs for reconstructing E_{vis} for a given segment interaction include the following: the two pulse area signals S_0 and S_1 from each segment end, the estimated number of photoelectrons collected per E_{vis} at the segment center by each PMT (n_0 and n_1), the pulse area signals per E_{vis} deposited at the segment center (g_0 and g_1), the reconstructed longitudinal position in the segment (z_{rec}), and the position-dependent light transport efficiency to each PMT ($\eta_0(z)$ and $\eta_1(z)$), normalized to 1 at the segment center. Combining all these factors leads to an expression of the form:

$$E_{vis} = \frac{S_0 n_0/g_0 + S_1 n_1/g_1}{n_0\eta_0(z_{rec}) + n_1\eta_1(z_{rec})} \tag{5.3}$$

To ensure precise reconstruction of neutron capture events for IBD analysis, semiweekly calibrations using cosmic background data are employed to monitor PMT gains and light transport effects over time. Cosmic interactions that produce neutrons generate consistent captures with sufficient statistics, which can be effectively separated from dominant γ-ray backgrounds using PSD and time correlations. However, the light yield from the ^{4}He-^{3}H pairs produced in the n+^{6}Li reaction is quenched due to nonlinear scintillator light production effects, making accurate prediction from first principles challenging. Instead, the observed distribution is related to known calibration sources by matching the detector response simulation

(see section 5.3.4) to these sources and using the parameterized fit to determine an absolute energy scale. This approach reveals that the center of the neutron capture peak visible energy distribution corresponds to 0.526 MeV_{ee}.

The remaining quantities in Eq. 5.3, namely g_i, n_i, and $\eta_i(z_{rec})$, are determined using neutron capture data. For example, g_i is calculated from the center of the neutron capture peak for signals at the center of the cell, while the segment-wide distribution of the neutron peak is used to fit the $\eta_i(z_{rec})$ parameter. Additionally, n_i is estimated from the width of the neutron capture peak in S_i space. The gain-stabilizing constants g_i are recorded in calibration databases and applied run-by-run. In contrast, the light transport $\eta_i(z_{rec})$ and photoelectron collection n_i constants are recorded and applied in two-week periods. The extent of the time variation in the position-dependent light transport that must be accounted for to obtain a stable E_{vis} calibration can be observed in Fig. 5.7.

The scintillator properties degraded throughout the data collection period, reporting a light yield reduction of ∼30%, causing a continuous gradual loss of E_{vis} resolution. To avoid complicated time-dependent uncertainties in the calculated IBD energy spectrum due to varying energy resolution, a quantity E_{smear} is used for the IBD analysis instead of the predicted E_{vis}. E_{smear} is the E_{vis} with added Gaussian smearing to approximate an energy resolution equal to the lowest resolution segment at the end of the data-taking period. This smearing results in an energy resolution of 325 photoelectrons per MeV_{ee} or 5.5% at 1 MeV. An illustration of the detector averaged energy resolution over time using E_{vis} and E_{smear} is shown in Fig. 5.8 generated by tracking the energy resolution for ^{215}Po produced from naturally ^{227}Ac that was dissolved in the scintillator.

5.2.7 Cluster-based event reconstruction

The previous sections explained how pulse features extracted from raw waveforms are calibrated and converted into relevant physics quantities that describe particle

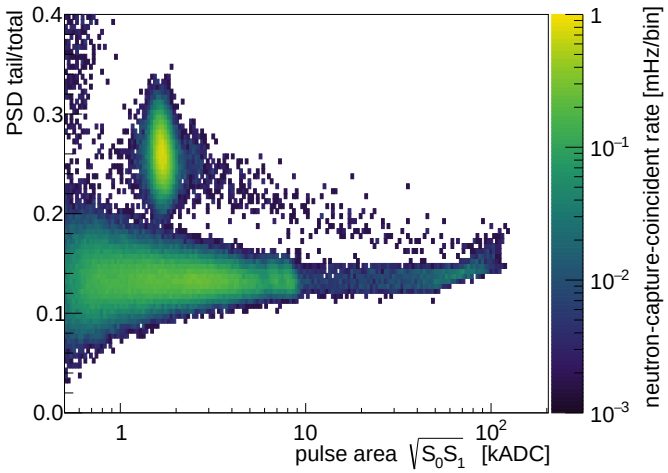


Figure 5.6: Calibrated pulse PSD value plotted against signal amplitude for one hour of pulses coinciding with cosmic muon signals. The amplitude is the product of the segment's pulse areas, S_0 and S_1. Neutron capture signals on ^{6}Li are visible in a distinct region of high amplitude and high PSD, positioned above a band of low PSD signals generated by gamma rays. Source [70].

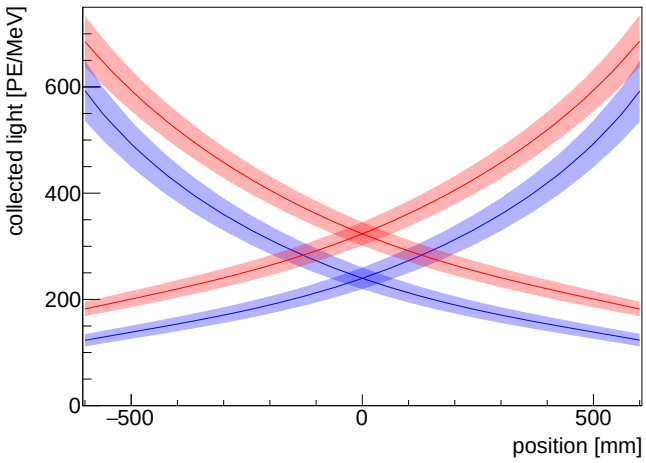


Figure 5.7: Light collection $n_i \eta_i(z)$ averaged over channels at the beginning (upper red curves) and end (lower blue curves) of the data period used for the present analysis. Bands indicate the RMS spread between channels. Source [70].

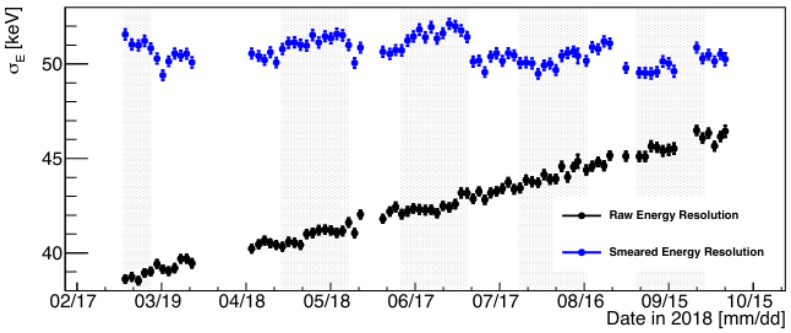


Figure 5.8: Energy resolution σ_E over time for ^{215}Po interactions from ^{219}Rn $\rightarrow$ ^{215}Po $\alpha - \alpha$ decays. Blue points show the resolution after applying smearing to maintain uniformity over time. Source [70].

interactions with the liquid scintillator. In the PROSPECT analysis, a calibrated `DetPulse` is known as a `PhysPulse`. Since most interactions in the PROSPECT inner detector produce pulses across multiple detector segments, analyzing physics events at the cluster level is essential. As section 5.2.2 explains, the clustering procedure constructs clusters from `PhysPulses`. Once these clusters are formed, reconstructed cluster physics metrics are calculated and serve as the primary inputs for the main high-level physics analyses.

Firstly, cluster energy, E_{rec}, is defined as the sum of the reconstructed smeared energies, E_{smear}, of all contained pulses. One challenge in understanding the detector's energy response is the variation in low-energy thresholds across different segments over time. As a result, a 90 keV threshold for the cluster energy is applied consistently across all segments and periods during the analysis process. An additional 5 keV uncertainty is incorporated to account for variations in the energy response.

Additionally, cluster time, T_{rec}, is defined as the median t_{rec} of the individual pulse times. Cluster z-position and segment number, Z_{rec} and S_{rec}, are determined by the z_{rec} and segment number of the highest-energy contained pulse. Cluster segment multiplicity and the energies, PSD values, and z-positions of each segment pulse are also stored for subsequent analysis steps. All these cluster-related variables are used in the IBD signal selection process. Cluster E_{rec} and S_{rec} are primary inputs for the

sterile neutrino oscillation analysis, while E_{rec} is also a primary input for the ^{235}U $\bar{\nu}_e$ spectrum analysis.

5.2.8 Performance of calibrated physics metrics

After the calibrated segment pulses were clustered, it was necessary to evaluate the stability of the reconstructed metrics as a function of time, which was done via a variety of background events present in the physics data-taking runs.

One set of events chosen were the decays of ^{214}Bi and ^{212}Bi, which produce a β followed by an α particle from the ^{238}U and ^{232}Th decay chains due to natural radioactive contamination in the inner detector. These are denoted **BiPo** events, and their decays are of the form

$$^{214}\text{Bi} \rightarrow {}^{214}\text{Po} + \beta \tag{5.4}$$

$$^{214}\text{Po} \rightarrow {}^{210}\text{Pb} + \alpha \tag{5.5}$$

$$^{212}\text{Bi} \rightarrow {}^{212}\text{Po} + \beta \tag{5.6}$$

$$^{212}\text{Po} \rightarrow {}^{208}\text{Pb} + \alpha \tag{5.7}$$

the selection criteria used to study these events were,

- ^{214}BiPo events are identified by detecting a pair of signals: a prompt electronic recoil with $0.05 < \text{PSD} < 0.22$ and $0.0\,\text{MeV} < \text{E}_{\text{rec}} < 4.00\,\text{MeV}$, followed by a delayed nuclear recoil with $0.17 < \text{PSD} < 0.34$ and $0.72\,\text{MeV} < \text{E}_{\text{rec}} < 1.00\,\text{MeV}$. These events occur with a time difference of 0.7 ms and a spatial separation of 20 cm.

- ^{212}BiPo events are identified by detecting a pair of signals: a prompt electronic recoil with $0.05 < \text{PSD} < 0.22$ and $0.0\,\text{MeV} < \text{E}_{\text{rec}} < 3.00\,\text{MeV}$, followed by a delayed nuclear recoil with $0.17 < \text{PSD} < 0.34$ and $0.95\,\text{MeV} < \text{E}_{\text{rec}} <$

1.27 MeV. These events occur with a time difference of 1 μs and a spatial separation of 20 cm.

An additional set of α events was used, which came from a high-purity sample of detector-intrinsic (^{219}Rn,^{215}Po) correlated α decays produced by ^{227}Ac deliberately dissolved into the scintillator. These events are denoted **RnPo**, and their decays are of the form

$$^{219}\mathrm{Rn} \rightarrow^{215} \mathrm{Po} + \alpha \tag{5.8}$$

$$^{215}\mathrm{Po} \rightarrow^{211} \mathrm{Pb} + \alpha \tag{5.9}$$

the selection criteria used to study these events was,

- RnPo events are identified by detecting a pair of signals: a prompt nuclear recoil with $0.19 < \mathrm{PSD} < 0.36$ and $0.57\,\mathrm{MeV} < \mathrm{E_{rec}} < 1.15\,\mathrm{MeV}$, followed by a delayed nuclear recoil with $0.19 < \mathrm{PSD} < 0.36$ and $0.66\,\mathrm{MeV} < \mathrm{E_{rec}} < 1.15\,\mathrm{MeV}$. These events have a time difference of 5 ms and a spatial separation of 20 cm.

In addition to **RnPo** and **BiPo** events, pure γ-ray sources can be used to evaluate the stability of the calibrated physics metrics. Examples include the monoenergetic 2.22 MeV γ-ray emitted after a muon-induced neutron capture on hydrogen, as well as γ-rays originating from intrinsic ^{208}Tl contamination in the detector and the capture of reactor-generated neutrons on metals in the HFIR complex and the PROSPECT shielding package. Fig. 5.9 summarizes the time-stability of energy and z-related reconstruction metrics across these various sources. Each metric and event type's stability is referenced to its mean value over the entire dataset. In contrast, stability between reactor-on and reactor-off periods is referenced to the mean values during these respective phases.

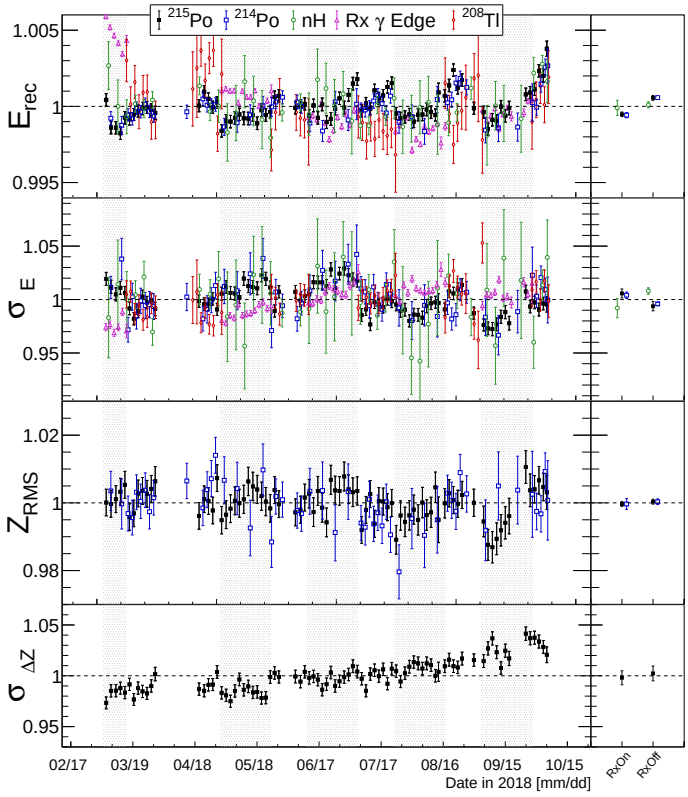


Figure 5.9: Stability of pulse-level reconstructed physics metrics related to energy and longitudinal position (z) is shown over time and between reactor-on and reactor-off periods. Metrics are calculated for ^{215}Po (black) and ^{214}Po (blue) α decays uniformly distributed throughout the detector, for nH captures (green), for γ-ray full-energy peaks from single ^{208}Tl decay (red), and for the highest-energy reactor neutron capture peak (pink) during reactor-on and -off periods. All quantities are shown relative to the dataset average, with light gray bands indicating reactor-on periods. The right panel shows relative changes between reactor-on and reactor-off datasets. Error bars represent statistical uncertainties. Source [70].

5.3 Antineutrino energy response simulation

Building on the calibrated cluster-based analysis overview, this section will describe the MC simulation package developed for the experiment. This package is responsible for establishing the relationship between the reconstructed cluster energy, E_{rec}, and the incoming antineutrino energy, E_ν. Furthermore, the MC package accurately reproduces the detector's energy response to radioactive source calibration and intrinsic background radiation, allowing for a precise determination of the experiment's absolute energy scale. This approach differs from that of other reactor $\bar{\nu}_e$ experiments, such as Daya Bay, which independently model and parameterize geometric, scintillator, and electronics effects and then match energy nonlinearities to empirical fits of calibration and background energy spectra [54].

5.3.1 PROSPECT Monte Carlo strategy

Relating incoming antineutrino energy to reconstructed visible energy is a complex task due to the unique characteristics of the PROSPECT detector. These characteristics include dead material throughout the antineutrino target, segmented detector geometry, small target size, and nonlinear light production in the scintillator. To address these challenges, the collaboration chose Geant4 as the primary simulation package, using the framework known as PROSPECT Geant4 (`PG4`). `PG4` features an accurate model of the detector geometry and surrounding shielding, incorporating panels, support rods, calibration tubes, source enclosures, the LiLS volume, acrylic and steel containers, PMT housings and openings, and shielding geometries. Geant4 precisely models radiation transport through the detector, with energy depositions in the scintillator recorded in an HDF5 file. Fig. 5.10 illustrates a visualization of the entire detector geometry simulated with `PG4`.

Simulating the scintillation process and transport of the resulting optical photons is highly time-consuming. Therefore, a parameterized model is used to estimate light production and particle quenching effects instead. In Geant4, each particle's

track is divided into discrete steps where interactions can occur, with the step length determined by the particle's energy. The energy deposited as ionization is tracked at each step, and the scintillation energy output is calculated using Birk's empirical model for quenching [96], as follows:

$$\frac{dE_{scint}}{dx} = \frac{\frac{dE}{dx}}{1 + k_{B1}\frac{dE}{dx} + k_{B2}(\frac{dE}{dx})^2} \tag{5.10}$$

At each step i, the energy deposited as ionization is divided by the distance traveled during that step. k_{B1} and k_{B2} are first- and second-order Birks constants fitted to the data, and dE/dx is the true deposited energy in that step. Furthermore, high-energy electrons from gamma and cosmic interactions induce Cherenkov radiation within the scintillator. This radiation ionizes the medium, resulting in the production of scintillation light, which is modeled at the step level using the formula:

$$E_c = k_c \sum_{\lambda} N_\lambda E_\lambda \tag{5.11}$$

Here, E_c represents the energy of scintillation light due to Cherenkov radiation. The parameter k_c is a normalization parameter that scales Cherenkov light production

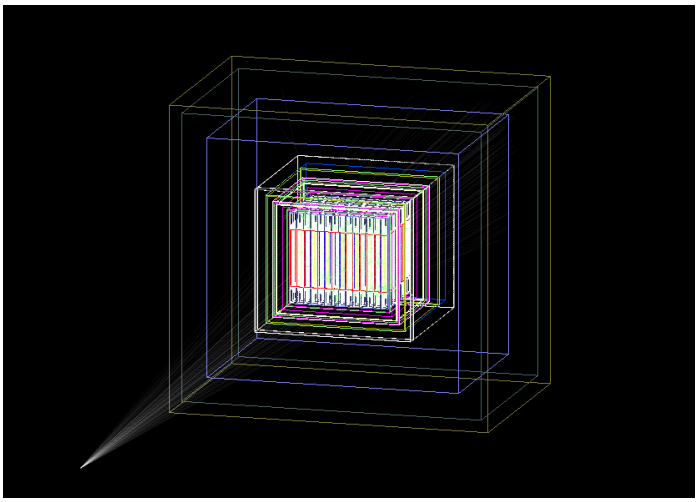


Figure 5.10: Visualization of the full PROSPECT geometry simulated with the `PG4` framework.

relative to a default estimate based on simple scintillator refractive index assumptions. N_λ denotes the number of Cherenkov photons emitted per unit wavelength λ, and E_λ denotes the energy of those photons. Thus, the total scintillation light energy produced for a particle track is calculated by summing the contributions of Cherenkov and ionization energies over all steps i:

$$E_{MC} = A \sum_i (E_{scint,i}(k_{B2}, k_{B2}) + E_{c,i}(k_c)), \tag{5.12}$$

where A is a scaling constant that adjusts the overall energy conversion to scintillation light. This summation is performed for each segment where the particle track deposits energy.

5.3.2 Simulated waveforms

Simulated waveforms are generated using the energy-weighted positions of energy depositions and E_{MC}. These waveforms are derived from templates based on individual pulses sampled from background data. The templates consist of averaged pulses for two distinct PSD values: one representing low PSD within the electron-like recoil band and the other representing high PSD within the nuclear recoil band. Each simulated PMT is randomly assigned a low PSD and a high PSD template pulse.

Waveform shape for a simulated energy deposition is calculated based on the $\frac{dE}{dx}$ value in the simulation; the position-dependent signal area, timing, and PSD values are determined by inverting the segment's calibration curves described in Sections 5.2.3, 5.2.5, and 5.2.6. This process yields the PSD and signal area for each PMT. The high and low PSD template waveforms assigned to each PMT are then linearly combined to match the assigned PSD and are scaled and time-shifted to align with the calculated area and timing. These PSD values are calibrated to match observed cosmic and gamma backgrounds. Concurrent energy depositions in time and space are summed within the same waveform channel to simulate pileup accurately.

The subsequent analysis of the simulated waveforms follows the same procedures as real data analysis, providing a consistent interface.

5.3.3 Determining absolute energy response

PG4 MC simulated waveforms, processed through P2X, are utilized to generate simulated cluster E_{rec} distributions and pulse multiplicities in response to various energy depositions, using different combinations of absolute energy response parameters (A, k_{B1}, k_{B2}, k_c). To determine the optimal parameter set, a grid search was conducted to minimize the total χ^2 value fitting the observed energy spectra from calibration sources deployed at the center of the detector: ^{22}Na (2×0.511 + 1.27 MeV), ^{137}Cs (0.66 MeV), and ^{60}Co (1.17 + 1.33 MeV). This minimization also included multiplicity spectra for each gamma source. Furthermore, the χ^2 value from neutron capture on hydrogen, producing a 2.22 MeV gamma from a ^{252}Cf source at the detector center, was considered. Finally, the electron spectrum from ^{12}B, originating from cosmic radiation, was compared with the simulation results.

The χ^2 value is calculated as follows:

$$\chi^2_{data-MC} = \sum_{\gamma} \chi^2_{\gamma} + \sum_{multi} \chi^2_{multi} + \chi^2_{^{12}\mathrm{B}}, \tag{5.13}$$

where χ^2_{γ} is the χ^2 value for each γ-ray E_{rec} distribution, χ^2_{multi} is the χ^2 value for each of the two included γ-ray multiplicity distributions, and $\chi^2_{^{12}\mathrm{B}}$ is the χ^2 value of the ^{12}B E_{rec} distribution. The grid point providing the lowest χ^2 value is selected as the nominal energy model. Reconstructed energy and multiplicity distributions for the data and best-fit PG4 are shown in Fig. 5.11. The shape and scale of these distributions show good agreement between data and the best-fit Monte Carlo.

In this analysis, the points in the k_{B1}, k_{B2}, and k_c space were varied simultaneously, while A was scaled to best fit the data for each set of k_{B1}, k_{B2}, and k_c values. The best-fit parameters were found to be (A, k_{B1}, k_{B2}, k_c) = (1.0026±0.004, 0.132±0.004 cm/MeV, 0.023±0.004 cm^2/MeV^2, 37±2%), with a χ^2/DOF (degrees

of freedom) of 581.5/420. The uncertainties in the best-fit parameters were estimated by calculating the parameter variations that yield a χ^2 difference within 30 units of the minimum. In the best-fit model, light is predominantly contributed by direct scintillation from excitation and ionization. For example, for the 2.22 MeV n-H capture de-excitation γ-ray, only 3.5% of E_{MC} is contributed by the Cherenkov process (E_c).

The uncertainties in the best-fit parameters were estimated by identifying parameter variations that resulted in a χ^2 difference within 30 units of the minimum. Parameter values varied within their uncertainties across numerous toy MC simulations to propagate energy response uncertainties. The covariance matrix, representing both uncertainties and cross-correlated uncertainties for each energy bin, was derived from the variances observed in these simulations. This approach does not consider other energy uncertainties, such as the dead mass fraction of the scintillator panels, which affects the total energy deposited as detectable light. These additional uncertainties were incorporated by varying the thickness of the reflector panels by 0.3 mm in the toy simulations, and these variations were included in the energy uncertainty covariance matrix. The individual covariance matrices were then summed to create the final covariance matrix, representing the systematic uncertainties for the energy spectrum. Detailed information on this process can be found in Section 7.2.3.

The overall agreement between the measured and predicted responses across the E_{rec} energy distribution is depicted in Fig. 5.12, which shows the ratio of the reconstructed γ-ray energy between the data and the best-fit `PG4` calibration dataset. This ratio remains within $\pm 1\%$ of unity for all γ-ray calibration datasets used in the fit, with residuals falling within the error bands defined by the energy model and the per-segment energy threshold uncertainties.

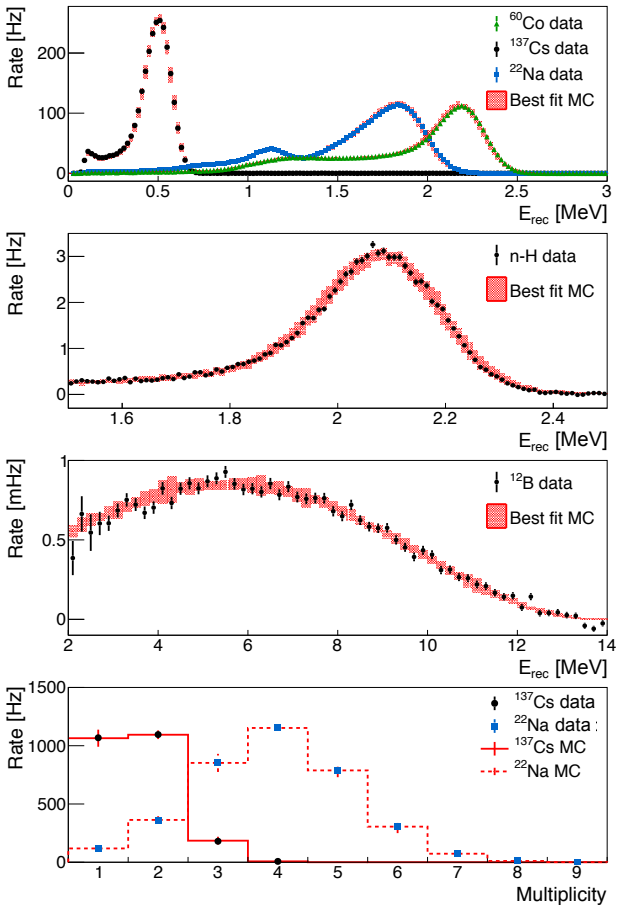


Figure 5.11: Reconstructed distributions for calibration and best-fit PG4 MC datasets: Top: E_{rec} for γ-ray source deployments at the detector center; Center top: E_{rec} for n-H captures from a ^{252}Cf source at the detector center; Center bottom: E_{rec} for cosmic ^{12}B; Bottom: pulse multiplicity for ^{137}Cs and ^{22}Na source deployments at the detector center, representing the calibration datasets with the highest and lowest multiplicity. Error bands reflect statistical (data) and systematic (PG4) uncertainties. Due to nonlinearity and energy loss in inactive materials, the true and reconstructed energies are not expected to match exactly. Source [70]

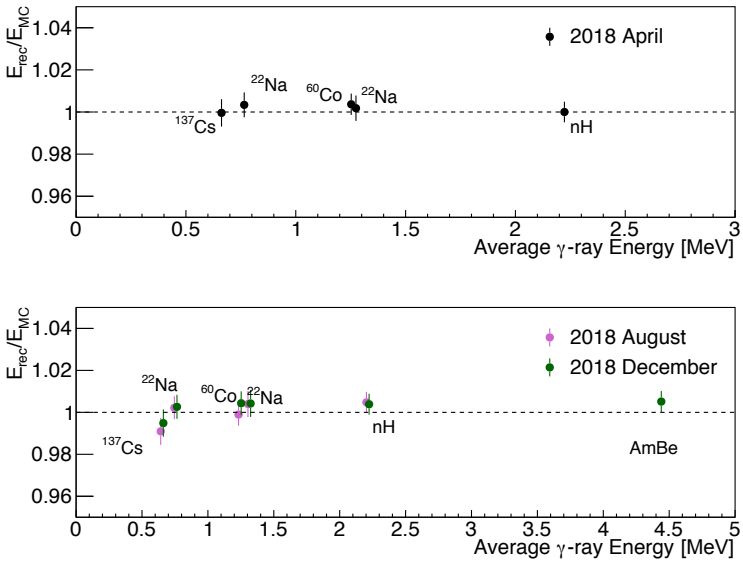


Figure 5.12: Ratios of reconstructed energy peak locations for γ calibration sources between data and best-fit PG4 MC simulations, shown as a function of reconstructed γ-ray energy. Error bars indicate statistical and systematic uncertainties. Top: ratios for datasets used to derive the best-fit PG4 response model. Bottom: ratios for datasets taken during different run periods. All ratios are within 1% of unity. Source [70].

5.3.4 Energy resolution

The reconstructed energy resolution was also characterized for calibration γ-ray events by smearing the PG4 energy model with a Gaussian distribution whose σ value was fitted with a parameterized model fit of the form

$$\frac{\sigma_E}{E_{rec}} = \sqrt{a^2 + \frac{b^2}{E_{rec}} + \frac{c^2}{E_{rec}^2}}, \tag{5.14}$$

where a accounts for light collection inefficiency variations, b represents energy-dependent photostatistics, and c is related to PMT and electronics noise. The best-fit parameters were found to be $a = 1.15\% \pm 0.47\%$, $b = 4.61\% \pm 0.24\%$, and $c = 0.0 \pm 1.3\%$. Since the simulation is processed through the same analysis chain as the real data, the resolution is artificially reduced to 325 PE/MeV$_{\text{ee}}$. The uncertainty in this energy resolution is estimated by randomly varying the smearing parameter within 5% of its nominal value and repeating the analysis multiple times. Fig. 5.13 shows the best-fit energy resolution as a function of energy deposition.

5.3.5 Determination of position-dependent energy response variation

In addition to modeling absolute energy response effects at the center of the PROSPECT detector, PG4 MC simulations must accurately account for position-dependent variations in IBD prompt E_{rec} response due to proximity to the target boundary and non-active segments. PG4 IBD MC simulations show that variations in the leakage of annihilation γ-ray energy into these regions result in a consistent shift in reconstructed IBD prompt E_{rec}. This proper modeling of leakage effects was verified by performing segment-by-segment E_{rec} comparisons between data and Monte Carlo for multiple ^{22}Na source deployment locations. As a positron emitter, the ^{22}Na source reflects changes in IBD energy scales resulting from variations in annihilation γ-ray

energy leakage with detector position, as well as the distribution of IBD positron annihilation γ-ray energies among different detector segments.

The reconstructed spectrum from a ^{22}Na source, as shown in Fig. 5.14, demonstrates good agreement between the data and the best-fit `PG4` energy response model for both one-ring and three-ring segment configurations. The relative data-`PG4` scale shifts are 4±1 keV and 5±1 keV, respectively. Gamma energy leakage effects are further examined by comparing data and `PG4` energy distributions for different ^{22}Na deployments, showing good general agreement and relative scale shifts of 8±1 keV and 7±1 keV for central and corner detector positions, respectively. This study confirms that `PG4` IBD MC simulations accurately reproduce prompt energy scale variations due to annihilation γ-ray energy leakage with keV-level precision. An ±8 keV uncertainty is included in subsequent analyses to account for this effect.

5.4 Chapter summary

This chapter summarizes the data processing and analysis of the PROSPECT experiment, covering everything from processing raw digitized pulses from each PMT in the detector segments to pairing, calibration, and clustering of these pulses. This process results in a cluster-based analysis that utilizes low-level physics quantities such as time, energy, position, and PSD, which are essential for accurately selecting IBD candidates and conducting high-level physics analyses. Additionally, the chapter describes the design of the simulation package used to determine the experiment's energy response and energy scale. The following chapter will detail the procedures for IBD detection and selection using the data structures discussed here, the primary background sources related to IBD detection, and the IBD simulation used to validate the measured signal.

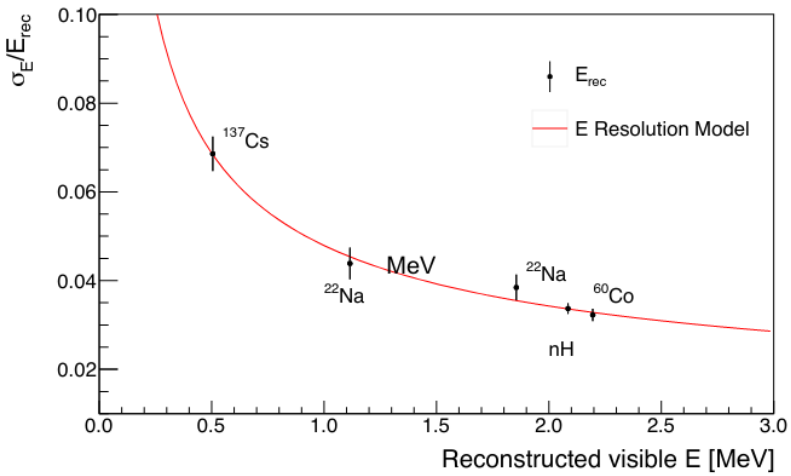


Figure 5.13: Energy resolution measurements for various labeled radioactive sources deployed at the center of the detector. The line represents the parameterized model fit described by Eq. 5.14. Error bars reflect both systematic and statistical uncertainties. Source [70].

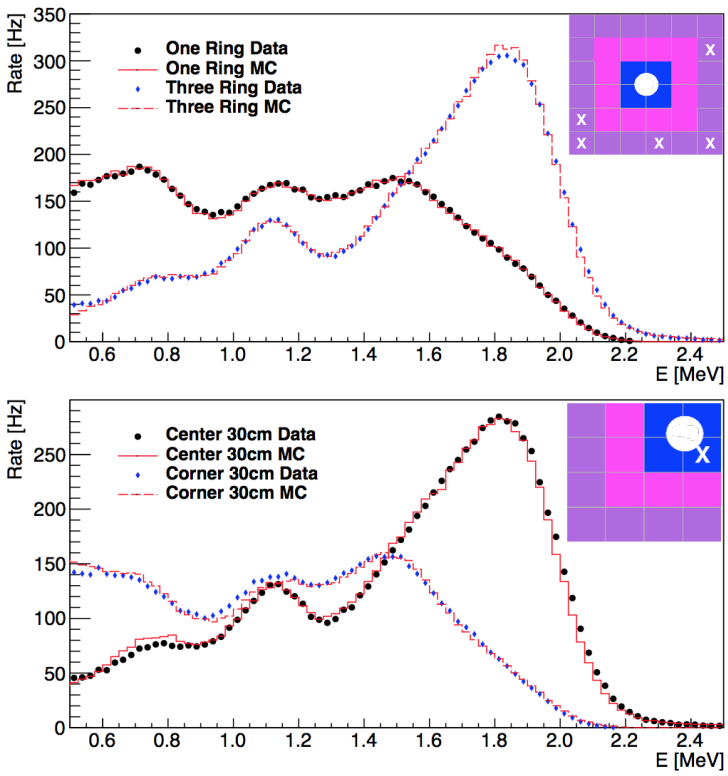


Figure 5.14: Reconstructed energy distributions for calibration and best-fit PG4 MC ^{22}Na source deployment datasets. Insets show the source deployment axis and ring definitions, with 'X' indicating inactive segments. This calibration run, taken earlier in the data collection period, has fewer inactive segments than the IBD selection. Top: Energy distributions integrated over the detector center, including the nearest one or three rings of segments. Bottom: Three-ring energy distributions for source deployments at $z = 30$ cm along the detector center and corner calibration axes. Source [70].

Chapter 6

Antineutrino detection

After the technical overview of the detector in Chapter 4 and the description of the relevant calibrated data structures for physics analyses in Chapter 5, this chapter will describe the IBD candidate event selection procedure, including a detailed explanation of the primary backgrounds affecting the experiment and the methods developed to mitigate them. Additionally, the chapter covers the development, implementation, and optimization of selection cuts used to identify IBD-like candidates during both reactor-on and reactor-off periods and the background subtraction method applied post-selection to produce the IBD spectrum. A summary of the latest analysis methods designed to handle a time-evolving detector configuration is presented, resulting in a multi-period analysis. This summary will include a comparison with previous results and a report on the final IBD statistics for the experiment. Furthermore, the chapter will explain how the `PG4` framework simulates IBDs and calculates IBD efficiencies, along with multiple data-MC crosschecks performed to validate the final IBD measured signal.

6.1 Description of datasets

The primary dataset from the PROSPECT experiment spans from March 5, 2018, to October 6, 2018. During this period, which included five HFIR fuel cycles, the

PROSPECT detector was in physics data-taking mode for 183 days, with the HFIR reactor operating for 105 of those days and shut down for 78 days. An additional eight days were dedicated to calibration data-taking. Due to PMT HV or other data quality issues identified after data collection, physics data from eight reactor-on days and five reactor-off days were excluded from the analysis. Ultimately, data from 95.6 reactor-on days and 73.1 reactor-off days were used for the main physics analyses.

PMTs in 64 of the 154 detector segments exhibited current instabilities during physics data-taking. These segments, linked to one or both PMTs, experienced intermittent shutdowns due to scintillator leakage into the PMT housing. As a result, only data from consistently operational segments throughout the entire data collection period were used. This approach aimed to streamline the analysis and simplify the evolution of the detector response function. Sections 6.2 through 6.6 describe the development of selection criteria for the analysis using a single detector configuration, along with the final statistics obtained leading to the results published in the summer of 2020 [70].

6.2 IBD detection strategy in PROSPECT

PROSPECT detects $\bar{\nu}_e$ events via the IBD interaction, where $\bar{\nu}_e$ produced during the fission of ^{235}U interact with hydrogen nuclei in liquid organic scintillator. The IBD signal consists of time- and position-correlated energy depositions produced by an IBD positron and the capture of the corresponding IBD neutron on ^{6}Li doped into the liquid scintillator. Fig. 6.1 shows a schematic representation of the interaction in the LiLS filling the inner detector.

Incoming $\bar{\nu}_e$ produced by HFIR span an energy range from sub-eV to tens of MeV. During an IBD interaction, in the process of generating $e^+ + n$, there is a gain in the rest mass energy difference of $m_n - m_p = 1.29$ MeV plus the rest mass energy of the positron $m_e = 0.511$ MeV. Therefore, the IBD interaction has a threshold energy given by:

$$E_{\bar{\nu_e},th} = \frac{(m_e + m_n)^2 - m_p^2}{2m_p} = 1.80573 \text{ MeV} \tag{6.1}$$

while the reconstructed energy deposited by the IBD positron can be related to that of the incoming neutrino by:

$$E_e = E_{\bar{\nu_e}} - 0.78\ MeV - E_n, \tag{6.2}$$

with outgoing IBD neutron kinetic energy, E_n, of order 10 keV or less.

The IBD positron deposits up to 8 MeV of kinetic energy with a max multiplicity of 3 detector segments, where the highest energy deposition typically occurs in the segment where the IBD interaction took place. The positron then annihilates, typically producing two 511 keV γ-rays, which deposit energy in segments within a few tens of centimeters of the IBD interaction point. These low-density energy depositions related to the positron occur on nanosecond timescales.

On the other hand, the neutron produced by the IBD interaction has a kinetic energy of less than a few tens of keV, leading to minimal scintillation light as it slows down. It then captures, within a few tens of centimeters from the IBD interaction point, with a time constant of about 50 μs. Approximately 75% of these neutrons capture on ^{6}Li, forming a ^{3}H-^{4}He pair that releases a total visible energy of 0.526 MeV. The high ionization density tracks of these capture products end within micrometers of the neutron capture point, producing scintillation light in a single segment.

The unique kinematic properties of the IBD interaction, combined with the optimized design of the PROSPECT detector, allow for sensitivity to these specific signatures. However, the detector is still subject to various background sources that can mimic an IBD-like interaction. To address this, a series of selection cuts based on temporal, kinematic, and topological features were developed, optimized, and implemented. These cuts are essential for accurately extracting the IBD signal and minimizing the impact of background interference and are defined in the following subsections.

6.2.1 IBD cuts

- **Prompt cut**
  - Cluster size ≥ 1
  - Each pulse in the cluster must have a reconstructed energy E_{smear} between 0.8 and 7.2 MeV.
  - The calibrated PSD for each pulse in the cluster must be all within 2.0 standard deviations of the mean of the calibrated energy-dependent electron-like PSD band ($\sim$0.13 (as shown in Fig. 5.6)).
- **Delayed cut**
  - Single-pulse cluster with (E_{rec},PSD) phase space consistent with n-Li capture (as shown in Fig. 5.6).
  - Cluster must have a reconstructed energy E_{rec} within $\pm 3\sigma$ of the mean value of 0.526 MeV.
  - PSD for single-pulse cluster in the cluster must within $\pm 2\sigma$ of the PSD mean value ($\sim$0.25).
- **Time coincidence cut**
  - Delayed cluster must appear within 120 μs of the prompt cluster.
- **Distance cut**
  - The delayed cluster is also required to travel no further than segments vertically/horizontally adjacent to the segment with the highest prompt-cluster E_{rec}.
  - If prompt-delayed cluster events occur in the same segment, the prompt-delayed Z_{rec} difference is required to be less than 140 mm
  - If prompt-delayed cluster events occur in adjacent segments, the prompt-delayed Z_{rec} difference must be less than 100 mm.

6.2.2 Background vetoes

The veto cuts in the PROSPECT analysis are designed to minimize the impact of the primary background sources: time-correlated cosmic backgrounds and accidental backgrounds originating from the reactor building (see Section 6.3).

- **Muon veto**
  - Muon tracks traversing the detector deposit large amounts ($\geq$ 15 MeV) of scintillation light and induce showers of fast and slow neutrons.
  - IBD candidates are rejected if their delayed cluster is within 200 μs of a preceding cluster with $E_{rec} \geq 15$ MeV.
  - This removes interaction secondaries from the cosmic ray that may drift into the detector to produce a ^{6}Li capture.
- **Neutron veto**
  - IBD candidates with a delayed capture occurring within 400 μs of another neutron capture event are rejected.
  - This rejects multi-neutron showers from cosmic ray interactions in the materials surrounding the detector.
- **Recoil veto**
  - IBD candidates are rejected if their delayed capture occurs within 250 μs of a preceding cluster with $E_{rec} > 0.25$ MeV and includes at least one pulse with a PSD greater than 2σ above the peak of the electron-like PSD band.
  - This rejects cosmic ray interactions that produce heavy secondaries.

These three vetoes define what is known in the PROSPECT experiment as the cosmogenic veto. A graphical description of their implementation is shown in Fig. 6.2.

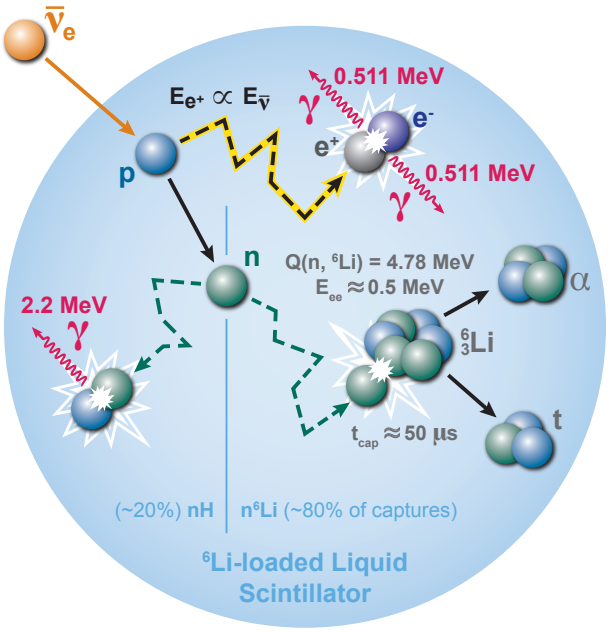


Figure 6.1: Schematic of the kinematics of the IBD interaction in the LiLS of the PROSPECT detector.

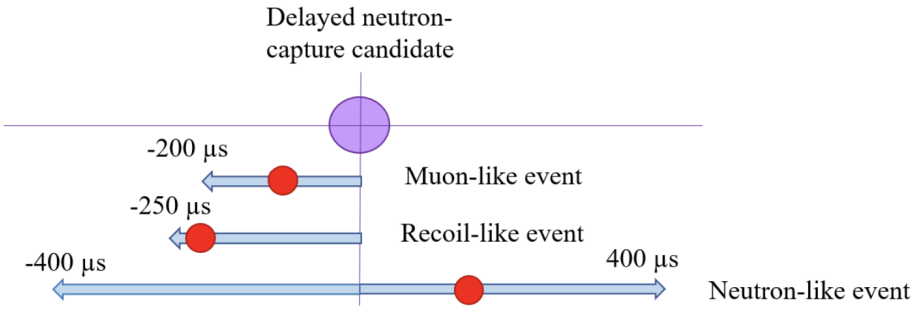


Figure 6.2: Scheme of implementation of cosmic shower veto. Delayed neutron-capture the candidate is shown in purple, veto-triggering events are shown in red, and time windows are represented with blue arrows. Source [161].

- **Fiducial Cut**
  - Simulations of cosmogenic backgrounds indicate high neutron-related background on the outer layer of the segments, shown in Fig. 6.3. Thus, IBD candidates are rejected if either of the clusters occurs in segments located in the outermost layer of the detector.
  - Similarly, IBD candidates are rejected if prompt or delayed Z_{rec} values are within ± 400 mm of the segment center.
  - Additional gamma background coming from the neutron beamlines underneath the experiment hall causes larger backgrounds in the southeast region of the detector (as shown in Fig. 6.11). As a result, events with maximum E_{smear} within segments 25 and 26 were also removed from the analysis.
- **Pile-up veto**
  - IBD candidates are also rejected if either prompt or delayed clusters occur within 0.8 μs of a previous cluster.

6.2.3 Implementation of IBD selection criteria

The cuts and vetoes described earlier define the IBD selection criteria used for the analysis with a single detector configuration. Each cut and veto was optimized sequentially, following the procedure outlined in Section 6.7.2, to maximize the number of effective IBD statistics described in Section 6.4. Fig. 6.4 illustrates the final detector configuration used, consisting of 70 fully operational segments as the fiducial volume and 22 non-fiducial operational segments (those in the outermost layer of the detector, as well as segments 25 and 26). Additionally, 62 segments with one or both PMTs non-operational were excluded from the analysis.

The impact of the subsequent application of the selection cuts and vetoes is illustrated in Fig. 6.5, where a reduction in the number of IBD candidates of ~ 3

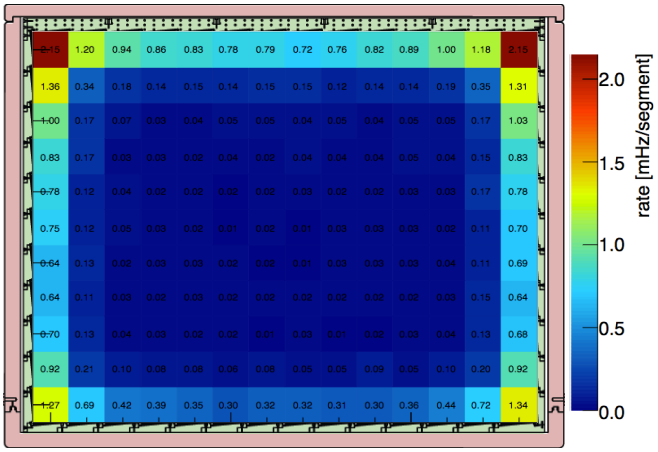


Figure 6.3: Simulated background rates of cosmogenic neutron interactions that mimic the IBD signal after topology cuts and segment-end fiducialization. The background rate is notably higher in the outermost ring of segments (rows 1 and 11, columns 1 and 14) than in the fiducial volume used for analysis (rows 2-10, columns 2-13). The segments are enclosed by the acrylic support structure and the inner detector's acrylic containment tank. Source [78].

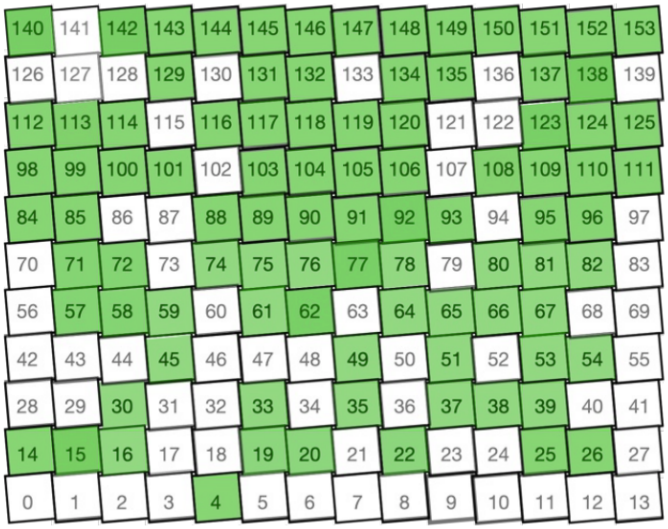


Figure 6.4: The segment status map used for the single detector configuration analysis [70] is illustrated. Segments with both PMTs fully operational throughout the data collection period are highlighted in green. In contrast, segments where one or both PMTs exhibited gain instabilities at any point during data collection are shown in white and are excluded from this analysis.

orders of magnitude is obtained, resulting in a significant background suppression. However, peak-like features in both E_{rec} and PSD spectra of prompt-like signals remain after the application of cuts, indicating the presence of residual background post-IBD selection. These features will be explained in detail in Section 6.3.

Another way to evaluate the impact of the selection criteria on the IBD candidate sample is by examining the E_{rec} vs. PSD distribution of events that pass all cuts, as shown in Fig. 6.6. The figure displays the total summed prompt E_{rec} and the PSD value for the highest energy pulse within the prompt cluster. The low PSD elongated band includes IBD candidates and some non-IBD events with high PSD values, likely due to inelastic scattering. Fig. 6.6 also highlights two IBD-like background regions: one at low energy and high PSD from time-coincident neutron captures on ^{6}Li, and another across a wide energy range and high PSD from single neutron scattering and capture on ^{6}Li. These event classes, (n-Li, n-Li) and (n-p, n-Li), help investigate multi-neutron showers and cosmogenic neutron effects on the IBD signal. The distribution in Fig. 6.6 demonstrates the effective reduction of multi-neutron and fast-neutron backgrounds through PROSPECT's prompt PSD capabilities, with an additional high PSD band likely due to fast neutron recoils on heavier nuclei.

Lastly, an important factor to consider when applying these selection criteria cuts is the resulting deadtime from each veto. When a veto is active, the detector does not record any data during that time window, reducing the detector's livetime to account for the deadtime introduced by each veto. Fig. 6.7 illustrates the implementation of cosmic deadtime.

The surrounding time window is considered deadtime for each veto-triggering event, as any potential delayed-like candidate (for the cosmic veto) or prompt-like candidate (for the pile-up veto) would be vetoed during this period. As a result, a deadtime correction factor α_{dt} can be defined on a per-run basis by

$$\alpha_{dt} = \frac{t_{run}^2}{(t_{run} - dt_{prompt})(t_{run} - dt_{delayed})} \tag{6.3}$$

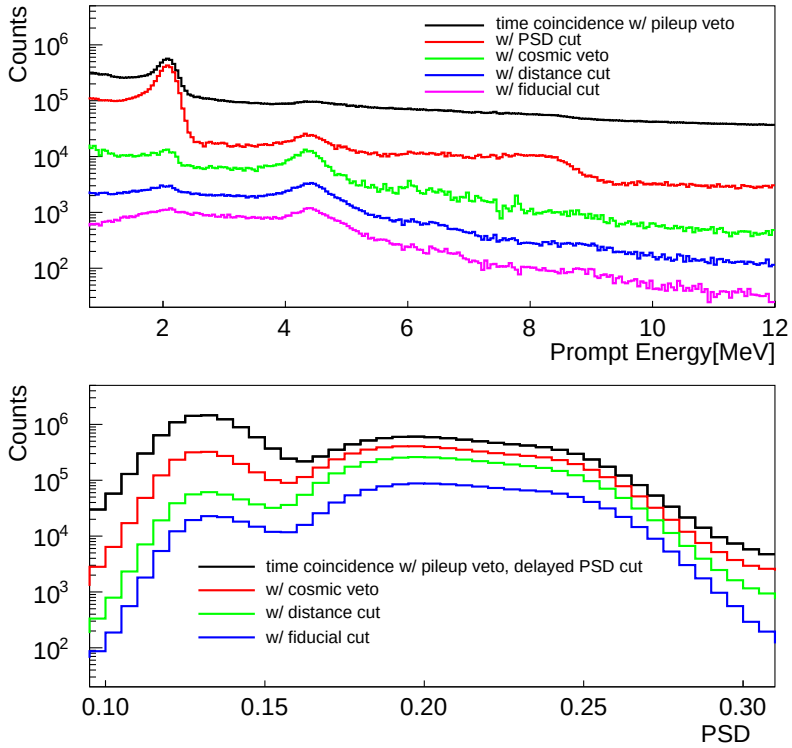


Figure 6.5: Distributions of prompt E_{rec} (top) and reconstructed PSD (bottom) of the highest-E_{smear} prompt as IBD selection cuts are sequentially added to the PROSPECT reactor-on dataset. Accidental backgrounds described in Section 6.3.1 have been subtracted from these distributions. Source [70].

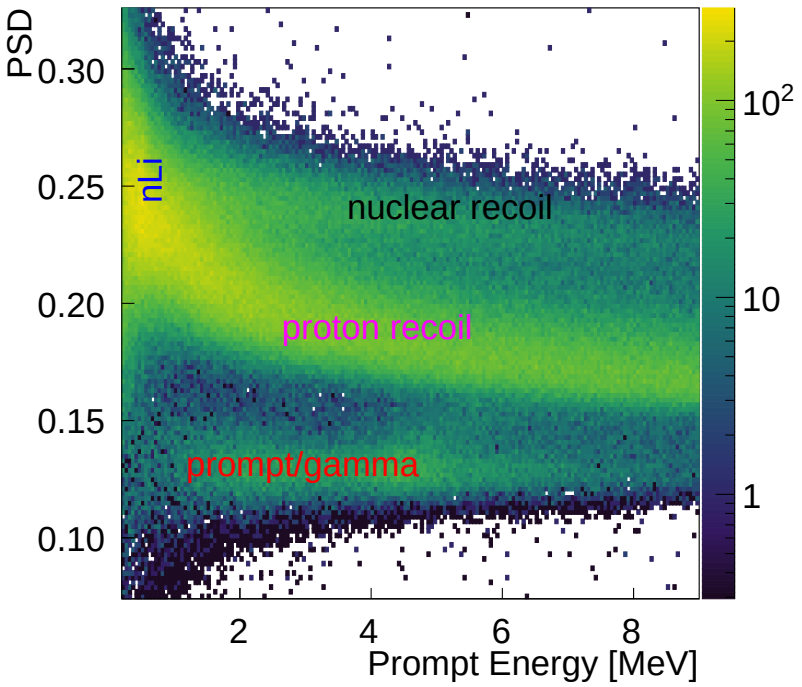


Figure 6.6: E_{rec}vsPSD distributions for selected IBD-like events from a single reactor-on cycle. The plot shows the total prompt E_{rec} and the PSD value for the pulse with the highest reconstructed energy within the prompt cluster. The labeled regions indicate IBD candidates (red), coincident (n-Li, n-Li) captures (blue), (n-p, n-Li) scattering and captures of fast neutrons on protons (magenta), and on other heavier nuclei (black). It is noted that some prompt clusters within the IBD candidate region may contain high-PSD pulses and thus will not be selected as IBD candidates. Source [70].

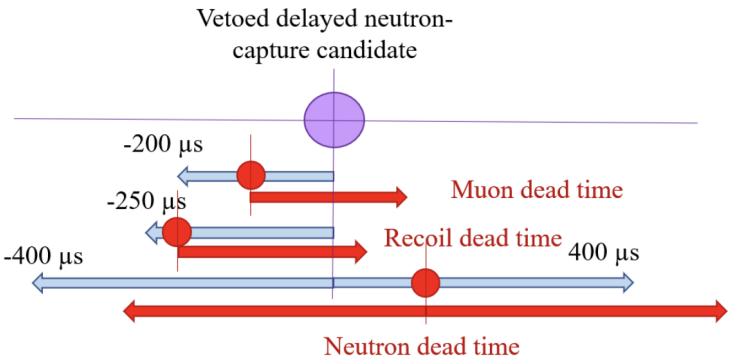


Figure 6.7: Schematic of the deadtime introduced by the cosmic shower veto implementation. The delayed neutron-capture candidate is indicated in purple, veto-triggering events are shown in red, red arrows illustrate deadtime windows, and blue arrows represent veto time windows. Source [161].

where t_{run} corresponds to about one hour of data taking, while dt_{prompt} and $dt_{delayed}$ describe the amount of deadtime introduced by the prompt and delayed vetoes, respectively. Fig. 6.8 compares the fractional detector-wide deadtime rates over time for various veto types. Deadtime rates are higher during reactor-on periods and show a steady increase over time for neutron, recoil, and all other vetoes during both reactor-on and reactor-off periods. Accurate corrections for these deadtime differences are crucial for comparing IBD-like rates across different periods since the increase in deadtime impacts the efficiency of the IBD selection over time.

6.3 IBD backgrounds

Backgrounds for IBD interactions involve events within the electron-like PSD band occurring close in space and within tens of microseconds before an n-^{6}Li capture event. Recoiling protons and a small fraction of high PSD gammas in the 0.526 MeV energy region of the neutron capture window can mimic the capture signal. This results in reactor gamma backgrounds accidentally coinciding with true or false positive neutron capture signals, known as accidental backgrounds. Another primary source of backgrounds arises from events correlated with cosmic ray showers, which

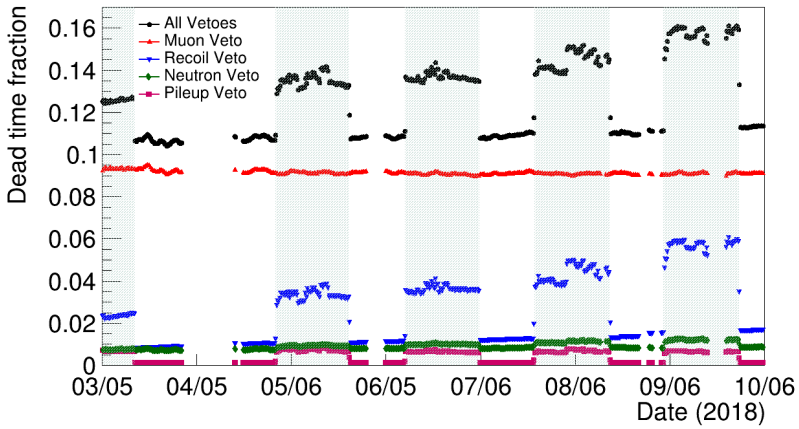


Figure 6.8: The total dead time fraction due to IBD selection veto cuts (black), along with the individual dead time fractions for each veto: muon (red), recoil (blue), neutron capture (green), and pile-up (pink). Vertical green shaded bands denote reactor-on periods. Source [70].

can produce multiple neutrons that mimic the topology of the IBD signal within the detector. Both types of background events are discussed in detail in the following subsections.

6.3.1 Accidental backgrounds

Single γ-rays and neutron captures from uncorrelated events can deposit energy in close temporal and spatial proximity within the PROSPECT detector, passing all IBD selection cuts and becoming a primary source of accidental background, as shown in Fig. 6.9.

During reactor-on periods, reactor-related gamma fluxes significantly contribute to accidental backgrounds due to their high rate. Since γ-rays cannot be distinguished from positron energy depositions based on their pulse shape, the analysis becomes challenging, especially as the IBD positron is the primary prompt-like signal in the detector. As the scintillator degraded, the ability to reject gamma backgrounds from the n-^{6}Li capture region decreased, leading to an increase in neutron capture-like signals over time, as shown in Fig. 6.10.

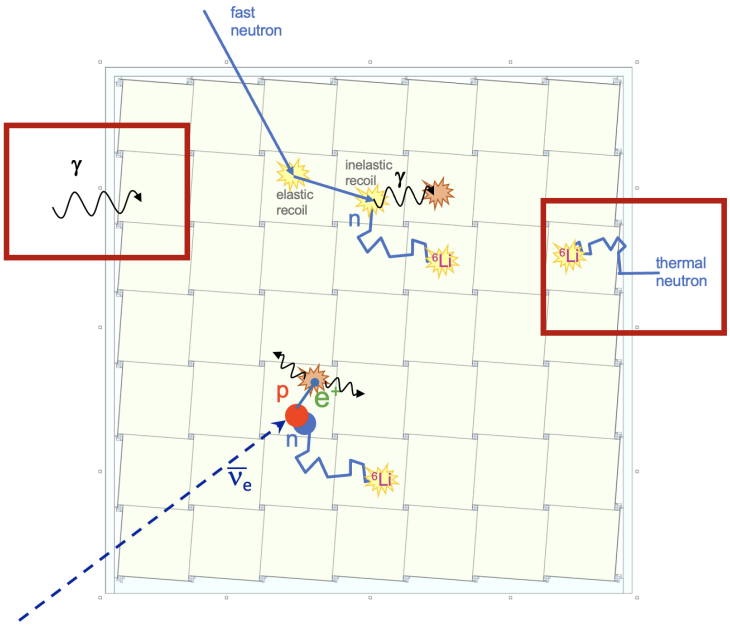


Figure 6.9: Graphical illustration of uncorrelated γ-rays and single thermal neutron captures in the PROSPECT inner detector resulting in accidental backgrounds mimicking the IBD signal.

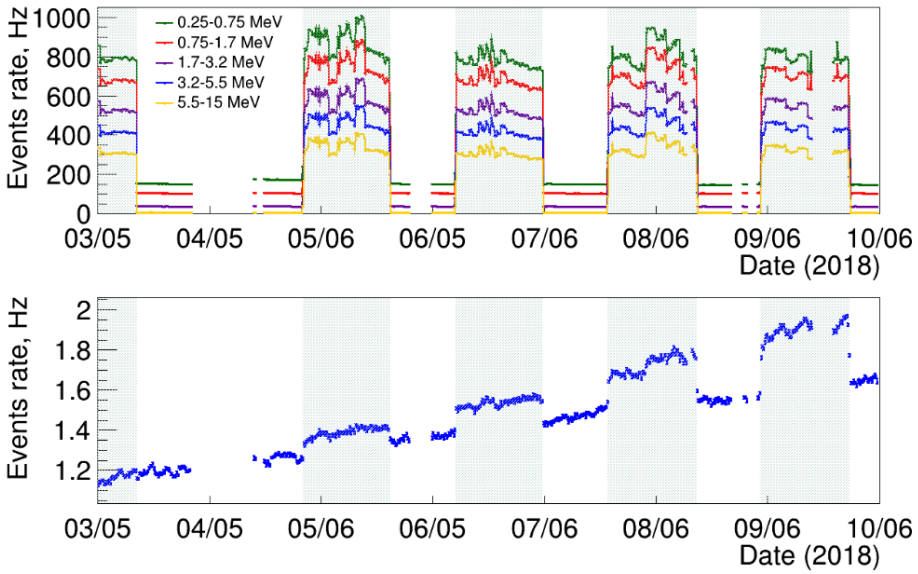


Figure 6.10: Top: IBD prompt-like signal rates over time in the detector. Bottom: Delayed-like signal rates over time. Variations during the reactor-on period are caused by neutron beam experiments, which alter gamma fluxes. The gradual increase in delayed-like signals is due to reduced light output over time, causing more gammas to appear in the high PSD region of the n-Li capture. Source [70].

The spatial distribution of reactor-on prompt-like signals is depicted in Fig. 6.11, with the detector facing east, positioning the reactor below and to the left of the diagram. A 10 ms window from -12 ms to -2 ms relative to a delayed cluster event is scanned for prompt-like signals to subtract accidental backgrounds accurately. As described in Section 6.2.1, the IBD time coincidence cut requires a delayed cluster to occur within 120 μs of the prompt signal. The chosen accidental window includes only events uncorrelated with the neutron capture, known as the off-window method. This approach allows for a high-statistics sampling of random accidentals with the n-^{6}Li signal. An accidental background scaling factor that accounts for differences between the accidental time window and the time coincidence cut is defined as follows:

$$\alpha_{acc} = \frac{t_{IBD}}{t_{acc}} = \frac{120\mu s}{10000\mu s} = 0.012 \tag{6.4}$$

α_{acc} together with α_{dt} described in Eq. 6.3 are applied to both reactor-on and reactor-off accidental IBD event samples. The accidental sample is then subtracted directly from the IBD candidates. The prompt E_{rec} distributions of accidental background events for reactor-on and reactor-off periods are shown alongside cosmic backgrounds in Fig. 6.13. The accidental rate during reactor-off periods is very close to zero.

6.3.2 Time-correlated cosmic ray induced backgrounds

Due to the minimal overburden at HFIR (< 1 mwe), the cosmic ray background in the HFIR building is significant. Most of these backgrounds originate from cosmogenic muon and neutron fluxes that can produce signals resembling an IBD interaction. Although the cosmic veto defined in Section 6.2.2 reduces cosmogenic backgrounds in reactor-on data samples, the post-selection dataset still contains substantial contributions from cosmic-induced, time-correlated prompt-like and delayed-like cluster pairs. These events in the prospect detector are illustrated in Fig. 6.12.

To maximize the removal of cosmic-induced IBD-like events in the reactor-on data sample, all cuts and vetoes described in Sections 6.2.1- 6.2.2 are applied to the data

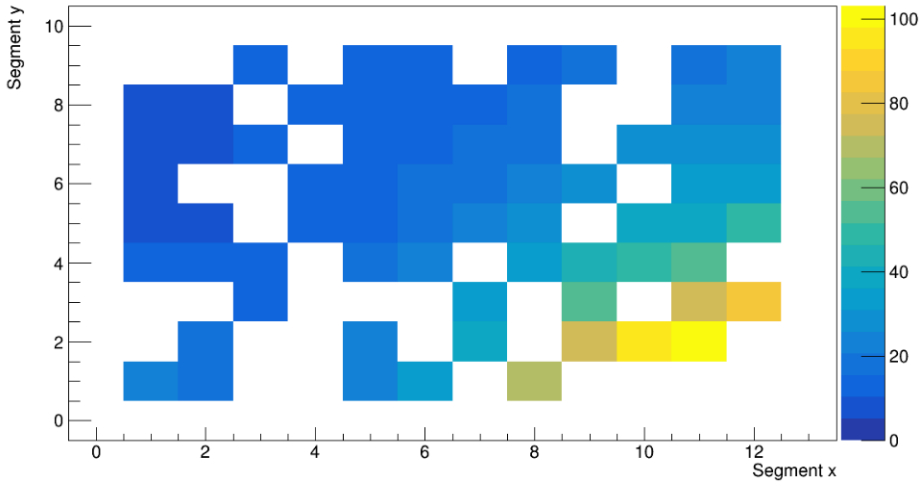


Figure 6.11: Reactor-on prompt-like signal rates for each active segment used in the 2020 analysis. The reactor is closest to the bottom left. Higher rates in the bottom right are due to neutron activation of materials surrounding the neutron beamline 4 beam splitter. Source [70].

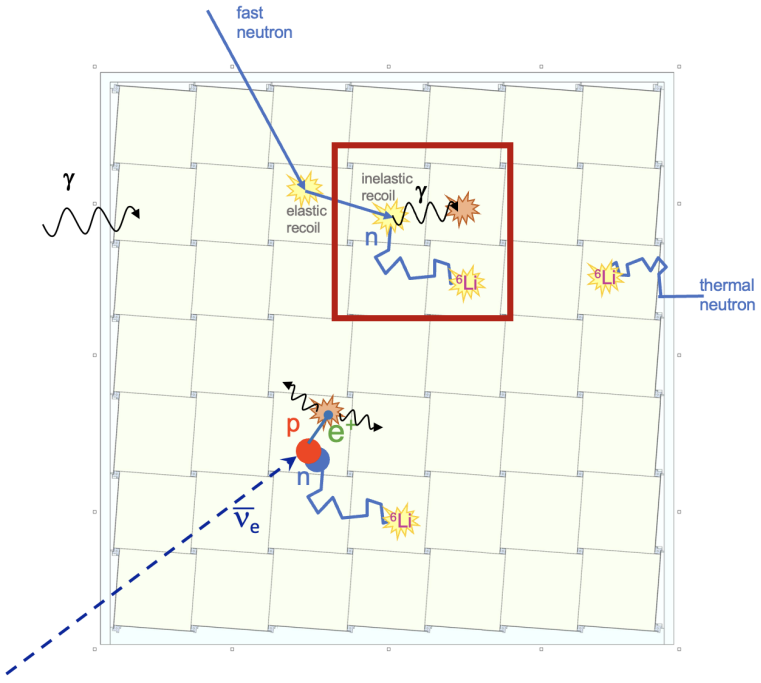


Figure 6.12: Graphical illustration of fast neutron produced background resulting in correlated backgrounds mimicking the IBD signal.

samples taken during reactor-off periods. Fig. 6.13 shows the accidental-subtracted prompt energy spectrum for events passing all IBD selection criteria. These are denoted as correlated events. As observed, both reactor-on and reactor-off prompt spectra exhibit similar peak-like features. The peak at 2.2 MeV corresponds to multi-neutron showers, where a neutron capture on hydrogen emits a gamma ray around 2.2 MeV, followed by a second neutron capture on ^{6}Li. The peak at 4.5 MeV results from the inelastic scattering of a neutron on ^{12}C, which emits a 4.43 MeV gamma, followed by a neutron capture on ^{6}Li. Both types of events are typical cosmic ray interactions that can mimic the IBD signal.

Cosmic background rates scale with atmospheric pressure. As pressure increases, the rates of correlated IBD backgrounds in the detector decrease due to fewer cosmic rays reaching the surface. This relationship is illustrated in Fig. 6.14, which shows reactor-off measured IBD candidates as a function of atmospheric pressure. A linear fit is applied to correct for pressure differences between reactor-on and reactor-off periods, ensuring accurate subtraction of the reactor-off sample explained in Section 6.4. This fit indicates a -0.70 $\pm$ 0.01 % mBar correlation. Based on the measured rate scaling and pressure differences, the scaling factor between reactor-off and reactor-on was determined to be $\alpha_{atm} = 1.00 \pm 0.03\%$.

The rates of other cosmogenic event classes, such as muons, neutron captures on ^{6}Li (n-Li), (n-Li, n-Li) coincident events, and (n-p, n-Li) events, were also analyzed relative to atmospheric pressure. These event rates showed scaling offsets between reactor-on and reactor-off periods within 0.1% of unity. To conservatively account for the effects of atmospheric changes, a 0.5% uncertainty in the atmospheric scaling factor is applied.

6.4 Measured IBD signal

The dataset obtained with the PROSPECT detector comprised 95.7 calendar days of reactor-on time and 73.1 calendar days of reactor-off time. After correcting for

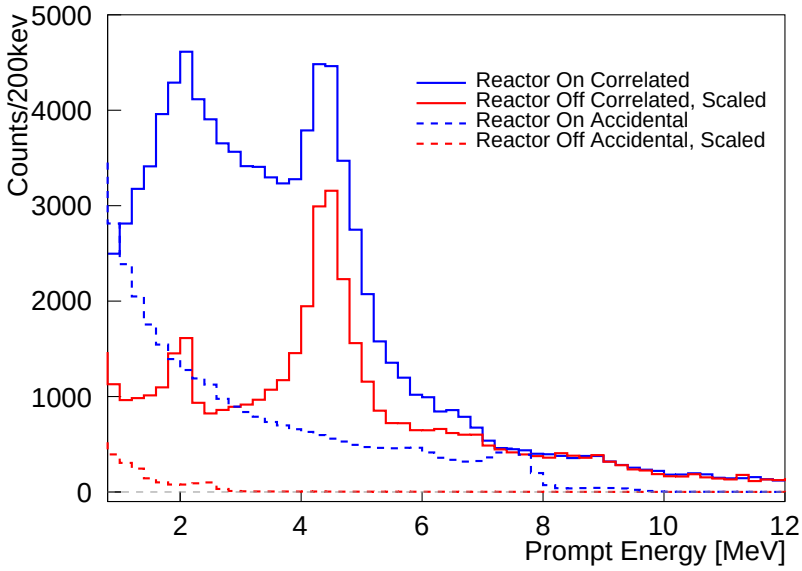


Figure 6.13: The measured prompt E_{rec} spectrum of correlated IBD-like candidates during reactor-on and reactor-off data periods. Accidental backgrounds, as described in the previous section, are shown with dashed lines in corresponding colors. The reactor-off correlated and reactor-off accidental spectra are scaled to match the reactor-on exposure time. Source [70].

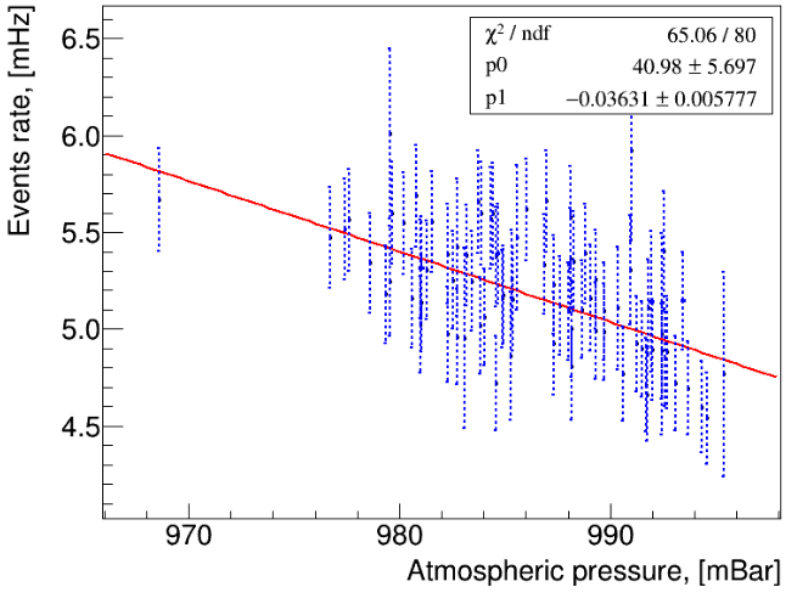


Figure 6.14: Reactor-off IBD candidate rates versus atmospheric pressure. A linear fit is applied to the data to correct for cosmogenic background rates between reactor-off and reactor-on measurements. Source [70].

deadtime, the total livetime was determined to be 82.2 days for reactor-on and 65.2 days for reactor-off. Applying the full IBD selection criteria to the entire dataset and focusing on the IBD energy region between 0.8 and 7.2 MeV, the single-detector configuration analysis reported a total of $115,852 \pm 340$ IBD-like events during reactor-on and $30,568 \pm 175$ during reactor-off. Of these, $87,494 \pm 341$ (reactor-on) and $29,259 \pm 175$ (reactor-off) were identified as correlated candidates, while $28,358 \pm 18$ (reactor-on) and $1,309 \pm 4$ (reactor-off) were accidental IBD-like events.

After applying livetime and atmospheric pressure scalings to the reactor-off correlated events, a total cosmogenic background estimate of $36,934 \pm 221$ for reactor-on was obtained. Subsequently, the total background-subtracted IBD prompt energy spectrum was derived by subtracting the reactor-on cosmogenic background from the reactor-on correlated IBD-like candidates. The resulting background-subtracted prompt energy IBD spectrum is shown in Fig. 6.15, along with the accidental-subtracted reactor-on and livetime-scaled reactor-off correlated candidates. The IBD signal's prompt energy distribution matches the expected shape for reactor antineutrinos ($\bar{\nu}_e$) interacting via inverse beta decay, with the highest count rates in the 1–7 MeV range. Beyond 7 MeV, the background-subtracted count rates are consistent with zero, confirming accurate data scaling during background subtraction. A statistical comparison from 8 MeV to 12 MeV yields a χ^2/DOF of 20.9/20, indicating no significant signal in this range.

The integrated IBD energy signal is calculated using the following equation:

$$N_{\mathrm{IBD}} = \sum_{i=0.8\,\mathrm{MeV}}^{7.2\,\mathrm{MeV}} \left(N_{\mathrm{On},i} - (\alpha_{\mathrm{acc}}\alpha_{\mathrm{dt}})N_{\mathrm{On,acc},i}\right) - R\alpha_{\mathrm{atm}}\left(N_{\mathrm{Off},i} - (\alpha_{\mathrm{acc}}\alpha_{\mathrm{dt}})N_{\mathrm{Off,acc},i}\right) \tag{6.5}$$

where $N_{\mathrm{On},i}$ and $N_{\mathrm{Off},i}$ represent the number of IBD candidates, including both correlated and accidental events, for the reactor-on and reactor-off periods, respectively. $N_{\mathrm{On,acc},i}$ and $N_{\mathrm{Off,acc},i}$ are the accidental IBD-like candidates determined using the off-window method for both periods. The variable R is the ratio of the on/off livetimes,

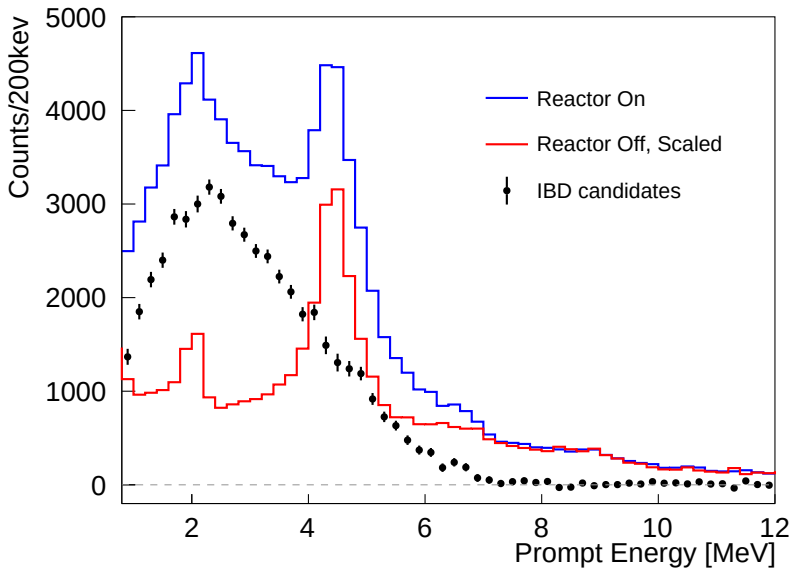


Figure 6.15: The reconstructed visible prompt energy E_{rec} spectrum (black) of IBD candidates, including statistical errors, is shown alongside the reactor-on (blue solid) and reactor-off (red solid) correlated candidates. The reactor-off spectrum is scaled to match the reactor-on livetime, with atmospheric scaling to account for the reactor-off background. All accidental events have been subtracted from these spectra. Source [70].

and α_{acc}, α_{atm}, and α_{dt} are the scaling factors for accidental events, atmospheric pressure, and deadtime, respectively. The total energy integrated IBD signal was found to be 50560±406 events.

In addition to the total IBD signal (N_{IBD}), the effective number of IBD statistics (N_{eff}) can be calculated from the background-subtracted IBD signal distribution. N_{eff} quantifies the statistical significance of the measured IBD signal by accounting for the combined statistical uncertainties of both signal and background (σ_{IBD}). It represents the equivalent number of background-free signal events that would yield the same statistical uncertainty. The expression for N_{eff} is given by:

$$N_{\text{eff}} = \sum_{i=0.8\,\text{MeV}}^{7.2\,\text{MeV}} \left(\frac{N_{\text{IBD,i}}}{\sigma_{\text{IBD,i}}} \right)^2$$

$$N_{\text{eff}} = \sum_{i=0.8\,\text{MeV}}^{7.2\,\text{MeV}} \frac{\left((N_{\text{On},i} - (\alpha_{\text{acc}}\alpha_{\text{dt}})N_{\text{On,acc},i}) - R\alpha_{\text{atm}}\left(N_{\text{Off},i} - (\alpha_{\text{acc}}\alpha_{\text{dt}})N_{\text{Off,acc},i}\right)\right)^2}{(N_{\text{On},i} + (\alpha_{\text{acc}}\alpha_{\text{dt}})^2 N_{\text{On,acc},i}) + (R\alpha_{\text{atm}})^2\left(N_{\text{Off},i} + (\alpha_{\text{acc}}\alpha_{\text{dt}})^2 N_{\text{Off,acc},i}\right)} \tag{6.6}$$

For this analysis, the total N_{eff} was found to be 18,100. The signal-to-background metrics for cosmic and accidental backgrounds were calculated to assess the background suppression capabilities further. These metrics are defined as the ratio of the IBD signal to the corresponding IBD-like background during reactor-on periods:

$$S:CB = \sum_{i=0.8\,\text{MeV}}^{7.2\,\text{MeV}} \frac{N_{\text{IBD}}}{R\alpha_{\text{atm}}\left(N_{\text{Off},i} - (\alpha_{\text{acc}}\alpha_{\text{dt}})N_{\text{Off,acc},i}\right)} \tag{6.7}$$

$$S:AB = \sum_{i=0.8\,\text{MeV}}^{7.2\,\text{MeV}} \frac{N_{\text{IBD}}}{(\alpha_{\text{acc}}\alpha_{\text{dt}})N_{\text{On,acc},i}} \tag{6.8}$$

The analysis reported $S:CB = 1.37$ and $S:AB = 1.78$, demonstrating excellent background rejection capabilities for an on-surface detector. The final IBD statistics obtained from the single-detector configuration analysis are summarized in Table 6.1. Following the successful extraction of the IBD signal, validation exercises were conducted using a `PG4`-IBD simulation to assess the effectiveness of the background subtraction process. The following sections detail the simulation of the IBD signal and the various crosschecks performed on the measured signal.

6.5 Simulating IBD interactions and efficiencies

IBD interactions are simulated by generating particles at random locations within the detector volume, using a $1/r^2$ probability distribution, where r is the distance from the center of the reactor core to a point within the detector. This approach ensures that vertices are selected from all potential signal-producing regions in the detector, including the PMT faces, optical grid, and support structures.

Table 6.1: Statistics of selected IBD candidates and accidental/cosmogenic backgrounds. Errors, where included, represent statistical uncertainties in the relevant signal and background datasets. Source [70].

Category	**Reactor-On**	**Reactor-Off**
Calendar Days	95.65	73.09
Live Days	82.25	65.16
IBD Candidates	115852	30568
Accidental Backgrounds	28358±18	1309±4
Correlated Candidates	87494 ± 341	29258±175
Rate Per Calendar Day	915± 4	400±2
Cosmogenic Backgrounds	36934±221	N/A
Total IBD Signal	50560±406	N/A
IBD Rate Per Calendar Day	529 ±4	N/A
Effective IBD counts	18100	N/A
Effective IBD Rate Per Calendar Day	189	N/A
S:CB	1.37	N/A
S:AB	1.78	N/A

A simple point-like model of the reactor core is employed to calculate IBD detection efficiencies. For a more realistic IBD distribution used in oscillation analysis, a cylindrical volume replicating the dimensions of the HFIR core, as detailed in Section 4.2, serves as the source. The angular distribution, characterized by $\cos\theta$, where θ is the angle between the incoming antineutrino and outgoing positron, is derived in [202]. The first-order expression in terms of the inverse nucleon mass M, $O(1/M)$, for the IBD angular distribution is given by the following expression:

$$\frac{d\sigma}{d\cos\theta} = \frac{\sigma_0}{2}\left[(g_V^2 + 3g_A^2) + (g_V^2 - g_A^2)v_e^{(1)}\cos\theta\right] E_e^{(1)} p_e^{(1)} - \frac{\sigma_0}{2}\left[\frac{\Gamma}{M}\right] E_e^{(0)} p_e^{(0)}. \quad (6.9)$$

where σ_0 is a normalizing constant; g_V and g_A are the vector and weak axial vector coupling constants, respectively; the superscripts (0) and (1) indicate zeroth- and first-order in $1/M$; Γ is a kinematic term as defined in [202]; and v_e, E_e, and p_e are the velocity, energy, and momentum of the IBD positron, respectively.

After selecting the positron angle, both the positron and neutron energies and the positron angle are used to determine the resulting neutron angle while conserving four-momentum. For reactor $\overline{\nu}_e$ energies of tens of MeV, the distribution in Eq. 6.9 is mostly oriented opposite to the direction of the incoming neutrino. Consequently, positrons are predominantly directed back toward the reactor, while neutrons are mainly directed away. The `PG4` simulation employs two of Geant4's neutron scattering libraries: `G4NeutronHPElastic` for neutron energies above 4 eV and `G4NeutronHP-ThermalScattering` for energies below 4 eV. Positrons are simulated using Geant4's default library for electromagnetic interactions, `emstandard`.

Following the procedure outlined and the description of the `PG4` framework and visible energy calibration detailed in Section 5.3, an energy response matrix that relates antineutrino energy to the reconstructed energy E_{rec} in the PROSPECT detector can be produced. This is achieved by generating 10,000 random IBD vertices for monoenergetic antineutrinos with energies ranging from 1.8057 MeV to

10.0 MeV in 0.1 MeV increments. The construction of the response matrix depends on the specific physics analysis being performed: for the spectral shape analysis (see Chapter 7), the entire detector volume is treated as a single unit (segment-integrated response), while for sterile neutrino oscillation analysis (see Chapter 8), each detector segment is considered an independent volume.

After simulating the energy deposition of the IBD products in the detector volume, the procedure described in Sections 5.2 and 5.3 is applied to simulate, cluster, pair, and calibrate the pulses these events would produce. The IBD selection criteria outlined in Section 6 are then applied to all simulated IBD events for each $\overline{\nu}_e$ value. Fig. 6.16 presents the response matrix used for spectral shape analysis in a single-detector configuration, showing the correlation between each $\overline{\nu}_e$ energy and its corresponding E_{rec}. The figure also includes a distribution depicting the $E_{\overline{\nu}}$-E_{rec} relationship for a 4.0 MeV monoenergetic $\overline{\nu}_e$, representing a vertical slice of the entire detector response matrix. A significant off-diagonal component is observed at low E_{rec}, primarily due to the positron kinetic energy deposited in non-active regions of the detector.

6.5.1 Determination of relative IBD efficiency

The efficiency of IBD detection varies across different locations within the detector and changes over time due to the degradation of optical properties and failing PMTs. Efficiency is reduced at the detector's edges, where neutrons originating from IBD interactions are more likely to escape the detectable region. Similarly, segments with more adjacent blind or single-ended segments experience lower detection efficiency.

To verify neutron mobility at thermal energies, simulations were performed using `PG4` with ^{252}Cf source deployments inside the detector. These simulations identified ^{252}Cf fission events by detecting a prompt electron-like signal from emitted gammas and a delayed ^{6}Li neutron capture event. The neutron capture rates in segments were measured based on their distance from the source and compared to results from

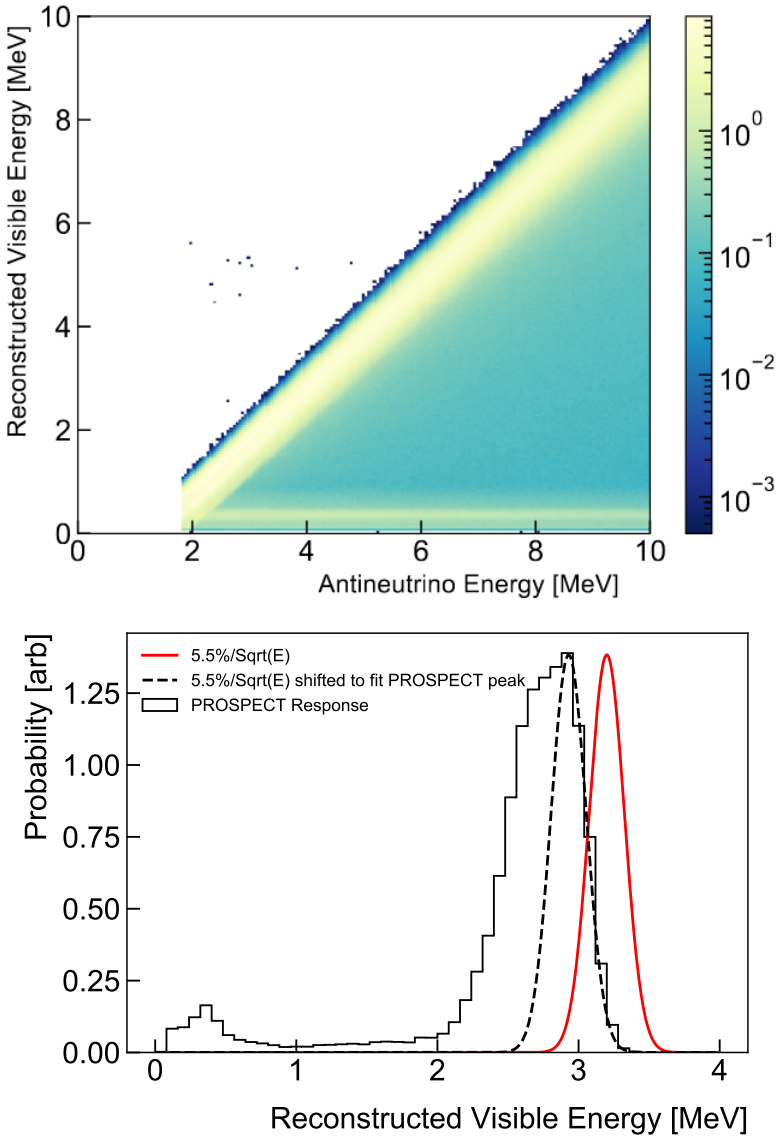


Figure 6.16: Top: The energy response matrix used to convert detected energy into antineutrino energy. The diagonal line corresponds to events with nearly complete positron energy deposition in the LiLS, approximately 0.8 MeV below the antineutrino energy. Nonzero values below this line reflect various levels of potential energy loss. Bottom: PG4-modeled E_{rec} distribution for a monoenergetic 4.0 MeV $\overline{\nu}_e$ uniformly distributed across the detector. Source [70].

simulations using a custom ^{252}Cf fission generator. The strong agreement between the simulation and experimental data, as depicted in Fig. 6.17, confirms the simulation's ability to accurately model position-dependent efficiency variations caused by neutron mobility.

The efficiency of each segment was calculated by taking the ratio of background-subtracted IBD candidates reconstructed in a segment to the number of PG4-simulated IBD events with vertices in the same segment. Fig. 6.18 displays the relative efficiency for all active segments, normalized to the segment with the highest efficiency.

Efficiency variations also arise from segment volume uncertainties and fiducialization differences. Instead of propagating these uncertainties through PG4-MC simulations, a conservative upper bound on their impact on relative efficiencies was determined based on empirical studies. Measurements of the optical grid revealed that segment volumes vary by less than 1% relative to one another. Differences in Z_{rec} resolution from detected **RnPo** events are less than 1 cm across segments, resulting in a variation in z fiducialization of less than 2% per segment. Additionally, slight deviations in PSD performance between segments are expected to cause efficiency variations at the sub-1% level. A 5% segment-uncorrelated uncertainty was assigned to the segment efficiency to account for all these uncertainties (see Section. 8.4.2).

6.6 Validation of IBD signal

The consistency of IBD-like datasets across different periods confirms the stability of the detector's energy scale, background subtraction method, and residual IBD-like background. To assess this stability, two separate comparisons were conducted between reactor-on and reactor-off periods. The selected periods for each comparison, depicted in Fig. 6.19, are interleaved, as shown in each panel's inset. This interleaving helps minimize the impact of any systematic variations in efficiency or energy response that may occur over longer periods. Furthermore, datasets are adjusted for relative differences in atmospheric pressure between each set of periods defined for comparison.

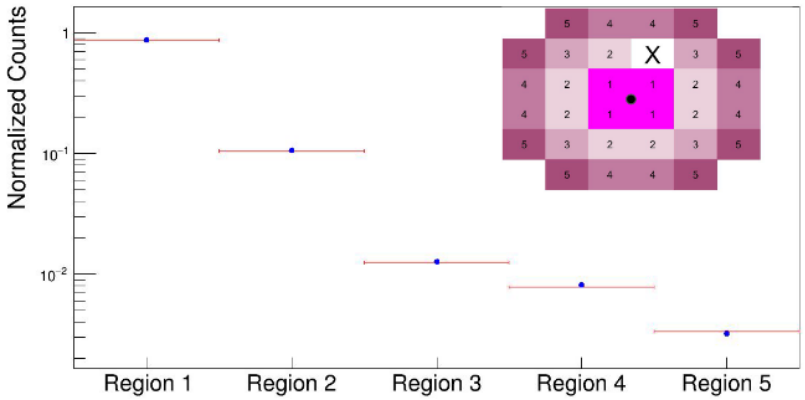


Figure 6.17: Data-simulation comparison for normalized neutron capture event rates from a ^{252}Cf source deployment, selected by a prompt gamma-like event followed by a delayed ^{6}Li neutron capture signal. The horizontal axis shows the distance from the source deployment, with the diagram in the upper right illustrating the segment location corresponding to each distance value. 'X' denotes inactive segments, blue dots correspond to data points, and red lines illustrate simulated results. Source [70].

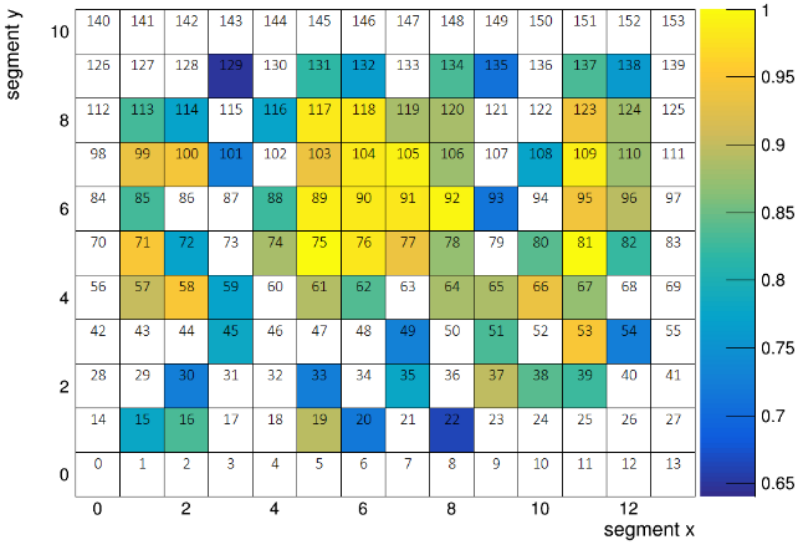


Figure 6.18: Simulated relative detection efficiency for IBD events based on single-detector configuration analysis of PROSPECT data. Segments with no values represent segments turned off for this analysis. Source [70].

As with the reactor-on and reactor-off datasets, the scaling factor for this off-off comparison is less than 1%. A χ^2/DOF metric was calculated for the IBD region, ranging from 0.8 to 7.2 MeV E_{rec}, for both comparisons, illustrating the consistency between reactor periods with the following results:

- **On-on comparison**: $\chi^2/\text{DOF} = 47.68/31$
- **Off-off comparison**: $\chi^2/\text{DOF} = 26.2/31$

In addition to evaluating time-dependent stability, analyzing the uniformity of the IBD signal across different regions within the detector is essential. Since the HFIR core acts as an isotropic source of $\overline{\nu}_e$, the reconstructed IBD signal is expected to follow a $1/r^2$ distribution relative to the distance from each detector segment to the reactor core. After correcting for segment efficiencies described in Section 6.5.1, the number of background-subtracted IBD events was calculated for each segment and plotted, as shown in Fig. 6.20. The bottom panel of Fig. 6.20 presents the best-fit inverse-square function applied to the efficiency-corrected IBD signal per segment baseline, resulting in a χ^2/DOF of 72.4/69.

In the PROSPECT detector, IBD interactions are expected to exhibit varying levels of γ-ray energy leakage due to differences between the innermost and outermost segments and inactive segments near the bottom. Consequently, these differences cause variations in the prompt E_{rec} spectra across different detector regions. To ensure these effects are accurately modeled, background-subtracted IBD signal distributions were compared across different detector regions, as shown in Fig. 6.21. The comparisons illustrated in Fig. 6.21 indicate that, while energy spectra and normalizations vary between regions due to uneven segment distribution, the deviations align with predictions from `PG4` MC simulations. Furthermore, the data-`PG4` spectrum ratios between regions are consistent within statistical limits, with χ^2/DOF values of 56.6/31 and 54.4/31 for inner-outer and upper-lower comparisons, respectively.

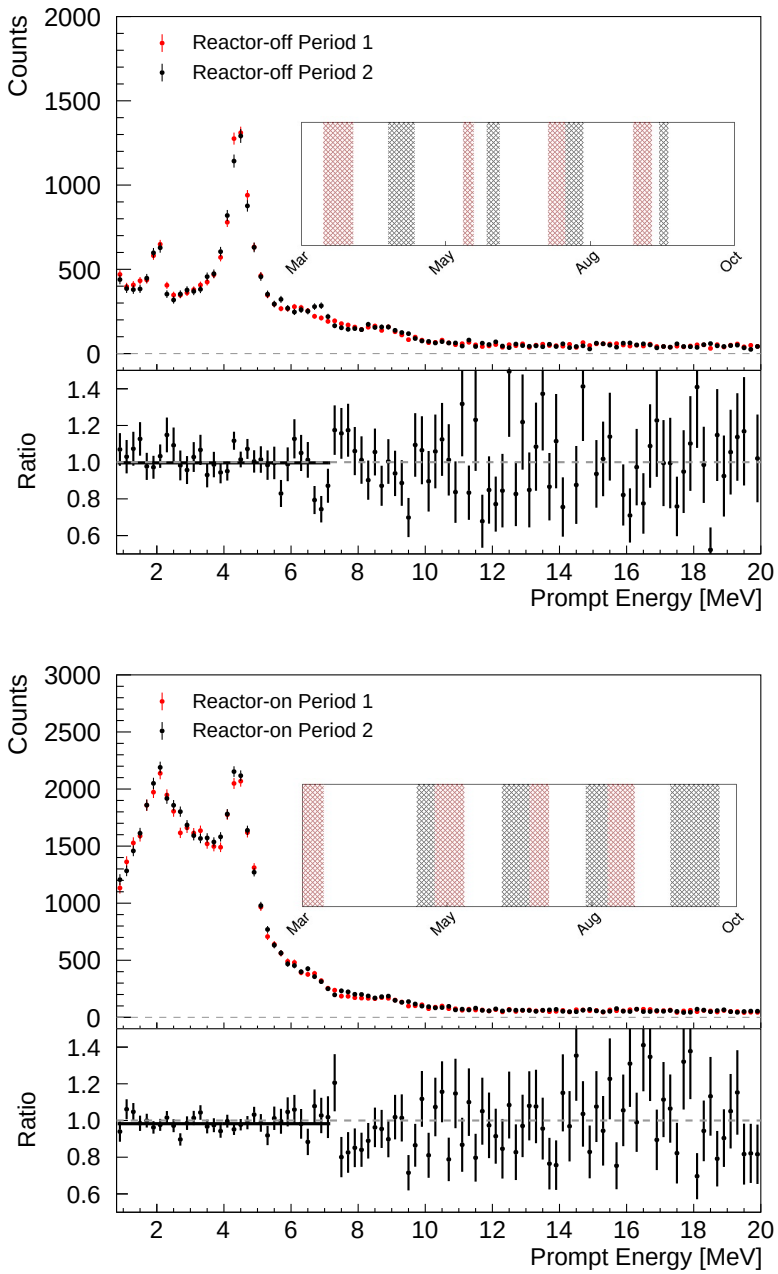


Figure 6.19: The top (bottom) panel shows the measured prompt energy spectrum of correlated candidates from reactor-off (on) data periods. Correlated candidates in period 2 are scaled to match the exposure of period 1 and adjusted for atmospheric differences between the two periods. The inset displays the breakdown of period 1 and 2 datasets for reactor-off (on) periods. The solid horizontal line in the bottom panel represents the best-fit normalization offset between the datasets in the 0.8–7.2 MeV E_{rec} range with error bars indicating statistical uncertainties. Source [70].

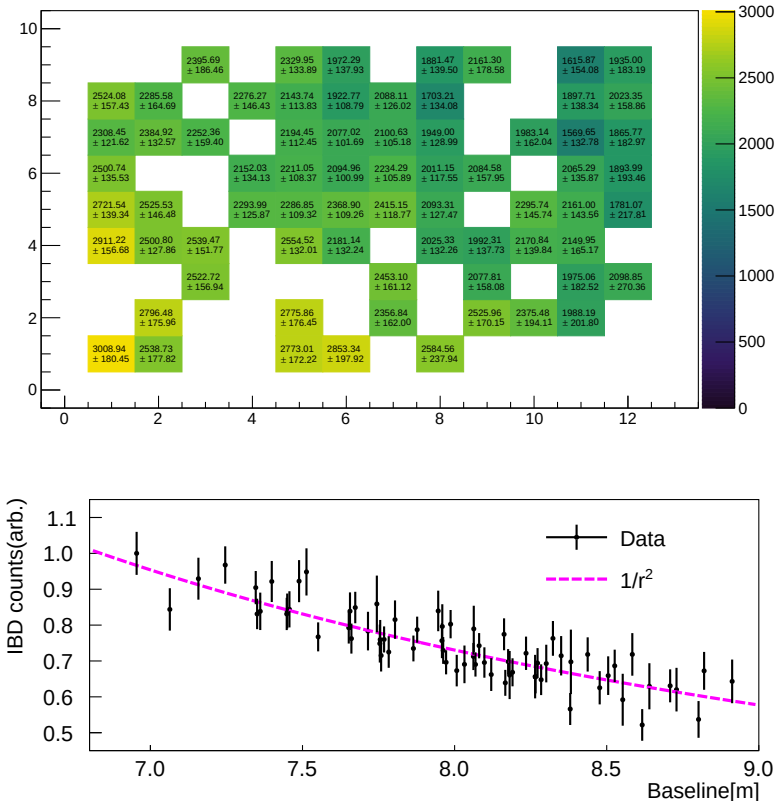


Figure 6.20: Top: Segment map for single-detector configuration analysis showing the efficiency-corrected IBD counts in each detector segment. Bottom: Baseline dependence of correlated IBD candidate rates, with the background-subtracted IBD signal plotted. Source [70].

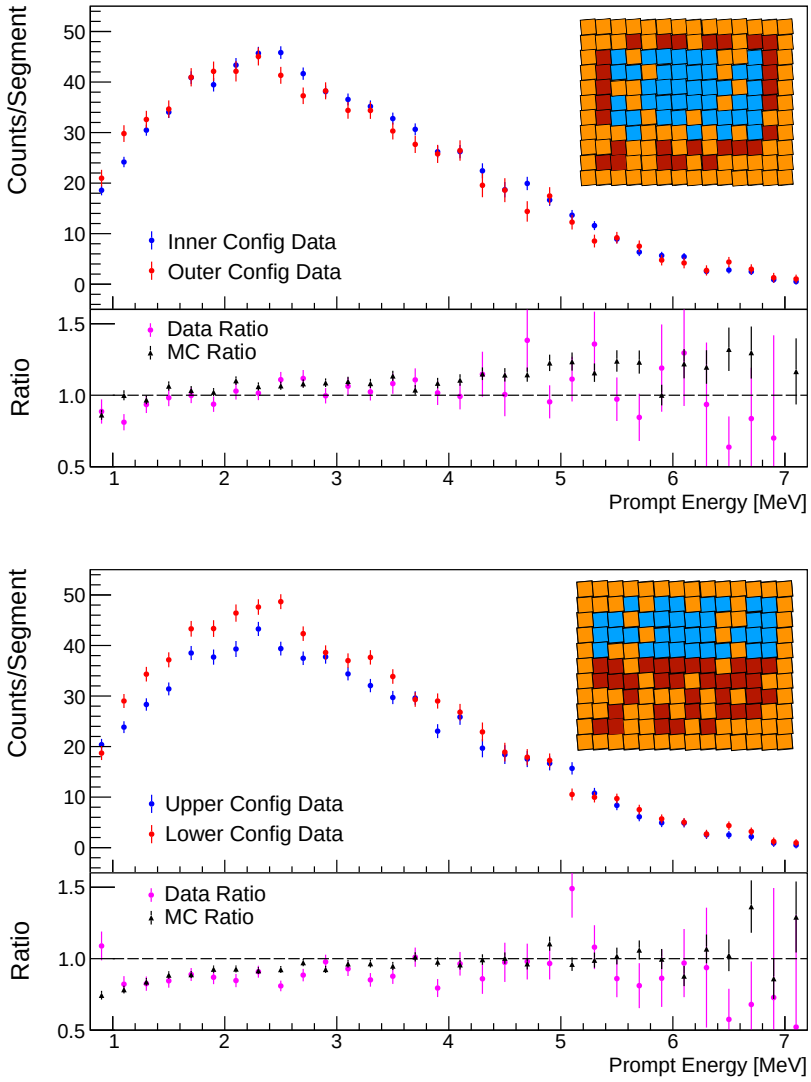


Figure 6.21: Prompt E_{rec} spectra and ratios of IBD events from different fiducial volume regions: comparisons between inner and outer detector regions (top) and between upper and lower detector regions (bottom). Error bars indicate statistical uncertainties. The data-derived ratios between these regions are compared to the `PG4` model predictions. Source [70].

Moreover, the PROSPECT detector's segmented design enables detailed cross-checks of IBD prompt signal energy and topology. Specifically, IBD interactions often result in reconstructed clusters spanning multiple segments due to positrons crossing optical grid separators and the migration of annihilation γ-rays. Fig. 6.22 demonstrates this by showing segment multiplicity distributions, with data and `PG4` MC simulations agreeing within systematic uncertainties dominated by a ± 5 keV analysis threshold. Additionally, accurate modeling of IBD event topology is confirmed by comparing the summed energy of all pulses (excluding the highest energy pulse) between data and simulations, highlighting precise modeling of annihilation γ-ray energy depositions.

6.7 Multi-Period Analysis

Sections 6.2 to 6.6 detail the analysis performed with one detector configuration resulting in a 2020 dataset reporting over 50000 IBD reconstructed events. This dataset was used for all the high-level physics analysis performed prior to 2023 including:

- First oscillation analysis (not full dataset) [82]
- First spectrum analysis (not full dataset) [74]
- Improved oscillation+spectrum [70]
- Boosted Dark Matter [69]
- Joint spectrum analysis Daya Bay and PROSPECT [48]
- Joint spectrum analysis STEREO and PROSPECT [56]

Despite the remarkable success of the initial method, the final statistical outcomes for all analyses were impacted by the significant amount of information excluded to maintain a single detector configuration. A new analysis of the PROSPECT-I

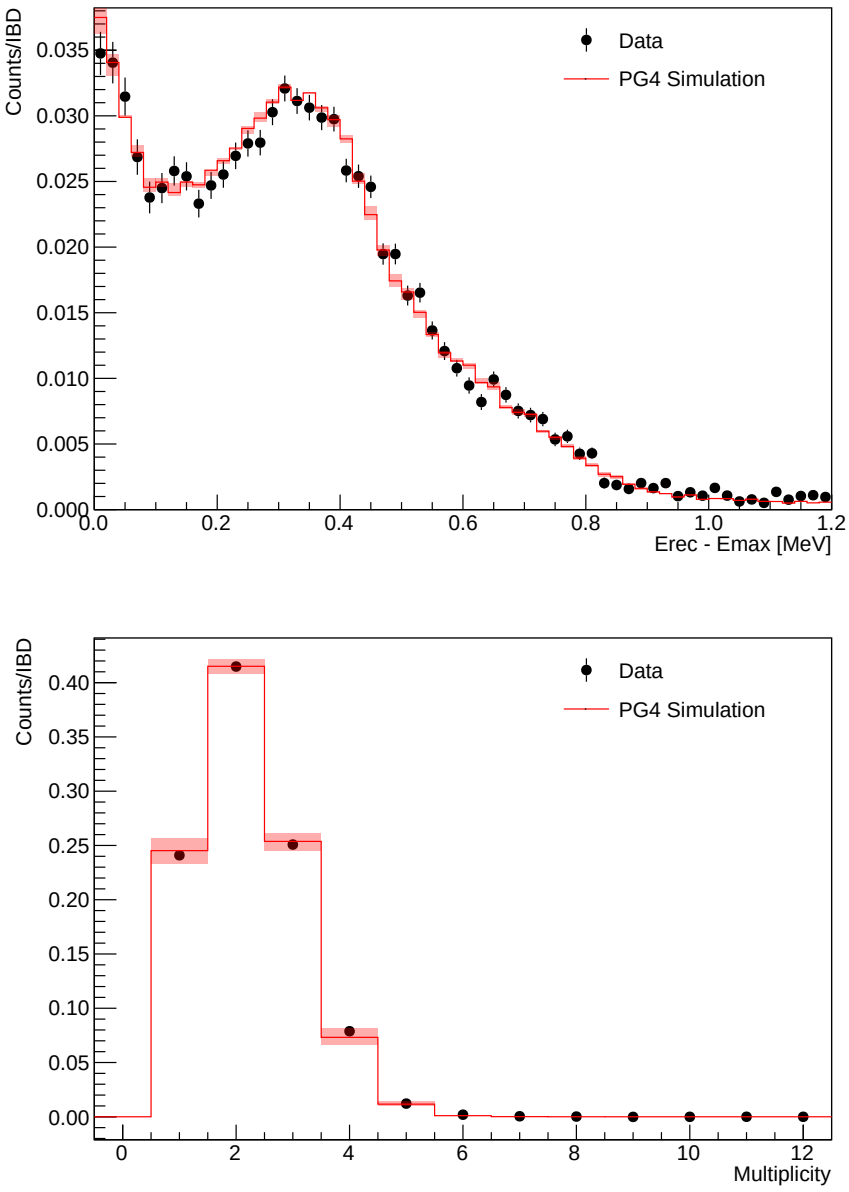


Figure 6.22: Top: Distribution of energy deposition outside the primary segment where the IBD occurs, mainly due to the transport of annihilation γ-rays. Bottom: Segment multiplicity of the prompt cluster. Error bands reflecting the 5 keV thresholding uncertainty are included in both panels for reference. Source [70].

dataset was undertaken to utilize previously overlooked information and enhance the statistical robustness of the dataset. This approach integrates new analysis techniques, including Data Splitting (DS) and Single Ended Event Reconstruction (SEER). The result is a multi-period dataset with significantly increased statistical power and improved signal-to-background ratios. This refined analysis recovered valuable data and provided a deeper understanding of the experimental results, enriching the scientific insights drawn from the PROSPECT-I experiment. This section describes the new analysis techniques implemented for the multi-period analysis, leading to a final event selection with improved IBD statistics. The results from this enhanced dataset were published in 2023 and 2024 and are discussed in later chapters.

6.7.1 Single Ended Event Reconstruction

Throughout the data collection campaign, 97 segments maintained full functionality with both PMTs operational. In contrast, 47 segments had only one functional PMT; in the remaining 10 segments, both PMTs failed. Based on the operational status of their PMTs, segments are classified into three categories: double-ended segments (DE), where both PMTs are operational; single-ended segments (SE), where only one PMT is operational; and blind segments, where both PMTs are non-functional. Fig. 6.23 illustrates the final distribution of DE, SE, and blind segments within the PROSPECT detector.

As discussed in Section 5.2.2, PMTs in SE segments still have their waveform features stored and reconstructed as pulses. However, the position-dependent collection of scintillation light hinders accurate energy reconstruction when using information from only one PMT in the cell. Despite this, SE pulses yield well-separated electronic and nuclear recoil PSD distributions over the relevant range of PMT pulse amplitudes, enabling background suppression without the need for complete deposited energy information. The single-ended event reconstruction

(SEER) analysis was developed, optimized, and integrated to supplement the nominal double-ended event reconstruction (DEER) procedure with additional insights.

Particle identification with SEER

PSD is used to identify neutron-proton recoils, electron-like interactions, and n-^{6}Li capture signatures. To evaluate the effectiveness of SEER PSD, neutron capture coincident events collected in DE segments are analyzed by examining the event distribution of PSD values and signal amplitudes (pulse areas) for data collected by (1) both PMTs and (2) a single PMT.

1. In DEER, as described in Section 5.2, the total signal amplitude is calculated using $\sqrt{S_0 S_1}$, where S_i represents the pulse integral of the left (i = 0) or right (i = 1) PMT. The DEER PSD value is computed as the weighted average of the values from both PMTs. The left panel of Fig. 6.24 illustrates the PSD and signal amplitude distribution for DEER.

2. For SEER, the PSD value and signal amplitude measured by a single PMT are recorded without adjustment. The right panel of Fig. 6.24 displays the SEER event distribution. Neutron coincident events are identified using DEER PMT pairs, and the SEER distribution is generated by analyzing only the data from single PMTs. As a result, both distributions are based on the same set of events.

The SEER PSD distribution reveals two distinct bands: gamma/electron events in the lower band and neutron/proton events in the upper band. However, the SEER distribution exhibits reduced resolution, indicated by a broader distribution, due to the decreased total light collection in SE segments compared to DE segments. Consequently, the n-^{6}Li capture region blends with the neutron-proton recoil band, preventing effective tagging of the n-^{6}Li signature. As a result, the implementation of SEER can be summarized as follows:

- SEER can differentiate between neutron and gamma-like events.

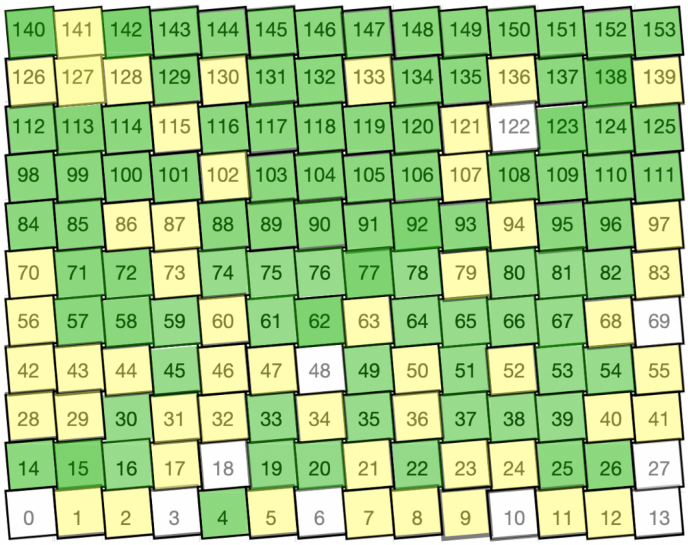


Figure 6.23: The segment status map for the single detector configuration analysis is shown, with DE segments in green, SE segments in yellow, and blind segments in white.

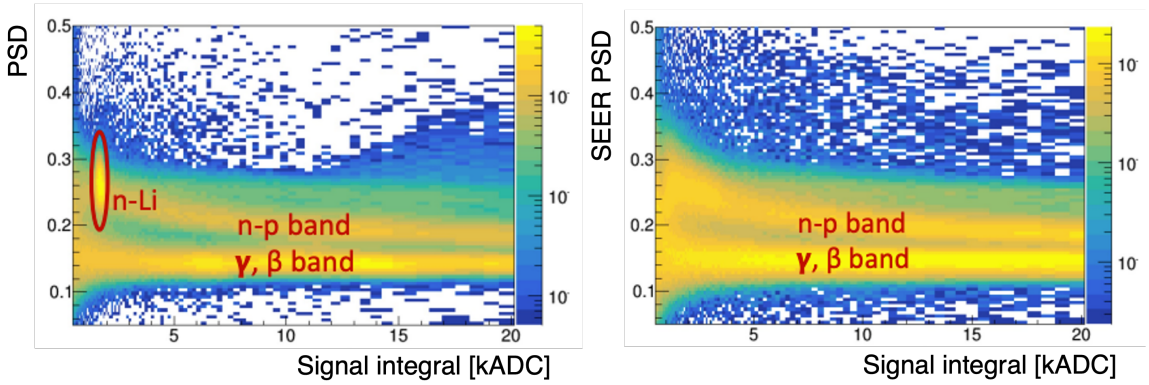


Figure 6.24: PSD-energy distribution of neutron-coincident events with (left) DEER and (right) SEER. A clear difference in the nuclear-recoil PSD band is observed, highlighting SEER's inability to efficiently tag n-^{6}Li events between lighter and heavier particles in both cases.

- The PSD value alone is insufficient for position reconstruction.
- SEER's energy reconstruction capability is very limited.
- SEER cannot distinguish n-Li capture from other nuclear-recoil events.

Therefore, in addition to previous IBD and veto cuts, SEER PSD can be used only to exclude IBD-like clusters with higher PSD values and to veto SEER-tagged neutron-like events. To estimate SE E_{rec}, the reconstructed position in a SE segment is always assumed to occur in the middle of the detector segment.

SEER cuts and vetoes

The SE PSD parameter is determined by fitting a two-parameter exponential function to each SE segment's PSD distribution. For seven energy ranges between 90 keV and 10.0 MeV, a Gaussian is fitted to the electron-like PSD band, with the mean (μ) and standard deviation (σ) of the fits recorded. The average of these means is stored in a new calibration database for each segment, similar to the DEER-only analysis. Incorporating SEER into the IBD selection criteria enhances background rejection capabilities by introducing a new cut and veto.

- **SE PSD Cut**
  - A two-parameter function, $\sqrt{a^2 + b^2/E}$, is fitted to the σ distribution as a function of energy.
  - This best-fit function is applied across all SE segments to determine if the SE PSD exceeds $\mu_i + n_\sigma\sqrt{a^2 + b^2/E}$, where μ_i is the mean SE PSD for segment i, and n_σ is the threshold in terms of sigma above the mean.
  - Prompt clusters containing SE pulses with $E_{rec} < 0.8$ MeV and a PSD value more than 3.5 σ above the mean of the electromagnetic PSD distribution are rejected, as they likely involve nuclear recoils.

- Prompt clusters with $E_{rec} > 0.8$ MeV are rejected regardless of PSD to enhance the screening of γ-like backgrounds.
- These SE requirements were established after finding that most IBD-like events in SE segments have an SE E_{rec} between 0 and 0.8 MeV, as shown in Fig. 6.25.

- **SE Recoil Veto**
  - Delayed clusters that include any SE pulses are rejected because neutron capture on ^{6}Li occurs in a single segment.
  - A veto window is created around events with segments showing SE PSD above the electron-like band.
  - IBD candidates that appear within 170 μs of a cluster containing only high-PSD SE segments are vetoed.

Incorporating both the SE PSD cut and SE recoil veto into the IBD selection criteria, which include IBD cuts (Section 6.2.1) and background vetoes (Section 6.2.2), establishes a new phase space of selection requirements. This new phase space must be optimized in the same manner as the DEER-only analysis.

6.7.2 Re-Optimization with SEER variables

The new phase space of IBD selection cuts and vetoes was optimized using the same procedure as the DEER-only analysis. This involved utilizing a 20% subset of the entire dataset evenly sampled across run times to prevent bias in the selection cuts. In accordance with a typical blind analysis approach, the final IBD spectrum was not revealed until the selection cuts were optimized.

Optimization was performed sequentially yet independently, allowing each cut or veto value to vary independently of other selection criteria. During each iteration of optimizing a specific cut, the full selection criteria were applied to the sample

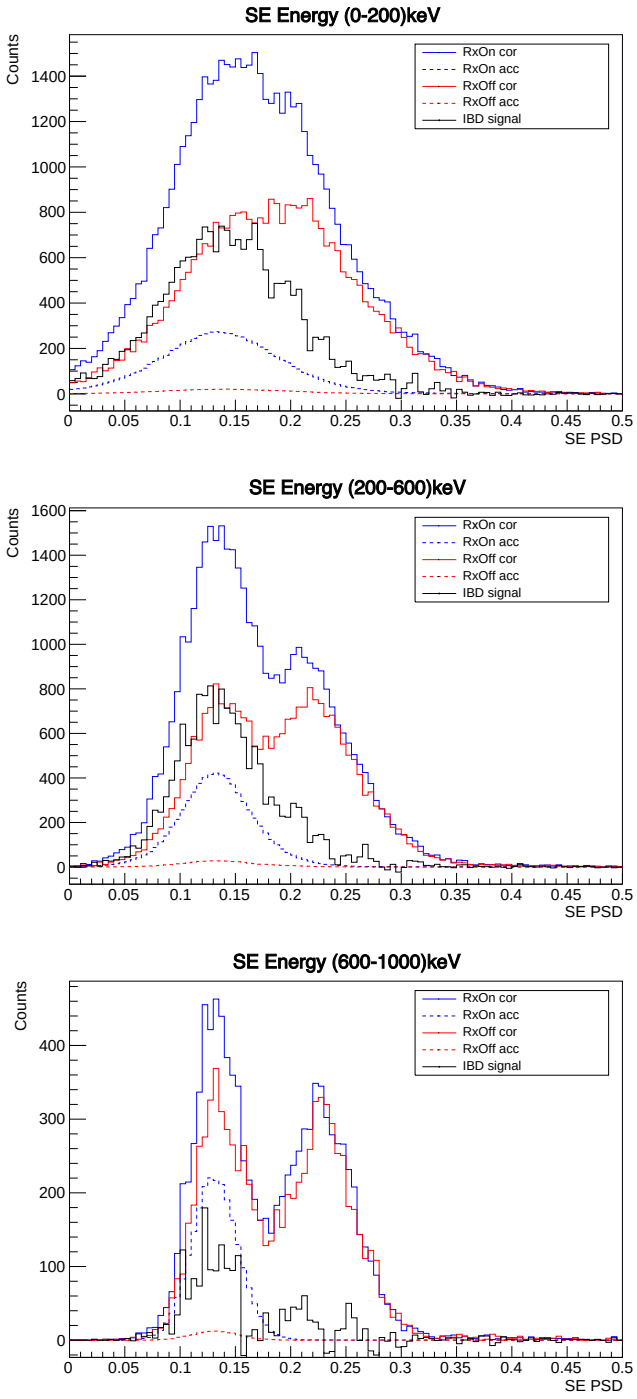


Figure 6.25: SE PSD distributions for different SE E_{rec} projections. Each energy projection illustrates the corresponding spectra of IBD-like candidates in reactor-on, reactor-off, and background-subtracted IBD candidates.

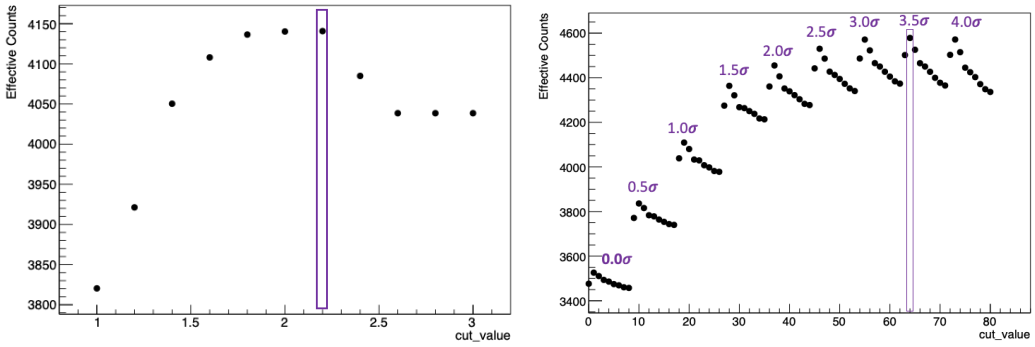


Figure 6.26: Cut optimization results for the IBD prompt PSD cut (left) and the SE PSD cut (right). The horizontal axis shows the optimized cut value in units of standard deviations, $n\sigma$, from the mean of the electron-like PSD and SE PSD gamma band distributions.

dataset to determine the IBD spectrum and the effective number of IBD events, N_{eff}. The N_{eff} metric served as the cost function for identifying the optimal value of each selection cut. The reference selection criteria for each iteration were based on those used in the DEER-only analysis. Once the optimal value for each cut was identified, it was considered the first 'step' in the minimization process, and the optimized values became the new reference. This procedure was repeated for three iterations.

Although a correlated approach might yield a more precise characterization of the IBD parameter phase space, the uncorrelated approach offers several advantages, including competitive statistical results, reduced computational time, and avoiding complexities inherent in managing correlated selection cut parameters. The only correlations considered were those pertinent to the individual parameters defining each cut or veto. While the optimization process treated each selection cut parameter independently, the remaining parameters used in the optimization approximated the physical properties inherent to the IBD process.

Figures 6.26 illustrate the final optimization results for the prompt PSD cut and the SE PSD cut, respectively. The following is a summary of the optimization procedure for each cut and veto:

- **Prompt Cut - PSD**
  - **Parameter varied**: The number of standard deviations ($n\sigma$) within which the PSD for each pulse in the prompt cluster must fall relative to the mean of the electron-like PSD band.
  - **Optimization window**: $[1.0 - 3.0]\sigma$ in increments of 0.2σ.
  - **Final optimized value**: 2σ.
- **Delayed cut - Energy**
  - **Parameter varied**: the number of standard deviations ($n\sigma$) within which the delayed cluster energy must fall relative to the mean value of 0.526 MeV.
  - **Optimization window**: [1.4-3.6]σ in steps of 0.2σ.
  - **Final optimized value**: 2σ.
- **Delayed cut - PSD**
  - **Parameter varied**: The number of standard deviations ($n\sigma$) within which the PSD for the pulse in the delayed cluster must fall relative to the mean of the electron-like PSD band.
  - **Optimization window**: [1.0-3.0]σ in steps of 0.2σ.
  - **Final optimized value**: 2.2σ.
- **Time coincidence cut**
  - Cut was not optimized, and DEER-only analysis cut value was kept.
  - **Final optimized value**: 120 μs.
- **Distance cut**
  - The parameters for this cut were varied as a pair

- **Parameters varied**: Z_{rec} for a prompt-delayed cluster pair happening in the same DE segment, and Z_{rec} for a prompt-delayed cluster pair happening in adjacent DE segments.
- **Optimization windows**: [100-180] mm for the same DE segment and [60-140] mm for adjacent DE segments, both windows are varied in steps of 20 mm.
- **Final optimized values**: (140,60) mm for prompt-delayed cluster pairs occurring in the same and adjacent DE segments, respectively.

- **SE PSD cut**
  - The parameters for this cut were varied as a pair
  - **Parameters varied**: The number of standard deviations ($n\sigma$) within which the PSD for each SE pulse found in a prompt cluster must fall relative to the mean of the electron-like SE PSD band, as well as the upper bound for SE E_{rec} for each SE pulse in a prompt cluster.
  - **Optimization windows**: [0-4.0] σ in steps of 0.5 σ for the SE PSD requirement, and [0.5-2.9] SE MeV in steps of 0.3 SE MeV.
  - **Final optimized values**: 3.5 σ and 0.8 SE MeV.

- **Muon veto**
  - **Parameter varied**: Time window size to tag muon-induced neutron capture events mimicking IBD-like signals.
  - **Optimization window**: [110-380] μs in steps of 30 μs.
  - **Final optimized value**: 200 μs.

- **Neutron veto**
  - **Parameter varied**: Time window size to tag multi-neutron showers from cosmic ray interactions in the materials surrounding the detector.

- **Optimization window**: [50-500] μs in steps of 50 μs.
- **Final optimized value**: 300 μs.

- **Recoil veto**
  - **Parameter varied**: Time window size to tag cosmic ray interactions that produce heavy secondaries.
  - **Optimization window**: [50-500] μs in steps of 50 μs.
  - **Final optimized value**: 200 μs. The requirements for E_{rec} and PSD remained the same as in the DEER-only analysis, i.e., $E_{rec} > 0.25$ MeV and a PSD greater than 2σ above the peak of the electron-like PSD band.

- **SE Recoil veto**
  - **Parameter varied**: Time window size to tag any high-PSD neutron capture-like delayed candidates producing SE pulses in prompt clusters.
  - **Optimization window**: [130-210] μs in steps of 30 μs.
  - **Final optimized value**: 170 μs. The requirement for SE PSD is consistent with the SE PSD cut.

- **Fiducial cut**
  - **Parameter varied**: Z_{rec} for both prompt and delayed cluster relative to the segment center defining fiducial volume along the cell.
  - **Optimization window**: [384-504] mm in steps of 20 mm.
  - **Final optimized value**: $\pm$484 mm

- **Pileup veto**
  - Cut was not optimized, and DEER-only analysis cut value was kept.
  - **Final optimized value**: 800 μs.

Implementation of DEER+SEER event selection

After the new event selection criteria were optimized, including SEER, it was applied to the entire dataset to generate updated results. The impact of the new cuts is shown in Figures 6.27 and 6.28. There is a significant reduction in the number of correlated IBD-like candidates for both reactor-on and reactor-off conditions. This improvement is due to the re-optimization of DEER cuts and the incorporation of SEER, effectively reducing the impact of correlated backgrounds forming the nH and nC peaks. Additionally, the enhanced γ-background suppression capabilities of SEER contribute to a decrease in the number of accidental events.

In terms of the main metrics for the IBD analysis, the implementation of SEER provided the following improvements:

- N_{eff} increased from 18100 to 26779
- $S:CB$ increased from 1.37 to 3.24
- $S:AB$ increased from 1.78 to 3.74

These results highlight the value of incorporating SE information, as it allows for a signal-to-background ratio greater than 1, which was the design expectation for the detector. As mentioned earlier, SEER provides new background rejection capabilities rather than a method for reconstructing IBD events occurring in SE segments. This is evident in the resulting IBD signal, N_{IBD}, which decreased to 47,996 events. This decrease is due to adding more selection cuts while maintaining the same number of DEER segments. Finally, all crosschecks and tests described in Section 6.6 were performed for the new DEER+SEER signal, yielding consistent results.

6.7.3 Data Splitting

Beyond SEER, the second analysis method introduced for this new effort aims to better utilize information from earlier periods of data collection where more DE

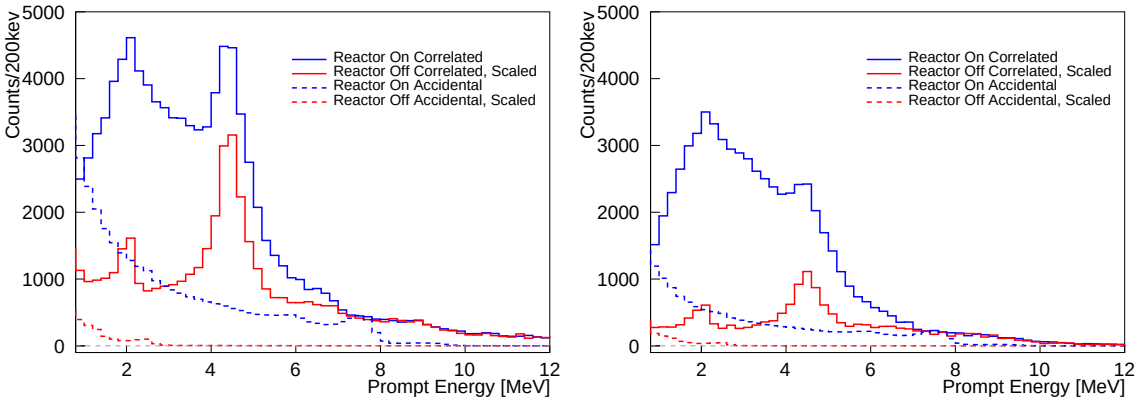


Figure 6.27: Comparison of the measured prompt E_{rec} spectrum of correlated and accidental IBD-like candidates during reactor-on and reactor-off data periods, using the old (left) and new (right) event selection criteria.

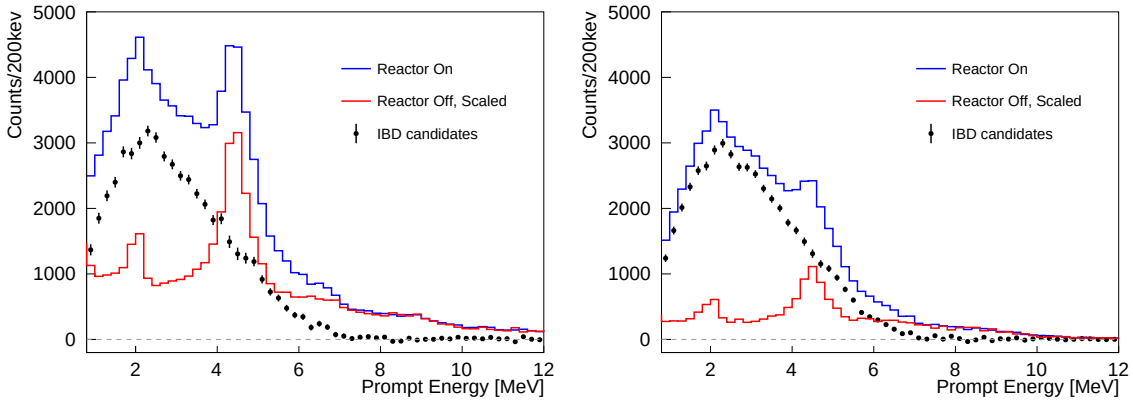


Figure 6.28: Comparison of the reconstructed visible prompt energy E_{rec} (black) spectrum of IBD candidates (statistical error only), along with reactor-on (blue solid) and reactor-off (red solid) correlated candidates, obtained using the old (left) and new (right) event selection criteria.

segments were available. This method denoted as Data Splitting (DS), consists of parsing the PROSPECT-I data into distinct periods to maximize the number of live segments in each period. The criteria implemented to split the data were

- Each period encompasses a complete operational cycle of the reactor, leading to five DS periods.
- In all periods, there is a set of data with the reactor off that frames the included reactor-on cycle, except for period 1. This deviation arises because the initial data collected by PROSPECT coincided with the reactor being in operation, eliminating the possibility of having an off-cycle for period 1.
- The reactor-off data is evenly distributed between adjacent periods.

Calibration campaigns served as convenient breakpoints in three of the four-period divisions. Additionally, all PMTs that were inoperative at any point during a DS period were excluded. Fig. 6.29 illustrates the time evolution of DE and SE segments. Generally, the number of SE segments increased over time, except from periods 1 to 2, when extra caution was exercised after the initial detection of unstable PMTs. This resulted in more PMTs being turned off than necessary.

This method results in a multi-period analysis that required modifications to the primary analysis framework, `P2X`, to properly handle the different numbers of DE and SE segments for a given detector configuration. To determine the status of each detector segment for each DS period, the behavior of each segment was tracked at the `DetPulse` level, as illustrated in Fig. 6.30 for segment 48. This figure shows that segment 48 remained a DE segment for periods 1 and 2; then, in period 3, the right PMT failed, making segment 48 an SE segment for periods 3 and 4 until it finally became a blind segment in period 5. This process was repeated for all detector segments, leading to the final detector configurations shown in Fig. 6.31.

The outer layer was designated as a non-fiducial volume for all detector configurations, and now SE segments are also incorporated. Additionally, segments

24, 25, 26, and 40, located over the γ hot spot, were also designated as non-fiducial segments. This adjustment to the fiducial cut was integrated into the event selection criteria. Implementing DS with DEER-only segments and cuts resulted in the following improvements:

- N_{IBD} increased from 50,560 to 64,323
- N_{eff} increased from 18,100 to 28,464
- $S : CB$ improved from 1.37 to 2.35
- $S : AB$ increased from 1.78 to 1.89

These improvements in all metrics are attributed to the increased active volume by utilizing different detector configurations. The following section discusses the impact of incorporating both DS and SEER into the IBD analysis.

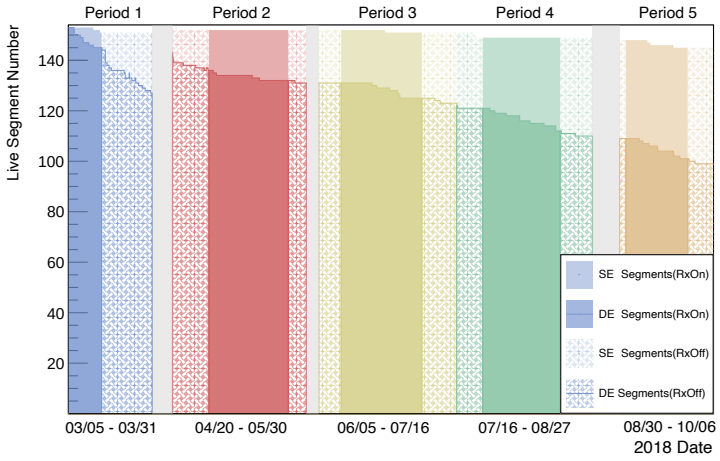


Figure 6.29: Time evolution of DE and SE segment numbers during reactor-on and reactor-off periods, along with the definition of the 5 DS periods. The number of DE segments decreases over time, while the total number of DE and SE segments shows a slight decline. The DE and SE segment numbers at the end of each DS period define the detector configuration used. Source [68].

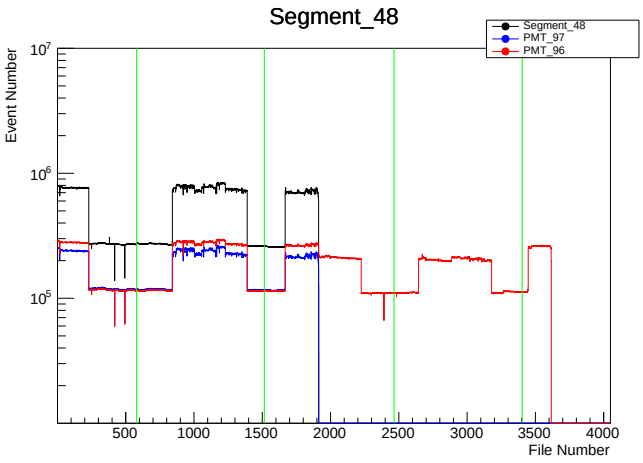


Figure 6.30: `DetPulse` Event rates for segment 48 for individual and paired pulses across all data runs. Green vertical lines indicate DS period boundaries.

6.7.4 Results of DS+SEER

Integrating DS and SEER into the IBD analysis produced an optimized multi-period dataset with significant improvements in statistical power and signal-to-background ratios. Figures 6.32 and 6.33 display the IBD-like spectra detected in each DS period using the optimized DEER+SEER selection criteria. Periods 2 and 3 show the highest performance, while period 5, with a detector configuration nearly identical to the single-detector setup, exhibits the lowest statistics.

A detector response matrix was generated for each DS period to validate the IBD signal measured in each DS period, incorporating differences in detector configuration and the new selection criteria. The resulting E_{rec} distributions for a 4 MeV neutrino are shown in Fig. 6.34, illustrating the gradual decline in detector response capabilities over time. Fig. 6.35 compares the single-detector configuration analysis and the DS+SEER analysis, with all reactor-on, reactor-off, and IBD signal spectra combined for each period. Table 6.2 summarizes the relevant event rates for previous and current analyses. The increase in N_{eff} is primarily attributed to enhanced background rejection and an expanded active volume.

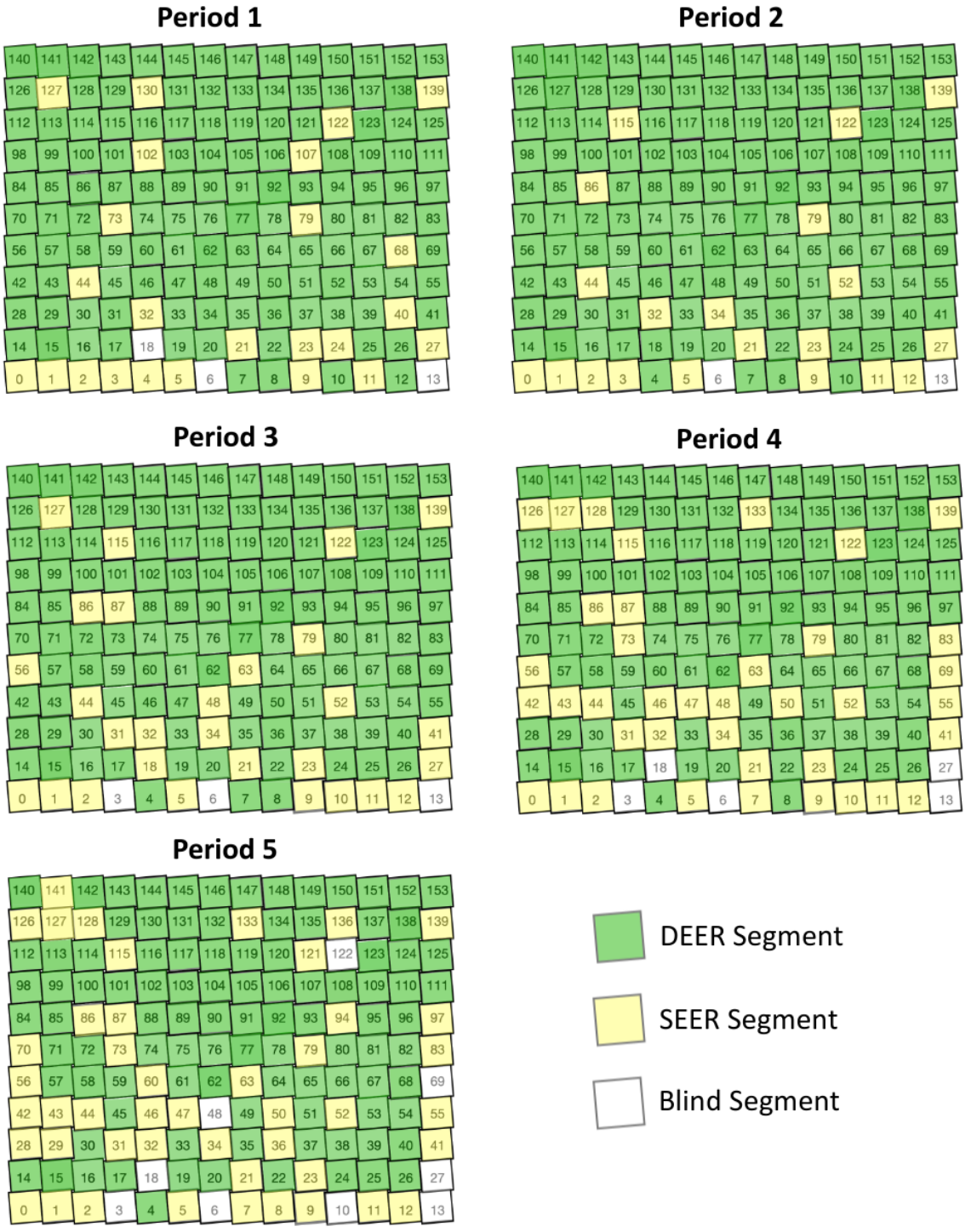


Figure 6.31: Detector configuration used for the 5-period analysis. Each period corresponds to a reactor on data taking period; see Fig. 6.29 for the reactor on and off data used for each period.

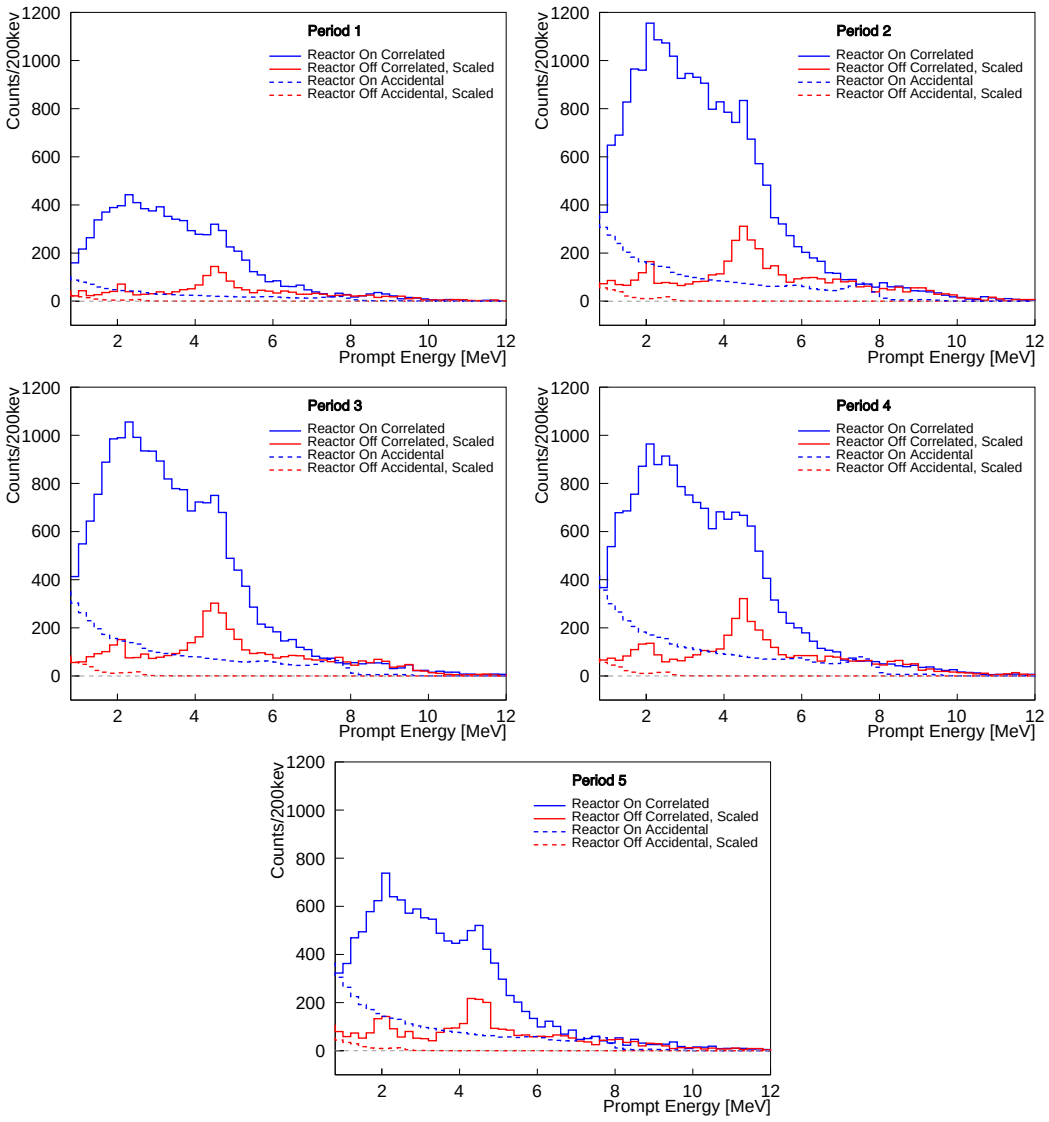


Figure 6.32: Reconstructed visible prompt energy E_{rec} (black) spectrum of IBD candidates (statistical error only), along with reactor-on (blue solid) and reactor-off (red solid) correlated candidates for each DS period, obtained using the new IBD event selection criteria. The reactor-off spectrum (including atmospheric corrections) is scaled to match the reactor-on live time in each case.

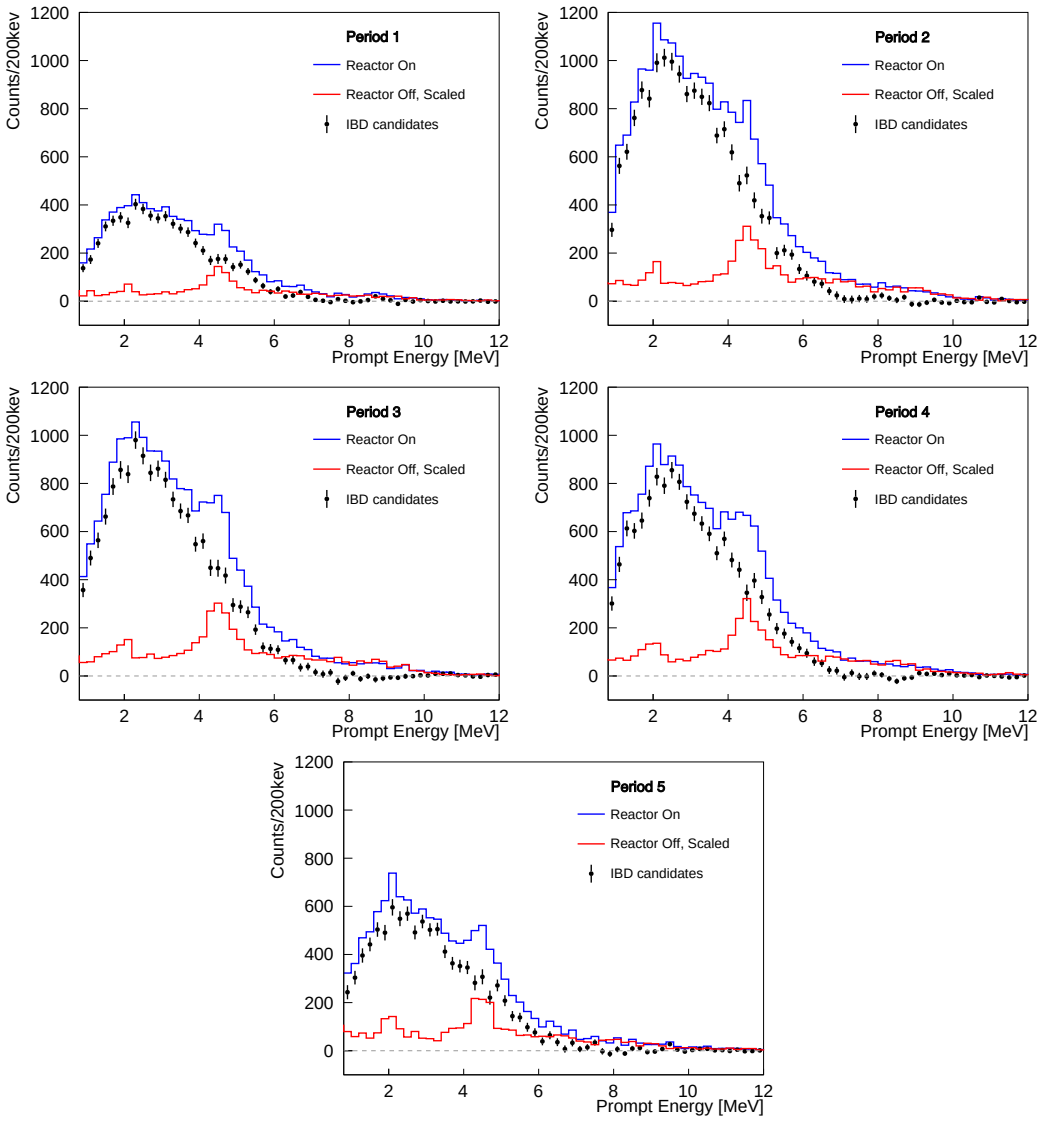


Figure 6.33: Reconstructed visible prompt energy E_{rec} (black) spectrum of IBD candidates (statistical error only), along with reactor-on (blue solid) and reactor-off (red solid) correlated candidates for each DS period, obtained using the new IBD event selection criteria. The reactor-off spectrum (including atmospheric corrections) is scaled to match the reactor-on live time in each case.

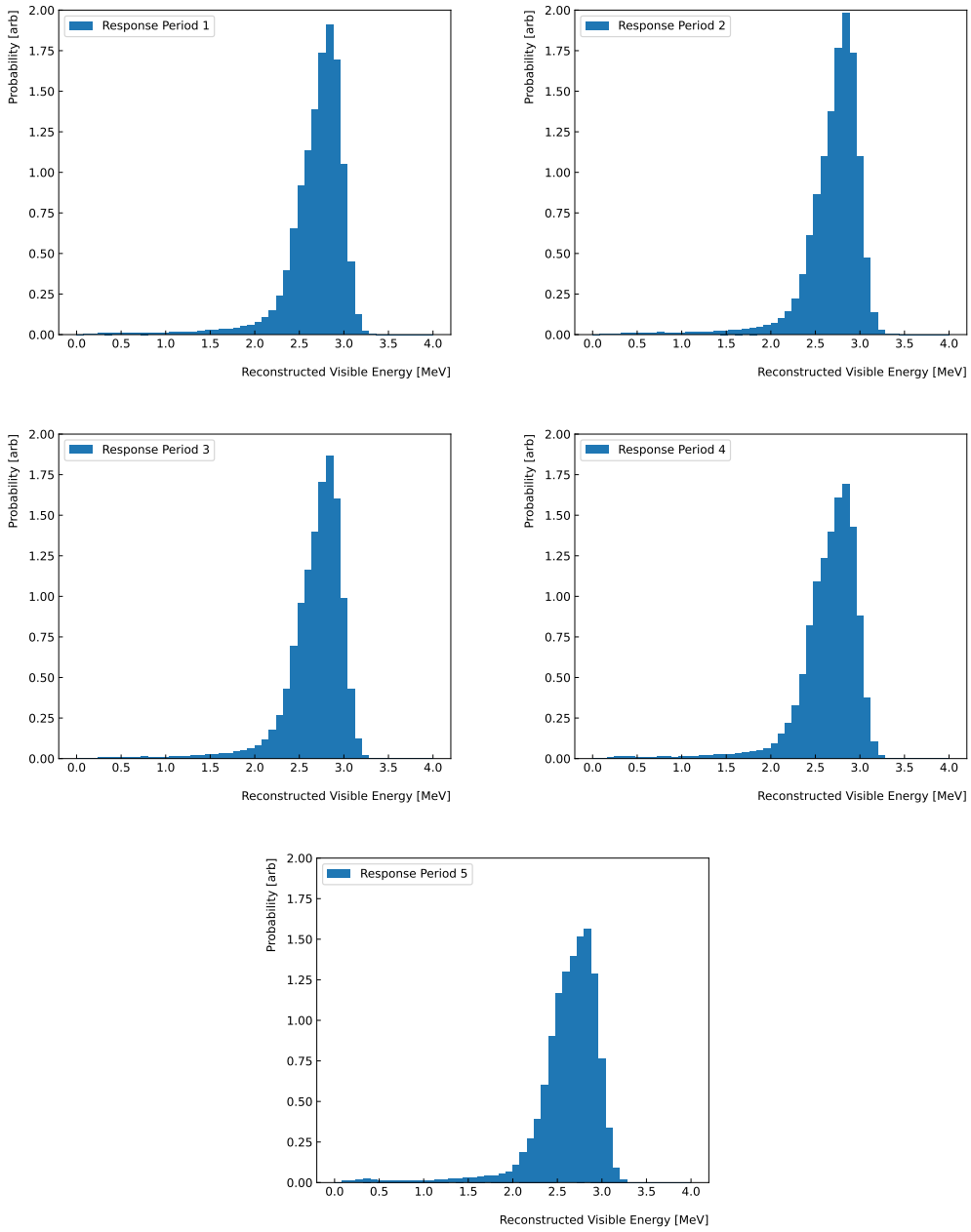


Figure 6.34: Comparison of the reconstructed E_{rec} distributions using the response matrix for each period, based on a 4 MeV monoenergetic neutrino.

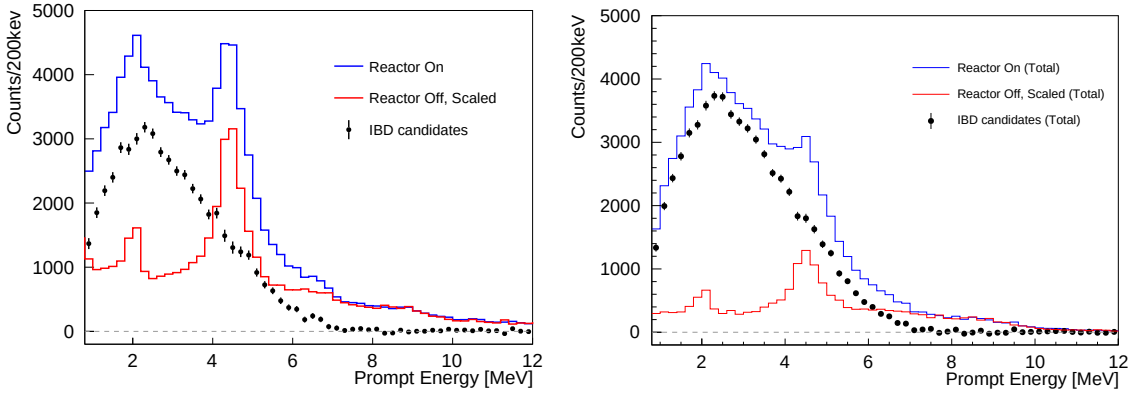


Figure 6.35: Comparison of the reconstructed visible prompt energy E_{rec} (black) spectrum of IBD candidates (statistical error only), along with reactor-on (blue solid) and reactor-off (red solid) correlated candidates, between the single-detector configuration analysis and the period-integrated multi-period analysis. The reactor-off spectrum is scaled to match the reactor-on live time in each case, with atmospheric scaling applied to adjust the reactor-off background.

Table 6.2: Final IBD event statistics for the previous and current analysis. Reactor-on (Rx-On) and -off (Rx-Off) data taking time is presented in units of calendar days. N_{IBD}, N_{eff} and both signal to cosmogenic background (S:CB) and signal to accidental background (S:AB) ratios are calculated over the IBD energy region of [0.8, 7.2] MeV for previous analysis in [70] and [0.8, 7.4] MeV for the current analysis. Source [68].

Dataset	**Rx-On(Off) Days**	$\mathbf{N_{IBD}}$	$\mathbf{N_{eff}}$	**S:CB(AB)**
Prev. Analysis	95.65(73.09)	50560 ± 406	18100	1.37(1.78)
DS+SEER Analysis	95.62(72.69)	61029 ± 338	36204	3.90(4.31)
Period 1	9.54(14.58)	6357 ± 100	4328	4.03(6.21)
Period 2	22.83(15.71)	16546 ± 172	10259	4.35(4.64)
Period 3	23.20(16.40)	15094 ± 166	9050	4.04(4.44)
Period 4	22.29(16.79)	13486 ± 161	7742	3.72(3.39)
Period 5	17.76(9.21)	9546 ± 146	4825	3.38(2.88)

The new DS+SEER analysis successfully recovered over 10,000 IBD candidates and significantly enhanced background rejection, nearly doubling PROSPECT's statistical power. This enhancement is evident in the increased effective statistics and the improved signal-to-background ratio, which rose from 1.58 to 4.11, closely matching the detector performance predicted during the design phase. The resulting, more robust multi-period dataset provides a solid foundation for advanced analyses that align with the experiment's primary objectives. These include a refined spectral shape analysis to investigate the 5 MeV bump further and a new neutrino oscillation analysis that will leverage the increased statistical power to improve the search for sterile neutrino oscillations.

6.8 Chapter summary

This chapter provided a comprehensive overview of the IBD selection strategy for the PROSPECT experiment, detailing the development, optimization, and implementation of various cuts and vetoes, as well as the simulation and validation of the IBD signal. It included a complete summary of the 2020 results obtained from a single-detector configuration analysis. Furthermore, a new analysis effort was described, incorporating novel methods and leading to an enhanced multi-period dataset with improved IBD statistics. The following chapter will present the final high-level physics analyses conducted by the PROSPECT experiment using this new dataset, focusing on spectral shape and sterile neutrino oscillations.

Chapter 7

Multi-Period Spectral Shape Analysis

As discussed in earlier chapters, it has become increasingly evident over the past few decades that phenomenological models do not fully account for the physics of antineutrino emission from reactor cores. Observed reactor antineutrino energy spectra consistently differ from predictions [53, 109, 35, 47, 70] based on both beta-spectrum conversion techniques [142, 149] and *ab initio* nuclear database calculations [118], mainly showing an excess in the 5-7 MeV range. The source of this discrepancy remains unclear, as does whether it arises universally across all fissioning isotopes or is primarily due to the misrepresentation of a single isotope. This ambiguity is especially difficult to resolve in commercial reactors with low-enriched uranium cores, where a time-varying mixture of isotopes is burned. Beyond addressing this modeling challenge, precise antineutrino spectrum measurements could be crucial in future reactor-based experiments and applications.

Building on this broader challenge, the PROSPECT experiment offers a targeted approach by focusing on the antineutrino spectrum from a purely ^{235}U-fueled reactor. Following a detailed discussion of the antineutrino detection strategy and the development of a new multi-period dataset with improved statistics, this chapter

presents the final PROSPECT-only spectral shape analysis. This analysis delivers one of the most precise measurements to date of the antineutrino spectrum from a ^{235}U-fueled reactor. Unlike previous PROSPECT analyses, this study is conducted in neutrino space, where the reconstructed multi-period prompt energy spectra are unfolded into a single antineutrino energy spectrum. This spectrum is then compared with the HM model [149] and the spectrum from a commercial reactor burning multiple fuel isotopes, primarily Daya Bay [55]. A local excess over the model is observed in the 5-7 MeV energy region. Comparing the PROSPECT results with those from commercial reactors offers new constraints on the origin of this excess, ruling out at 2.0 and 3.7 levels the hypotheses that antineutrino s from ^{235}U are solely responsible for, or are non-contributors to, the excess observed at commercial reactors.

7.1 Description of previous results

PROSPECT has conducted two spectral shape analyses using the single-detector configuration dataset described earlier. In both studies, the ^{235}U HM was used as the reference model for comparison with the measured prompt spectra (M_e), assuming no distortion of the spectrum due to potential sterile neutrino oscillations. The HM spectrum reference model in prompt space was generated by combining the theoretical prediction of the antineutrino flux ($\Phi_{HM,235}$) provided by [149] with the IBD cross-section (σ_{XIBD}) [201], resulting in a predicted spectrum in antineutrino space ($\hat{s}_{hm}$) to which the detector response matrix (R_{PROS}) detailed in Section 6.5 is applied. This process maps antineutrino energy to the reconstructed prompt energy in PROSPECT, generating an HM-based predicted prompt spectrum denoted as $\mathrm{P_e}$

$$\hat{s}_{hm} = \Phi_{HM,235} \cdot \sigma_{XIBD} \tag{7.1}$$

$$P_{\mathrm{e}} = R_{\mathrm{PROS}} \cdot \hat{s}_{HM} \tag{7.2}$$

The results from both analyses—one based on 40.3 days of reactor-on data and 37.8 days of reactor-off data [74], and the other using the full dataset [70]—are shown in Fig. 7.1. This figure compares the final M_e and P_e distributions, including a modified version of P_e incorporating contributions from ^{28}Al, ^{6}He, and non-equilibrium isotopes in the core, as discussed in Section 4.2.2. A deficit is observed in the 4-6 MeV range of the prompt energy spectrum, aligning with the bump-like feature reported by other experiments as mentioned in Section 3.3.1. Furthermore, constraints on the isotopic nature of this deficit were established using a method similar to that described in Section 7.5. Statistical uncertainties ultimately limited both analyses.

In addition to its independent efforts, PROSPECT has conducted joint spectral shape analyses with the Daya Bay (LEU-based) and STEREO (HEU-based) collaborations. In each of these studies, the ^{235}U prompt spectra from each experiment were combined and unfolded into a single ^{235}U spectrum in antineutrino energy space, enabling a detailed spectral shape analysis. In the case of Daya Bay, the contribution from ^{235}U to the total measured prompt spectrum was estimated by using the average fission fraction for this fissile isotope denoted as $\langle f_{235} \rangle = 0.536$. The results of analyses, both using HM as a reference, are presented in Fig. 7.2. In the PROSPECT-Daya Bay comparison [56], it was found that the ^{235}U prompt IBD energy spectra measured by Daya Bay and PROSPECT are consistent, with uncertainties in the jointly determined spectral shape reduced to 3%. In the PROSPECT-STEREO analysis [48], the unfolded ^{235}U antineutrino spectrum when compared with $\hat{s}_{\mathrm{HM}}$, revealed a preference for a bump in the 5–6 MeV region with 2.4σ significance. Both combined studies employed the Wiener-SVD unfolding method [195].

Motivated by the PROSPECT-only and joint spectral shape analyses, the final multi-period spectral shape analysis will build upon the experience gained from conducting model-comparison and hypothesis-testing studies in previous work, as well as the insights gained from implementing unfolding methods while also taking advantage of the improved dataset.

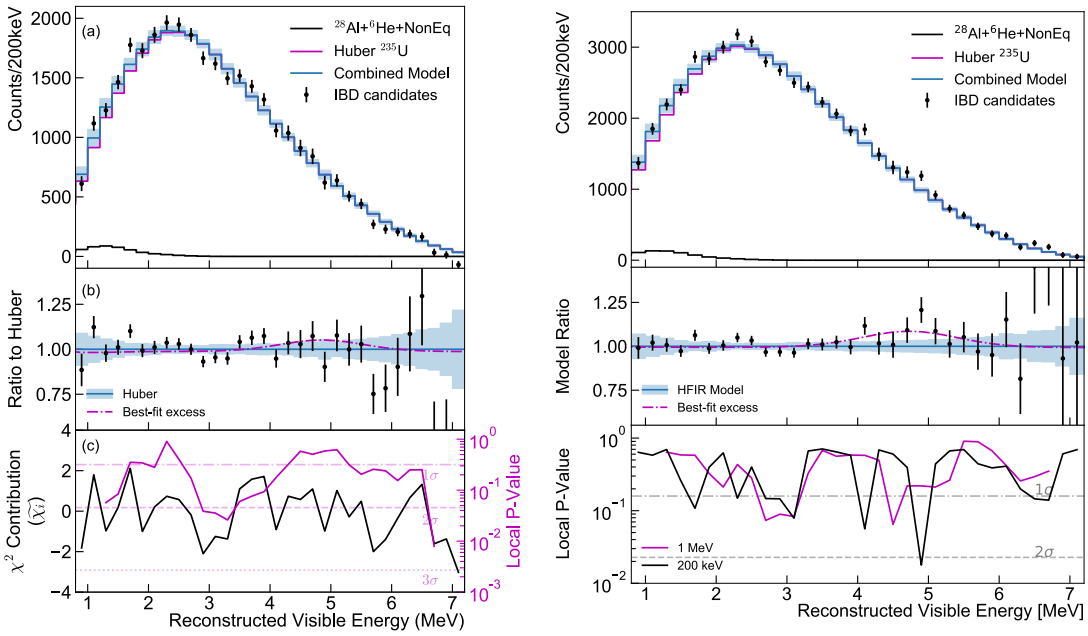


Figure 7.1: Left(right) figure illustrates the 2018(2020) PROSPECT spectral shape analysis. Top: Comparison of the ^{235}U model to the measured PROSPECT E_{rec} spectrum. Middle: The ratio of the measurement to the HFIR prediction is based on the HM. Bottom: The local p-value from 1 MeV- and 200 keV-wide sliding windows, quantifying any local deviations from the model prediction. Error bars on data points represent statistical uncertainties, while error bands on the model represent systematic uncertainty contributions. Source [74, 70].

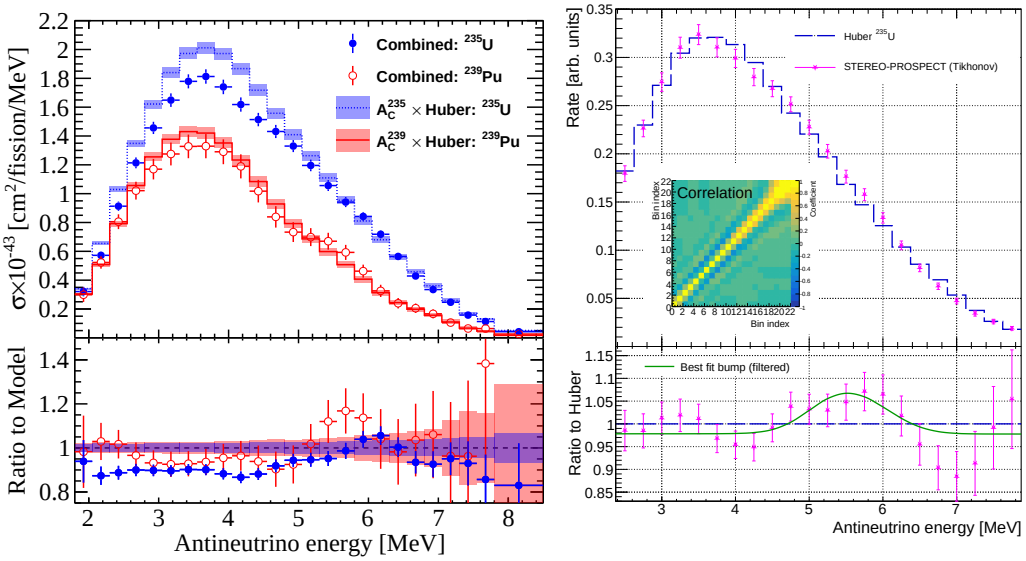


Figure 7.2: Left figure: Top: ^{235}U and ^{239}Pu antineutrino spectra unfolded from the jointly deconvolved Daya Bay and PROSPECT measurements. Bottom: Ratio of the measurements to their respective models, corrected by the smearing matrices $\boldsymbol{A}_c$ in both panels. **Right figure:** Top: Jointly unfolded ^{235}U spectrum for PROSPECT and STEREO with diagonal errors, and $\hat{s}_{\mathrm{HM}}$ normalized to unit area. The non-trivial correlation matrix is also displayed. Bottom: Jointly unfolded ^{235}U spectrum as a ratio to $\hat{s}_{\mathrm{HM}}$. The filtered best-fit bump is shown. Source [56, 47].

7.2 Description of datasets

7.2.1 Data inputs

As detailed in the previous chapter, the DS+SEER analysis produced five independent prompt energy spectra (M_e), which are presented in Fig. 7.3. This figure also includes the HM-based predicted prompt energy spectra (P_e) for each period, which were obtained by applying the joint response matrix depicted in Fig. 7.4 to $\hat{s}_{\mathrm{HM}}$ just as in Eq. 7.2. Each response matrix is scaled to align with the N_{IBD} for its respective period. The response matrices for the spectrum analysis are generated as described in Section 6.5, where each resulting matrix is 33x26 in size, with 33 representing the number of prompt energy bins covering the range [0.8, 7.4] MeV, and 26 corresponding to the number of antineutrino energy bins spanning [1.8, 8.3] MeV.

Fig. 7.5 presents the aggregated sum of all M_e distributions, with the lower panels illustrating the compatibility between periods by showing the ratio of each period's M_e to the average prompt spectrum $\overline{M_e}$ which is derived from the period-normalized sum of all M_e. The dotted lines represent the ratio of each P_e to $\overline{M_e}$. Despite significant variations in the number of inoperative PMT channels, the detector response remains consistent across DS periods, as evidenced by the flatness of these ratio plots. Minor deviations at the low and high energy edges indicate slight differences in the PG4-predicted response.

To thoroughly compare the measured spectra with a reference model, whether in prompt or antineutrino space, it is crucial to fully account for all statistical, systematic, and model uncertainties. In the PROSPECT experiment, each high-level analysis requiring comparing data and predictions utilizes a χ^2 test statistic based on a covariance matrix formalism described in A.1. The following sections detail the generation and implementation of all relevant covariance matrices for the spectrum analysis.

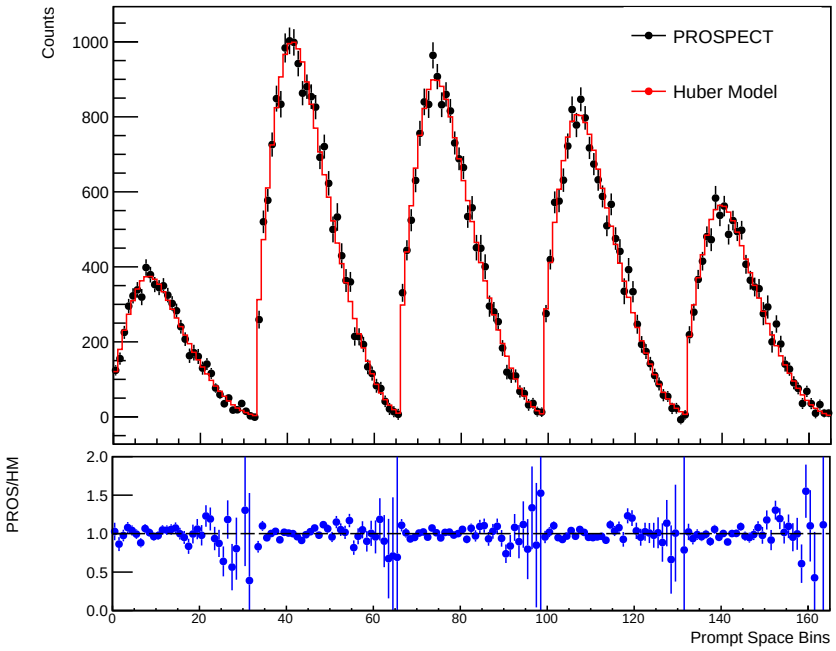


Figure 7.3: Measured prompt spectra (black) for all PROSPECT periods, shown alongside the HM-based predicted spectra. The bottom panel illustrates the data-to-model ratio for each period, revealing a clear excess in the 4–6 MeV range in every period/model comparison.

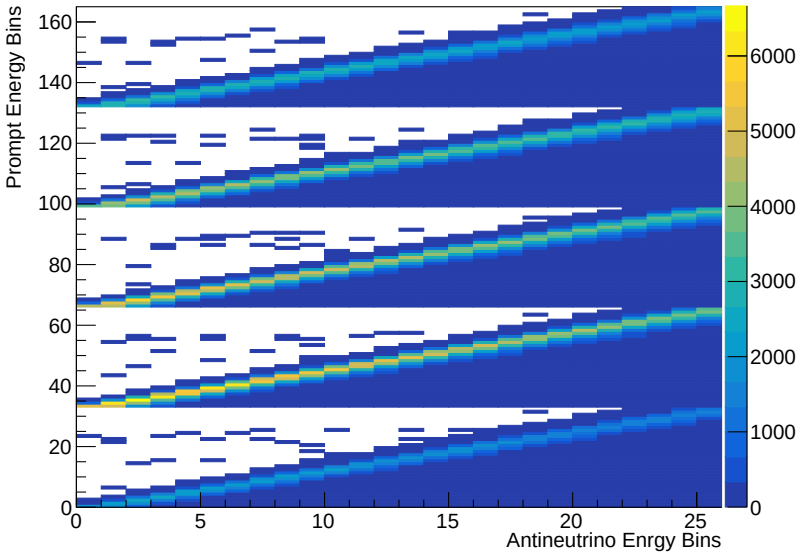


Figure 7.4: Combined response matrix, incorporating the individual responses from each period, ordered sequentially.

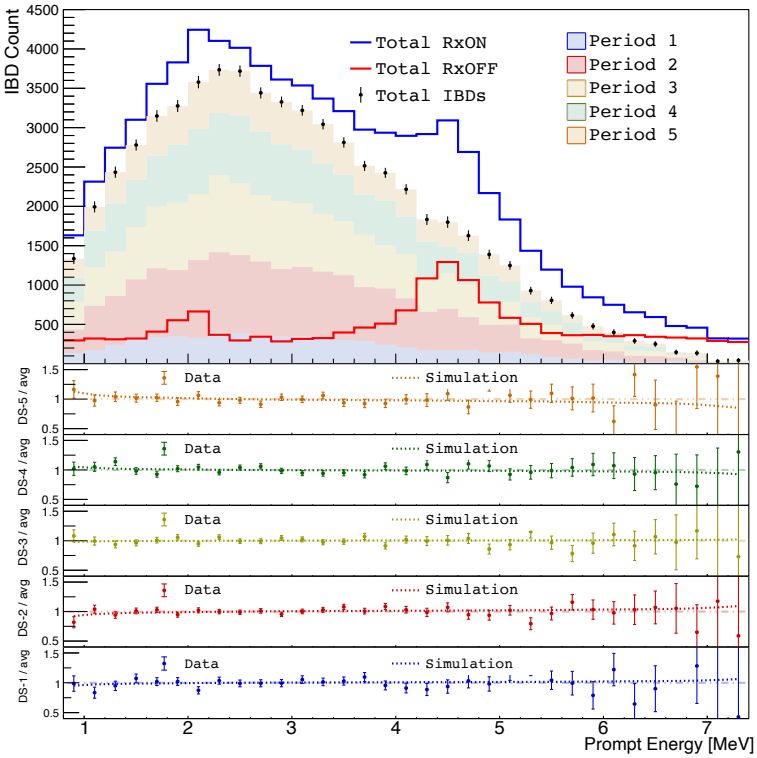


Figure 7.5: Top: Solid blue and red lines represent total reactor-on (RxOn) and -off (RxOff) prompt spectra, respectively, for all periods, while the point distribution is the result of their subtraction. Colored areas represent measured IBD prompt spectra for each period. Bottom: Point distributions represent the ratio between periods 1-5 and the total spectrum normalized to the integrated counts of each period, while the dotted line displays the expected behavior according to Monte Carlo simulations of the different detector configurations. Source [68].

7.2.2 Statistical uncertainty

Every covariance matrix for the spectrum analysis is presented as a 165x165 matrix, constructed as a 5x5 block matrix in units of square background subtracted IBD counts (N^2_{IBD}). The diagonal blocks correspond to each period's prompt covariance matrix, with each 33x33 diagonal block covering an energy range of [0.8-7.4] MeV and a bin width of 0.2 MeV. The off-diagonal elements represent the correlations between different periods.

The statistical covariance matrix, denoted as $\mathrm{V_{stat}}$, is primarily driven by reactor-on IBD candidates and the cosmogenic background estimate subtracted using reactor-off IBD candidate data, as illustrated in Eq. 6.5. The impact of subtracted accidental backgrounds during reactor-on and reactor-off periods on the overall statistical uncertainty is minimal due to their calculation's large offset time window. The period-uncorrelated statistical uncertainties from each DS period dataset, which form the diagonal of $\mathrm{V_{stat}}$, are determined by the Poisson error of each energy bin, adjusted for relative live time and environmental variations across datasets and data periods. Fig. 7.6 illustrates the total statistical covariance matrix.

7.2.3 Systematic uncertainties

The individual contributions from each systematic uncertainty impacting the spectrum analysis were determined through dedicated studies of each effect. A summary of the systematic uncertainties considered in the spectrum analysis is presented in Table 7.1.

For each systematic uncertainty parameter listed in Table 7.1, a covariance matrix V_x is generated by analyzing systematically fluctuated MC datasets as described in A.1.1. The detector configurations shown in Fig. 6.31 are used to create MC datasets that account for spatial and detector effects, including variations in dead and SE segments. This process starts with generating 10^3 MC datasets, each varying a single

Table 7.1: Systematic uncertainties considered for the spectrum analysis.

Parameter	**Uncertainty**	**Description**
Background Norm.	1%	Variations in background levels between reactor on and off periods.
n-H Peak	3%	Uncertainty in background subtraction within the n-H peak region.
Detector Non-linearity	0.002	Uncertainty in energy deposition due to Birks' non-linearity.
Cherenkov Contribution	0.41	Uncertainty in the contribution of Cherenkov radiation to detected photons.
Energy Scale	0.004	Uncertainty in the calibration of the linear energy scale.
Energy Resolution	5%	Uncertainty in the contribution of photostatistics to energy resolution.
Energy Loss	8 keV	Uncertainty in energy loss from escaping 511 keV γ-rays.
^{28}Al Activation	100%	Uncertainty in the contribution of ^{28}Al decay to the spectrum.
Non-equilibrium Corr.	100%	Uncertainty in contributions from long-lived fission products in antineutrino spectrum.
Panel Thickness	0.03 mm	Uncertainty in the mass of scintillator separator panels.
Z Fiducial Cut	25 mm	Uncertainty in event localization near the fiducial volume edge.
Energy Threshold	5 keV	Uncertainty in the energy threshold applied segment by segment.

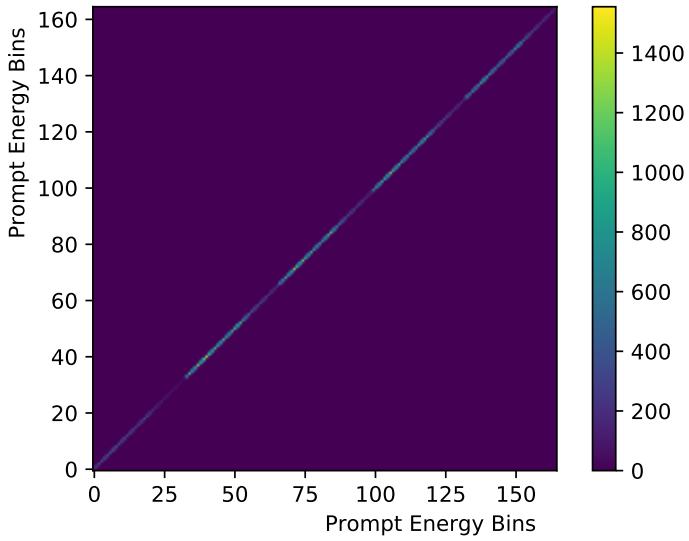


Figure 7.6: Total statistical covariance matrix V_{stat} used in the spectral shape analysis. No statistical correlation between periods is observed.

systematic uncertainty parameter according to a Gaussian distribution with a 1σ width, as specified in Table 7.1.

Toy MC distributions for energy resolution, leakage, and linear scale variations are generated by analytically adjusting the HM-based P_e prediction. Similarly, for background normalization uncertainty, fluctuated datasets are created by systematically varying the reactor-on cosmogenic background prediction. Additionally, toy MC distributions for energy threshold variations are produced using the default HM-based PG4 dataset, with a range of reconstructed pulse energy threshold requirements incorporated into the analysis chain.

For uncertainties related to reflector panel thickness and scintillator non-linearity parameters, MC distributions are generated using PG4 IBD datasets with adjusted simulation parameters regarding the Birks coefficients. For reactor-related spectrum uncertainties, a 100% uncertainty is assumed for all non-^{235}U corrections and the non-equilibrium correction.

Lastly, jointly unfolding data from closely related measurements requires careful consideration of correlated uncertainties between datasets. Systematic uncertainties arising from background variations and IBD spectrum background subtraction are treated as uncorrelated between periods, while all other systematic uncertainties are considered period-correlated. Similarly to the final statistical covariance matrix, the final systematic covariance matrix is built block-diagonally with non-zero contributions in the off-diagonal blocks.

Each systematic covariance matrix was generated using the procedure described in Section. A.1.1. Fig. 7.7 shows the total covariance matrix used for this analysis incorporating both statistic and systematic errors where the period-correlation contributions from systematic uncertainties can be observed. Furthermore, to illustrate the relative contribution from different uncertainty sources for the spectrum analysis, Fig 7.8 shows the relative uncertainty from the diagonal elements of the various sources of uncertainties for all periods and the impact of the evolving detector configuration. As observed, statistical uncertainty is the dominant source across all periods, with detector-related systematic uncertainties being the largest sub-dominant contributor. The primary sources of detector systematic uncertainties include the limitations in understanding the detector's E_{rec} scale and non-linearity, as well as the uncertainty in the total dead mass contributed by the reflecting walls of the optical grid. The total covariance matrix produced served as one of the main inputs for the unfolding procedure described in Section 7.3.

7.3 Unfolding strategy

Multi-period detector response unfolding enables the combination of spectra measured with varying detector responses in the different DS periods into a single antineutrino energy spectrum that can be compared to reactor models or other experimental measurements. The final PROSPECT spectral shape analysis uses the WienerSVD approach to perform the unfolding [195].

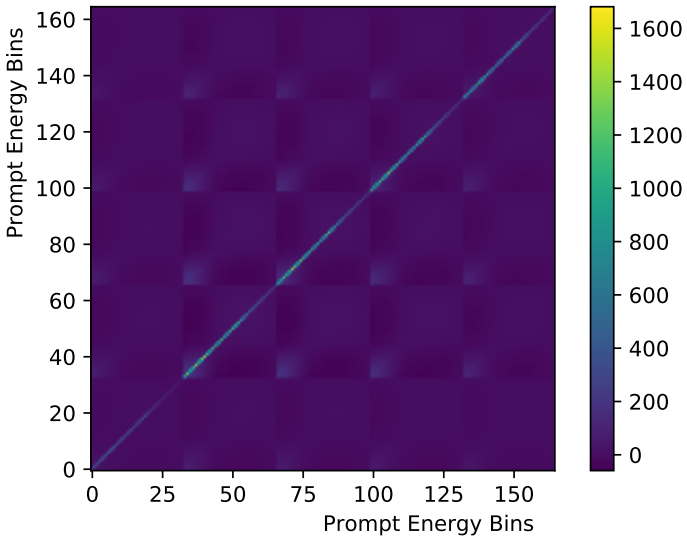


Figure 7.7: Uncertainties for each period of the PROSPECT ^{235}Uantineutrino spectrum measurement, represented by the relative uncertainty in the diagonal elements.

7.3.1 Unfolding PROSPECT Data

Following the unfolding formalism described in Section. A.2, the final PROSPECT unfolded ^{235}U spectrum, $\hat{s}_{\text{pros}}$, can be obtained as follows:

$$\hat{s}_{\text{pros}} = A_W \cdot ({R_{\text{pros}}}^T R_{\text{pros}})^{-1} \cdot {R_{\text{pros}}}^T \cdot M \tag{7.3}$$

where A_W is the smearing matrix containing the effects of regularization using the Wiener filter W_C. The response matrix R_{pros} contains the stacked responses for the separate periods, and the data matrix M is the stacked absolute prompt energy spectra (M_e) for each data period (1-5).

$$R_{pros} = \begin{pmatrix} R^1_{pros} \\ \vdots \\ R^5_{pros} \end{pmatrix}, \; M = \begin{pmatrix} M^1_e \\ \vdots \\ M^5_e \end{pmatrix} \tag{7.4}$$

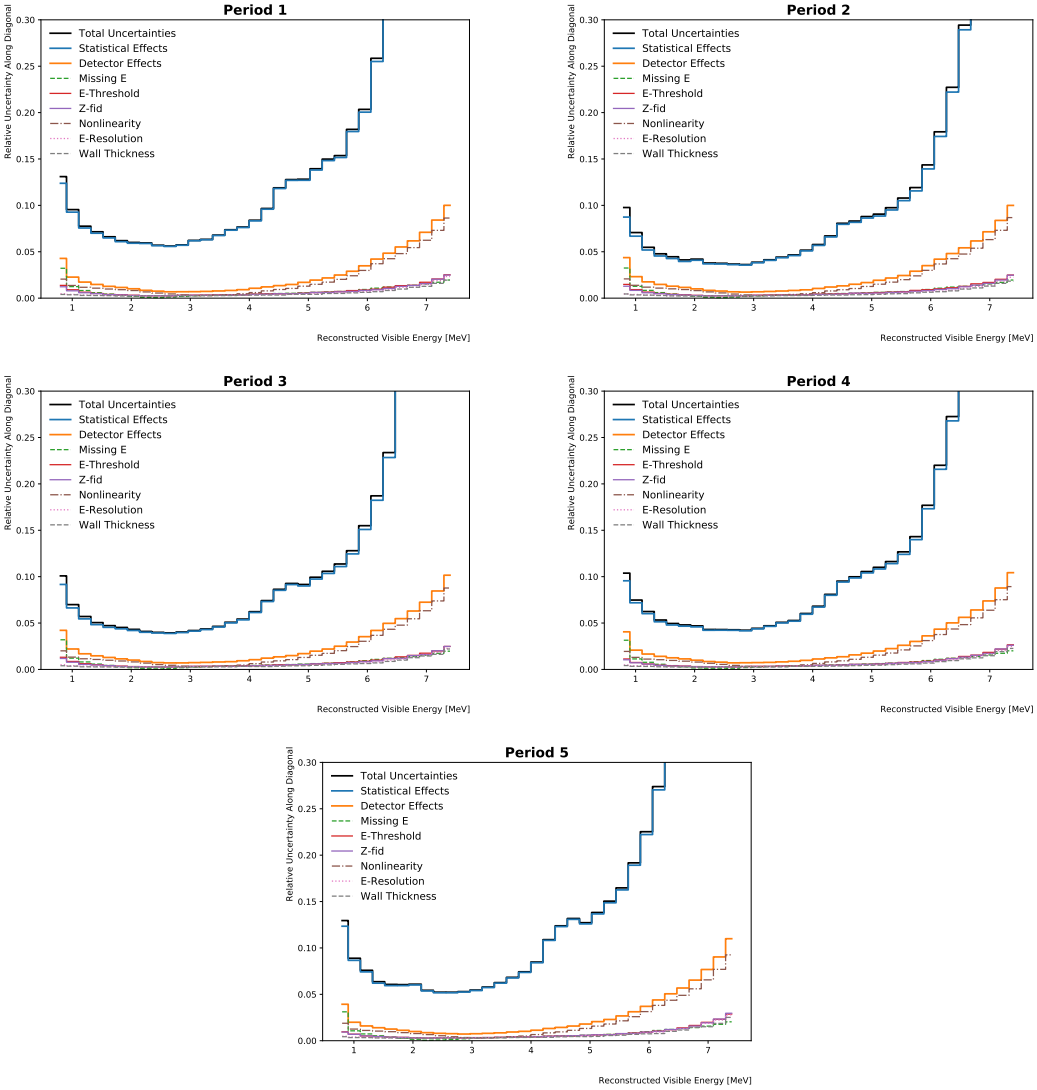


Figure 7.8: Relative uncertainty from diagonal elements of the different covariance matrices in the spectral shape analysis for each DS period.

The Wiener-SVD method relies on an estimate of the true spectrum given by $\hat{s}_{hm}$. A toy study was conducted to estimate the Wiener filter and the corresponding smearing matrix A_W.

7.3.2 Optimizing the Wiener filter

As outlined in Section A.2, the purpose of W_C is to optimize the scaling of each bin in the unfolded spectrum, maximizing the signal-to-background ratio while minimizing bias. The final W_C used for unfolding the PROSPECT data was derived as the average filter across 10,000 MC toys. Each toy was generated from the total covariance matrix V_{tot} using the procedure outlined in Section A.1.2. The Wiener-SVD technique was then applied to extract the filter corresponding to each fluctuated toy.

This process was iterated for 10,000 toys, with each iteration refining W_C and A_W by averaging the results from the preceding $N - i$ toys. As a result, the Nth toy comparison with the reference model utilized an optimized smearing matrix that effectively reduced bias while preserving a high signal-to-background ratio. Fig. 7.9 illustrates the evolution of the average bias introduced by the process, calculated as the difference between each unfolded toy and the model, showing that by approximately 7,000 toys, the filter has been optimized.

In addition, this procedure allowed for the generation of a total unfolded covariance matrix $V_{tot,\hat{s}}$ such that

$$V_{tot,\hat{s}_{pros}(j,k)} = \frac{1}{N_{toy}} \sum_{i}^{N_{toy}} (\hat{s}'_{i(j)} - A_{W,i} \cdot \ \hat{s}_{HM(k)}) \cdot (\hat{s}'_{i(k)} - A_{W,i} \cdot \ \hat{s}_{HM(j)}) \tag{7.5}$$

where $V_{tot,\hat{s}_{pros}(j,k)}$ corresponds to the (j,k) element of the unfolded covariance matrix and $\hat{s}'$ represents each of the unfolded toys. The resulting $V_{tot,\hat{s}}$ is illustrated in Fig. 7.10 along with the final smearing matrix A_W.

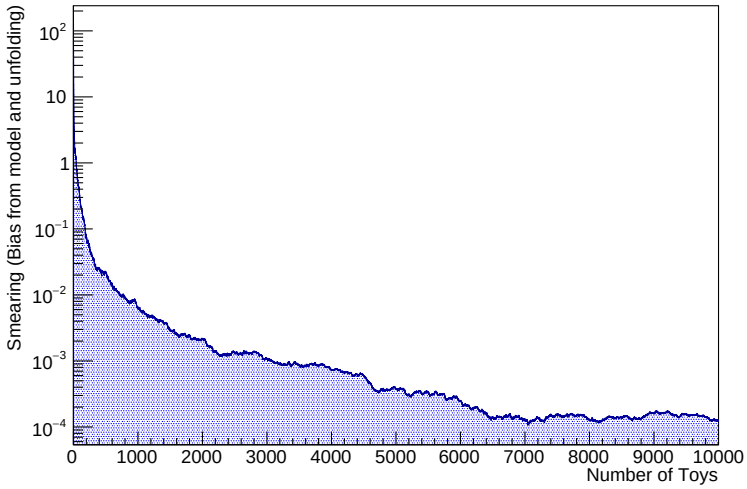


Figure 7.9: Smearing optimization procedure while building the final Wiener-SVD filter.

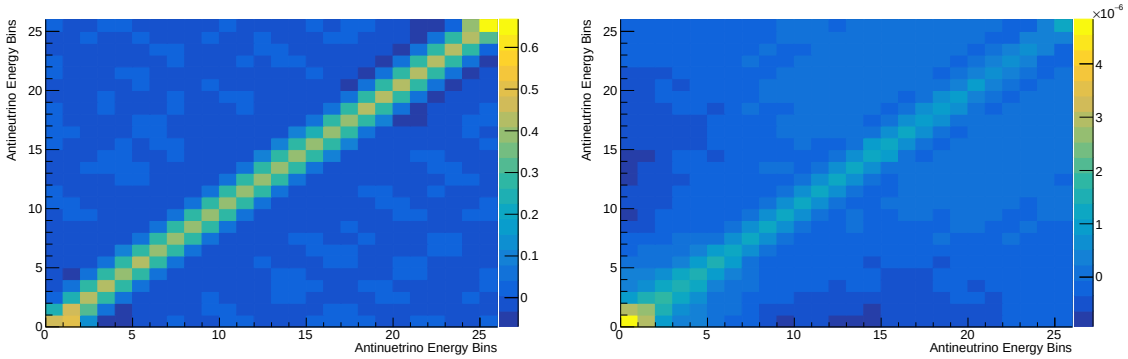


Figure 7.10: Left: Final smearing matrix A_W used for the unfolding process. Right: Unfolded PROSPECT covariance matrix. Both matrices have dimensions of 26x26, representing the energy range in antineutrino space from [1.8-8.3] MeV.

Following the completion of the optimization procedure, the resulting W_C and A_W were applied in Eq. 7.3 to obtain a single PROSPECT unfolded spectrum as depicted in the top panel of Fig. 7.11. The figure also contains the reference model spectrum $\hat{s}_{hm}$ to which the final A_W has been applied to account for unfolding bias, together with the reactor's estimations for non-fuel and non-equilibrium contributions.

7.4 Spectral shape comparison

The agreement between the unfolded spectrum $\hat{s}_p$ and the model $\hat{s}_{hm}$ is quantified using the covariance matrix-based χ^2 test statistic described in Section A.1.1. In this case, Eq. A.12 can be rewritten as

$$\begin{aligned} \chi^2 &= \boldsymbol{\Delta}^{\mathrm{T}} \mathbf{V}^{-1} \boldsymbol{\Delta} \\ \chi^2 &= (\hat{\boldsymbol{s}}_{\boldsymbol{pros}} - \boldsymbol{A_W} \cdot \hat{\boldsymbol{s}}_{\boldsymbol{hm}})^{\mathrm{T}} \cdot \mathbf{V}_{unfold}^{-1} \cdot (\hat{\boldsymbol{s}}_{\boldsymbol{pros}} - \boldsymbol{A_W} \cdot \hat{\boldsymbol{s}}_{\boldsymbol{hm}}) \end{aligned} \tag{7.6}$$

where $V_{unfold} = V_{tot,\hat{s}_{pros}} + V_{\hat{s},HM}$ is the sum of the respective unfolded covariance matrices for PROSPECT and the HM covariance [149]. Applying Eq. 7.6 yields a χ^2 value of $\bar{\chi}^2_{HM} = 30.2/25$, corresponding to a single-sided p-value of $p = 0.22$, indicating general agreement between the data and the model.

The second panel of Fig. 7.11 illustrates the ratio of $\hat{s}_p$ to $(A_W \cdot \hat{s}_{hm})$ where a local discrepancy is observed at energies between 5-7 MeV. This discrepancy is further investigated using a sliding window method [61, 70], where nuisance parameters are introduced within 1.25 MeV-wide windows along the spectrum. These windows are chosen based on the scale of deviations observed in previous experiments. The $\Delta\chi^2$ relative to the best fit is calculated for each window, along with its corresponding single-sided p-value. The results, depicted in Fig. 7.11, confirm the presence of a local excess in this energy range.

As previously noted, the persistent excess observed in the 5-7 MeV energy range has been consistently reported across various modern reactor antineutrino experiments [53, 109, 35, 47, 70]. A prominent case study worth comparing against

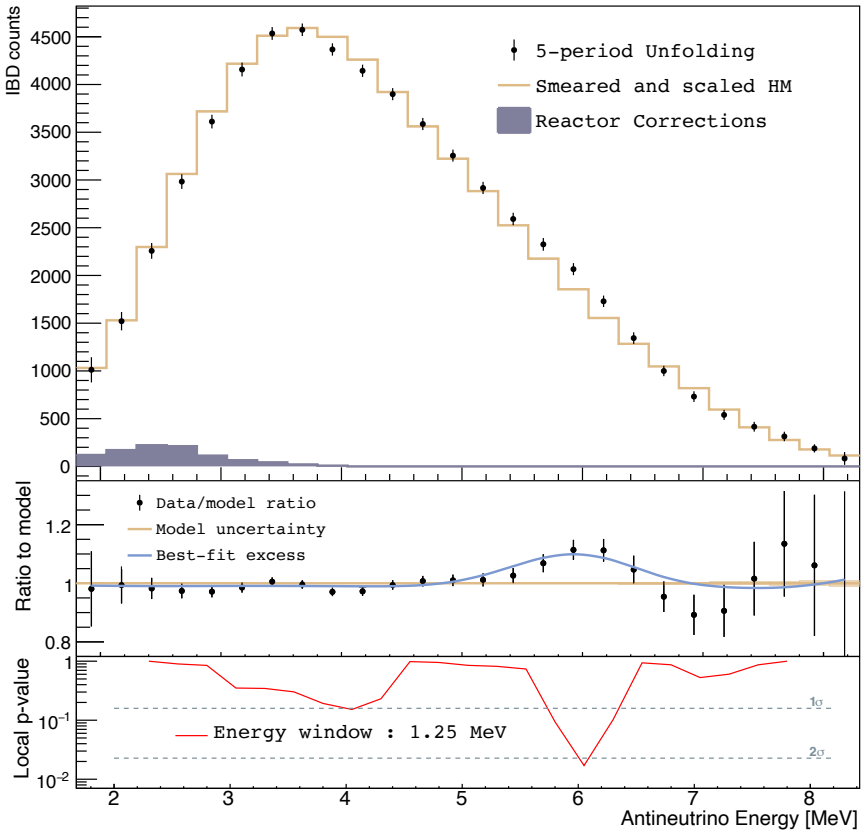


Figure 7.11: Unfolded antineutrino spectrum from the HEU reactor at HFIR. Top: The points represent PROSPECT's unfolded antineutrino spectrum, the magenta line indicates the HM ^{235}U prediction, and the gray shaded histogram shows the reactor's non-fuel and non-equilibrium contributions, which have been subtracted from the data. Middle: The ratio of data to the model is shown, along with the Gaussian function $G_{\mathrm{PRO}}(A \cdot r, \mu, \sigma)$ obtained from the simultaneous fit of the unfolded spectra from PROSPECT and DYB. Bottom: The local p-value is shown, derived from a 1.25 MeV-wide sliding window analysis. Source [68]

is the Daya Bay experiment, which analyzed LEU-derived spectra through a time-evolution study of fission fractions at the Daya Bay nuclear power complex [55]. When comparing PROSPECT's HEU-derived unfolded spectrum ($\hat{s}_{pros}$) with Daya Bay's LEU-derived ^{235}U unfolded spectrum ($\hat{s}_{dyb}$) using Eq. 7.6, where $\Delta = (\hat{s}_{pros} - \hat{s}_{dyb})$ and $V_{unfold} = V_{tot,\hat{s}_{pros}} + V_{tot,\hat{s}_{dyb}}$, a reduced χ^2 value of $\bar{\chi}^2_{DYB} = 20.2/23$ is obtained, corresponding to a p-value of $p = 0.63$. It is worth noting that the number of degrees of freedom presented for both $\bar{\chi}^2_{DYB}$ and $\bar{\chi}^2_{HM}$ is different because $\hat{s}_{hm}$ is presented as a 26-bin vector spanning an energy range of [1.8,8.3] MeV, while $\hat{s}_{dyb}$ is a 24-bin vector spanning an energy range of [1.8,7.8] MeV.

This result indicates a higher consistency between the two experimental spectra than the comparison made with the HM model, highlighting the need for more accurate models to predict antineutrino yields from nuclear reactors. However, the origin of the discrepancy observed by both experiments remains unclear, mainly whether it is a universal feature across all fissioning isotopes or primarily due to misrepresenting a specific isotope. To investigate the isotopic source of this excess, its intensity can be compared in composite HEU- and LEU-based measurements [144, 99, 151, 74, 70], as described in the next section. These comparisons utilize the total unfolded spectrum from Daya Bay, $\hat{s}_{dyb,all}$, which includes contributions from all fissioning isotopes.

7.5 Hypothesis testing

When addressing the question of the isotopic nature of the bump-like feature in the antineutrino spectrum resulting from data-model comparisons, three primary hypotheses are commonly discussed in the literature: (1) ^{235}U exhibits no excess, with the discrepancy between data and models attributed to sub-dominant fission isotopes (No-^{235}U hypothesis), (2) all isotopes contribute equally to the excess (Equal-Isotope hypothesis), and (3) ^{235}U is solely responsible for the entire observed excess (All-^{235}U hypothesis). To investigate these scenarios, the excess reported when comparing

both $\hat{s}_{pros}$ and $\hat{s}_{dyb,all}$ against their respective fuel-modeled HM spectra $\hat{s}_{HM,pros}$ and $\hat{s}_{HM,dyb,all}$ are quantified using a combined Gaussian excess fit procedure.

7.5.1 Gaussian excess fit - procedure

The first step in performing this fit is to quantify the magnitude of the excess observed by each experiment. This is done by comparing the unfolded spectrum from each experiment to modified versions of their respective fuel-modeled HM spectra, denoted as $\hat{s}'_{HM,pros}$ and $\hat{s}'_{HM,dyb,all}$. These modifications involve adding a Gaussian function, $G_{pros}(n_{pro}, A \cdot r, \mu, \sigma)$ for PROSPECT and $G_{dyb,all}(n_{dyb,all}, A, \mu, \sigma)$ for Daya Bay, to each model such that

$$\hat{\mathbf{s}}'_{\mathbf{HM,pros}} = \hat{\mathbf{s}}_{\mathbf{HM,pros}} \cdot (\mathbf{1} + G_{pros}(n_{pro}, A \cdot r, \mu, \sigma)) \tag{7.7}$$

$$\hat{\mathbf{s}}'_{\mathbf{HM,dyb,all}} = \hat{\mathbf{s}}_{\mathbf{HM,dyb,all}} \cdot (\mathbf{1} + G_{dyb,all}(n_{dyb,all}, A, \mu, \sigma)) \tag{7.8}$$

Since it is assumed that the nature of the reported excess is the same for both HEU and LEU measurements—where only the intensity of each excess varies depending on the fissile isotopic composition of the fuel—a common mean μ and standard deviation σ are chosen for the Gaussian functions, while their amplitudes are related by a scaling factor r, such that $A = A_{dyb,all}$ and $A_{pros} = A_{dyb,all} \cdot r$. In addition, a normalization factor n_x to the model, specific to each experiment, is included in each Gaussian function motivated by the lack of absolute flux information in the analysis.

As detailed in Section 7.3.1, before comparing the perturbed models in Eqs. 7.7-7.8 to their corresponding experimental data, each model must be carefully adjusted to account for the specific unfolding effects reported by each experiment by applying the respective final smearing matrices $A_{W,pros}$ and $A_{W,dyb,all}$.

Once the perturbed models have been appropriately smeared, the Gaussian excess fitting process can be carried out. In this analysis, the process involves the simultaneous minimization of two functions defined as:

$$
\begin{aligned}
f_{pros}\left(n_{pros}, A\cdot r, \mu, \sigma\right) &= \mathbf{\Delta}_{pros}^{T}\cdot\hat{\mathrm{V}}_{pros}^{-1}\cdot\mathbf{\Delta}_{pros} = \chi^2_{pros},\\
f_{dyb,all}\left(n_{dyb,all}, A, \mu, \sigma\right) &= \mathbf{\Delta}_{dyb,all}^{T}\cdot\hat{\mathrm{V}}_{dyb,all}^{-1}\cdot\mathbf{\Delta}_{dyb,all} = \chi^2_{dyb,all},
\end{aligned}
\tag{7.9}
$$

where

$$
\begin{aligned}
\mathbf{\Delta}_{pros} &= \hat{\mathbf{s}}_{\mathbf{pros}} - A_{W,pros}\cdot\hat{\mathbf{s}}'_{\mathbf{HM,pros}}\\
\mathbf{\Delta}_{dyb,all} &= \hat{\mathbf{s}}_{\mathbf{dyb,all}} - A_{W,dyb,all}\cdot\hat{\mathbf{s}}'_{\mathbf{HM,dyb,all}}
\end{aligned}
\tag{7.10}
$$

$$
\begin{aligned}
\hat{\boldsymbol{V}}_{pros} &= V_{tot,\hat{s}_{pros}} + \left(A_{W,pros}\cdot V_{tot,\hat{s}_{HM,pros}}\cdot A^{T}_{W,pros}\right)\\
\hat{\boldsymbol{V}}_{dyb,all} &= V_{tot,\hat{s}_{dyb,all}} + \left(A_{W,dyb,all}\cdot V_{tot,\hat{s}_{HM,dyb,all}}\cdot A^{T}_{W,dyb,all}\right)
\end{aligned}
\tag{7.11}
$$

The minimization function adjusts all six parameters to find the minimum value for the combined sum $\chi^2_{pro} + \chi^2_{dyb,all}$.

7.5.2 Gaussian excess fit - results

The simultaneous data-model described in Eq. 7.9 minimization yielded an excess amplitude of $A = 11 \pm 4\%$ and an HEU-to-LEU ratio of $r = 0.79^{+0.35}_{-0.25}$, with a reduced chi-square value of $\bar{\chi}^2_{\text{fit}} = 34.8/44$ ($p = 0.84$). Making use of these best fit parameters, the Gaussian function $G_{pros}(n_{pro}, A\cdot r, \mu, \sigma)$ is plotted in the second panel Fig. 7.11 demonstrated good agreement with the observed data-model ratio. In addition, the final $\Delta\chi^2$ profile for the combined minimization is illustrated by the solid line in Fig. 7.12 obtained by letting r vary while keeping A, μ and σ fixed. $\Delta\chi^2$ is defined as $\Delta\chi^2 = \chi^2 - \chi^2_{min}$, where χ^2_{min} was obtained for $r = 0.79^{+0.35}_{-0.25}$. The obtained excess amplitude for pure ^{235}U and the LEU spectrum makes it possible to assess spectral mis-modeling by considering the three hypotheses discussed earlier.

In the No-^{235}U scenario, a null-excess condition for PROSPECT ($r = 0$) must be satisfied irrespective of any excess in the Daya Bay spectrum. This scenario corresponds to a $\Delta\chi^2 = 13.6$ ($p = 2.26\cdot10^{-4}$), indicating that the PROSPECT data strongly disfavors this hypothesis, with a significance of 3.7σ. Under the equal-isotope hypothesis, PROSPECT and Daya Bay should observe identical excesses,

corresponding to $r = 1.0$. In Fig. 7.12, this hypothesis profiles at $\Delta\chi^2 = 0.4$ ($p = 0.53$), suggesting that the data from PROSPECT and Daya Bay are consistent with all isotopes contributing equally to the excess. Finally, according to the All-^{235}U hypothesis, the excess observed in the Daya Bay composite spectrum would be attributed solely to the average effective fraction of fissions from ^{235}U, which is $\langle f_{235} \rangle$=0.564 [55]. This hypothesis implies that PROSPECT should observe a larger excess amplitude than Daya Bay, specifically $r = \frac{1}{\langle f_{235} \rangle} = 1.77$. This scenario profiles at $\Delta\chi^2 = 3.9$ ($p = 0.05$) in Fig. 7.12, indicating that the PROSPECT data disfavor the All-^{235}U hypothesis with a significance of 2.0 σ.

The full set of uncertainties in the Daya Bay measurement, primarily influenced by detector systematics not included in previous PROSPECT analyses, are included in the simultaneous minimization, significantly affecting hypothesis rejection capabilities. The dashed profile in Fig. **??**llustrates this impact fig:DeltaChi2, which shows the effect of downscaling Daya Bay's covariance matrix by four orders of magnitude, effectively making Daya Bay's uncertainties negligible in the fit. In this adjusted scenario, the hypothesis rejection power for the All-^{235}U hypothesis improves dramatically, approaching nearly 5 σ, an enhancement over the results previously reported by PROSPECT in [70]. Given the substantial influence of uncorrelated detector systematics on this comparison, future measurements of HEU and LEU cores using a common detector [125, 71, 39] would be particularly valuable in further refining and testing the All-^{235}U hypothesis.

7.6 PROSPECT in the global context

The enhancement in the statistical power of the PROSPECT data and its impact on the new spectral shape analysis can be demonstrated by comparing the total relative uncertainties from this analysis with those from previous PROSPECT results and other reactor-based experiments. Fig. 7.13 presents a comparison of the relative uncertainties in the diagonal elements of the total covariance matrices for both the

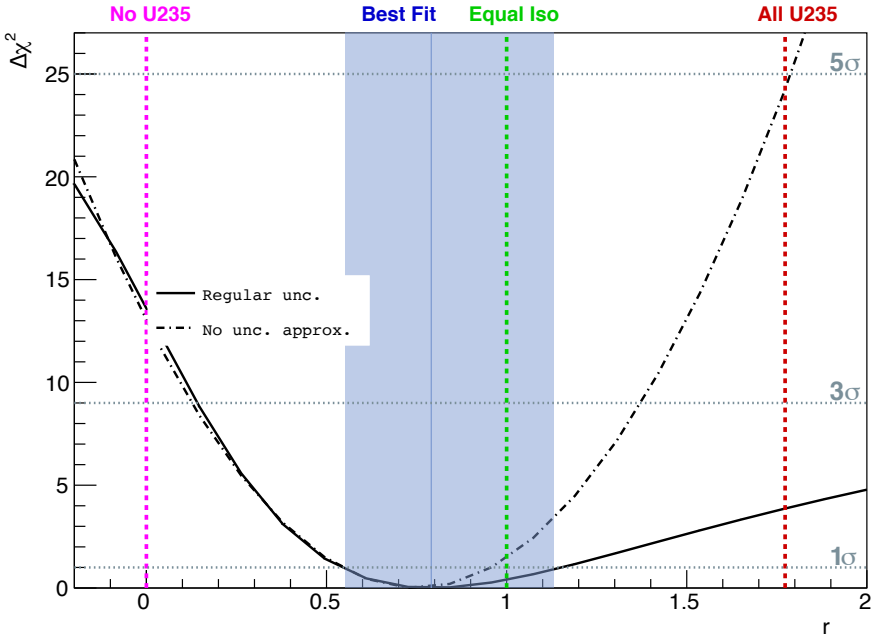


Figure 7.12: $\Delta\chi^2$ distributions for a simultaneous Gaussian-like excess fit of PROSPECT's and Daya Bay's unfolded spectra. The profile from the combined fit (solid black) shows asymmetric behavior, mainly due to the minimal impact of Daya Bay's spectrum in rejecting the No-^{235}U hypothesis. The best-fit value is $r = 0.79^{+0.35}_{-0.25}$, with $\Delta\chi^2 = 13.6(3.9)$ relative to $r = 0$ (No-^{235}U hypothesis, magenta line) and $r = 1.77$ (All-^{235}U hypothesis, red line). The green dotted line represents the equal-isotope hypothesis ($r = 1$), intersecting the profile at $\Delta\chi^2 = 0.4$. When Daya Bay's uncertainties are significantly reduced (dotted black), the distribution of the $\Delta\chi^2$ becomes symmetric. Source [68]

previous and final PROSPECT-only spectral shape analyses in prompt energy space, highlighting the improvements in the dataset. A significant reduction in uncertainty is observed, particularly in the 4-6 MeV region where the 'bump' is located.

Furthermore, Fig. 7.14 compares the relative uncertainties in the diagonal elements of the total unfolded covariance matrices from the latest results of the PROSPECT, STEREO, and Daya Bay experiments. While this comparison is somewhat complicated, given that PROSPECT does not include uncertainties related to absolute flux normalization as the other experiments do, the statistical power of the PROSPECT data is still clear, particularly in the 5-7 MeV region where the 'bump' anomaly has been observed. This highlights the high precision achieved by the PROSPECT analysis, even with a smaller data set compared to the other two collaborations.

7.7 Chapter summary

Leveraging the improved multi-period dataset, one of the most precise measurements of the ^{235}U antineutrino energy spectrum to date has been achieved from the HFIR HEU reactor by PROSPECT through a simultaneous multi-period unfolding using the WienerSVD formalism. Comparisons of the measured spectra with the HM ^{235}U model and LEU-based measurements reveal consistent high-energy spectral excesses between HEU and LEU reactors, effectively disfavoring both the No-^{235}U and All-^{235}U hypotheses at 3.7σ and 2.0σ, respectively, as explanations for the 5-7 MeV excess. In alignment with recent advancements in modeling and fission beta measurements [118, 157], these final PROSPECT-I results further reinforce the theoretically plausible scenario that all primary fission isotopes are subject to incorrectly predicted reactor antineutrino spectra.

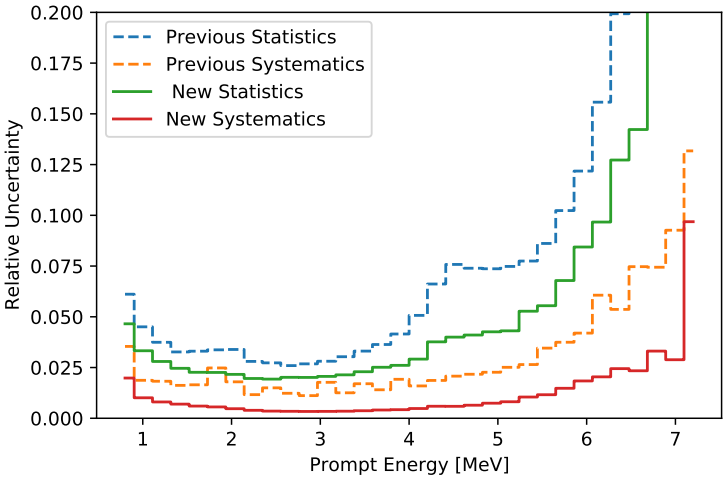


Figure 7.13: Comparison of the relative uncertainty contributions from the diagonal elements of the total prompt covariance matrices between the PROSPECT-only analyses. The new results (solid lines) and the old (dashed lines) illustrate the significant enhancement provided by the DS+SEER analysis.

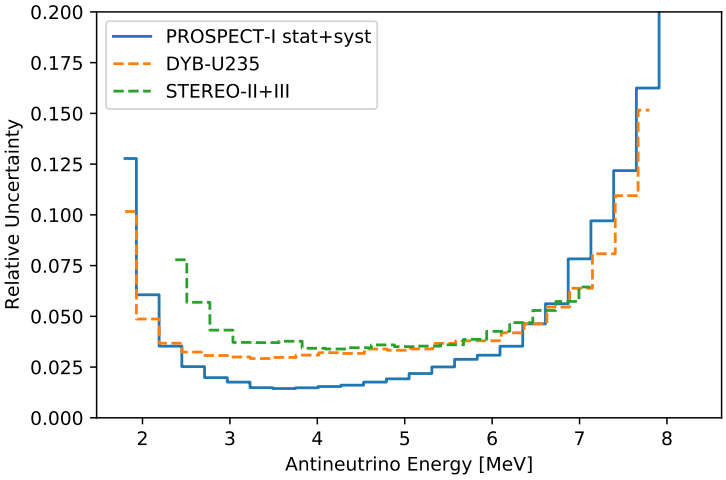


Figure 7.14: Comparison of the relative uncertainty contributions from the diagonal elements of the unfolded covariance matrices between PROSPECT, Daya Bay, and STEREO, illustrating the high precision achieved by the new multi-period analysis.

Chapter 8

Multi-Period Sterile Neutrino Oscillation Analysis

Reactor neutrino experiments, as discussed in earlier chapters, have played a crucial role in precisely determining three of the six parameters that describe neutrino mixing within the Standard Model: θ_{13}, Δm^2_{21}, and $|\Delta m^2_{31}|$ [194]. However, discrepancies between the observed and predicted reactor $\bar{\nu}_e$ fluxes [172] have prompted the development of new experiments and analyses aimed at exploring the active-sterile neutrino mixing parameters Δm^2_{41} and θ_{14} [127]. As outlined in Section 2.7.1 ,the possible existence of a sterile neutrino, which would indicate new BSM physics, could account for observed deficits in electron-flavor neutrino detection rates when compared to theoretical predictions in reactor [170] and radioactive source neutrino experiments [50, 7]. The disappearance probability describes these deficits:

$$P_{\text{dis}} = \sin^2 2\theta_{14} \sin^2 \left(1.267 \Delta m^2_{41}(\text{eV}^2) \frac{L(\text{m})}{E_\nu(\text{MeV})} \right), \tag{8.1}$$

where Δm^2_{41} represents the mass-squared difference, θ_{14} is the mixing angle that quantifies the electron flavor content of the new mass state, and E_ν and L are the neutrino energy and travel distance (baseline), respectively.

Sterile neutrino oscillations in the PROSPECT dataset are analyzed by comparing prompt E_{rec} spectra across different detector baselines. The following chapter will discuss the distribution of the PROSPECT datasets across various baseline bins, outline the statistical methods employed to detect unexpected relative variations in E_{rec} spectra between baselines and present new findings based on the multi-period dataset described in Chapter 6. These findings establish new constraints on sterile neutrino oscillations in previously unexplored regions between 0.2 and 20 eV^2. This analysis results in the exclusion, at the 95% confidence level, of sterile neutrinos in the areas above 3 eV^2, previously unprobed by terrestrial experiments, including the entire region below 10 eV^2 suggested by the recently reinforced Gallium Anomaly [88]. Moreover, the best-fit point of the Neutrino-4 [190] reactor experiment's claimed observation of short-baseline oscillation is excluded at more than five standard deviations.

8.1 Description of previous analysis

PROSPECT has conducted two searches for sterile neutrino oscillations using the single-detector configuration dataset described in Chapter 6: one based on a partial dataset [82] and the other on the full dataset [70]. Both analyses compared relative spectral shapes across detector baselines ranging from 6.7 to 9.2 meters, as shown in Fig. 8.1. The first analysis employed a uniformly spaced baseline binning with six intervals. The second used a non-uniform binning with ten intervals to ensure equal statistics across baselines, thereby minimizing potential biases. Both analyses utilized 16 energy bins covering a prompt energy range of 0.8 to 7.3 MeV. To assess sensitivity and exclusion contours, as well as to establish confidence level intervals indicating the preference of the PROSPECT data for the no-oscillation (Null) hypothesis, both studies employed statistical methods such as Gaussian CLs and Feldman-Cousins, which are detailed Sections A.4 and A.5 respectively. The results, shown in Fig. 8.2,

reveal that the first analysis disfavored the RAA best-fit point at a $2.2\,\sigma$ confidence level, while the second analysis disfavored it at $2.5\,\sigma$.

Despite the success of these rigorous analyses in expanding the neutrino community's understanding of the sterile neutrino oscillation phase space, particularly in addressing the RAA, both efforts—like the initial spectral shape studies—were constrained by statistical limitations. Building on the development of the improved multi-period dataset, a new oscillation analysis was undertaken, leveraging the enhanced statistical power provided by DS and SEER.

8.1.1 Motivation shift since last oscillation result

Recent findings in the reactor experiment sector, including Daya Bay's $\bar{\nu}_e$ flux measurements [62], along with advances in nuclear theory [145, 118, 181] and experimental work [158], suggest that inaccuracies in reactor $\bar{\nu}_e$ model predictions are likely responsible for the observed $\bar{\nu}_e$ deficits. This has led to a diminished interest in the RAA as a direct indicator of BSM physics.

Nonetheless, the acquisition of additional high-precision data from short-baseline reactor experiments remains crucial, particularly in light of the Neutrino-4 experiment, which recently reported a deficit with an amplitude similar to the RAA and an L/E_ν dependence indicative of sterile-induced oscillations [190]. Furthermore, electron-flavor deficits continue to be observed in MeV-scale radioactive source measurements, known as the 'Gallium Anomaly' [88], which cannot be explained by the reactor model inconsistencies that are believed to account for the RAA [128]. Both of these serve as motivation for a new search for sterile neutrinos with the PROSPECT-I dataset.

The Neutrino-4 experiment

The Neutrino-4 experiment [190], conducted at the SM-3 reactor in Dimitrovgrad, Russia, aimed to detect possible oscillations of reactor antineutrinos into sterile states

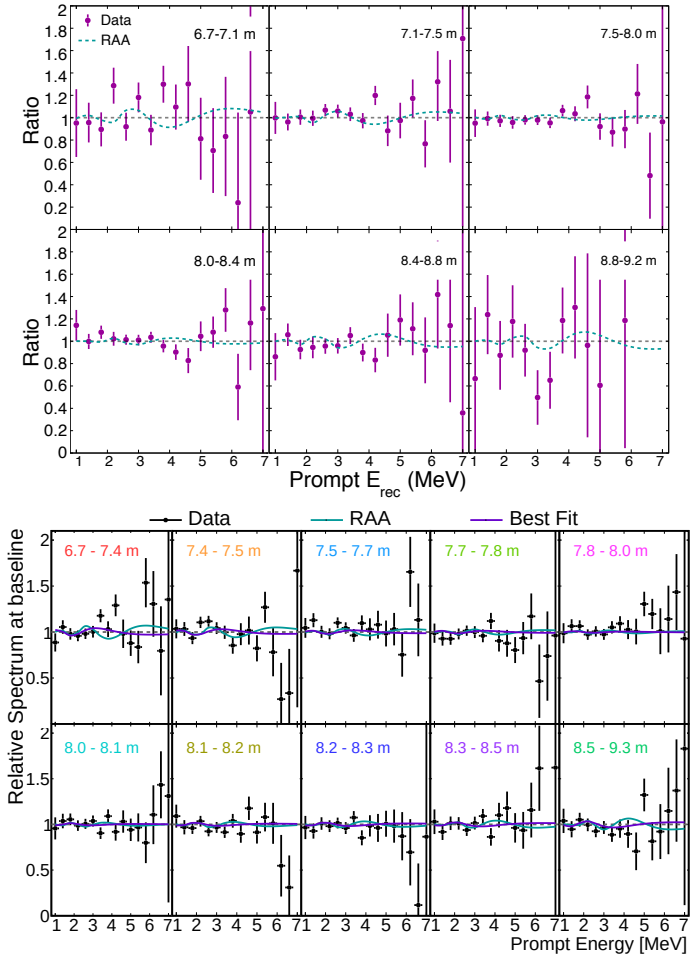


Figure 8.1: Ratio of the measured IBD prompt $E_{\mathrm{rec},p}$ spectra to the baseline-integrated spectrum for the first (top) and second (bottom) PROSPECT oscillation analyses. Also shown are the no-oscillation (flat) expectation and the oscillated expectation corresponding to the RAA best-fit oscillation parameters [170] for both analyses. Source [82, 70].

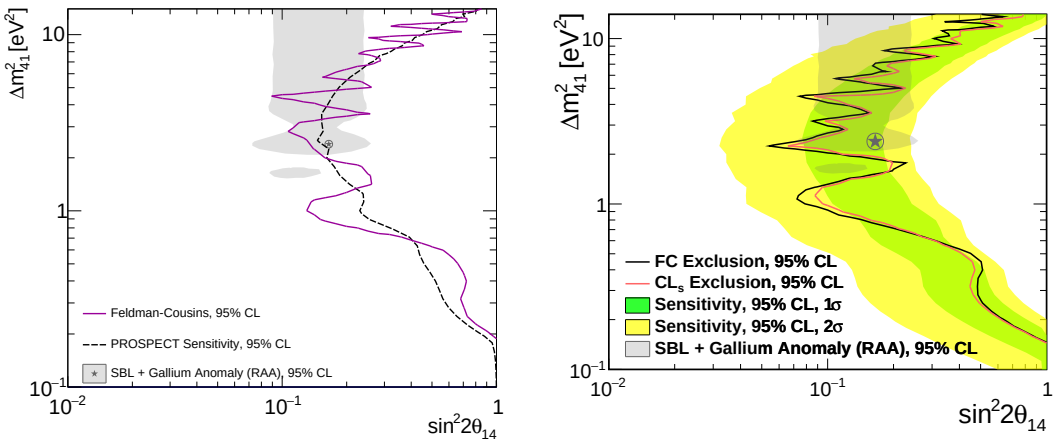


Figure 8.2: Exclusion contours from the first (left) and second (right) sterile neutrino oscillation analyses performed by PROSPECT. Both analyses show a preference for the null oscillation hypothesis. Source: [82, 70].

by measuring their flux and spectrum at varying distances from the reactor core. The experiment employed a compact, movable detector system capable of measuring antineutrino flux at distances ranging from 6 to 12 meters from the reactor core. The detector, segmented into 50 sections filled with gadolinium-doped liquid scintillator, was explicitly designed to detect IBD events. The detector was encased in heavy passive shielding composed of steel, lead, and borated polyethylene to minimize background noise, particularly from cosmic rays and fast neutrons. The mobility of the detector was crucial for identifying potential oscillation effects.

Similar to the approach used in the PROSPECT experiment, Neutrino-4 alternated between reactor-on and reactor-off periods to distinguish antineutrino signals from background noise. The collected data revealed a deficit in the expected antineutrino flux, consistent with neutrino oscillations involving sterile neutrinos. The analysis focused on determining the oscillation parameters, Δm^2_{14} and $\sin^2(2\theta_{14})$, which describe the mass-squared difference and mixing angle between the active and sterile neutrino states. The best-fit parameters were $\Delta m^2_{14} = 7.3 \pm 1.17$ eV^2 and $\sin^2(2\theta_{14}) = 0.36 \pm 0.12$, derived from the observed antineutrino flux deficit as a function of distance from the reactor core. These oscillations were detected with a

statistical significance of 2.9σ, suggesting the presence of sterile neutrinos. The main results from this experiment are illustrated in Fig. 8.3.

The authors plan to enhance the Neutrino-4 experimental setup to achieve greater sensitivity and reduce systematic uncertainties. By improving measurement accuracy by a factor of three, they aim to provide more definitive evidence regarding the existence of sterile neutrinos. Future experiments will focus on extending the range of measurement distances and further refining background suppression techniques.

The BEST experiment

The Baksan Experiment on Sterile Transitions (BEST) [88], conducted at the Baksan Neutrino Observatory deep in the Caucasus mountains of Russia, was specifically designed to test the hypothesis of electron-neutrino transitions to sterile states. Utilizing two concentric zones of liquid gallium (Ga) as the neutrino target, BEST employed a ^{51}Cr radioactive source, which emits primarily monoenergetic neutrinos, ideal for probing short-baseline oscillations. This two-zone design enabled the experiment to measure neutrino interaction rates at two different distances from the source, providing a unique opportunity to search for oscillations on a meter scale.

The inner zone of the target contained approximately 7.47 tons of liquid Ga, while the outer zone held around 39.96 tons. The experiment focused on measuring

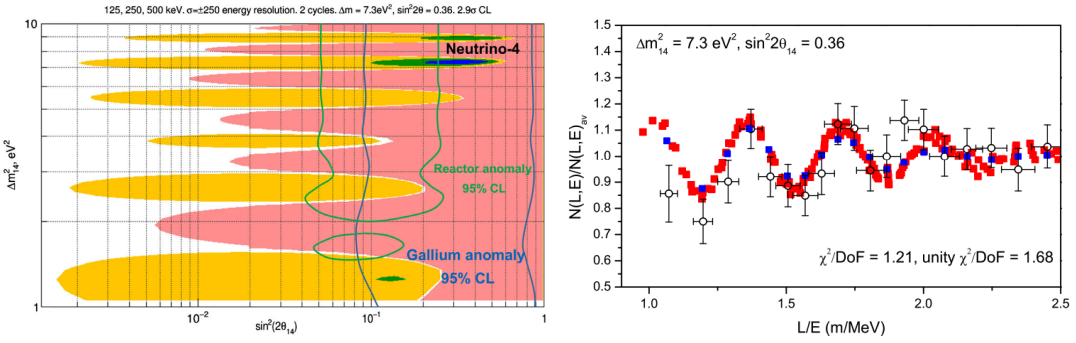


Figure 8.3: Allowed region for the Neutrino-4 result reporting a best-fit at $\Delta m^2_{14} = 7.3 \pm 1.17$ eV^2 and $\sin^2(2\theta_{14}) = 0.36 \pm 0.12$, as well as an apparent oscillatory L/E_ν data distribution. Source [190].

the production rates of the radioactive isotope ^{71}Ge, which is produced by the interaction of electron neutrinos (ν_e) with Ga. From July 5 to October 13, 2019, the ^{51}Cr source irradiated the Ga target with an activity of 3.414 MCi, resulting in 20 independent extractions of ^{71}Ge. These extractions were analyzed using low-background proportional counters, with rigorous calibration and event selection procedures to ensure accurate differentiation between true ^{71}Ge decay events and background noise.

The experiment observed deficits in the ^{71}Ge production rates in the inner and outer target zones, compared to the predicted rates based on known neutrino interaction cross sections. Specifically, the measured production rates were approximately 54.9 atoms/day for the inner zone and 72.6 atoms/day for the outer zone, showing significant deviations from the expected values without sterile neutrino oscillations. These observed deficits were analyzed under the '3+1' framework of neutrino oscillations involving sterile neutrinos (see Section. 2.7.1). The best-fit parameters for this model indicated a mass-squared difference of $\Delta m^2 = 3.3^{+\infty}_{-2.3}$ eV^2 and a mixing angle of $\sin^2(2\theta) = 0.42^{+0.15}_{-0.17}$. These results, illustrated in Fig. 8.4 suggest that if sterile neutrinos are responsible for the gallium anomaly, they would involve a surprisingly large mixing angle with active neutrinos, a characteristic not typically expected in sterile neutrino models.

8.2 Description of datasets

To perform the final oscillation analysis, the prompt spectra (M_e) from each data period are divided into 6 different groups based on segments of common baseline (L) range, where L is defined as the distance from the IBD β^+ cluster's S_{rec} midpoint to the reactor center. Unlike in previous analyses, IBD candidates in each baseline group are further categorized by their cluster's E_{rec} into 0.2 MeV wide bins, ranging from 0.8 to 7.4 MeV. This ensures that the prompt energy binning aligns with the final spectrum analysis described in Chapter 7. The choice for both L and E_{rec} binning

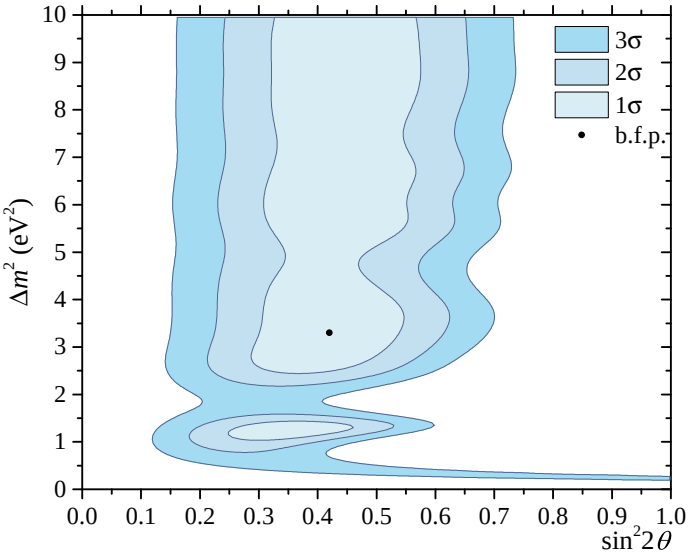


Figure 8.4: Allowed regions for two BEST results. The best-fit point is $\sin^2 2\theta = 0.42^{+0.15}_{-0.17}$, $\Delta m^2 = 3.3^{+\infty}_{-2.3}$ eV^2 and is indicated by a point. Source [88].

resulted from the optimization procedure described in the next Section 8.4.4. Fig. 8.5 illustrates the baseline assignment for each segment in every detector configuration across all DS periods.

8.2.1 Data inputs

Using the binning scheme described in the previous section, the PROSPECT data can be represented by the measured prompt spectra for each baseline, denoted as $M_{l,e}$, where:

$$M_e = \sum_{l=1}^{6} M_{l,e} \tag{8.2}$$

Figures 8.6–8.10 illustrate these distributions, showing the correlated and accidental IBD candidates during reactor-on and reactor-off periods, along with the background-subtracted IBD candidates for each data-taking period. These figures correspond to the $M_{l,e}$ distributions, analogous to Fig. 6.33, which presents the baseline-integrated M_e distributions. For the oscillation analysis, a total of 990 bins

are used: 5 data-taking periods, 6 baseline bins, and 33 reconstructed energy bins, resulting in $5 \times 6 \times 33$ bins.

Response matrices

In addition to the format in which the measured spectra are presented, a fundamental difference in this analysis is the method used to generate the response matrices, as described in Section 6.5. Unlike in the spectral shape analysis, the response matrices here are generated by treating each active detector segment in each period as an independent volume. As a result, a separate response matrix is generated for every active segment by simulating 10,000 random IBD vertices for monoenergetic antineutrinos with energies ranging from 1.8 MeV to 10.0 MeV in 0.1 MeV bins, using the PG4 framework, following the procedure outlined in Section 6.5. Considering the distribution of DE, SE, and blind segments for period 5, illustrated in Fig. 6.31, it is expected that the more SE and blind segments surrounding a DE segment, the poorer the energy response will be. This effect is demonstrated in Fig. 8.11, which shows the reconstructed prompt energy distributions for three different antineutrino energies obtained from the response matrices of segments 45, 90, and 138 in period 5. Segment 90 has the best response, while segment 45 has the worst.

A similar check can be performed by comparing the response of a single segment across different periods, as shown in Fig. 8.12. This figure demonstrates how changes in the distribution of DE, SE, and blind segments over time affect the response of an individual segment, specifically segment 45. It is evident that the energy response of segment 45 deteriorates over successive periods. By utilizing these response matrices for each segment in every period, both un-oscillated and oscillated spectra can be simulated accurately for each segment and subsequently for each baseline.

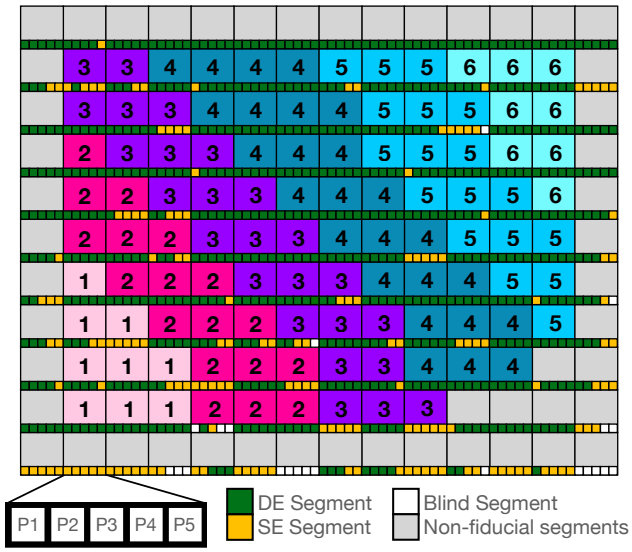


Figure 8.5: Baseline binning designation and operational status for each PROSPECT detector segment. The number and color of each segment represent its assigned baseline bin. In contrast, the colors of the small boxes within each segment indicate its operational status across the five DS periods (P1 to P5). Segments that are unnumbered and non-fiducial are displayed in light gray. Source [178].

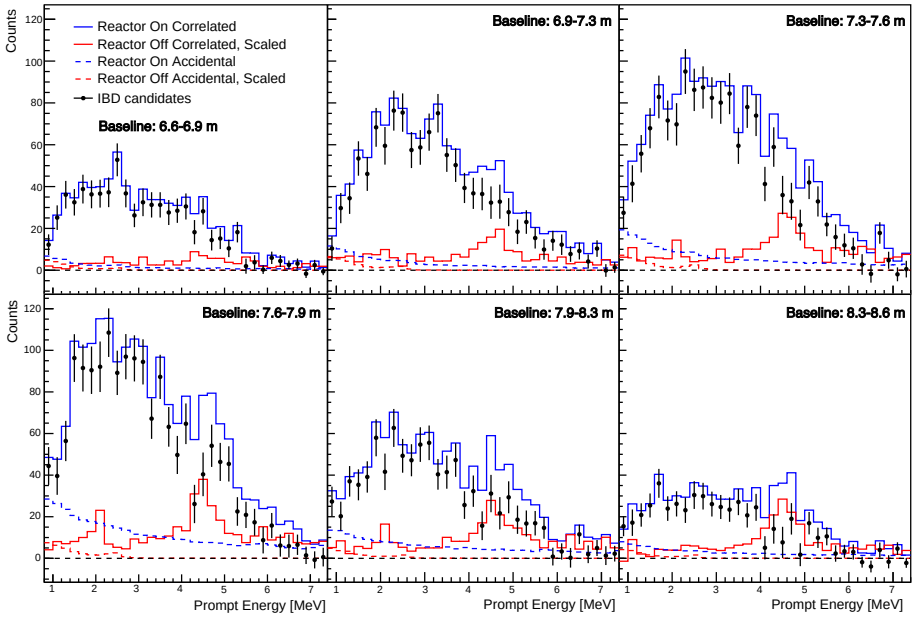


Figure 8.6: Period 1 - Reconstructed visible prompt energy E_{rec} (black) spectrum of IBD candidates (statistical error only), along with reactor-on (blue solid) and reactor-off (red solid) correlated candidates for each baseline bin.

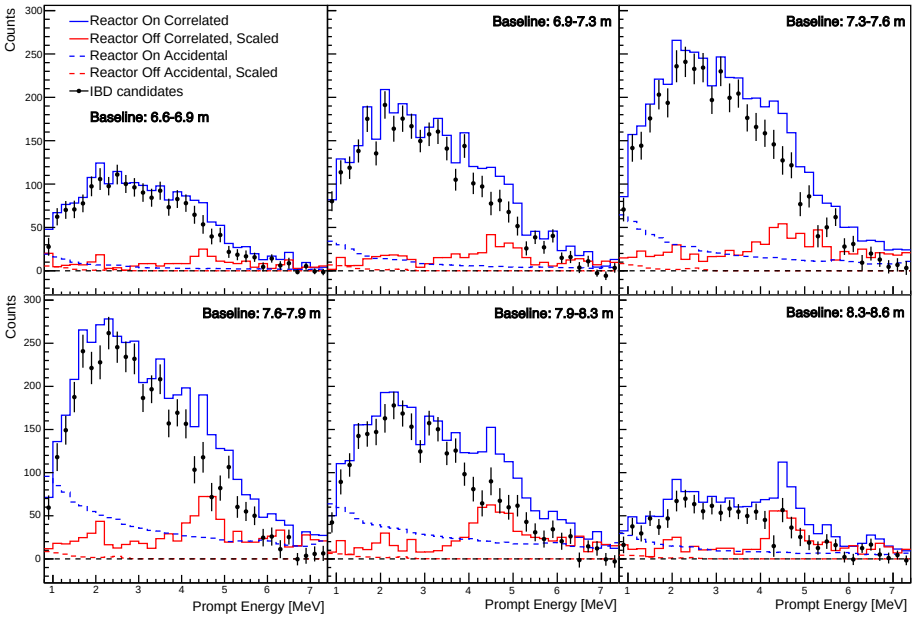


Figure 8.7: Period 2 - Reconstructed visible prompt energy E_{rec} (black) spectrum of IBD candidates (statistical error only), along with reactor-on (blue solid) and reactor-off (red solid) correlated candidates for each baseline bin.

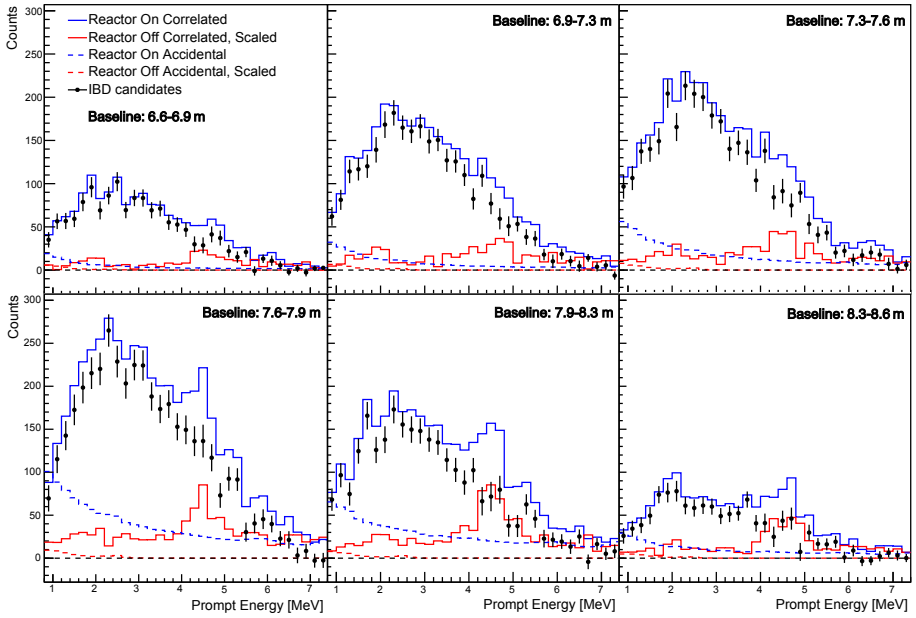


Figure 8.8: Period 3 - Reconstructed visible prompt energy E_{rec} (black) spectrum of IBD candidates (statistical error only), along with reactor-on (blue solid) and reactor-off (red solid) correlated candidates for each baseline bin.

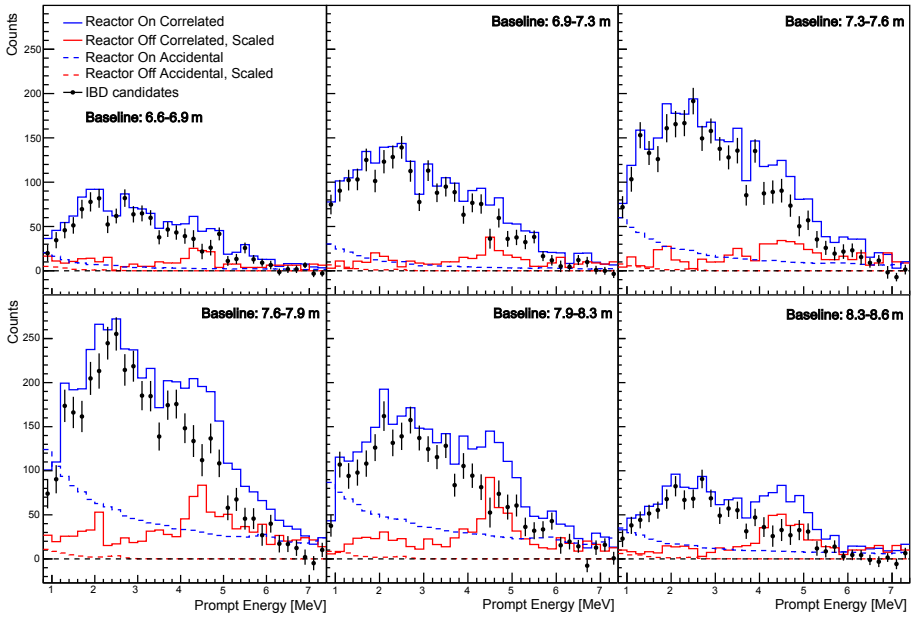


Figure 8.9: Period 4 - Reconstructed visible prompt energy E_{rec} (black) spectrum of IBD candidates (statistical error only), along with reactor-on (blue solid) and reactor-off (red solid) correlated candidates for each baseline bin.

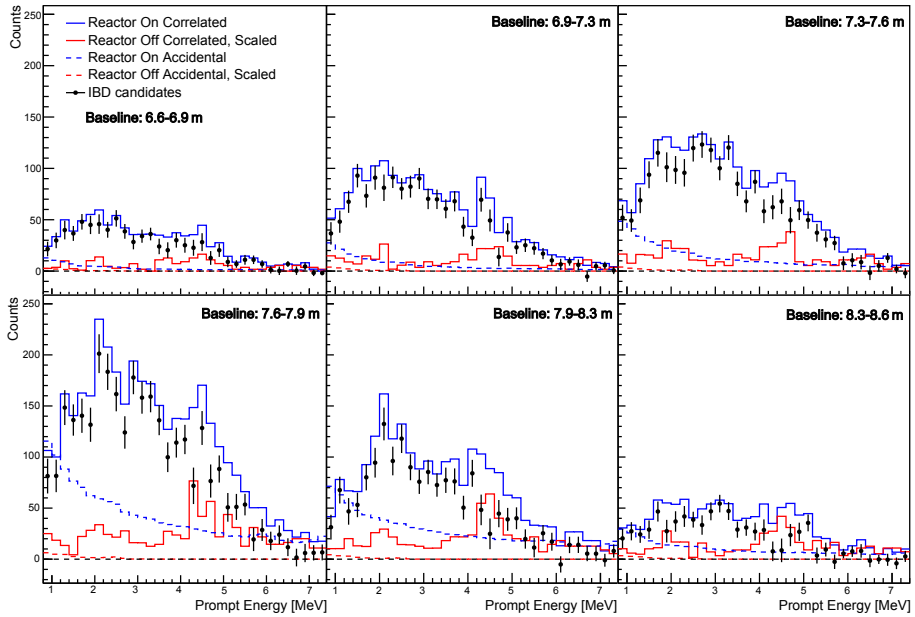


Figure 8.10: Period 5 - Reconstructed visible prompt energy E_{rec} (black) spectrum of IBD candidates (statistical error only), along with reactor-on (blue solid) and reactor-off (red solid) correlated candidates for each baseline bin .

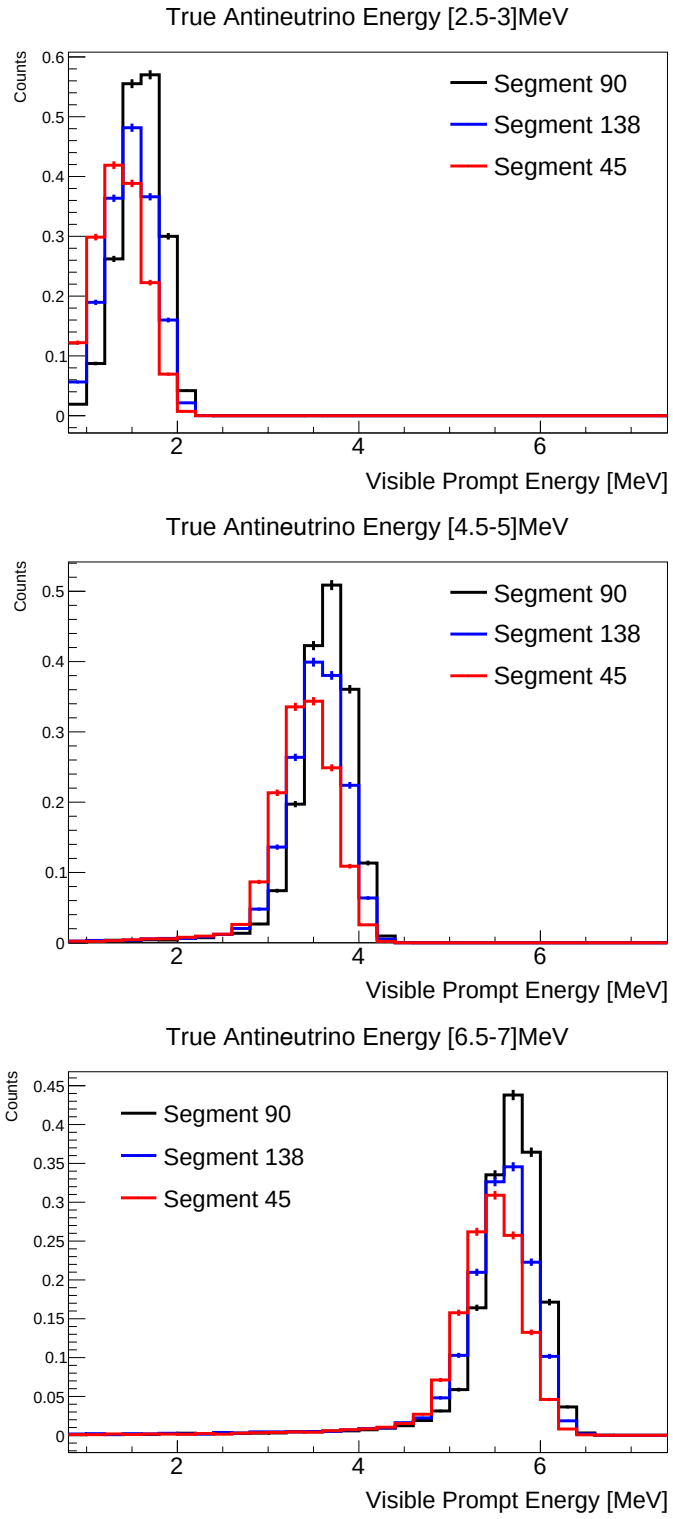


Figure 8.11: E_{rec} distributions obtained from three different monoenergetic neutrino simulations using the response matrices for segments 45, 90, and 138 in period 5. Segment 90 shows a better response overall, as more DE segments surround it compared to segments 45 and 138.

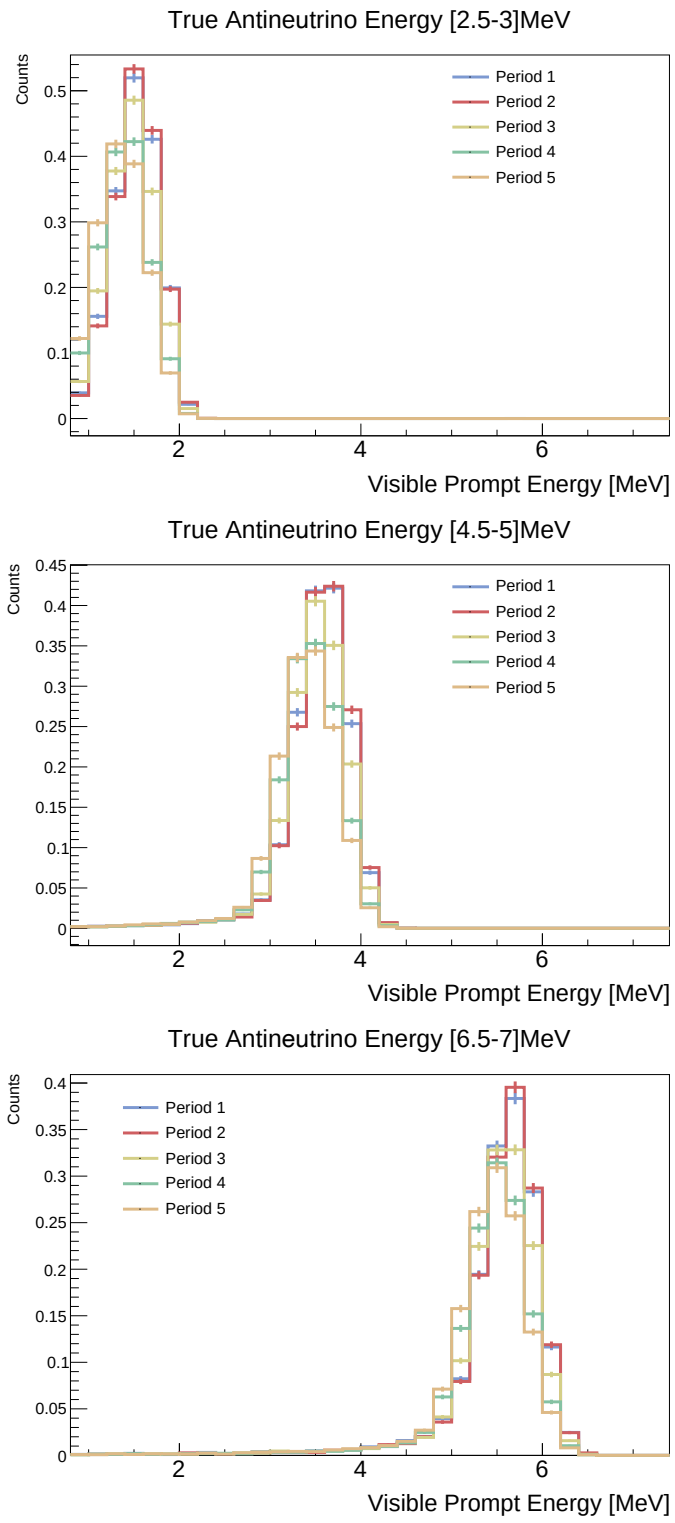


Figure 8.12: Energy response of segment 45 across different periods, showing the impact of surrounding DE, SE, and blind segments on its performance.

8.3 Generating predictions of un-oscillated and oscillated spectra

Rather than using the PG4 framework to generate simulated spectra, the oscillation analysis employs a standalone framework known as PROSPECT-CNP [153]. This framework handles the entire oscillation analysis, including the modeling of the HFIR reactor and the PROSPECT detector, generation of un-oscillated and oscillated prompt energy distributions per baseline ($P_{l,e}$), data input handling, statistical and systematic covariance matrix generation, data-model comparison, hypothesis testing, and the generation of sensitivity and exclusion contours.

Unlike the approach used by the PG4 framework, PROSPECT-CNP simulates the HFIR core as a finite-sized cylinder, accurately reflecting the dimensions described in Section 4.2. The PROSPECT detector is modeled as a rectangular prism with dimensions $(x, y, z) = (2044.7\text{ mm}, 1606.6\text{ mm}, 1176\text{ mm})$, subdivided into segments by imaginary boundaries based on a segment width of 14.605 cm. The detector is positioned at coordinates $(6.08721\text{ m}, 0\text{ m}, 5.08508\text{ m})$ relative to the reactor, with an azimuthal angle of 11.31°. This coordinate system corresponds to the one in Fig. 4.2, translated into cylindrical coordinates.

The generation of $P_{l,e}$ distributions begins with an event generator that simulates approximately 10^7 reaction points, representing the locations where neutrinos are produced within the reactor and the corresponding detection points where IBD interactions occur within the detector. To ensure consistency with the procedures for generating detector response matrices, the segment in which each simulated IBD interaction occurs is designated as the reconstructed IBD event's prompt segment, S_{rec}. While this method effectively disregards a potential source of worsened resolution in the true $\overline{\nu}_e$ baselines, this contribution is minimal compared to the position resolution smearing caused by the finite geometry of the reactor core and the L bin width.

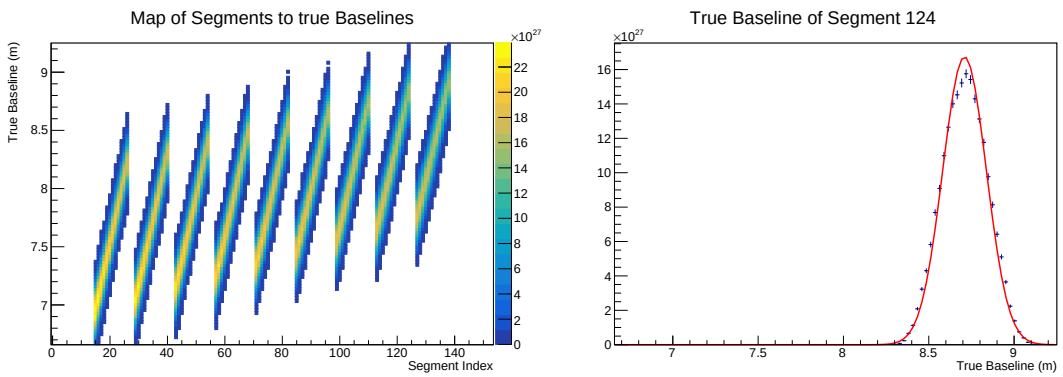


Figure 8.13: Left: Baseline coverage of each segment. Right: Baseline distribution of segment 124 fitted with a normal distribution.

Using the dimensions of the detector and the reactor core, the true baseline coverage for a detector segment i can be calculated as

$$L_{i,\text{true}} = W_{i,l} = \frac{1}{4\pi r^2} \frac{\rho_p \cdot V_{\text{det}}}{N_{\text{evt}}} \cdot P_{\text{reactor}} \cdot t_{\text{RxOn}}, \tag{8.3}$$

where $W_{i,l}$ is a position weight factor for each neutrino detection-reaction event. Here, r is the distance between the detection and reaction vertices, ρ_p is the proton density, V_{det} is the volume of the detector, P_{reactor} is the reactor thermal power, N_{evt} is the number of simulated events, and t_{RxOn} is the reactor-on livetime. Fig. 8.13 illustrates the effective baseline coverage for each active segment and the effective baseline covered by segment 124 during period 2.

Similar to the approach used in the spectral analysis, a reference un-oscillated model for the antineutrino spectrum was employed. Specifically, this analysis utilized the Daya Bay ^{235}U E_ν model [55], denoted as $\hat{s}$, with all non-fuel and non-equilibrium HFIR contributions, as detailed in Section 4.2.2, added to it. The model $\hat{s}$ was extrapolated to form an 82-bin E_ν spectrum spanning the energy range of 1.8–10 MeV, matching the binning for each response matrix. Using the position weight factor $W_{i,l}$ from Eq. 8.3, which accounts for the effective baseline coverage of each segment, the un-oscillated antineutrino energy distribution per segment ($P^{\text{Null}}_{\text{seg},E_\nu}$) can be expressed as:

$$P^{\text{Null}}_{\text{seg},E_\nu\{j,i\}} = \hat{s}_j \cdot \sum_{l=1}^{N_l} W_{i,l}, \tag{8.4}$$

where N_l represents the number of true baseline bins, illustrated on the y-axis of the left panel of Fig. 8.13. In this equation, i denotes the segment index, and j denotes the E_ν index. Fig. 8.14 shows the resulting un-oscillated P_{seg,E_ν} distribution for period 1, along with the modified Daya Bay model spectrum used as the reference, normalized to the N_{IBD} for period 1.

Before applying the detector response to generate prompt E_{rec} distributions for each segment, the true $\overline{\nu}_e$ energy distributions for IBD interactions in each segment can be modified to account for potential sterile neutrino oscillations. To simulate the oscillation effect for a given $(\sin^2 2\theta_{14}, \Delta m^2_{41})$ parameter pair, the oscillation probability in each segment is first calculated as a function of neutrino energy using Eq. 8.1.

$$P^{Osc}_{seg,E_\nu\{j,i\}} = \hat{s}_{\{j\}} \cdot \sum_{l=1}^{N_l} W_{\{i\},l} \sin^2\left(1.267\Delta m^2_{41}\frac{L_l}{E_\nu}\right) \tag{8.5}$$

The calculation of the neutrino oscillation probability depends on both the neutrino energy and the true baseline, as shown in Eq. 8.1. However, in a binned analysis, the discrete binning can obscure the oscillation signature, especially at high

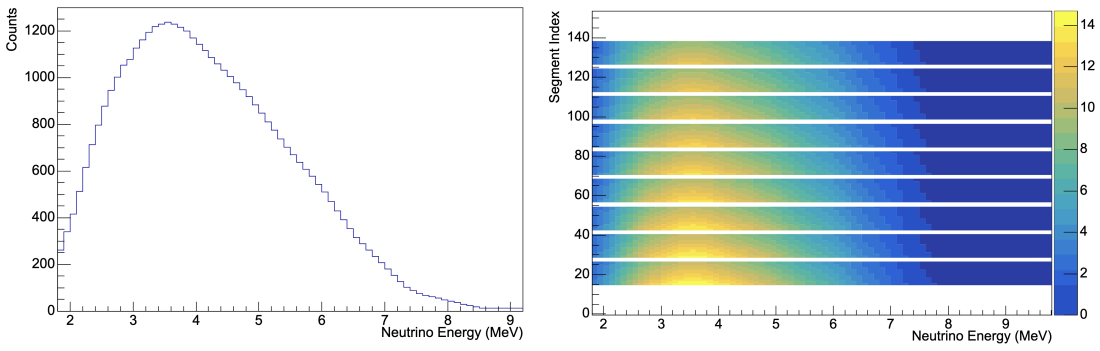


Figure 8.14: Left: Predicted antineutrino spectrum based on the Daya Bay ^{235}U reference spectrum, with HFIR contributions included. Right: Un-oscillated antineutrino energy predicted distributions for all DE segments in period 1.

oscillation frequencies. To mitigate the smearing effect introduced by finite baseline binning, the position weight factor for each segment, $W_{i,l}$, is incorporated. To address energy smearing, two methods are commonly used in the literature [**?**]: the bin-center method and the bin-edge method. The bin-center method uses the center of each bin as the neutrino energy, E_ν, whereas the bin-edge method considers the bin edges $[E^a, E^b]$. The bin-edge method provides a more accurate estimate when the oscillation frequency is comparable to the bin width, which was chosen for this analysis. The approximation of the neutrino oscillation frequency using the bin-edge method is given by Eq. 8.6.

$$\left\langle \sin^2\left(1.267\Delta m^2_{41}\frac{L}{E_\nu}\right)\right\rangle = 0.5 + \frac{\sin\left(1.267\frac{2\Delta m^2_{41}L}{E^b}\right) - \sin\left(1.267\frac{2\Delta m^2_{41}L}{E^a}\right)}{1.267\Delta m^2_{41}L\left(\frac{4}{E^a}-\frac{4}{E^b}\right)} \tag{8.6}$$

After properly correcting for both baseline and energy smearing effects, the resulting oscillated distribution, $P^{\text{Osc}}_{\text{seg},E_\nu\{j,i\}}$, based on the best-fit point reported by Neutrino-4, $(\sin^2 2\theta_{14}, \Delta m^2_{41}) = (0.36, 7.3\,\text{eV}^2)$ [190], is shown in Fig. 8.15.

Next, the response matrix for each detector segment is applied to both the un-oscillated and oscillated predictions to convert antineutrino energy into prompt

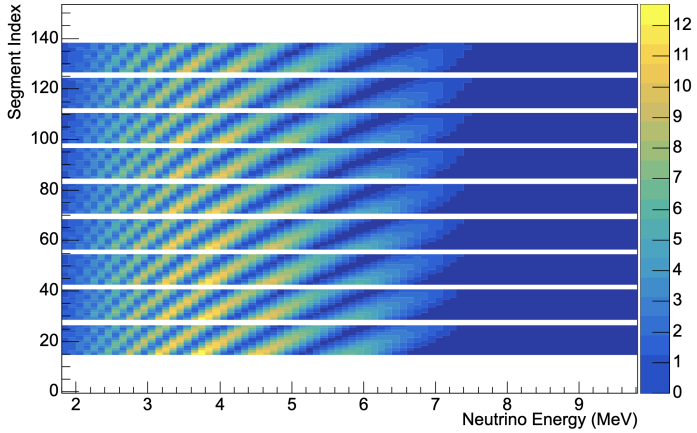


Figure 8.15: Oscillated antineutrino energy predicted distributions, based on Neutrino-4 best-fit point, for all DE segments in period 1.

energy, resulting in $P^{\text{Null/Osc}}_{\text{Seg},E_{\text{rec}}}$. Segment bins are then mapped into one of the six baseline bins according to the segment map shown in Fig. 8.5, producing the E_{rec} distributions per baseline: $P^{\text{Null}}_{L,E_{\text{rec}}}$ and $P^{\text{Osc}}_{L,E_{\text{rec}}}$. The final oscillated distribution, $P^{\text{Surv}}_{L,E_{\text{rec}}}$, is obtained by calculating the survival probability associated with the distortion dictated by a given pair of parameters, $(\Delta m^2_{41}, \sin^2 2\theta_{14})$, as follows:

$$P^{\text{Surv}}_{L,E_{\text{rec}}} = P^{\text{Null}}_{L,E_{\text{rec}}} - \sin^2 2\theta_{14} \cdot P^{\text{Osc}}_{L,E_{\text{rec}}}. \tag{8.7}$$

Both $P^{\text{Surv}}_{L,E_{\text{rec}}}$ and $P^{\text{Null}}_{L,E_{\text{rec}}}$ are then normalized to the integral of the background-subtracted IBD signal $M_{l,e}$ for each period. For the remainder of this chapter (and the next), $P^{\text{Null}}_{L,E_{\text{rec}}}$ distributions will be referred to as $P_{l,e}$, where:

$$P_e = \sum_{l=1}^{6} P_{l,e}. \tag{8.8}$$

The distinction between Null and oscillated distributions will be made in the text. Figures 8.16–8.20 illustrate the measured background-subtracted prompt $M_{l,e}$ distributions for all DS periods, along with the Null and Neutrino-4's best-fit point predicted $P_{l,e}$ distributions.

To minimize the impact of uncertainties related to the shape and normalization of the reference model on the oscillation analysis, PROSPECT's approach focuses on relative comparisons between the measured prompt E_{rec} distributions. The $M_{l,e}$ distributions are compared to the normalized predicted per-baseline spectra, represented as $M_e \cdot \frac{P_{l,e}}{P_e}$. This approach helps reduce the influence of the reactor $\overline{\nu}_e$ model and adjusts for energy response differences across the baseline bins.

The ratios of these two quantities for each baseline and period are shown in Figures 8.21–8.25. In the absence of short-baseline oscillations, M_e will produce a flat ratio at unity. However, if oscillation effects are present in $M_{l,e}$ and M_e, this ratio will deviate from unity. This behavior is also illustrated in Figures 8.21–8.25, where, instead of representing measured data, $M_{l,e}$ and M_e correspond to Asimov unfluctuated predictions based on the Neutrino-4 best-fit point, allowing for comparisons

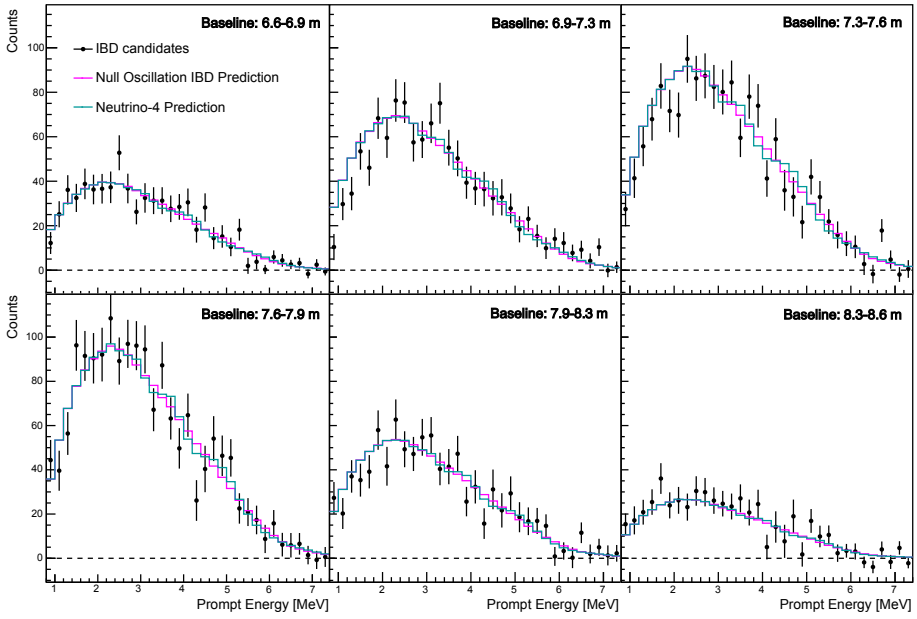


Figure 8.16: Period 1 - Reconstructed visible prompt energy E_{rec} distributions (black) of IBD candidates per baseline bin $M_{l,e}$. Also shown are the predicted prompt spectra per baseline $P_{l,e}$ for the null oscillation case (magenta) and an oscillation scenario predicted by the Neutrino-4 best-fit point (cyan).

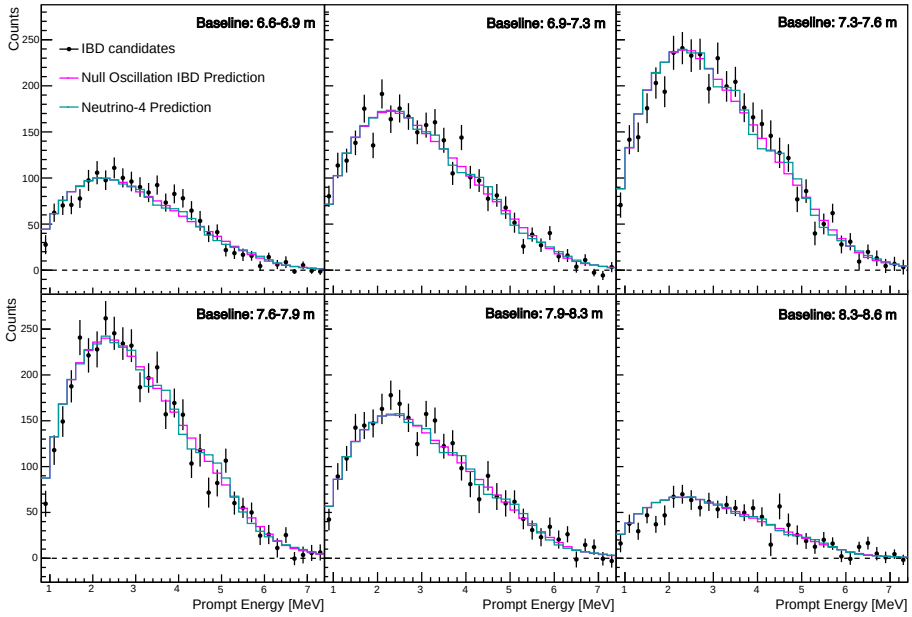


Figure 8.17: Period 2 - Reconstructed visible prompt energy E_{rec} distributions (black) of IBD candidates per baseline bin $M_{l,e}$. Also shown are the predicted prompt spectra per baseline $P_{l,e}$ for the null oscillation case (magenta) and an oscillation scenario predicted by the Neutrino-4 best-fit point (cyan).

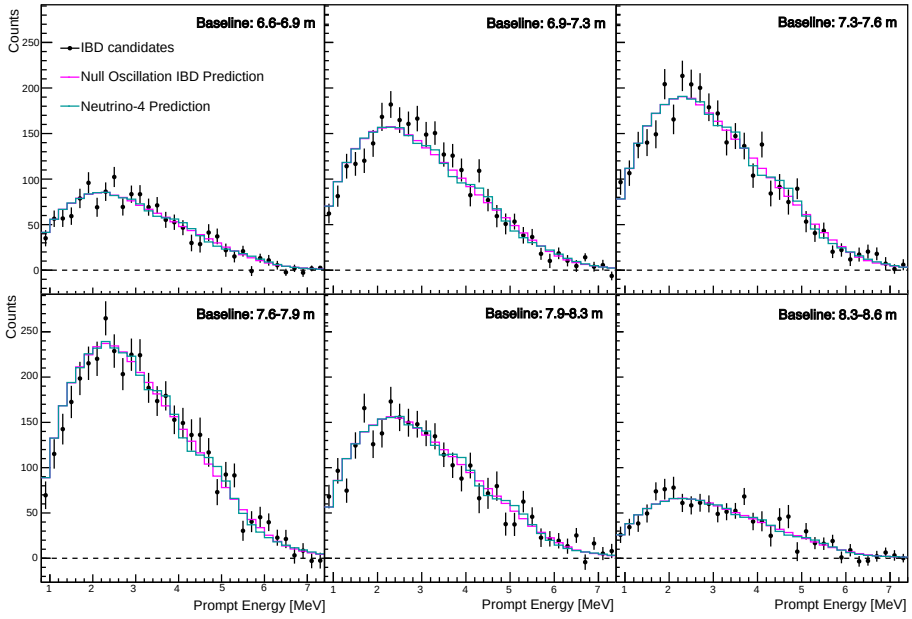


Figure 8.18: Period 3 - Reconstructed visible prompt energy E_{rec} distributions (black) of IBD candidates per baseline bin $M_{l,e}$. Also shown are the predicted prompt spectra per baseline $P_{l,e}$ for the null oscillation case (magenta) and an oscillation scenario predicted by the Neutrino-4 best-fit point (cyan).

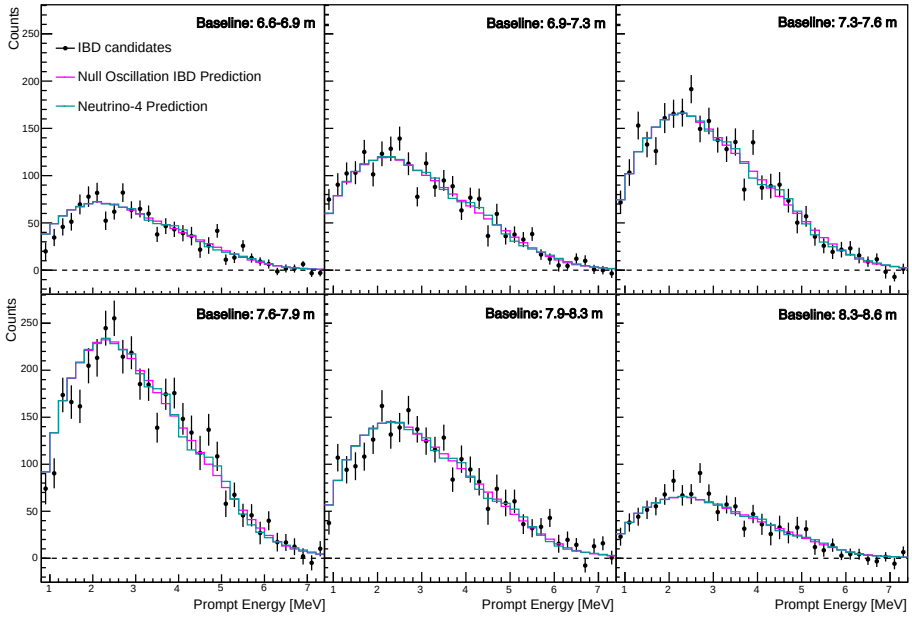


Figure 8.19: Period 4 - Reconstructed visible prompt energy E_{rec} distributions (black) of IBD candidates per baseline bin $M_{l,e}$. Also shown are the predicted prompt spectra per baseline $P_{l,e}$ for the null oscillation case (magenta) and an oscillation scenario predicted by the Neutrino-4 best-fit point (cyan).

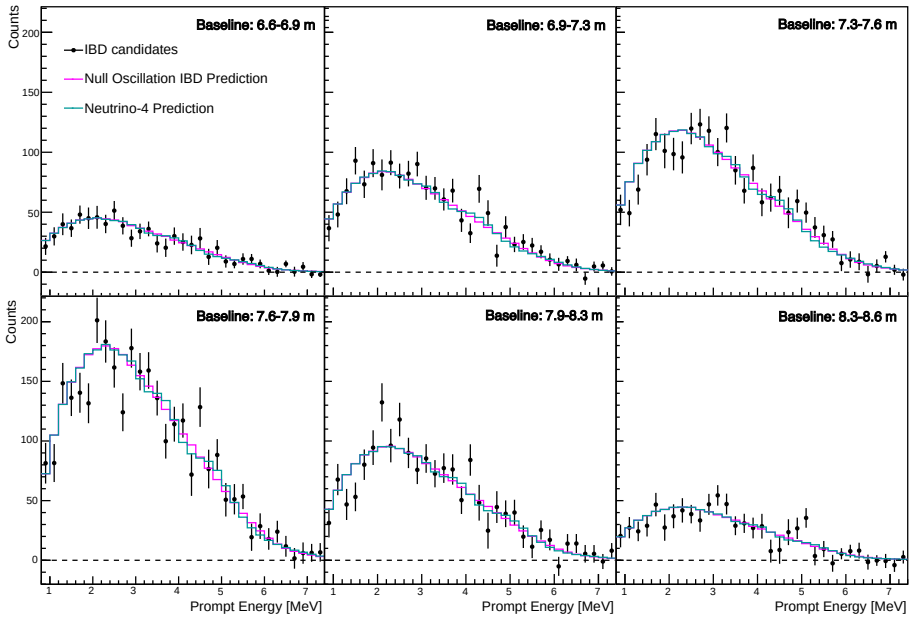


Figure 8.20: Period 5 - Reconstructed visible prompt energy E_{rec} distributions (black) of IBD candidates per baseline bin $M_{l,e}$. Also shown are the predicted prompt spectra per baseline $P_{l,e}$ for the null oscillation case (magenta) and an oscillation scenario predicted by the Neutrino-4 best-fit point (cyan).

between oscillated and un-oscillated predictions. Upon examining the measured ratios in Figures 8.21–8.25, there are no clear indications of non-flat trends that would suggest the presence of large-amplitude sterile neutrino oscillations. However, a proper statistical analysis is required to make quantitative statements about the absence or presence of oscillations in the data.

8.3.1 Visualizing data in L/$E_{\overline{\nu}}$ space

Neutrino oscillations can be visualized by grouping IBD data into bins of common L/E_ν. While a full mapping from E_{rec} to E_ν would require a comprehensive per-baseline unfolding procedure, this analysis instead follows the approach of Ref. [59], where the mapping is performed to a common bin of average neutrino energy, $\langle E_\nu \rangle$. $\langle E_\nu \rangle$, is determined for each E_{rec} bin in each period using the segment-integrated energy response matrix R_{pros} for that period. This allows each prompt energy bin, E_{rec}, to be mapped to a corresponding $\langle E_\nu \rangle$ bin as follows:

$$\langle E_\nu \rangle = \frac{1}{N_\nu} \sum_{\nu=1}^{82} \hat{s}_\nu \cdot R_{\text{pros},\{\nu,e\}}, \tag{8.9}$$

where N_ν is the total number of neutrino energy bins in the response matrix $R_{\nu,e}$ over the range 1.8–10 MeV, and $\hat{s}$ denotes the reference model. This method results in a one-to-one mapping from the 33 E_{rec} values to their corresponding $\langle E_\nu \rangle$ values.

Fig. 8.26 shows the results of this mapping for all periods. As illustrated in the right panel, variations in detector response introduce small differences in the E_{rec} to $\langle E_\nu \rangle$ mapping across different periods. To maintain a consistent binning definition when transitioning from $M_{l,e}$ to a measured per-baseline average neutrino energy $M_{l,\langle E_\nu \rangle}$, the lowest $\langle E_\nu \rangle$ value from period 2 was chosen as the lower bin-edge, and the highest $\langle E_\nu \rangle$ value from period 5 as the upper bin-edge. This resulted in a binning scheme of 33 bins spanning a range of $\langle E_\nu \rangle$ values from 2.32 to 8.39 MeV. With this binning definition, both $M_{l,\langle E_\nu \rangle}$ and the relativized $P_{l,\langle E_\nu \rangle}$ can be constructed for each

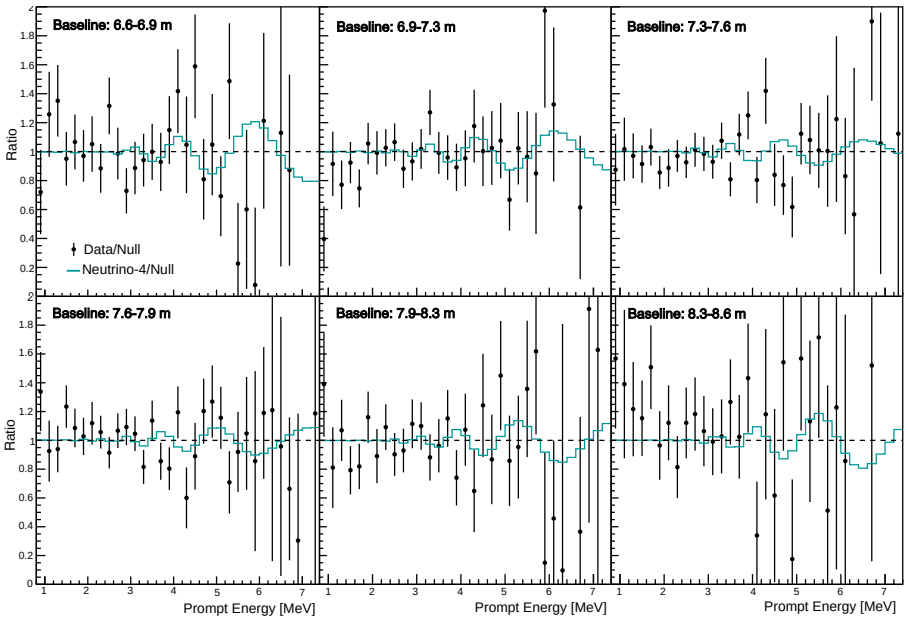


Figure 8.21: Period 1: Measured prompt E_{rec} spectrum ratios ($\frac{M_{l,e}}{M_e}$, corrected by $\frac{P_{l,e}}{P_e}$) for the six baseline bins defined in Figure 8.5. Predicted ratios in the presence of sterile neutrino oscillations, corresponding to the best-fit point of Neutrino-4, are shown as solid cyan lines. In the absence of oscillations, the predicted ratio is unity for all energy-baseline bins. Error bars represent statistical uncertainties.

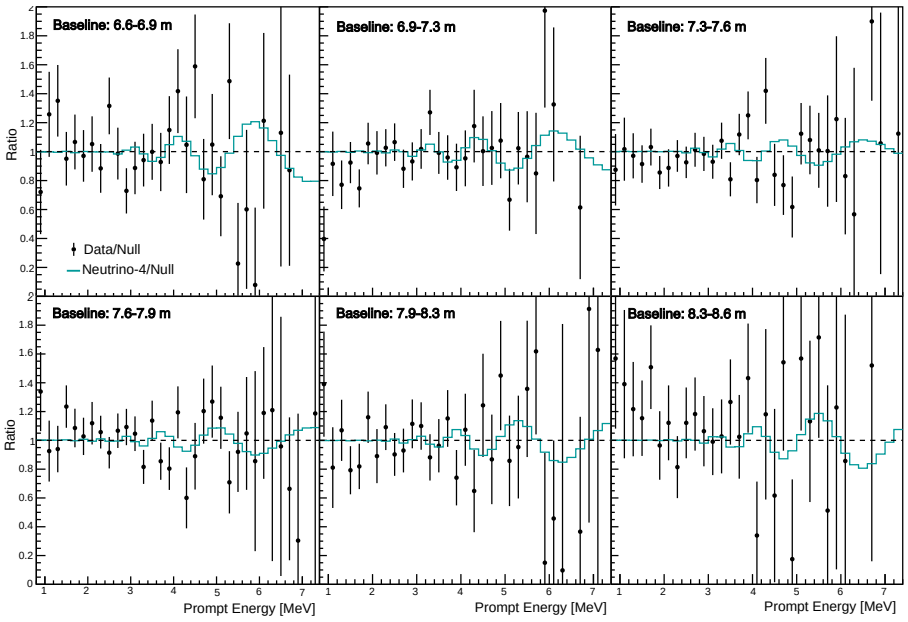


Figure 8.22: Period 2: Measured prompt E_{rec} spectrum ratios ($\frac{M_{l,e}}{M_e}$, corrected by $\frac{P_{l,e}}{P_e}$) for the six baseline bins defined in Figure 8.5. Predicted ratios in the presence of sterile neutrino oscillations, corresponding to the best-fit point of Neutrino-4, are shown as solid cyan lines. In the absence of oscillations, the predicted ratio is unity for all energy-baseline bins. Error bars represent statistical uncertainties.

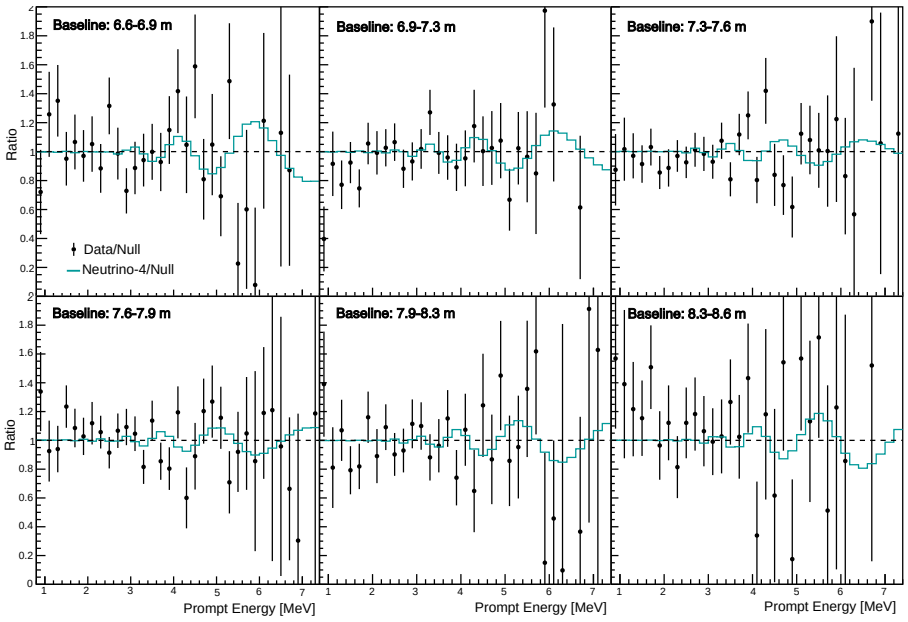


Figure 8.23: Period 3: Measured prompt E_{rec} spectrum ratios ($\frac{M_{l,e}}{M_e}$, corrected by $\frac{P_{l,e}}{P_e}$) for the six baseline bins defined in Figure 8.5. Predicted ratios in the presence of sterile neutrino oscillations, corresponding to the best-fit point of Neutrino-4, are shown as solid cyan lines. In the absence of oscillations, the predicted ratio is unity for all energy-baseline bins. Error bars represent statistical uncertainties.

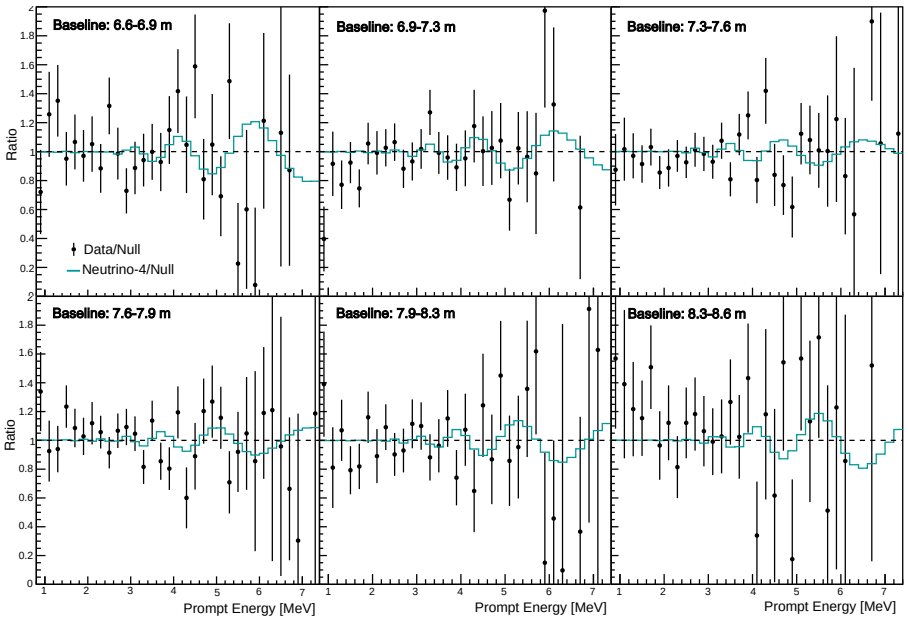


Figure 8.24: Period 4: Measured prompt E_{rec} spectrum ratios ($\frac{M_{l,e}}{M_e}$, corrected by $\frac{P_{l,e}}{P_e}$) for the six baseline bins defined in Figure 8.5. Predicted ratios in the presence of sterile neutrino oscillations, corresponding to the best-fit point of Neutrino-4, are shown as solid cyan lines. In the absence of oscillations, the predicted ratio is unity for all energy-baseline bins. Error bars represent statistical uncertainties.

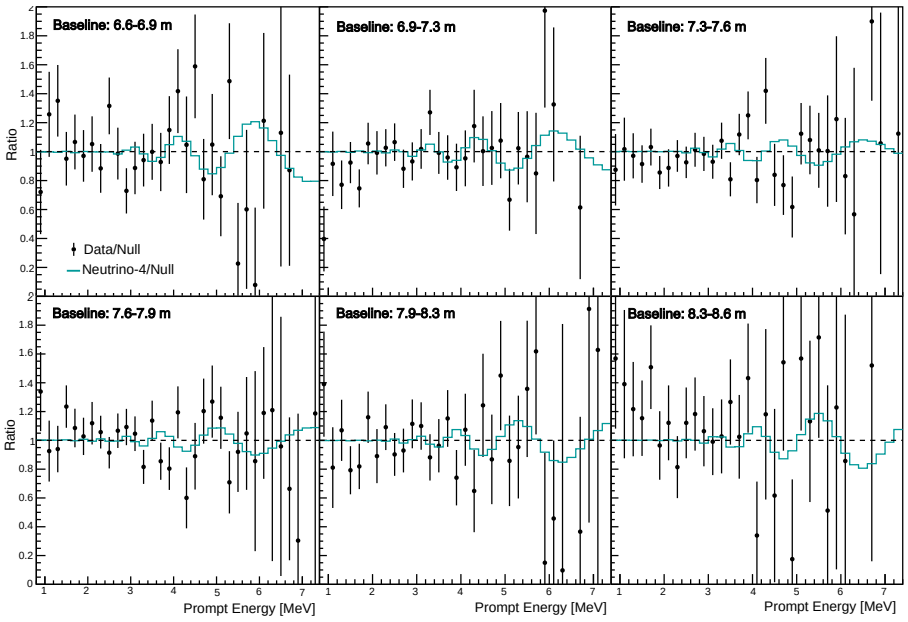


Figure 8.25: Period 5: Measured prompt E_{rec} spectrum ratios ($\frac{M_{l,e}}{M_e}$, corrected by $\frac{P_{l,e}}{P_e}$) for the six baseline bins defined in Figure 8.5. Predicted ratios in the presence of sterile neutrino oscillations, corresponding to the best-fit point of Neutrino-4, are shown as solid cyan lines. In the absence of oscillations, the predicted ratio is unity for all energy-baseline bins. Error bars represent statistical uncertainties.

period as:

$$M_{l,\langle E_\nu\rangle} = \sum_{l=1}^{6}\sum_{e=1}^{33} M_{l,e} \text{ and } P_{l,\langle E_\nu\rangle}\cdot\left(\frac{M_{\langle E_\nu\rangle}}{P_{\langle E_\nu\rangle}}\right) = \sum_{l=1}^{6}\sum_{e=1}^{33} P_{l,e}\left(\frac{M_e}{P_e}\right). \tag{8.10}$$

The final period-integrated measured $M_{l,\langle E_\nu\rangle}$ and $M_{l,e}$ distributions are shown in Fig. 8.27.

Once total distributions for both $M_{l,\langle E_\nu\rangle}$ and $P_{l,\langle E_\nu\rangle}\cdot\left(\frac{M_{\langle E_\nu\rangle}}{P_{\langle E_\nu\rangle}}\right)$ have been generated, $L/\langle E_\nu\rangle$ distributions can be sampled from them. The effective range of these distributions is [0.83, 3.84] m/MeV, where 0.83 m/MeV is the ratio of the lowest L to the highest $\langle E_\nu\rangle$ value, and 3.84 m/MeV is the ratio of the highest L to the lowest $\langle E_\nu\rangle$ value. For a given pair $i = (l, \langle E_\nu\rangle)$ of L and $\langle E_\nu\rangle$ values, each bin in the total $L/\langle E_\nu\rangle$ distribution can be defined as:

$$\left(\frac{L}{\langle E_\nu\rangle}\right)_i = \frac{L_l}{\langle E_\nu\rangle_{\langle\nu\rangle}} M_{l,\langle E_\nu\rangle}. \tag{8.11}$$

Fig. 8.28 presents the background and measured IBD signal for all 990 (L, E_{rec}) bins, regrouped into bins of common $L/\langle E_\nu\rangle$. The structure observed in both the signal and background in Fig. 8.28 results from the interplay between the shape of the E_ν spectrum, the (L, E_{rec}) binning, and the geometry of the detector. This representation of the full dataset demonstrates meaningful statistical sensitivity

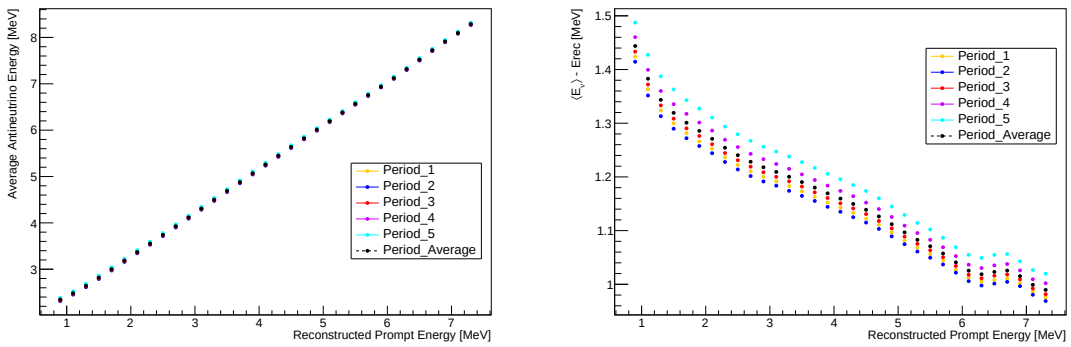


Figure 8.26: Left: Relationship between each E_{rec} and the corresponding $\langle E_\nu\rangle$ for each period. Right: Differences in the E_{rec} to $\langle E_\nu\rangle$ mapping across periods.

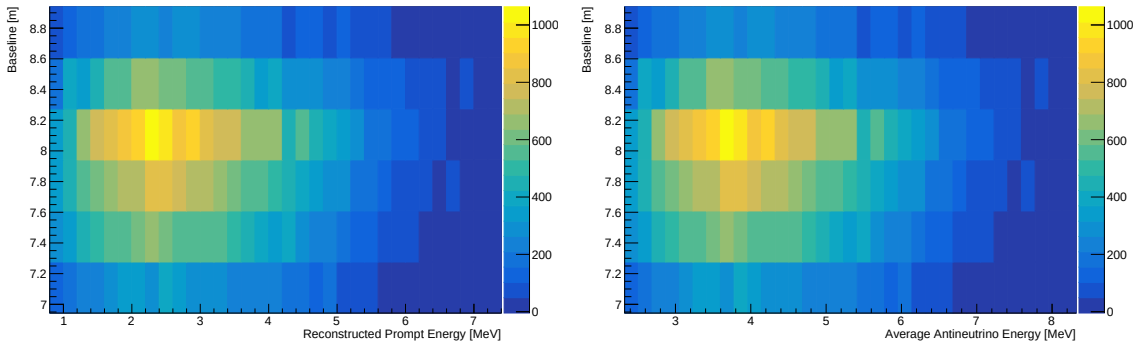


Figure 8.27: Left: Period-integrated measured $M_{l,e}$ distributions. Right: Period-integrated measured $M_{l,\langle E_\nu \rangle}$ distributions after applying the mapping shown in Fig. 8.26.

above 1.0 m/MeV, with the average signal-to-background ratio improving from approximately 2 below 1.5 m/MeV to over 6 in the range of 1.5–2.75 m/MeV. Correlated cosmogenic events constitute the largest background to $M_{l,e}$ at the lowest $L/\langle E_\nu \rangle$ (corresponding to the highest E_{rec}), while accidental backgrounds dominate at higher $L/\langle E_\nu \rangle$ (corresponding to lower E_{rec}). The $L/\langle E_\nu \rangle$ distribution based on the relativized Null oscillation prediction, $P_{l,e}$, is also shown in Fig. 8.28.

Un-oscillated and oscillated behaviors can be visualized in $L/\langle E_\nu \rangle$ space by taking the ratio of the distributions $\left(\frac{L}{\langle E_\nu \rangle}\right)_{\text{IBD}}$ to $\left(\frac{L}{\langle E_\nu \rangle}\right)_{\text{Null}}$, as shown in Fig. 8.29. Any deviation of this ratio from unity indicates L-dependent variations in the observed energy spectrum within PROSPECT, rather than L-independent deviations from a reference E_ν model. Fig. 8.29 also shows the predicted ratio for fluctuation-free Asimov $M_{l,e}$ datasets based on the best-fit point reported by Neutrino-4. This ratio, denoted as $\left(\frac{L}{\langle E_\nu \rangle}\right)_{N4}$ to $\left(\frac{L}{\langle E_\nu \rangle}\right)_{\text{Null}}$, allows for comparisons between the predicted and Null oscillation scenarios.

It is important to note that while a non-zero θ_{14} induces $L/\langle E_\nu \rangle$ oscillations in $M_{l,e}$, it also affects the applied $\frac{M_e}{P_e}$ factor. As a result, an $L/\langle E_\nu \rangle$ representation that aggregates multiple (L, E_{rec}) bins—each with different $\frac{M_e}{P_e}$ values—will exhibit suppressed oscillation features compared to the original (L, E_{rec}) representation. This suppression effect is minimal for oscillation wavelengths shorter than the detector size,

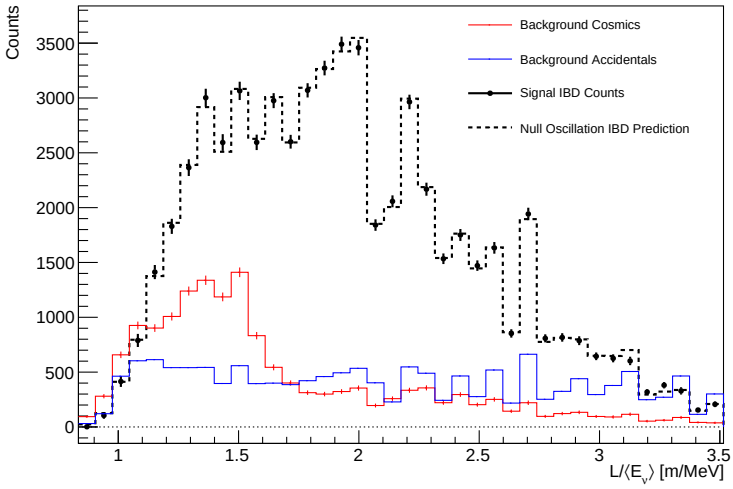


Figure 8.28: The $L/\langle E_\nu \rangle$ spectrum of background-subtracted IBD signals (black points) alongside the estimated correlated (solid red) and accidental (solid blue) backgrounds during PROSPECT-I reactor-on periods. The predicted IBD signal for the null oscillation scenario is shown as a dashed black line. Error bars represent 1σ statistical uncertainties. Source [178].

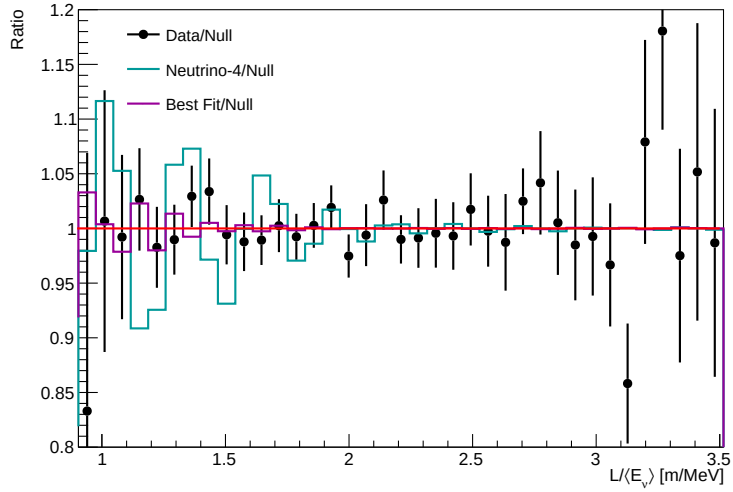


Figure 8.29: Ratio of $L/\langle E_\nu \rangle$ features between the PROSPECT IBD signal and its null oscillation prediction. As detailed in the text, the predicted $\langle E_\nu \rangle$ spectra are adjusted by the ratio of the detector-integrated measured to predicted spectra, $\left(\frac{\mathrm{M}_e}{\mathrm{P}_e}\right) \mathrm{P}_{l,e}$. Error bars represent the statistical uncertainty of the measured IBD spectrum, $\mathrm{M}_{l,e}$. Also shown are the expected ratios from oscillations at the best-fit points of the PROSPECT data (magenta line) and Neutrino-4 (blue line). Source [178].

as is the case for Neutrino-4's most favored oscillation parameters, where oscillatory features are distinguishable below 2.5 m/MeV. At higher $L/\langle E_\nu \rangle$ values, the damping is primarily due to energy smearing caused by IBD positron and annihilation gamma energy leakage into non-active detector regions and, to a lesser extent, by baseline smearing due to the finite size of the reactor.

Based on Fig. 8.29, the measured data appears to be qualitatively consistent with the Null hypothesis of no oscillations. It is important to emphasize that the $L/\langle E_\nu \rangle$ representation is only intended for visualization. All inputs required for the statistical analysis, including those needed to perform the fit for sterile neutrino searches (as described in the next section), are based on E_{rec} per baseline distributions, specifically $M_{l,e}$ and $P_{l,e}$.

8.4 Strategy for sterile neutrino search

Previous sections have described the datasets that serve as inputs for the final multi-period oscillation analysis. Although visual inspection of Figures 8.21-8.29 suggests that the measured data may favor the Null oscillation hypothesis, a rigorous statistical analysis is necessary to provide quantitative statements about this observation. To test for the possible existence of sterile neutrino oscillations, the measured $M_{l,e}$ distributions are quantitatively compared to the relativized predicted spectra, $M_e \frac{P_{l,e}}{P_e}$, in the presence of oscillation effects in $P_{l,e}$ and P_e, governed by the parameters Δm^2_{41} and $\sin^2 2\theta_{ee}$. This comparison is performed using a covariance matrix-based χ^2 test statistic, as described in Section A.1, of the form:

$$\chi^2 = \mathbf{\Delta}^{\mathrm{T}} \mathrm{V}_{\mathrm{tot}}^{-1} \mathbf{\Delta}, \tag{8.12}$$

where, in contrast to the spectral analysis, $\mathbf{\Delta}$ is a 990-element vector representing the data-prediction agreement in per-baseline E_{rec} spectra, with each period contributing

198 elements:

$$\Delta_{l,e} = M_{l,e} - M_e \frac{P_{l,e}}{P_e}. \tag{8.13}$$

Statistical and systematic uncertainties, along with their correlations between energy bins, are incorporated into Eq. 8.12 using the covariance matrix V_{tot}. This matrix is constructed as the sum of the individual statistical and systematic matrices, V_{stat} and V_{sys}, similar to the approach used in the spectrum analysis. However, the covariance matrices for the oscillation analysis differ because they also include correlations between baseline bins and between energy bins and data periods. As a result, each cumulative covariance matrix is a 990x990 matrix that spans the entire baseline-prompt energy phase space. The following sections describe the different statistical and systematic uncertainties that impact the oscillation analysis.

8.4.1 Statistical uncertainties

A key component of the final sterile neutrino analysis is the implementation of a new statistical method, the Combined Neyman-Pearson (CNP) approach [153], which reduces biases introduced by bins with low statistics. Unlike previous analyses that used uneven baseline binning to ensure equal statistics across all bins, the CNP method allows for an even binning scheme in both baseline and energy. The CNP χ^2 test is defined as a linear combination of the Neyman [176] and Pearson [186] χ^2 test statistics:

$$\chi^2_{\text{CNP}} = \frac{1}{3}\left(\chi^2_{\text{Neyman}} + 2\chi^2_{\text{Pearson}}\right). \tag{8.14}$$

Using Eq. 8.12, the statistical uncertainty for the CNP method can be expressed in terms of covariance matrices as:

$$\begin{aligned}\chi^2_{\text{CNP}} &= \frac{1}{3}\left(\chi^2_{\text{Neyman}} + 2\chi^2_{\text{Pearson}}\right) \\ &= \boldsymbol{\Delta}^T \left(\frac{1}{3}V_{\text{Neyman}} + \frac{2}{3}V_{\text{Pearson}} + V_{\text{sys}}\right)^{-1} \boldsymbol{\Delta},\end{aligned} \tag{8.15}$$

where V_{Neyman} and V_{Pearson} represent the Neyman and Pearson statistical uncertainty contributions, respectively, and V_{sys} is the total systematic covariance matrix.

As a result, the total statistical covariance matrix for the CNP method is defined as $V_{\text{stat}} = \frac{1}{3}V_{\text{Neyman}} + \frac{2}{3}V_{\text{Pearson}}$. A full derivation of both Neyman and Pearson uncertainties for a relativized analysis is provided in Section A.3, resulting in:

$$\sigma^2_{\text{Neyman}}\left(M_{l,e} - \frac{M_e}{P_e}P_{l,e}\right) = (1-2k)\cdot\sigma^2(M_{l,e}) + k^2\cdot\sigma^2(M_e), \tag{8.16}$$

$$\sigma^2_{\text{Pearson}}\left(M_{l,e} - \frac{M_e}{P_e}P_{l,e}\right) \approx M_e^2\cdot k^2\left(\left(\frac{\sigma(P_{l,e})}{P_{l,e}}\right)^2 + \left(\frac{\sigma(P_e)}{P_e}\right)^2 - 2\frac{\sigma^2(P_{l,e})}{P_{l,e}P_e}\right), \tag{8.17}$$

where $k = \frac{P_{l,e}}{P_e}$. Inserting these expressions into Eq. 8.15 provides the final covariance-based χ^2_{CNP} test. Additionally, it is important to note that accidental and cosmogenic uncertainties from reactor on-off subtraction are incorporated into the uncertainty of the un-oscillated Asimov dataset $P_{l,e}$ when constructing the total statistical covariance matrix, as described in Eq. 8.20:

$$\sigma^2(P_{l,e}) = \sigma^2_{\text{IBD}} \tag{8.18}$$

$$= \sigma^2_{\text{On}} + \sigma^2_{\text{On,acc}} + \left(\frac{t_{\text{On}}}{t_{\text{Off}}}\right)^2\left(\sigma^2_{\text{Off}} + \sigma^2_{\text{Off,acc}}\right) \tag{8.19}$$

$$= \left(N_{\text{On}} + (\alpha_{\text{acc}}\alpha_{\text{dt}})^2 N_{\text{On,acc}}\right) + \left(\frac{t_{\text{On}}}{t_{\text{Off}}}\right)^2\alpha^2_{\text{atm}}\left(N_{\text{Off}} + (\alpha_{\text{acc}}\alpha_{\text{dt}})^2 N_{\text{Off,acc}}\right) \tag{8.20}$$

Statistical uncertainties, represented by V_{stat}, are primarily driven by reactor-on IBD candidates and the subtracted cosmogenic background estimate based on the reactor-off IBD candidate dataset. The subtracted accidental backgrounds during reactor-on and reactor-off periods contribute minimally to the statistical uncertainty due to the large offset time window used to determine them. Uncorrelated statistical

uncertainties from each dataset, which form the diagonal elements of V_{stat}, are mainly determined by a combination of both Neyman and Poisson errors for each (l, e) bin, given the presence of the relativization factor $\left(\frac{M_e}{P_e}\right)$ applied to the prediction $P_{l,e}$. Additionally, since each $M_{l,e}$ is a subset of the baseline-integrated spectrum M_e, correlations in the statistical uncertainties of $\Delta_{l,e}$ will exist between different l, leading to off-diagonal contributions in V_{stat}. Fig. 8.30 illustrates the total V_{stat} used in the analysis.

8.4.2 Systematic uncertainties

As mentioned earlier, the oscillation analysis shares most of the systematic uncertainties included in the spectrum analysis (see Section 7.2.3). The main difference is that the oscillation analysis considers energy, baseline, and period correlations for each systematic uncertainty. One systematic uncertainty not included in the spectrum analysis is a relative signal normalization uncertainty, which accounts for variations in volume and efficiency between different baseline bins, as well as a baseline uncertainty related to the precise determination of the distance between the reactor core and each detector segment. Toy MC $P_{l,e}$ distributions for baseline and relative signal normalization were generated by analytically adjusting the Null $P_{l,e}$ prediction. Table 8.1 summarizes the systematic uncertainties used in the oscillation analysis and their corresponding uncertainty values, nominal values, and correlation assignments between baseline and energy bins.

A covariance matrix for each systematic uncertainty was generated using a method similar to that employed in the spectrum analysis, involving the creation and characterization of fluctuated Asimov datasets (see Section 7.2.3) and following the procedure outlined in Section A.1.1. In addition, signal and detector response systematics are treated as correlated across periods, while background systematics are considered uncorrelated, consistent with the approach taken in the spectrum analysis. A key difference from the spectrum analysis is that each systematic covariance matrix

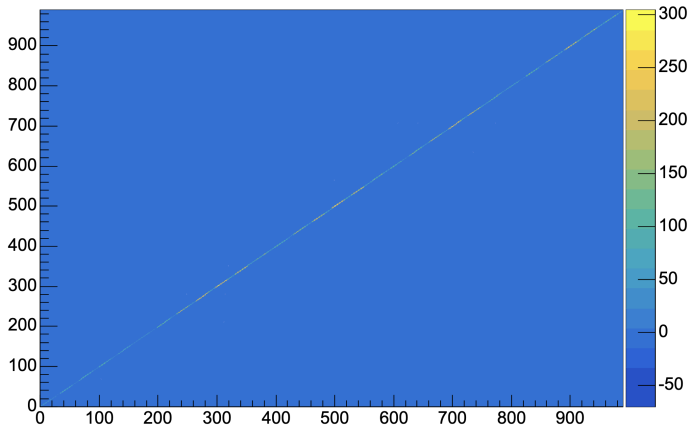


Figure 8.30: Total statistical covariance matrix used for the oscillation analysis, computed using the CNP formalism.

Table 8.1: Summary of systematic uncertainties taken into account in the oscillation systematic covariance matrix V_{sys}. Where applicable, nominal parameter values are provided. Source [70].

Parameter	Nominal Value	Uncertainty	Correlations
Absolute background normalization	-	1.0%	Correlated between energies and baselines
Absolute n-H peak normalization	-	3.0%	Correlated between energies and baselines
Relative signal normalization	-	5%	Correlated between energies
Baseline uncertainty	-	10 cm	Correlated between energies and baselines
First-order Birks constant	0.132 MeV/cm	0.004 MeV/cm	Correlated between baselines
Second-order Birks constant	0.023 MeV/cm	0.004 MeV/cm	Correlated between baselines
Cherenkov contribution	37%	2%	Correlated between baselines
Absolute energy scale	-	0.6%	Correlated between baselines
Absolute photostatistics resolution	-	5%	Correlated between baselines
Absolute energy leakage	-	8 keV	Correlated between baselines
Absolute energy threshold	-	5 keV	Correlated between baselines
Relative energy scale	-	0.6%	Uncorrelated between baselines
Relative photostatistics resolution	-	5%	Uncorrelated between baselines
Relative energy leakage	-	8 keV	Uncorrelated between baselines
Relative energy threshold	-	5 keV	Uncorrelated between baselines
Reflector panel thickness	1.18 mm	0.03 mm	Uncorrelated between baselines

here is formulated as a reduced covariance matrix, which serves as a statistics-agnostic counterpart to the conventional covariance matrix. Each covariance matrix, $\overline{V}$, is defined by modifying Eq. A.14 as follows:

$$\overline{\mathbf{V}}_{i,j} = \frac{1}{N_{\text{Toy}}} \sum_{k=1}^{N_{\text{Toy}}} \frac{(P_i - \overline{P}_i)(P_j - \overline{P}_j)}{\overline{P}_i \cdot \overline{P}_j}, \tag{8.21}$$

where P_i and $\overline{P}_i$ represent the fluctuated and un-fluctuated $P_{l,e}$ distributions, respectively. The use of a reduced covariance matrix is motivated by the need to compute χ^2_{CNP} grid points in the ($\sin^2 2\theta_{14}$, Δm^2_{41}) parameter space, as described in the next section.

Fig. 8.31 presents zoomed-in views of the reduced covariance matrices for the relative signal normalization and absolute energy scale systematics, highlighting the correlations between periods 1 and 2. A zoomed in view of the complete reduced systematic covariance matrix, $\overline{V}_{\text{sys}}$, is shown in Fig. 8.32 illustrating energy, baseline and period correlations between periods 1 and 2.

8.4.3 χ^2 Grid search

With all necessary inputs defined—namely, the measured and predicted prompt energy per baseline, $M_{l,e}$ and $P_{l,e}$, as well as the total statistical and reduced systematic covariance matrices, V_{stat} and $\overline{V}_{\text{sys}}$—a χ^2_{CNP} scan over the ($\sin^2 2\theta_{14}$, Δm^2_{41}) oscillation parameter space can be performed. For each grid point, Eq. 8.15 becomes:

$$\chi^2_{\text{CNP}} = \mathbf{\Delta}^T \left(V_{\text{tot}}\right)^{-1} \mathbf{\Delta} \tag{8.22}$$

$$= \mathbf{\Delta}^T \left(V_{\text{stat}} + V_{\text{sys}}\right)^{-1} \mathbf{\Delta} \tag{8.23}$$

$$= \left(M_{l,e} - M_e \frac{P_{l,e}}{P_e}\right)^T \left(\frac{1}{3} V_{\text{Neyman}} + \frac{2}{3} V_{\text{Pearson}} + \left(P_{l,e} \cdot \overline{V}_{\text{sys}} \cdot P_{l,e}\right)\right)^{-1} \left(M_{l,e} - M_e \frac{P_{l,e}}{P_e}\right), \tag{8.24}$$

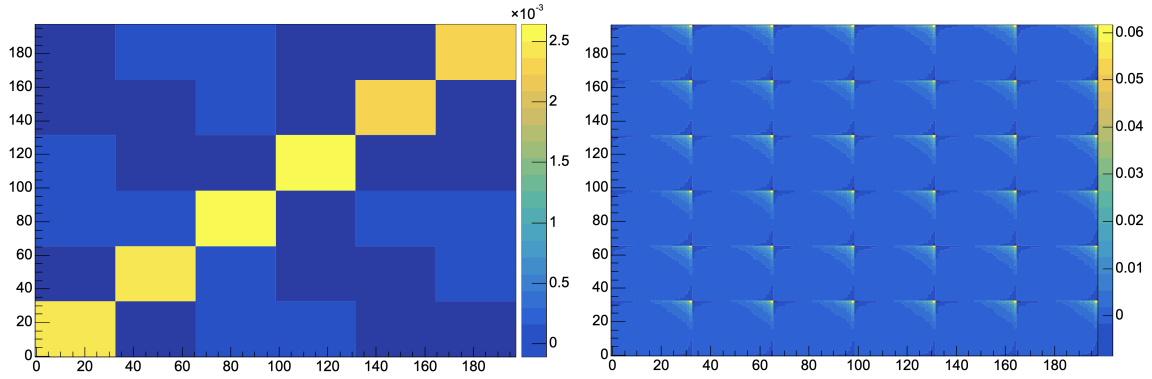


Figure 8.31: Left: Baseline-uncorrelated relative signal normalization reduced covariance matrix, illustrating correlations between periods 1 and 2. Right: Baseline-correlated energy scale reduced covariance matrix, showing correlations between periods 1 and 2.

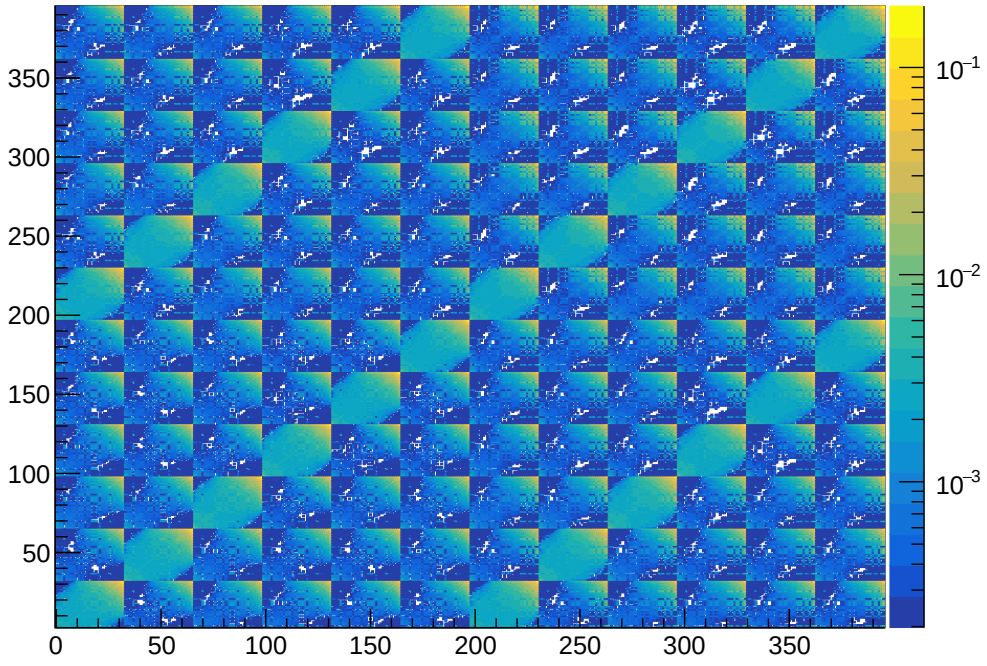


Figure 8.32: Total reduced systematic covariance matrix for periods 1 and 2 highlighting energy, baseline and period correlations.

where $P_{l,e}$ corresponds to the oscillated prediction derived from each set of ($\sin^2 2\theta_{14}$, Δm^2_{41}) values.

A minimum $\chi^2_{\text{CNP, min}}$ of 863 is identified for the measured dataset at $(0.421, 15.2\,\text{eV}^2)$. The predicted $L/\langle E_\nu \rangle$ behavior at this point is illustrated in Fig. 8.29. This result, corresponding to $\chi^2_{\text{min}}/\text{DOF} = 1.04$, differs from previous results where a $\chi^2_{\text{CNP, min}}$ had been reported at $(0.11, 1.78\,\text{eV}^2)$ [70] and $(0.35, 0.5\,\text{eV}^2)$ [82], with $\chi^2_{\text{min}}/\text{DOF}$ values of 0.84 and 0.74, respectively. The resulting $\Delta\chi^2$ values relative to the best-fit point in phase space are shown in Fig. 8.33. Additionally, $\Delta\chi^2$ values for three points of interest are summarized in Table 8.2, corresponding to the Null oscillation point, the Neutrino-4 best-fit point, and the left-most point at the boundary of the Neutrino-4 exclusion. Before drawing any conclusions from the obtained $\Delta\chi^2$ values regarding the preference of the measured data for a given hypothesis, a proper statistical method is required to define the oscillation parameter space regions allowed and excluded by the data.

8.4.4 Sensitivity and exclusion contours

Using the $\Delta\chi^2$ map shown in Fig. 8.33, the Gaussian CL_s method [182], described in Section. A.4, was implemented to generate exclusion contours. Additionally, median sensitivity curves for the full dataset were obtained using the Gaussian CL_s method, where the $\Delta\chi^2$ distribution was generated by replacing $M_{l,e}$ in Eq. 8.22 with the Null un-fluctuated Asimov prediction $P_{l,e}$. The sensitivity contours at the 95% confidence

Table 8.2: Difference in chi-square between the minimum and relevant oscillation parameters.

Test point	**Parameters** $(\sin^2 2\theta, \Delta m^2)$	$\Delta\chi^2 = \chi^2_{(\sin^2 2\theta, \Delta m^2)} - \chi^2_{\textbf{data, min}}$
Null	(0.0021, 0.0187)	2.64
N-4 edge	(0.36, 7.3)	1.42
N-4	(0.1, 7.3)	29.36

level (C.L.) for each DS period are shown in Fig. 8.34. As expected, period 2 provides the best sensitivity, attributed to having the largest number of DE segments.

Furthermore, the individual impact of each systematic uncertainty can be assessed using sensitivity projections, as illustrated in Fig. 8.35. Here, the median sensitivity for period 2 is calculated by adding each systematic uncertainty one at a time. As observed, the most significant impact comes from the baseline-uncorrelated relative normalization uncertainty.

Lastly, both the L and E_{rec} binning configurations were optimized for the final oscillation analysis by assessing the impact of each configuration on the expected sensitivity. Fig. 8.36 shows the results of this binning optimization, where the sensitivity contour for period 2 was calculated in two scenarios: one with a fixed L while varying E_{rec}, and the other with a fixed E_{rec} while varying L. As a result, 6 L bins spanning a baseline range of [6.94–8.94] m and 33 E_{rec} bins spanning a prompt energy range of [0.8–7.4] MeV were used.

8.4.5 Results

Fig. 8.37 presents the final 95% confidence level (C.L.) and 5σ exclusion contours, along with the expected median sensitivity obtained with the entire dataset. As shown, most of the region suggested by Neutrino-4 lies outside the 95% C.L. exclusion contour, with the Neutrino-4 best-fit point excluded at more than 5σ C.L. The 95% C.L. contour also excludes regions of the 3+1 sterile neutrino parameter space above 3 eV^2 that were previously unexplored by other neutrino experiments [154, 43, 49, 14, 38], including the entire region below 10 eV^2 suggested at 2σ C.L. by the BEST and other Gallium Anomaly experiments [88].

While the Gaussian CLs method provides a conservative exclusion region that can be easily combined with results from other experiments, it does not directly assess how consistent the data is with the 3 points of interest outlined in Table 8.2. To address this, a Feldman-Cousins frequentist compatibility test [120] was conducted

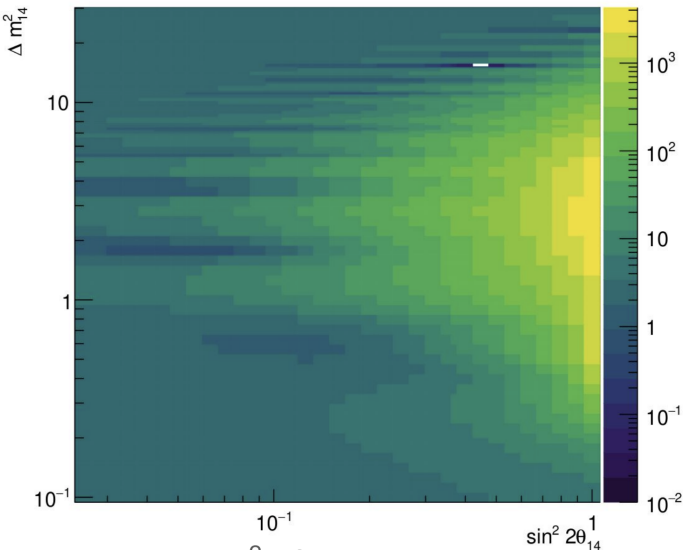


Figure 8.33: The value of $\Delta\chi^2$ obtained for each ($\sin^2 2\theta_{14}$,Δm^2_{41}) grid point, relative to the best-fit point (white square) at (0.421,15.2 eV^2). The χ^2 definition is provided in Eq. 8.22. The white spot corresponds to the location of the best-fit point ($\Delta\chi^2 = 0$).

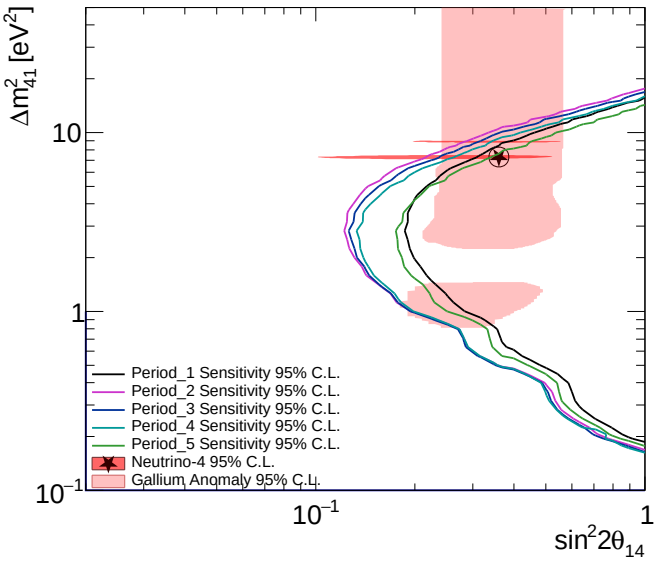


Figure 8.34: Median expected sensitivity for each DS period calculated with the Gaussian CL*s* method. These sensitivity projections include all systematic uncertainties.

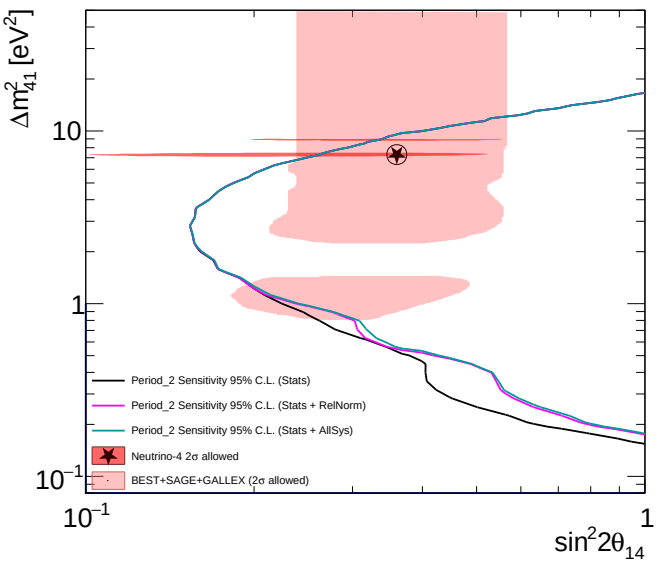


Figure 8.35: Illustration of the impact of statistical and systematic uncertainties on the expected sensitivity projections for period 2. The black curve represents statistical errors only, the pink curve includes both statistical errors and relative normalization uncertainty, and the cyan curve incorporates statistical errors plus all systematic uncertainties. The relative normalization uncertainty has the largest impact on the sensitivity.

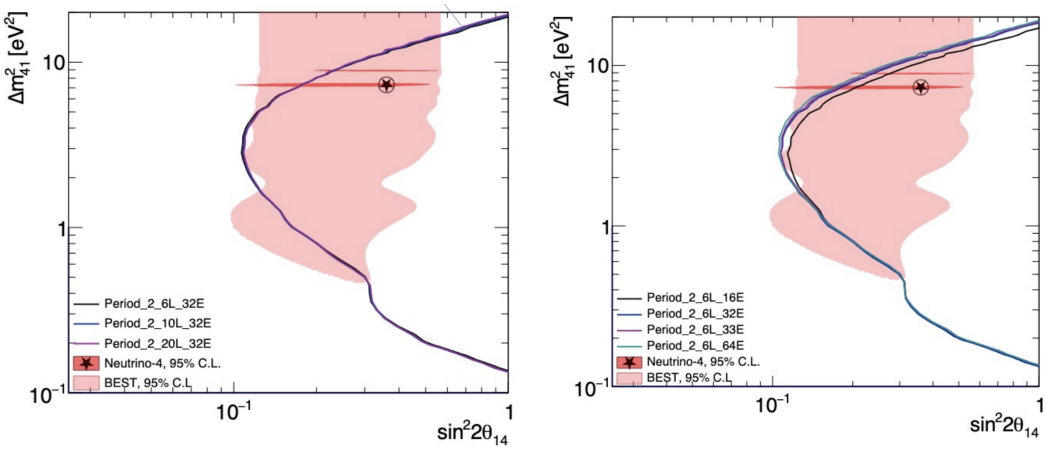


Figure 8.36: Binning optimization results illustrating the impact of each binning configuration on the expected sensitivity for period 2. Left: L binning optimization shows that the choice of 6 baseline bins is reasonable, as the differences in sensitivity obtained with 6, 10, and 20 L bins are negligible. Right: E_{rec} binning optimization demonstrates the gain in sensitivity when increasing the number of E_{rec} bins. A configuration of 33 bins was chosen to match the binning used in the spectrum analysis. Although a 64-bin configuration provides slightly greater sensitivity, the increase is insignificant enough to justify the added computational complexity.

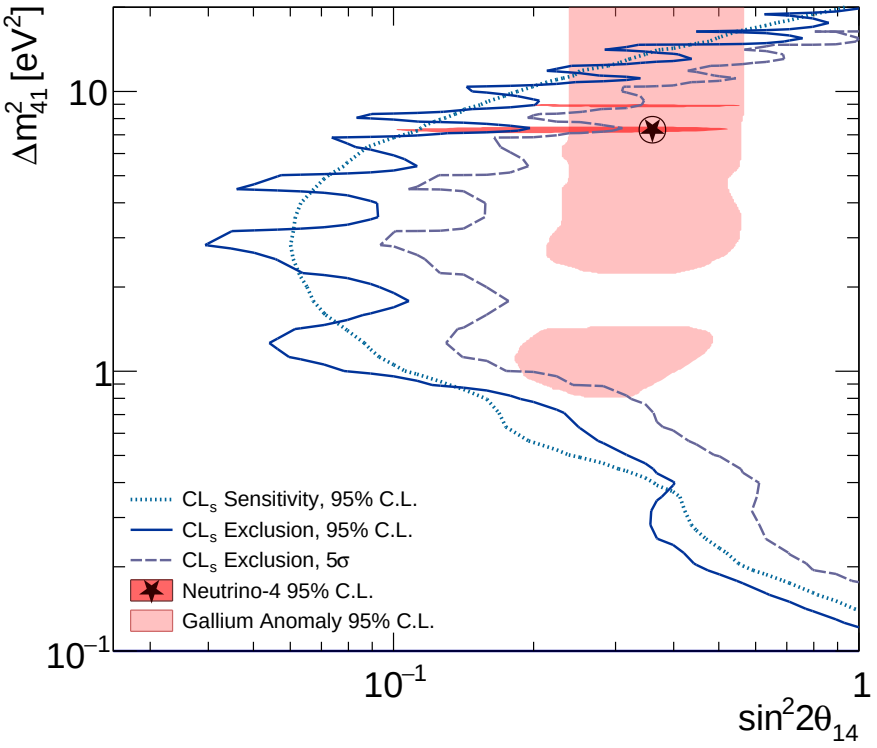


Figure 8.37: The phase space for 3+1 sterile neutrino oscillations excluded by the multi-period PROSPECT-I dataset. The solid and dotted curves show the exclusion and sensitivity limits at the 95% confidence level (C.L.), generated using the Gaussian CL$_s$ method. The dashed line also indicates a 5σ C.L. exclusion limit. The shaded regions correspond to the phase space suggested by the Gallium Anomaly [88] (light pink) and Neutrino-4 [190] (red). Source [178]

to calculate the p-value, which quantifies the statistical significance of the measured data compared to specific oscillation parameters.

This test involved generating 2000 toy datasets (either Null or oscillated) for each of the three points of interest. These toy datasets included both statistical and systematic fluctuations, applied using Cholesky decomposition of the total covariance matrix, V_{tot}, as described in Section A.1.2. For each toy dataset, denoted as $T_{l,e}$, a full χ^2 grid search was performed following the method outlined in Section 8.4.3, using the equation:

$$\chi^2_{\text{CNP}} = \left(T_{l,e} - T_e\frac{P_{l,e}}{P_e}\right)^T \left(\frac{1}{3}V_{\text{Neyman}} + \frac{2}{3}V_{\text{Pearson}} + \left(P_{l,e}\cdot\overline{V}_{\text{sys}}\cdot P_{l,e}\right)\right)^{-1} \left(T_{l,e} - T_e\frac{P_{l,e}}{P_e}\right). \tag{8.25}$$

This process allowed for the calculation of the minimum $\chi^2_{\text{CNP, toy, min}}$ value for each toy dataset. A $\Delta\chi^2_{\text{toy}}$ value is obtained by comparing $\chi^2_{\text{CNP, toy, min}}$ to the χ^2 value at the toy's reference true grid point, denoted as $\chi^2_{\text{CNP, toy, tgp}}$, such that:

$$\Delta\chi^2_{\text{toy}} = \chi^2_{\text{CNP, toy, min}} - \chi^2_{\text{CNP, toy, tgp}}. \tag{8.26}$$

This procedure is repeated for each of the 2000 toy datasets for every point of interest, generating a $\Delta\chi^2_{\text{toy}}$ distribution. Additionally, a $\Delta\chi^2_{\text{data}}$ value is calculated by comparing $\chi^2_{\text{CNP, toy, min}}$ with $\chi^2_{\text{CNP, data, min}}$ for each case. Fig. 8.38 shows the $\Delta\chi^2_{\text{toy}}$ distributions for all points of interest, along with the corresponding $\Delta\chi^2_{\text{data}}$ value. The frequentist p-value is then calculated as the area of the $\Delta\chi^2_{\text{toy}}$ distribution that falls to the right of the $\Delta\chi^2_{\text{data}}$ value, divided by the total area of the $\Delta\chi^2_{\text{toy}}$ distribution:

$$p = \frac{\sum_{\Delta\chi^2_{\text{data}}}^{\infty} P(\Delta\chi^2_{\text{toy}})}{\sum_0^{\infty} P(\Delta\chi^2_{\text{toy}})}. \tag{8.27}$$

Based on the results shown in Fig. 8.38, a p-value of 0.73 was determined for the comparison between the data and the Null hypothesis, indicating consistency of the measured data with the absence of sterile neutrino oscillations. In contrast, the comparison between the data and the Neutrino-4 best-fit point yielded a p-value of 0, indicating strong ($>3\sigma$) incompatibility with PROSPECT's data.

8.5 PROSPECT in the global context

The enhancement in the statistical power of the PROSPECT data provided by the multi-period analysis, compared to previous results, and its impact on the new oscillation analysis are illustrated in Figures 8.39 and 8.40. Fig. 8.39 shows the improvement in relative statistical uncertainties for each $L/\langle E_\nu \rangle$ bin when comparing the multi-period and single-period analyses. Additionally, Fig. 8.40 presents the exclusion contours obtained by the PROSPECT experiment over the years, highlighting the significant increase in phase space coverage observed in the final results.

This new result contributes to global efforts by short-baseline reactor-based neutrino experiments searching for sterile neutrino oscillations, as illustrated in Fig. 8.41. It demonstrates that the final limits set by the PROSPECT experiment on eV-scale sterile neutrinos are the most stringent among short-baseline reactor efforts for most Δm^2_{41} values above 3 eV^2. Fig. 8.42 further compares this result with those from long-baseline reactor experiments and non-reactor-based experiments, highlighting that reactor-based constraints on θ_{14} are significantly stronger across most of the phase space explored by terrestrial experiments.

Additionally, Fig. 8.42 compares the final PROSPECT exclusion with the eV-scale sterile neutrino mixing limits derived from cosmological data. Cosmological constraints are obtained from a combination of CMB measurements, including temperature and polarization anisotropies [25] and the lensing power spectrum [24], as provided in the Planck 2018 data release [40, 23]. Late-time measurements of

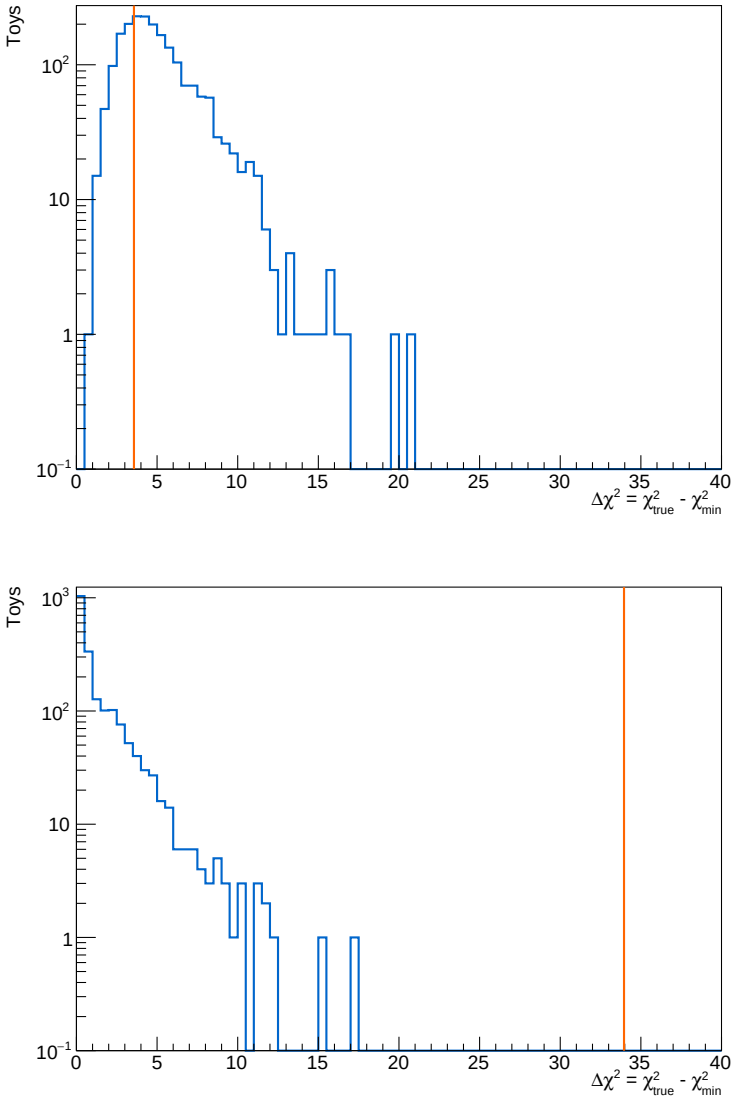


Figure 8.38: $\Delta\chi^2_{toy}$ distributions for the Null oscillation (top) and Neutrino-4 best-fit point (bottom). The orange vertical lines show corresponding $\Delta\chi^2_{data}$. The observed value sits in the middle (higher end) of the distribution for the Null (Neutrino-4) grid point, indicating good (poor) compatibility of the data with representative toy datasets from that grid point.

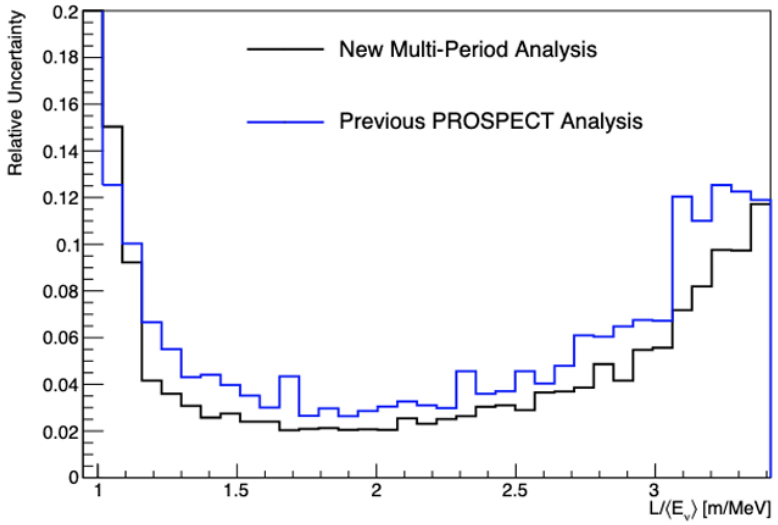


Figure 8.39: Relative statistical uncertainty improvements for the multi-period analysis compared to the single-period analysis across each $L/\langle E_\nu \rangle$ bin.

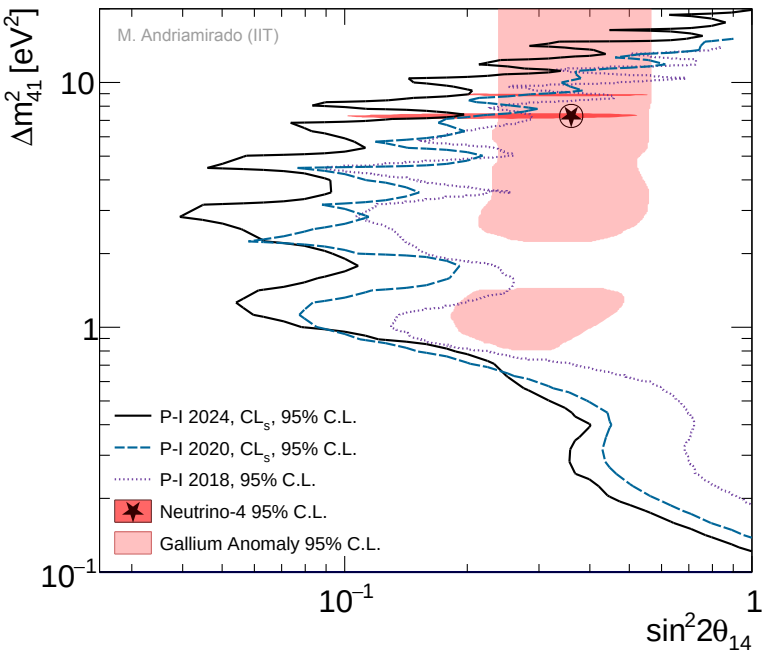


Figure 8.40: Exclusion contours obtained by the PROSPECT experiment over time, demonstrating the increased phase space coverage in the final results.

distances and the cosmic expansion rate are also incorporated using baryon acoustic oscillation (BAO) data from the 6dFGS [93], SDSS-MGS [185], and BOSS DR12 [41] surveys. While cosmology-derived limits impose strong constraints in phase space regions below $\sin^2(2\theta_{14}) = 10^{-2}$, tensions remain relative to terrestrial measurements, particularly in the reactor sector.

These findings emphasize the importance of future short- and long-baseline reactor antineutrino experiments to explore the remaining uncharted parameter space. Key initiatives include the second phase of the PROSPECT experiment, PROSPECT-II [67], for short-baseline studies and the future JUNO [51] medium-baseline reactor experiment.

8.6 Chapter summary

Using the new multi-period dataset, a new neutrino oscillation analysis was performed using the complete data sample from the PROSPECT-I detector operated at the High Flux Isotope Reactor in 2018. The analysis was able to set new limits on electron-flavor disappearance caused by mixing. The data excludes at 95% confidence level the existence of sterile neutrinos in regions above 3 eV^2 previously unexplored by terrestrial experiments, including all space below 10 eV^2 suggested by the recently strengthened Gallium Anomaly. The best-fit point of the Neutrino-4 reactor experiment's claimed observation of short-baseline oscillation is ruled out at more than five standard deviations.

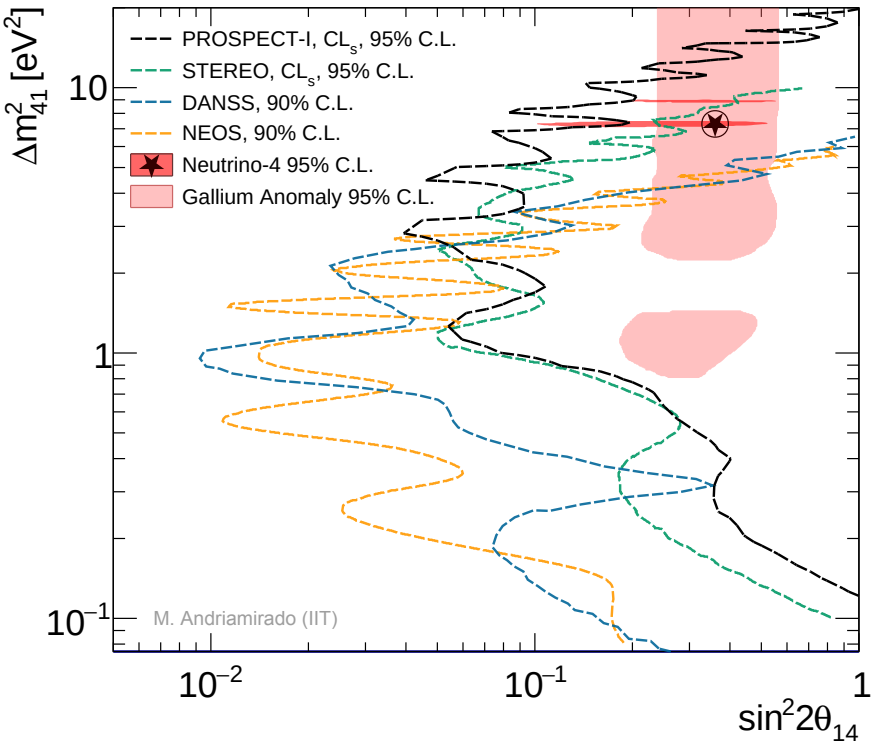


Figure 8.41: Comparison of the final exclusion contours obtained by the PROSPECT experiment against results from other SBL reactor antineutrino experiments [49, 165, 154]. It can be observed that PROSPECT provides world-leading limits for sterile neutrino oscillations for Δm^2_{41} values above 3 eV^2.

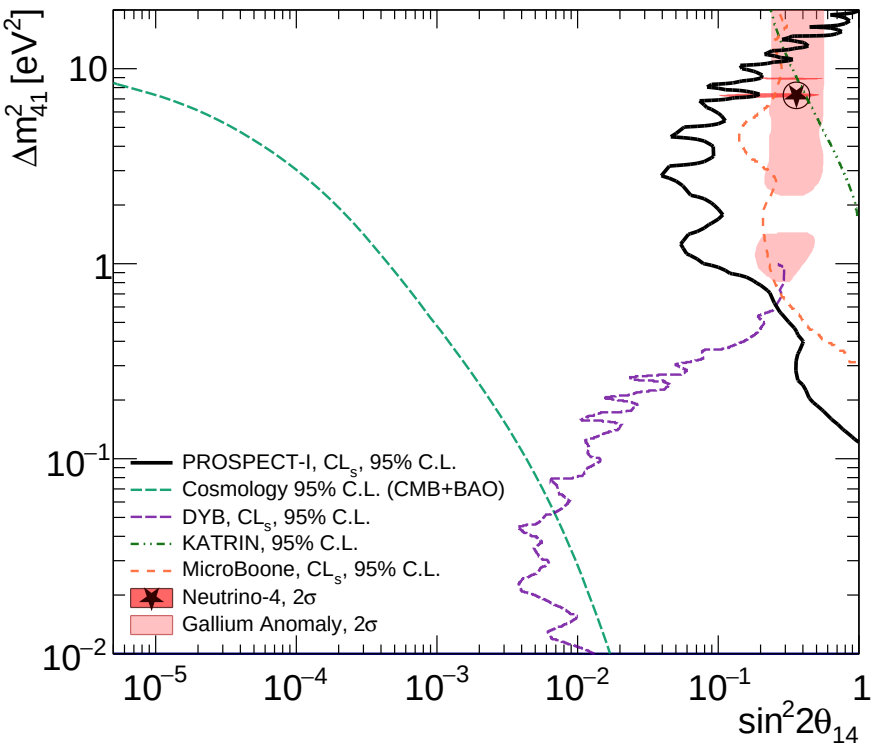


Figure 8.42: Comparison of the final exclusion contours obtained by the PROSPECT experiment with results from a long-baseline reactor antineutrino experiment [55], an accelerator-based experiment [103], and an absolute neutrino mass-focused experiment [36] highlights the unique strength of reactor experiments in constraining θ_{14}. Cosmological limits, derived from CMB and BAO measurements [138], are shown in green, emphasizing the persistent tension between cosmological and terrestrial experimental results.

Chapter 9

Joint Oscillation Analysis

9.1 Introduction

The final benchmark results from the PROSPECT-I experiment, as described in Chapters 7 and 8, include a high-precision measurement of the ^{235}U spectrum from a highly enriched uranium reactor and new limits on electron-flavor disappearance due to mixing with sterile states for most Δm^2_{41} values above 3 eV^2. These results present new opportunities for collaboration with other experiments.

Joint analyses among different neutrino experiments are essential for advancing our understanding of neutrino physics. By combining data from experiments with varying types of detectors, baseline distances, neutrino sources, and energy ranges, these analyses maximize scientific output, improve sensitivity to rare phenomena, and enhance measurement precision. This comprehensive approach increases the overall sample size, reduces statistical uncertainties, and provides broader parameter space coverage. Consequently, it allows for more accurate determination of critical parameters, such as mixing angles, mass-squared differences, and the CP-violating phase, which are essential for testing theoretical models and understanding the fundamental properties of neutrinos.

Additionally, joint analyses increase sensitivity to physics beyond the Standard Model, such as sterile neutrinos or non-standard interactions. They are also crucial for global fits that provide the most precise estimates of oscillation parameters, contributing to a more complete understanding of neutrino behavior. Some notable examples of joint analyses include:

- **Super-Kamiokande and IceCube Collaboration on Supernova Neutrinos:** Merging data from Super-Kamiokande and IceCube to detect neutrino bursts from core-collapse supernovae, improving temporal and directional resolution [4].

- **Joint Analysis of Neutrinoless Double-Beta Decay ($0\nu\beta\beta$) Searches:** Combining results from GERDA, MAJORANA, EXO-200, and KamLAND-Zen to increase sensitivity to $0\nu\beta\beta$ decay through different isotopes and detector technologies [27].

- **Combined Reactor Neutrino Analysis (Daya Bay, RENO, Double Chooz):** Refining the measurement of the mixing angle θ_{13} and examining the reactor neutrino flux by integrating data from multiple reactor neutrino experiments [64].

- **IceCube and ANTARES Collaboration for Neutrino Point Source Searches:** Enhancing the search for high-energy neutrino point sources by combining data from IceCube and ANTARES, thereby achieving full-sky coverage [42].

- **Global Neutrino Analysis by NuFit:** Conducting global fits of all known neutrino oscillation parameters by consolidating results from various neutrino oscillation experiments [117].

- **KM3NeT and ORCA/PINGU for Neutrino Mass Hierarchy:** Determining the neutrino mass hierarchy by integrating data from atmospheric neutrinos observed at different locations, depths, and detector technologies [20].

In 2023, a joint analysis was initiated between the Daya Bay, STEREO, and PROSPECT collaborations. This effort marks the first time that data from these three experiments will be combined to simultaneously extract the sterile neutrino parameters θ_{14} and Δm^2_{14}, the ^{235}U fission neutrino spectrum, and the combined fission neutrino spectrum of ^{239}Pu and ^{241}Pu. By uniting their data, the experiments will not only assess compatibility among their results but also compare their findings against the HM [149] and Kopeikin [157] flux and spectrum models, providing valuable insights for future particle and nuclear physics research.

This joint analysis will extend the sensitivity of oscillation parameter studies into the large Δm^2_{14} region, potentially motivating further measurement of the ^{238}U fission neutrino spectrum to enhance precision. Such comprehensive objectives exceed any single experiment's capability, underscoring this collaborative approach's importance. This chapter presents a summary of the current status of the oscillation-only approach led by the PROSPECT collaboration in the Daya Bay-PROSPECT-STEREO (DPS) analysis, resulting in the projected median sensitivity obtained by combining the ^{235}U spectra measured by PROSPECT and STEREO while using the ^{235}U Daya Bay unfolded spectrum as a reference model.

9.2 Motivation and strategy

The development of the necessary frameworks capable of performing both multi-period spectrum and oscillation analyses (see Chapters 7 and 8) enables the possibility of a new joint study with the Daya Bay [55] and STEREO [49] collaborations. This effort will focus on a combined search for sterile neutrino oscillations using the final datasets from all three experiments. STEREO recently published their final datasets presented in a multi-period analysis. For the joint analysis, STEREO's data will be integrated into the existing framework as two new data periods, each with its detector response and covariance matrix.

Additionally, the primary modification to the statistical analysis described in Section 8.4 involves a slight adjustment to Eq. 8.12:

$$\chi^2_{CNP,DPS} = \mathbf{\Delta}^{\mathrm{T}} \mathrm{V}^{-1}_{\mathrm{tot}} \mathbf{\Delta}, \tag{9.1}$$

where

$$\Delta_{l,e} = M_{l,e} - P_{l,e}. \tag{9.2}$$

In this modified approach, the covariance-based χ^2 test statistic is constrained by using Daya Bay's ^{235}U antineutrino spectrum as a reference for the spectral shape, without incorporating the normalization term $\left(\frac{M_e}{P_e}\right)$, resulting in a model-dependent analysis. While the spectral shape information is included in the fit, flux information is excluded from this analysis.

The combination of data from two HEU short-baseline experiments and one LEU long-baseline experiment provides unique sensitivity to different Δm^2_{41} regions, as illustrated in Fig. 9.1. Specifically:

- For $\Delta m^2_{41} < 10^{-3}$ eV^2: The oscillation period is too long to be observed at the given baselines, resulting in no sensitivity for all three experiments.
- For $\Delta m^2_{41} \in [10^{-3}, 10^{-1}]$ eV^2: The sensitivity will be dominated by the Daya Bay experiment due to its kilometer-long baseline.
- For $\Delta m^2_{41} \in [10^{-1}, 10]$ eV^2: The sensitivity will be primarily driven by the STEREO and PROSPECT experiments.
- For $\Delta m^2_{41} > 10$ eV^2: The oscillation induced by sterile neutrinos occurs relatively rapidly. In this scenario, the survival probability becomes consistent across the three experiments due to their long baselines relative to the sterile neutrino oscillation length.

This new joint analysis will result in enhanced sensitivity at low Δm^2_{41} from the 'near-far' ^{235}U spectrum comparison and improved sensitivity at high Δm^2_{41} due

to the combined statistics from PROSPECT and STEREO. It will also mitigate the statistical limitations inherent in the model-independent method. The following sections briefly describe the Daya Bay and STEREO experiments and the respective inputs incorporated into the DPS analysis.

9.3 Daya Bay

9.3.1 Experimental description

The Daya Bay experiment is located near the Daya Bay Nuclear Power Plant and the Ling Ao Nuclear Power Plant, approximately 55 km northeast of Hong Kong. The site was chosen for its proximity to powerful nuclear reactors that produce a high flux of electron antineutrinos. The experiment employs a total of eight antineutrino detectors (ADs), which are grouped into three experimental halls: two 'near halls' (EH1 and EH2) situated 360-500 meters from the reactor cores, and one 'far hall' (EH3), located about 1.6 km away, as illustrated in Fig. 9.2. Each AD consists of three nested cylindrical vessels: the innermost vessel contains a liquid scintillator doped with gadolinium to detect IBD events, the middle vessel contains a layer of undoped liquid scintillator for shielding purposes, and the outermost vessel holds mineral oil to protect against background radiation. Surrounding the ADs are photomultiplier tubes that detect the light emitted when antineutrinos interact with the scintillator. Fig. 9.2 shows a schematic of an AD.

With almost 6 million IBD events detected, the experiment has produced significant findings in antineutrino spectrum analysis, flux measurement, and neutrino oscillation studies, significantly advancing the field of neutrino physics. One of the most notable results is the consistent observation of a bump in the 4-6 MeV prompt energy region. Additionally, Daya Bay reported a total antineutrino flux approximately 6% lower than theoretical predictions, consistent with the Reactor Antineutrino Anomaly, indicating potential inaccuracies in reactor models, especially

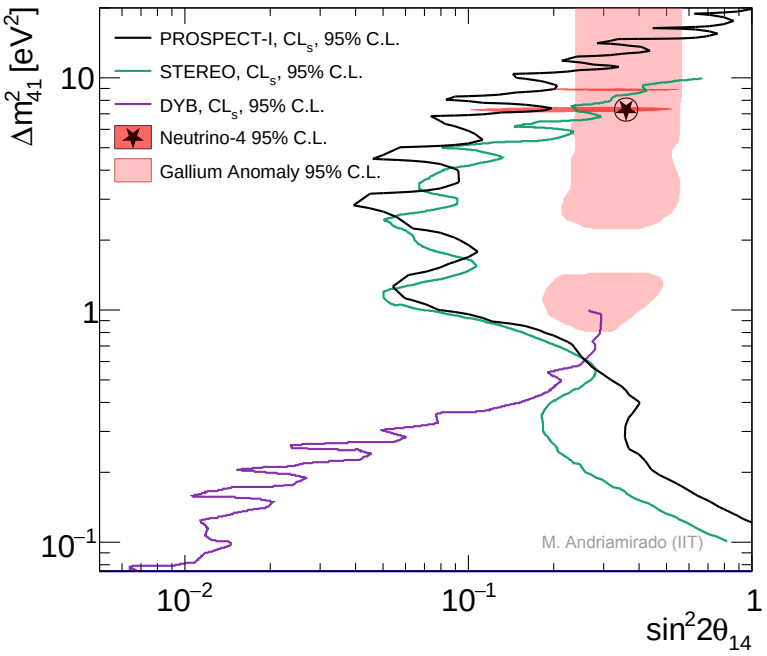


Figure 9.1: Recent results from the search for eV-scale sterile neutrinos by the PROSPECT [178], STEREO [49], and Daya Bay [19] experiments demonstrate the potential of a combined analysis that leverages their sensitivities.

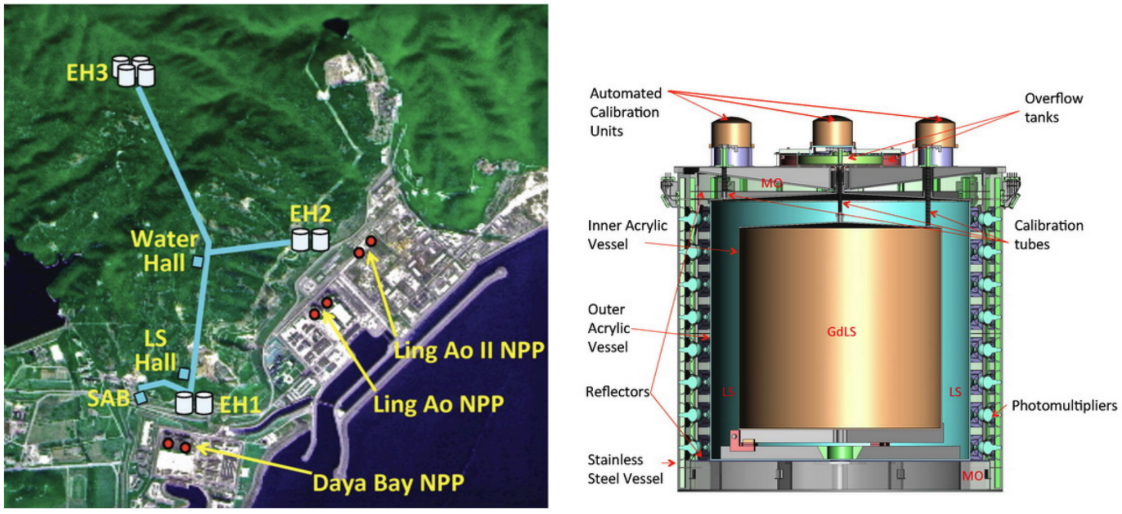


Figure 9.2: Left: Layout of the Daya Bay experiment, showing the arrangement of its components; Right: schematic of one of the Antineutrino Detector (AD) modules. Source [52].

regarding contributions from different fission isotopes such as ^{235}U, ^{238}U, ^{239}Pu, and ^{241}Pu. The experiment's precise flux measurements have contributed to refining these models and understanding the complexities of antineutrino production.

In terms of oscillation studies, Daya Bay achieved the first high-precision measurement of the neutrino mixing angle θ_{13}, finding $\sin^2(2\theta_{13}) = 0.092 \pm 0.016\,(\text{stat.}) \pm 0.005\,(\text{syst.})$, confirming that θ_{13} is non-zero. This measurement was a key result for the three-neutrino oscillation model and opened new possibilities for investigating CP violation in the lepton sector. The experiment also provided a precise value for the effective mass-squared difference, $\Delta m^2_{ee} \approx (2.50 \pm 0.08) \times 10^{-3}\,\text{eV}^2$, which is crucial for understanding neutrino oscillations. Fig. 9.3 illustrates some of the main results from the different studies conducted by the Daya Bay collaboration.

9.3.2 Inputs for DPS analysis

As mentioned earlier, the oscillation-focused DPS analysis uses the ^{235}U unfolded spectrum ($\hat{s}_{dyb}$) and its corresponding unfolded covariance matrix ($V_{tot,\hat{s}_{dyb}}$). The reference spectrum is presented as a 24-element vector in antineutrino energy space, spanning an energy range of 1.8-7.8 MeV, which means that the covariance matrix corresponds to a 24x24 matrix. Both of these inputs are illustrated in Fig. 9.4.

The implementation of $\hat{s}_{dyb}$ into the PROSPECT-CNP framework to generate $P_{l,e}$ predictions was explained in Section 8.3; however, a new aspect of the DPS analysis involves the incorporation of $V_{tot,\hat{s}_{dyb}}$ into the analysis. This matrix must be transformed into the prompt energy space of both the PROSPECT and STEREO experiments. This procedure is outlined in Section 9.5.1.

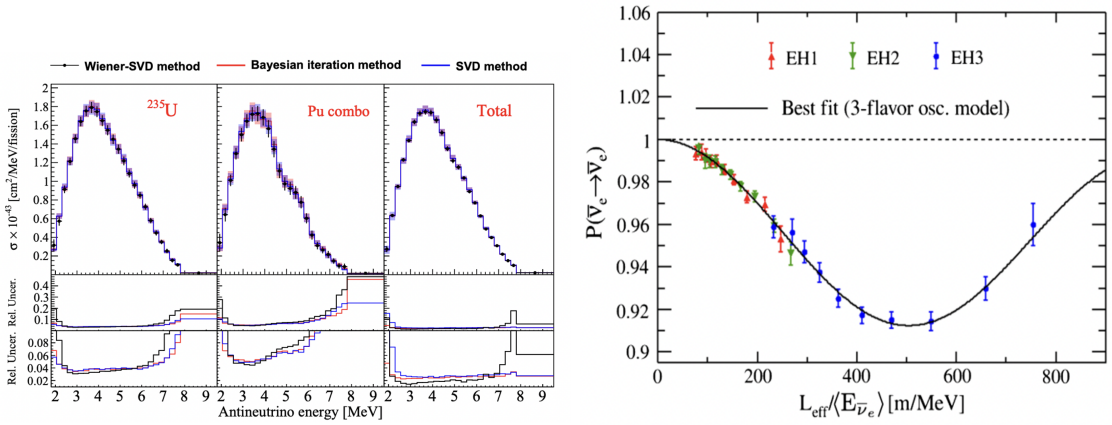


Figure 9.3: Top: Unfolded energy spectra of antineutrinos, including contributions from ^{235}U and combined plutonium isotopes, weighted by the IBD cross-section. Bottom: Observed disappearance probability plotted as a function of the ratio between the effective baseline, L_{eff}, and the average antineutrino energy, $\langle E_{\overline{\nu}} \rangle$. Source: [55, 57].

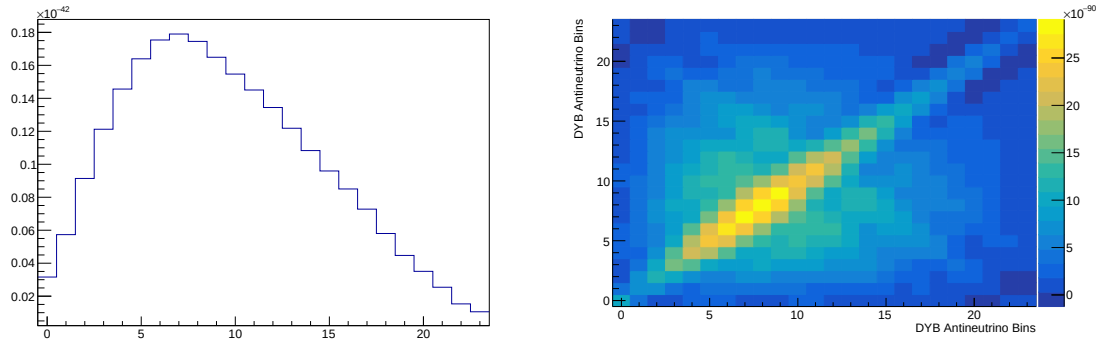


Figure 9.4: ^{235}U antineutrino spectrum and covariance matrix resulting from Daya Bay data unfolding. Spectrum is presented as a 24-element vector in antineutrino energy space, spanning an energy range of 1.8-7.8 MeV, which means that the covariance matrix corresponds to a 24x24 matrix. Source [55].

9.4 STEREO

9.4.1 Experimental description

The STEREO (Search for Sterile Reactor Neutrino Oscillations) experiment aims to detect eV-scale sterile neutrinos by measuring antineutrinos from ^{235}U fission at the Institut Laue-Langevin (ILL) research reactor in Grenoble, France. The detector has six cells filled with 1.8 cubic meters of gadolinium-doped liquid scintillator, allowing independent measurements of antineutrino spectra at 9-11 meters from the reactor core. The cells are surrounded by a 'γ-catcher' with an undoped liquid scintillator to reduce energy leakage. The detector is shielded with lead and polyethylene to block external gamma rays and neutrons.

As in the case of PROSPECT, STEREO operates above ground, subjecting it to significant cosmic ray backgrounds. To mitigate this, it uses a water Cherenkov muon veto, iron, and boron-loaded rubber shielding, and a water channel above the detector to reduce vertical muon flux by about four times, lowering cosmic ray backgrounds to levels comparable to the antineutrino signal. Fig. 9.5 shows a schematic of the STEREO detector and the phases of its data collection campaign.

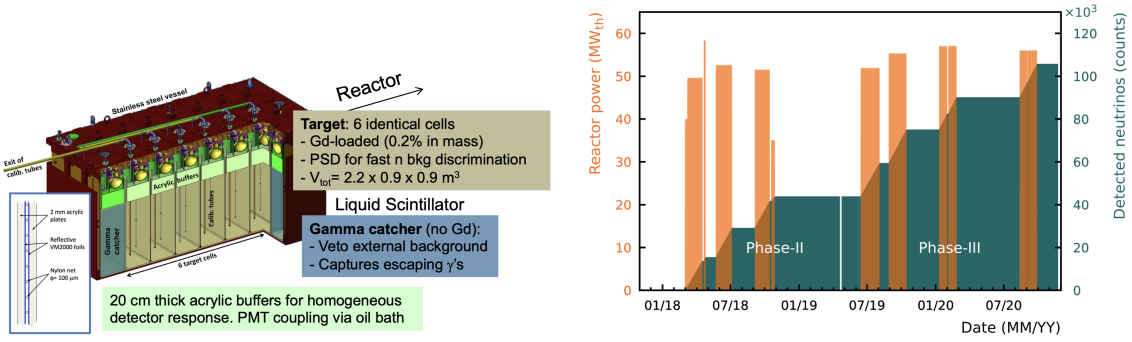


Figure 9.5: Left: Diagram of the STEREO detector, detailing its primary components. Right: Summary of the STEREO data-taking campaigns, illustrating the alternation between reactor-on and reactor-off periods, the changes in reactor power, and the total number of neutrinos detected. Source [49].

The analysis focused on data from Phases II and III, detecting over 100,000 IBD events. This data allowed STEREO to exclude the parameter space favored by the RAA up to a few eV^2 at a 95% confidence level and rule out the Neutrino-4 best-fit points with a significance of 3.3σ. It also established a new reference for the ^{235}U antineutrino spectrum and found a flux deficit of 5.5% ± 2.1% compared to the Huber-Mueller prediction, suggesting that the deficit is likely due to biases in nuclear data or conversion models rather than the presence of sterile neutrinos. Fig. 9.6 illustrates some of the final results from the STEREO collaboration.

9.4.2 Inputs for DPS analysis

Data and response matrices

The STEREO data are incorporated into the DPS analysis in the same format as the PROSPECT data described in Section 8.2.1, specifically as the measured prompt energy spectra per baseline, $M_{l,e}$, for both Phases II and III. In Phase II (III), the STEREO experiment recorded approximately 43,420 (63,122) IBD counts with an average signal-to-background ratio (S:B) of 0.8 (1.0), covering a prompt energy range of 1.625–7.125 MeV in 500 keV bins, which differs from the binning used in the PROSPECT experiment. As illustrated in Fig. 9.5, the STEREO detector consists of six cells, allowing each baseline bin to correspond directly to a different detector cell, spanning a total baseline range of 9.43–11.18 m.

Additionally, response matrices for each detector cell in both phases ($R_{\text{ste}}^{\text{cell,phase}}$) are included in the analysis. Each response matrix is formatted as an 11x82 matrix, where 11 represents the number of prompt energy bins, and 82 represents the number of antineutrino energy bins, covering an energy range of 1.8–10 MeV, consistent with the format used in the PROSPECT experiment.

Statistical and systematic errors

STEREO's oscillation analysis employed a model-independent approach similar to the one used by PROSPECT, as described in Section 8.4. Consequently, the total statistical covariance matrix, $V_{\text{ste,stat}}$, derived from the uncertainties in the background-subtracted IBD spectra, includes off-diagonal contributions resulting from the normalization process. The matrix $V_{\text{STE,stat}}$, along with the cumulative systematic covariance matrices for STEREO, are represented as 132x132 matrices, corresponding to 6 baseline bins, 11 E_{rec} bins, and 2 detector phases.

For systematic uncertainties, the STEREO experiment utilized a different method for their χ^2 test statistic, adopting a pull-term approach rather than a covariance matrix-based approach. To incorporate these systematic uncertainties into the DPS analysis, systematic covariance matrices were generated based on the reported uncertainty contributions, as summarized in Table 9.1.

The PROSPECT-CNP framework is equipped to reproduce the energy reconstruction systematic, as it is the same as the baseline-uncorrelated energy scale systematic described in Section 8.4.2. It also incorporates the relative cell volume and neutron efficiency systematics, whose combined contributions are equivalent to the relative signal normalization included in the PROSPECT analysis. However, the selection cuts and relative phase normalization uncertainties will not be included, as

Table 9.1: Summary of systematic uncertainties incorporated in STEREO's final oscillation analysis. Source [49].

Type	**Source**	**Nuisance parameter**	**Uncertainty**	**Correlations**		
				Energy	**Cell**	**Phase**
Energy scale	Energy reconstruction	$\alpha_l^{\text{EscaleU}}$	1%	1	0	1
	Time stability	α^{EscaleC}	0.25%	1	1	0
Signal	Selection cuts	α^{Cuts}	0% to 2%	1	1	1
	Reactor background	$\alpha_l^{\text{ReactorBg}}$	5% to 0%	1	0	1
Normalization	Relative cell volume	α_l^{NormU}	0.83%	1	0	1
	Neutron efficiency	α^{NormU}	0.63%	1	0	0.91
	Relative norm phase-II/phase-III	$\alpha^{\text{II vs III norm}}$	1.5%	1	1	-

these uncertainties are related to the absolute flux normalization from STEREO, which is excluded from the oscillation-only approach due to the absence of flux information. Fig. 9.7 illustrates the total reduced covariance matrix $\overline{V}_{ste,prompt,BU}$, including the contributions from the energy scale and relative signal normalization baseline-uncorrelated uncertainties for the STEREO experiment.

All relevant baseline-uncorrelated uncertainties for the DPS from STEREO can be easily reproduced using the PROSPECT-CNP framework. However, incorporating the STEREO baseline-correlated systematics, as summarized in Table 9.2, requires a different procedure. These baseline-correlated uncertainties correspond to those considered during the spectral shape oscillation analysis conducted by the STEREO experiment. Similar to the PROSPECT experiment, the STEREO collaboration performed a multi-period unfolding procedure, combining data from each phase to produce a single unfolded antineutrino energy spectrum, $\hat{s}_{\text{ste}}$, accompanied by an unfolded covariance matrix, $V_{\text{tot},\hat{s}_{\text{ste}}}$. To incorporate these uncertainties into the analysis, the matrix $V_{\text{tot},\hat{s}_{\text{ste}}}$ must be transformed into the prompt energy space for each detector cell in each experimental phase. This transformation is achieved using a joint-response matrix that includes the response matrix for every cell in each phase, denoted as $R_{\text{ste,joint}}$.

Thus, the resulting vectorized cumulative spectra-per-baseline, s_{prompt}, in prompt space, and the cumulative baseline-correlated covariance matrix, $V_{\text{ste,prompt,BC}}$, can be defined as:

$$s_{ste,prompt} = \begin{pmatrix} s^{II}_{prompt} \\ s^{III}_{prompt} \end{pmatrix} = \begin{pmatrix} R^{1,\text{II}}_{\text{ste}} \\ \vdots \\ R^{6,\text{II}}_{\text{ste}} \\ R^{1,\text{III}}_{\text{ste}} \\ \vdots \\ R^{6,\text{III}}_{\text{ste}} \end{pmatrix} \cdot \hat{s}_{\text{ste}} \tag{9.3}$$

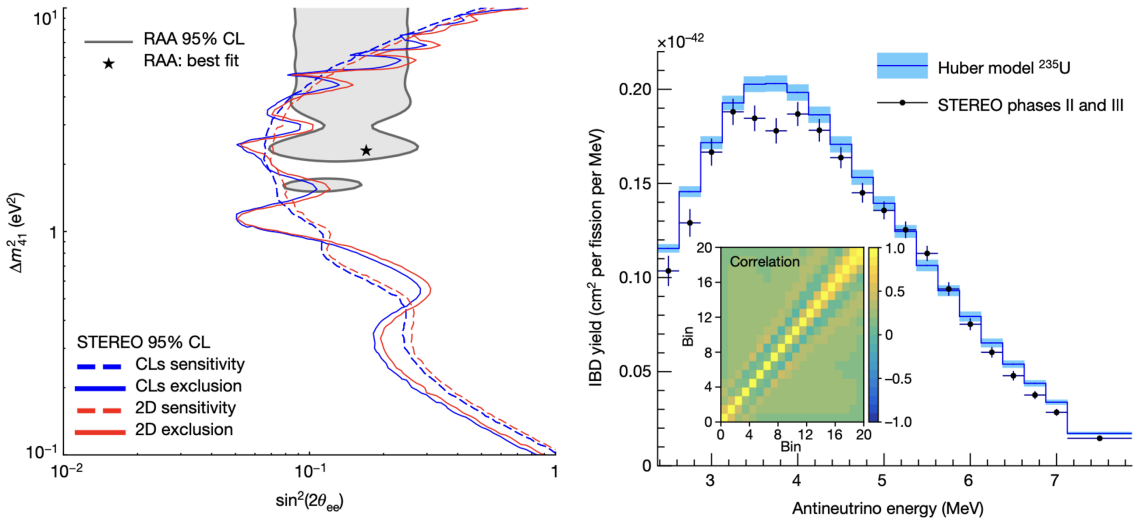


Figure 9.6: The final exclusion region from the STEREO experiment, incorporating all data from Phases II and III, along with the ^{235}U antineutrino spectrum derived from multi-phase data unfolding. Source: [49].

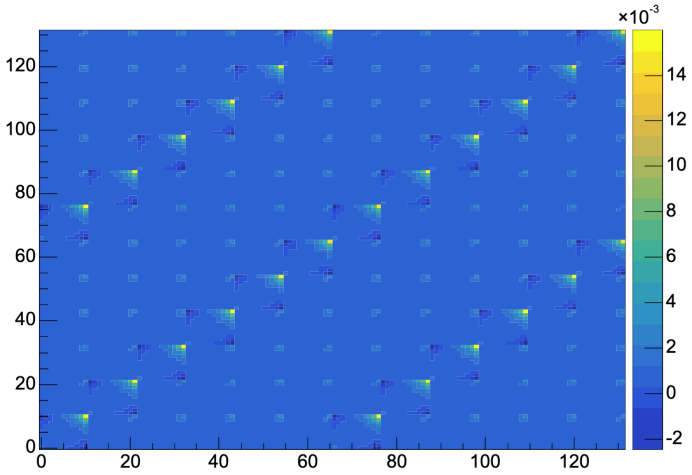


Figure 9.7: STEREO's baseline-uncorrelated reduced covariance matrix for the DPS analysis.

Table 9.2: Summary of Systematic Uncertainties incorporated in STEREO's final spectral shape analysis. Source [49].

Type	**Source**	**Uncertainty**	**Correlations**	
			Energy	**Phase**
Energy scale	Energy reconstruction	0.41%	1	1
	Time stability	0.25%	1	0
	→ Total	**0.5%**	1	**0.73**
Signal	Selection cuts	0% to 2%	1	1
	Reactor background	5% to 0%	1	1
Non-^{235}U flux	Off equilibrium	30%	1	1
	^{28}Al	5%	1	1
Normalization	Reactor thermal power	1.4%	1	0.46
	Proton number	1.0%	1	1
	Neutron efficiency	0.7%	1	0.92
	Neutrino extraction method	0.7%	1	1
	Solid angle	0.5%	1	1
	Others[5]	0.3%	1	1
	→ Total	**2.1%**	1	**0.72**

$$V_{ste,prompt,BC} = \begin{pmatrix} V_{prompt}^{II} & V_{prompt}^{II,III} \\ V_{prompt}^{III,II} & V_{prompt}^{III} \end{pmatrix} = \begin{pmatrix} R_{\text{ste}}^{1,\text{II}} \\ \vdots \\ R_{\text{ste}}^{6,\text{II}} \\ R_{\text{ste}}^{1,\text{III}} \\ \vdots \\ R_{\text{ste}}^{6,\text{III}} \end{pmatrix} \cdot V_{\text{tot},\hat{s}_{\text{ste}}} \cdot \begin{pmatrix} R_{\text{ste}}^{1,\text{II}} \\ \vdots \\ R_{\text{ste}}^{6,\text{II}} \\ R_{\text{ste}}^{1,\text{III}} \\ \vdots \\ R_{\text{ste}}^{6,\text{III}} \end{pmatrix}^{T} \tag{9.4}$$

where s_{prompt}^{II} and s_{prompt}^{III} represent the vectorized $M_{l,e}$ distributions for phases II and III. In addition, the diagonal elements V_{prompt}^{II}, V_{prompt}^{III} correspond to the absolute covariance matrices for phases II and III. In contrast, $V_{prompt}^{II,III}$ and $V_{prompt}^{III,II}$ represent the off-diagonal contributions to the cumulative covariance matrix describing the correlation between phases. As a result, the total reduced baseline-correlated covariance matrix is defined as $\overline{V}_{ste,prompt,BC}$

$$\overline{V}_{ste,prompt,BC} = \begin{pmatrix} \frac{V_{prompt}^{II}}{s_{prompt}^{II} \cdot s_{prompt}^{II}} & \frac{V_{prompt}^{II,III}}{s_{prompt}^{II} \cdot s_{prompt}^{III}} \\ \frac{V_{prompt}^{III,II}}{s_{prompt}^{III} \cdot s_{prompt}^{II}} & \frac{V_{prompt}^{III}}{s_{prompt}^{III} \cdot s_{prompt}^{III}} \end{pmatrix} \tag{9.5}$$

Finally, the total reduced covariance matrix for STEREO in prompt space is given by $\overline{V}_{ste,prompt} = \overline{V}_{ste,prompt,BU} + \overline{V}_{ste,prompt,BC}$ and it is illustrated in Fig. 9.8.

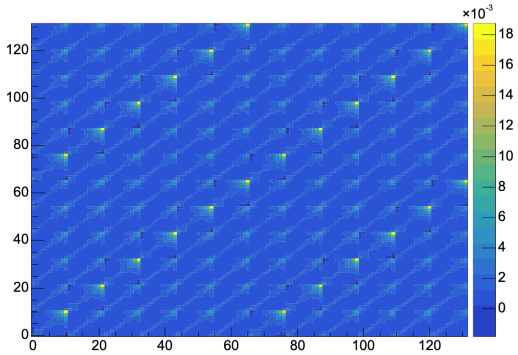


Figure 9.8: STEREO's total reduced systematic covariance matrix for the DPS analysis, showing correlations between energy, baseline, and detector phase bins.

9.4.3 Reproducing STEREO results

After describing how all the STEREO inputs were incorporated into the analysis framework, the joint fit can be performed. However, before combining PROSPECT and STEREO data, it is necessary to ensure that the STEREO-only results can be reproduced with the PROSPECT-CNP framework. Figs. 9.9-9.9 illustrates the measured $M_{l,e}$ distributions and the predicted $P_{l,e}$ distributions generated with the PROSPECT-CNP framework, demonstrating good agreement between measurements and predictions.

In addition, by using the Gaussian CL_s method as well as the model-independent fit, the median projected sensitivity for STEREO can be computed and compared with the final results from STEREO, as shown in Fig. 9.11. The small differences between the published sensitivities, described by the dashed lines, and the sensitivity curve reproduced with the PROSPECT-CNP framework can be attributed to differences in how the analyses are conducted and the implementation of systematics. STEREO's model-independent fit utilizes a normalization factor obtained after the fit, resulting in an optimized parameter, in contrast to the $\frac{M_e}{P_e}$ factor used by PROSPECT. Despite these minor differences, the results were sufficient to proceed with the joint analysis.

9.5 Expected combined median sensitivity

The previous sections described the inputs from the STEREO collaboration required to perform a joint fit between PROSPECT and STEREO. Combined with the same inputs used in the PROSPECT-only analysis, the total size of the $M_{\mathrm{DPS},l,e}$ and $P_{\mathrm{DPS},l,e}$ objects in Eq. 9.2 is 1122. This is based on the PROSPECT data, which includes 5 periods, 6 baseline bins, and 33 E_{rec} bins, and the STEREO data, which consists of 2 phases, 6 baseline bins, and 11 E_{rec} bins. Consequently, the total covariance matrix, $V_{\mathrm{DPS,tot}}$, is a 1122x1122 matrix.

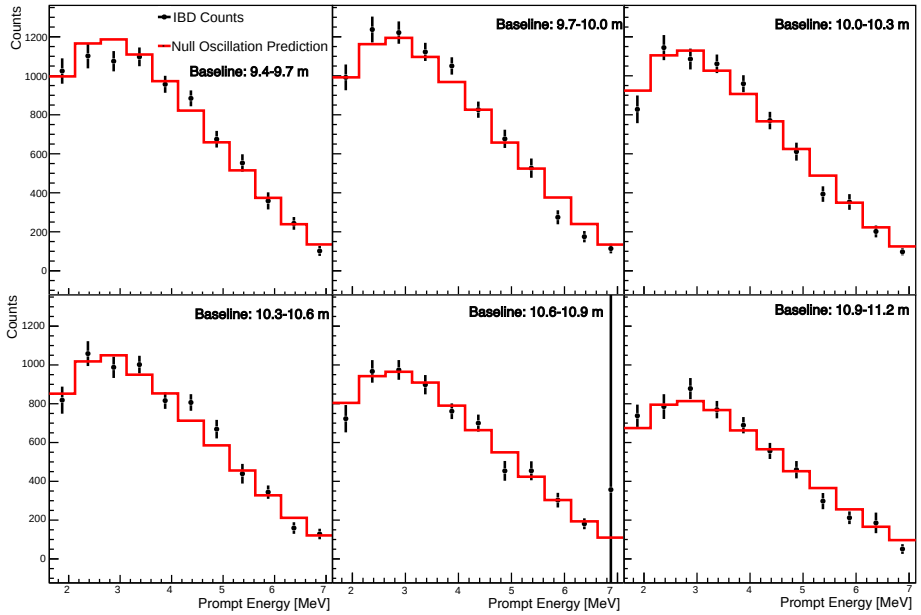


Figure 9.9: Phase II - Reconstructed visible prompt energy E_{rec} distributions (black) $M_{l,e}$ for STEREO. Also shown are the predicted prompt spectra per baseline $P_{l,e}$ for the null oscillation case (red).

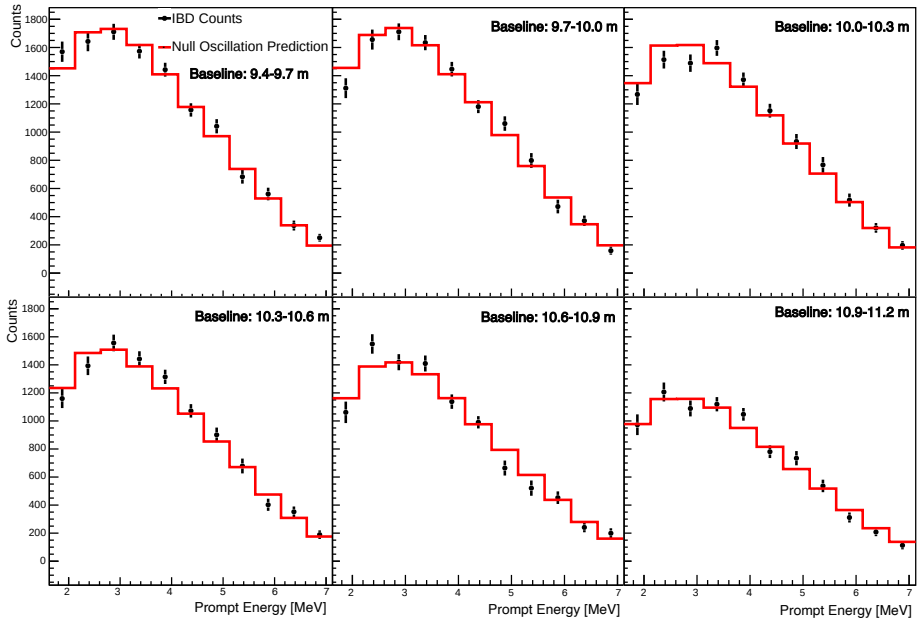


Figure 9.10: Phase III - Reconstructed visible prompt energy E_{rec} distributions (black) $M_{l,e}$ for STEREO. Also shown are the predicted prompt spectra per baseline $P_{l,e}$ for the null oscillation case (red).

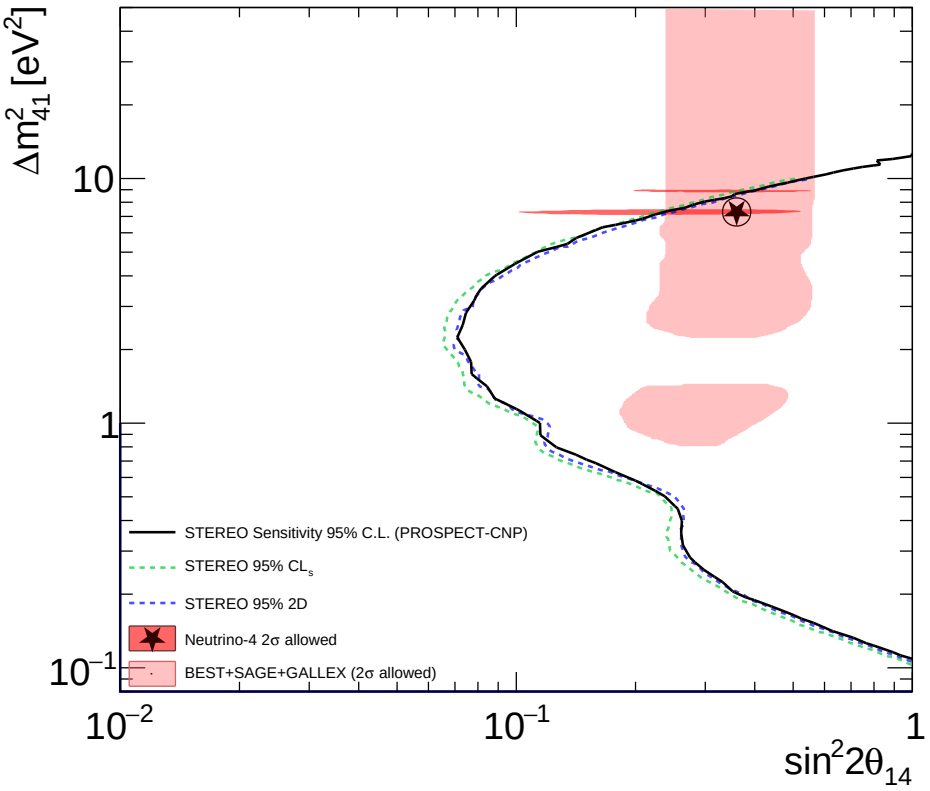


Figure 9.11: The expected median combined sensitivity for STEREO Phases I and II, as reproduced using the PROSPECT-CNP framework. The plot also includes the original sensitivity projections reported by STEREO, demonstrating strong agreement with the reproduced results.

For the remainder of this chapter, the model-independent χ^2_{CNP} with statistic $\Delta_{l,e} = M_{l,e} - M_e \frac{P_{l,e}}{P_e}$ will be referred to as Method 1 (M1), while the model-dependent approach used in the DPS analysis with $\Delta_{l,e} = M_{l,e} - P_{l,e}$ is denoted as Method 2 (M2). Before calculating sensitivity contours using these inputs, the uncertainty from the Daya Bay reference spectrum, $V_{\text{tot},\hat{s}_{\text{dyb}}}$, must be included. This is the only systematic uncertainty considered to be correlated across baseline, period/phase, and experiments.

9.5.1 Incorporating Daya Bay's ^{235}U model uncertainty

The procedure for including $V_{\text{tot},\hat{s}_{\text{dyb}}}$ in the fit is similar to the one used to incorporate STEREO's baseline-correlated uncertainties, as outlined in Section 9.4.2, with the additional consideration of correlations between PROSPECT periods and STEREO phases. For example, this matrix can be generated to account for correlations between period 1 of PROSPECT and phase 2 of STEREO using a joint response matrix, $R_{\text{DPS,joint}}$, which includes the response matrices for all live segments in PROSPECT's period 1 and all cells in STEREO's phase 2. Consequently, a model uncertainty covariance matrix in prompt space, $V_{\text{dyb,prompt}}$, can be constructed as

$$s_{dyb,prompt} = \begin{pmatrix} s^{pros_1}_{prompt} \\ s^{ste_{II}}_{prompt} \end{pmatrix} = \begin{pmatrix} R^{0,1}_{\text{pros}} \\ \vdots \\ R^{153,1}_{\text{pros}} \\ R^{1,\text{II}}_{\text{ste}} \\ \vdots \\ R^{6,\text{II}}_{\text{ste}} \end{pmatrix} \cdot \hat{s}_{dyb} \tag{9.6}$$

$$V_{dyb,prompt} = \begin{pmatrix} V_{prompt}^{pros_1} & V_{prompt}^{pros_1,ste_{II}} \\ V_{prompt}^{ste_{II},pros_1} & V_{prompt}^{ste_{II}} \end{pmatrix} = \begin{pmatrix} R_{\text{pros}}^{0,1} \\ \vdots \\ R_{\text{pros}}^{153,1} \\ R_{\text{ste}}^{1,\text{II}} \\ \vdots \\ R_{\text{ste}}^{6,\text{II}} \end{pmatrix} \cdot V_{\text{tot},\hat{s}_{\text{dyb}}} \cdot \begin{pmatrix} R_{\text{pros}}^{0,1} \\ \vdots \\ R_{\text{pros}}^{153,1} \\ R_{\text{ste}}^{1,\text{II}} \\ \vdots \\ R_{\text{ste}}^{6,\text{II}} \end{pmatrix}^T \tag{9.7}$$

Before calculating the final reduced covariance matrix, it is important to note that when incorporating the PROSPECT inputs, a response matrix is provided for each segment rather than for each baseline. This requires modifications to $s_{\text{prompt}}^{\text{pros},1}$, $V_{\text{prompt}}^{\text{pros}_1}$, $V_{\text{prompt}}^{\text{pros}_1,\text{ste}_{\text{II}}}$, and $V_{\text{prompt}}^{\text{ste}_{\text{II}},\text{pros}_1}$ to ensure that the contributions from each segment are correctly mapped to their corresponding baseline bins. The modified inputs are denoted as $\tilde{s}_{\text{prompt}}^{\text{pros}_1}$, $\tilde{V}_{\text{prompt}}^{\text{pros}_1}$, $\tilde{V}_{\text{prompt}}^{\text{pros}_1,\text{ste}_{\text{II}}}$, and $\tilde{V}_{\text{prompt}}^{\text{ste}_{\text{II}},\text{pros}_1}$, such that the reduced covariance matrix $\overline{V}_{\text{dyb,prompt}}$ for this case can be computed as:

$$\overline{V}_{\text{dyb,prompt}} = \begin{pmatrix} \frac{\tilde{V}_{\text{prompt}}^{\text{pros}_1}}{\tilde{s}_{\text{prompt}}^{\text{pros},1} \cdot \tilde{s}_{\text{prompt}}^{\text{pros},1}} & \frac{\tilde{V}_{\text{prompt}}^{\text{pros}_1,\text{ste}_{\text{II}}}}{\tilde{s}_{\text{prompt}}^{\text{pros},1} \cdot s_{\text{prompt}}^{\text{ste,II}}} \\ \frac{\tilde{V}_{\text{prompt}}^{\text{ste}_{\text{II}},\text{pros}_1}}{s_{\text{prompt}}^{\text{ste,II}} \cdot \tilde{s}_{\text{prompt}}^{\text{pros},1}} & \frac{V_{\text{prompt}}^{\text{ste}_{\text{II}}}}{s_{\text{prompt}}^{\text{ste,II}} \cdot s_{\text{prompt}}^{\text{ste,II}}} \end{pmatrix} \tag{9.8}$$

where the diagonal elements correspond to the reduced covariance matrices for PROSPECT's period 1 and STEREO's phase 2, while the off-diagonal elements represent contributions to the cumulative reduced covariance matrix describing the correlation between the experimental periods. Fig. 9.12 illustrates both of the off-diagonal terms in Eq. 9.8, showing the difference in E_{rec} binning between the experiments, which results in non-square off-diagonal reduced covariance matrices.

This procedure was repeated for all PROSPECT periods and STEREO phases, resulting in the total reduced model uncertainty covariance matrix, $\overline{V}_{\text{dyb,prompt,tot}}$ illustrated in Fig. 9.13.

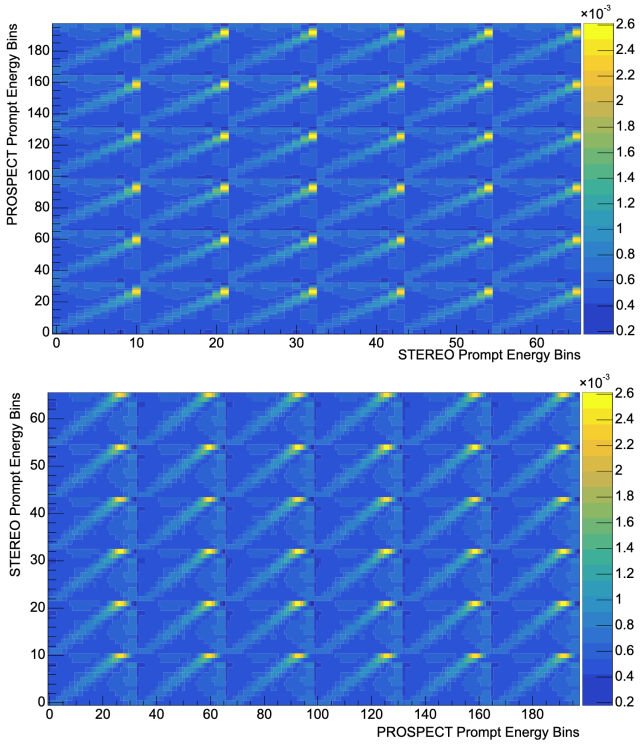


Figure 9.12: Model uncertainty reduced covariance matrices illustrating the correlations between PROSPECT's period 1 and STEREO's phase 2.

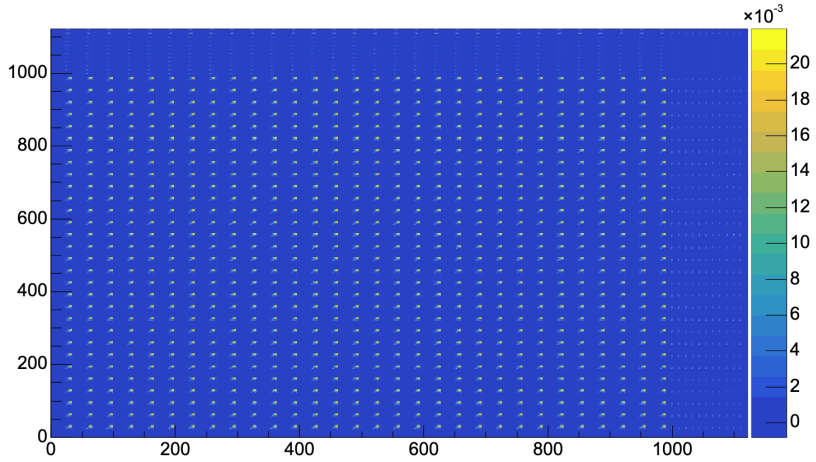


Figure 9.13: Total reduced model uncertainty covariance matrix for all PROSPECT periods and STEREO phases.

9.5.2 Current Results

After a detailed description of all the inputs incorporated into the DPS analysis, the expected sensitivity for this joint effort can be calculated. Following a $\chi^2_{CNP,DPS}$ grid search, as detailed in Section 8.4.3, the Gaussian CL_s method was used to determine the sensitivity. Fig. 9.14 presents a comparison of sensitivity contours obtained with different inputs and methods. This figure shows the final PROSPECT-only sensitivity obtained with Method 1 (M1) and the impact of combining PROSPECT and STEREO data using M1. Additionally, it shows the combined sensitivity for PROSPECT and STEREO using Method 2 (M2), where an increase in sensitivity is observed due to the inclusion of spectral shape information constrained by the reference spectrum from Daya Bay.

The most significant improvement in phase space coverage is observed in the region of $\Delta m^2_{41} < 3$ eV^2, attributed to the inclusion of Daya Bay inputs, which allow for a "near-far" comparison. As of this writing, a full exclusion contour and hypothesis testing exercise have not yet been performed. These procedures require inputs from separate analysis groups within the DPS collaboration regarding the compatibility of the spectra measured by all three experiments, as well as a potential refinement of the ^{235}U unfolded spectrum from Daya Bay. However, this effort demonstrates the potential of a joint analysis among all three experiments in achieving a phase-space coverage unattainable by any single experiment. These results will serve as inputs for a comprehensive fitting framework aimed at performing both spectrum and oscillation joint fits.

9.6 Chapter Summary

This chapter presented the current progress of a new joint analysis effort involving the Daya Bay, PROSPECT, and STEREO collaborations. While PROSPECT has previously collaborated with Daya Bay and STEREO individually, this marks the

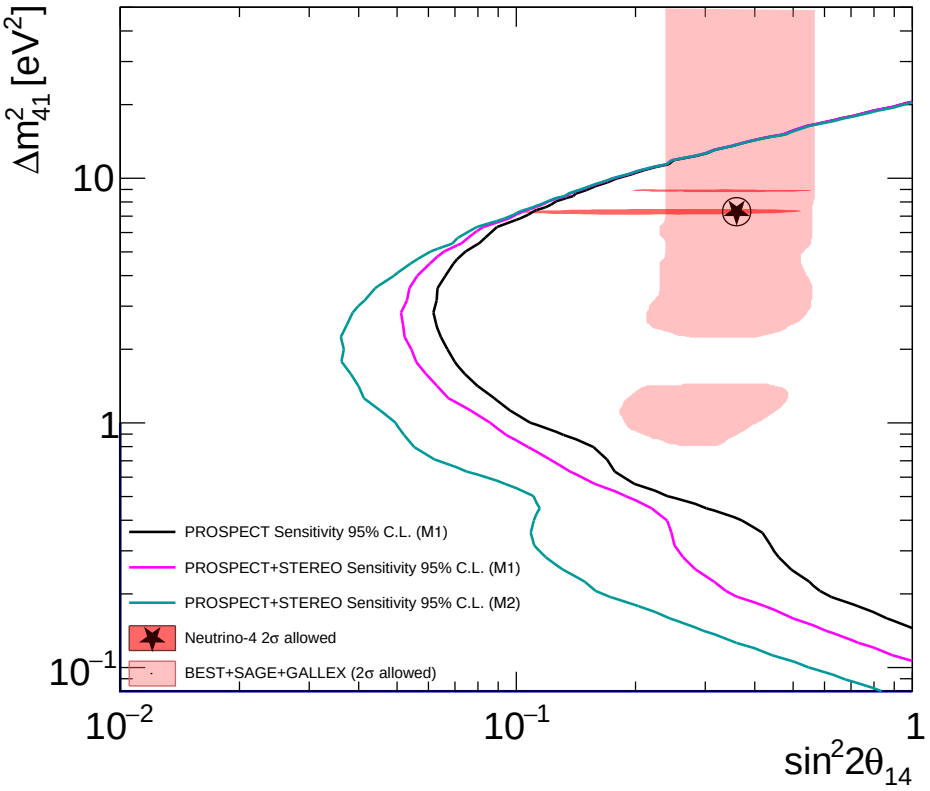


Figure 9.14: The expected median combined sensitivity for the DPS analysis is shown by the cyan curve. The plot also includes results from the PROSPECT-only and PROSPECT+STEREO model-independent analyses. A significant increase in sensitivity is observed with the addition of STEREO data and by using the Daya Bay spectrum as a model for the spectral shape.

first instance where all three experiments have joined forces for a unified analysis. Although the ultimate goal is to perform a comprehensive study of both the spectral shape and neutrino oscillations, the current focus for PROSPECT has been on an oscillation-only approach using spectra solely from ^{235}U. This choice was driven by the capabilities of the PROSPECT-CNP framework, which supports multi-period oscillation studies.

The PROSPECT-CNP framework has been adapted to accommodate different detector geometries, reactor power characteristics, and energy binning schemes, enabling the integration of STEREO data. A preliminary result of the expected median sensitivity was achieved by combining data from PROSPECT and STEREO and using a model-dependent analysis that utilizes Daya Bay's ^{235}U data as the reference spectral shape. This result highlights the promising potential of this collaborative effort to significantly extend the phase space coverage for sterile neutrino searches beyond what any single experiment could achieve alone.

Chapter 10

Conclusion

Discrepancies reported by reactor-based antineutrino experiments, such as the Reactor Antineutrino Anomaly (RAA), have motivated the development of high-precision short-baseline experiments to search for the hypothesized sterile neutrino as a potential solution to these discrepancies. One example of a successful high-precision experiment is PROSPECT (Precision Reactor Oscillation and Spectrum Experiment), which was designed to search for eV-scale sterile neutrino oscillations. Using approximately 4 tons of pulse shape discrimination (PSD)-capable ^{6}Li-doped liquid scintillator as a target within a highly segmented detector, PROSPECT demonstrated exceptional on-surface antineutrino detection capabilities, detecting over 60,000 inverse beta decay (IBD) events with an average signal-to-background ratio of 4.11.

This dissertation presents the development of the final multi-period data set collected by the PROSPECT-I detector at the compact High Flux Isotope Reactor (HFIR) at Oak Ridge National Laboratory, along with the final physics analyses of the ^{235}U spectral shape and the search for sterile neutrino oscillations. Using the new data set, one of the most precise measurements of the ^{235}U antineutrino energy spectrum from a high-enriched uranium (HEU) reactor was achieved through a simultaneous multi-period unfolding using the WienerSVD formalism. This measurement revealed

consistent high-energy spectral excesses between HEU and LEU reactors, placing new constraints on the origin of the observed 5–7 MeV excess. These findings align with recent advances in reactor modeling and fission beta measurements, suggesting that the predicted antineutrino spectra for all primary fission isotopes may be inaccurate.

Furthermore, a new neutrino oscillation analysis has set world-leading limits on short-baseline eV-scale sterile neutrino oscillations, with results consistent with the null hypothesis of no sterile neutrino oscillations. The data exclude the existence of sterile neutrinos at a 95% confidence level in regions above 3 eV^2, previously unexplored by terrestrial experiments, including the entire parameter space below 10 eV^2 suggested by the recently updated Gallium Anomaly. Additionally, the best-fit point from the Neutrino-4 reactor experiment's claimed observation of short-baseline oscillation is ruled out at more than five standard deviations.

Lastly, this final data set can be combined with results from other experiments to enhance the search for sterile neutrinos. The first sensitivity projections for a combined model-dependent fit among the Daya Bay, STEREO, and PROSPECT experiments have been obtained, providing additional evidence supporting the null oscillation hypothesis.

Bibliography

[1] *Eljen EJ-309 Liquid Scintillator*, 2016. http://www.eljentechnology.com/index.php/products/liquid-scintillators/73-ej-309. 60

[2] Hans - Jürgen Daum. Neutrino physics with the frejus underground detector. *Nuclear Physics B - Proceedings Supplements*, 14(2):167–177, 1990. ISSN 0920-5632. doi: https://doi.org/10.1016/0920-5632(90)90378-8. URL https://www.sciencedirect.com/science/article/pii/0920563290903788. 24

[3] M. G. Aartsen et al. The IceCube Neutrino Observatory: Instrumentation and Online Systems. *JINST*, 12(03):P03012, 2017. doi: 10.1088/1748-0221/12/03/P03012. 24

[4] M.G. et al. (IceCube Collaboration) Aartsen and K. et al. (Super-Kamiokande Collaboration) Abe. Real-time supernova neutrino detection in super-kamiokande and icecube. *Astroparticle Physics*, 123:102489, 2021. doi: 10.1016/j.astropartphys.2021.102489. 240

[5] K. N. Abazajian et al. Light sterile neutrinos: A white paper, 2012. 27, 30, 32

[6] M Abbes et al. The Bugey-3 neutrino detector. *Nucl. Instrum. Meth. A*, 374: 164–187, 1996. doi: 10.1016/0168-9002(96)00220-3. 40

[7] J. N. others Abdurashitov and SAGE Collaboration. Solar neutrino flux measurements by the Soviet-American gallium experiment (SAGE) for half the

22-year solar cycle. *Soviet Journal of Experimental and Theoretical Physics*, 95: 181–193, August 2002. doi: 10.1134/1.1506424. 22, 31, 187

[8] K. Abe and others. Solar neutrino results in Super-Kamiokande-III. , 83(5): 052010, March 2011. doi: 10.1103/PhysRevD.83.052010. 23

[9] K. Abe et al. Indication of Electron Neutrino Appearance from an Accelerator-produced Off-axis Muon Neutrino Beam. *Phys. Rev. Lett.*, 107:041801, 2011. doi: 10.1103/PhysRevLett.107.041801. 39

[10] S. Abe et al. Precision Measurement of Neutrino Oscillation Parameters with KamLAND. *Phys. Rev. Lett.*, 100:221803, 2008. doi: 10.1103/PhysRevLett.100.221803. 37, 39, 40

[11] Y. Abe et al. Reactor electron antineutrino disappearance in the Double Chooz experiment. *Phys. Rev. D*, 86:052008, 2012. doi: 10.1103/PhysRevD.86.052008. 39

[12] Y. Abe et al. Improved measurements of the neutrino mixing angle θ_{13} with the Double Chooz detector. *JHEP*, 1410:086, 2014. doi: 10.1007/JHEP1502(2015)074,10.1007/JHEP10(2014)086. [Erratum: JHEP1502,074(2015)]. 58

[13] B Abi, R Acciarri, M.A Acero, G Adamov, D Adams, M Adinolfi, F Filthaut, S.B Henry, C Mariani, J Matthews, T Miedema, W.T Wu, V Zutshi, and R Zwaska. Long-baseline neutrino oscillation physics potential of the dune experiment: Dune collaboration. *The European physical journal. C, Particles and fields*, 80(10):1–34, 2020. ISSN 1434-6044. 26

[14] P. Abratenko et al. Search for an Excess of Electron Neutrino Interactions in MicroBooNE Using Multiple Final-State Topologies. *Phys. Rev. Lett.*, 128(24): 241801, 2022. doi: 10.1103/PhysRevLett.128.241801. 228

[15] Y. Abreu and others. SoLid: a short baseline reactor neutrino experiment. *Journal of Instrumentation*, 16(02):P02025–P02025, feb 2021. doi: 10.1088/

1748-0221/16/02/p02025. URL https://doi.org/10.1088/1748-0221/16/02/p02025. 40

[16] C. V. Achar et al. Detection of muons produced by cosmic ray neutrinos deep underground. *Phys. Lett.*, 18:196–199, 1965. doi: 10.1016/0031-9163(65)90712-2. 24

[17] P. Adamson and others. Measurement of ν_μ and ν_e events in an off-axis horn-focused neutrino beam. *Phys. Rev. Lett.*, 102:211801, May 2009. doi: 10.1103/PhysRevLett.102.211801. URL https://link.aps.org/doi/10.1103/PhysRevLett.102.211801. 27

[18] P. Adamson et al. Improved search for muon-neutrino to electron-neutrino oscillations in MINOS. *Phys. Rev. Lett.*, 107:181802, 2011. doi: 10.1103/PhysRevLett.107.181802. 39

[19] D. et al. (Daya Bay Collaboration) Adey. Search for light sterile neutrino mixing with the daya bay reactor neutrino experiment. *Physical Review Letters*, 128 (24):241801, 2022. doi: 10.1103/PhysRevLett.128.241801. 244

[20] S. et al. (KM3NeT Collaboration) Adrian-Martinez and M.G. et al. (IceCube Collaboration) Aartsen. Sensitivity of km3net/orca and pingu to neutrino mass ordering. *European Physical Journal C*, 79:234, 2019. doi: 10.1140/epjc/s10052-019-6675-3. 240

[21] A. I. Afonin, A. A. Borovoi, Yu. L. Dobrynin, S. N. Ketov, V. I. Kopeikin, L. A. Mikaelyan, M. D. Skorokhvatov, S. V. Tolokonnikov, and A. N. Kheruvimov. NEUTRINO EXPERIMENT IN THE REACTOR OF THE ROVNO ATOMIC POWER PLANT: CROSS-SECTION FOR INVERSE BETA DECAY. *JETP Lett.*, 41:435–438, 1985. 40

[22] N Agafonova and others. Final results of the opera experiment on ν_τ appearance in the cngs neutrino beam. *Physical review letters*, 120(21):211801–211801, 2018. ISSN 1079-7114. 26

[23] N. Aghanim et al. Planck 2018 results. VI. Cosmological parameters. 2018. 233

[24] N. Aghanim et al. Planck 2018 results. VIII. Gravitational lensing. 2018. 233

[25] N. Aghanim et al. Planck 2018 results. V. CMB power spectra and likelihoods. 2019. 233

[26] M Aglietta, G Badino, G Bologna, C Castagnoli, A Castellina, B. D'Ettorre Piazzoli, W Fulgione, P Galeotti, G Mannocchi, P Picchi, O Saavedra, G Trinchero, and S Vernetto. Experimental study of upward stopping muons in NUSEX. *Europhysics Letters (EPL)*, 15(5):559–564, jul 1991. doi: 10.1209/0295-5075/15/5/015. URL `https://doi.org/10.1209/0295-5075/15/5/015`. 24

[27] M. et al. (GERDA Collaboration) Agostini, J.B. et al. (EXO-200 Collaboration) Albert, A. et al. (KamLAND-Zen Collaboration) Gando, and C.E. et al. (MAJORANA Collaboration) Aalseth. Search for neutrinoless double-beta decay with gerda, exo-200, kamland-zen, and majorana demonstrator: Joint analysis. *Nature Physics*, 18:145–151, 2022. doi: 10.1038/s41567-021-01312-5. 240

[28] A. Aguilar and others. Evidence for neutrino oscillations from the observation of $\overline{\nu}_e$ appearance in a $\overline{\nu}_\mu$ beam. *Phys. Rev. D*, 64:112007, Nov 2001. doi: 10.1103/PhysRevD.64.112007. URL `https://link.aps.org/doi/10.1103/PhysRevD.64.112007`. 27, 31

[29] A. A. Aguilar-Arevalo and others. Event excess in the miniboone search for $\overline{\nu}_\mu \rightarrow \overline{\nu}_e$ oscillations. *Phys. Rev. Lett.*, 105:181801, Oct 2010. doi: 10.

1103/PhysRevLett.105.181801. URL https://link.aps.org/doi/10.1103/PhysRevLett.105.181801. 27

[30] A. A. Aguilar-Arevalo et al. A Search for Electron Neutrino Appearance at the $\Delta m^2 \sim 1eV^2$ Scale. *Phys. Rev. Lett.*, 98:231801, 2007. doi: 10.1103/PhysRevLett.98.231801. 27, 31

[31] A. A. Aguilar-Arevalo et al. Unexplained Excess of Electron-Like Events From a 1-GeV Neutrino Beam. *Phys. Rev. Lett.*, 102:101802, 2009. doi: 10.1103/PhysRevLett.102.101802. 27

[32] A. A. Aguilar-Arevalo et al. Improved Search for $\bar{\nu}_\mu \to \bar{\nu}_e$ Oscillations in the MiniBooNE Experiment. *Phys. Rev. Lett.*, 110:161801, 2013. doi: 10.1103/PhysRevLett.110.161801. 27

[33] B. Aharmim and others. Electron energy spectra, fluxes, and day-night asymmetries of ^{8}b solar neutrinos from measurements with nacl dissolved in the heavy-water detector at the sudbury neutrino observatory. *Phys. Rev. C*, 72:055502, Nov 2005. doi: 10.1103/PhysRevC.72.055502. URL https://link.aps.org/doi/10.1103/PhysRevC.72.055502. 23, 39

[34] S. N. Ahmed and others. Measurement of the total active ^{8}B solar neutrino flux at the sudbury neutrino observatory with enhanced neutral current sensitivity. *Phys. Rev. Lett.*, 92:181301, May 2004. doi: 10.1103/PhysRevLett.92.181301. URL https://link.aps.org/doi/10.1103/PhysRevLett.92.181301. 23, 39

[35] J. Ahn et al. *Phys. Rev. Lett.*, 108:191802, 2012. 39, 40, 58, 162, 178

[36] M. Aker, K. Altenmüller, M. Arenz, M. Babutzka, J. Barrett, S. Bauer, J. Behrens, T. Bergmann, A. Berlev, P. Bieringer, and et al. (KATRIN Collaboration). Search for light sterile neutrinos with the first four-week science run of the katrin experiment. *Physical Review D*, 105(7):072004, 2022. doi:

10.1103/PhysRevD.105.072004. URL https://doi.org/10.1103/PhysRevD.105.072004. 238

[37] M. Aker et al. Direct neutrino-mass measurement with sub-electronvolt sensitivity. *Nature Phys.*, 18(2):160–166, 2022. doi: 10.1038/s41567-021-01463-1. 17

[38] M. Aker et al. Improved eV-scale sterile-neutrino constraints from the second KATRIN measurement campaign. *Phys. Rev. D*, 105(7):072004, 2022. doi: 10.1103/PhysRevD.105.072004. 228

[39] O. A. Akindele and others. High energy physics opportunities using reactor antineutrinos, 2022. 34, 38, 183

[40] Y. Akrami et al. Planck 2018 results. I. Overview and the cosmological legacy of Planck. 2018. 233

[41] Shadab Alam et al. The clustering of galaxies in the completed SDSS-III Baryon Oscillation Spectroscopic Survey: cosmological analysis of the DR12 galaxy sample. *Mon. Not. Roy. Astron. Soc.*, 470:2617–2652, 2017. doi: 10.1093/mnras/stx721. 236

[42] A. et al. (ANTARES Collaboration) Albert and M.G. et al. (IceCube Collaboration) Aartsen. Joint point source search using data from icecube and antares neutrino telescopes. *The Astrophysical Journal*, 892:92, 2020. doi: 10.3847/1538-4357/ab791c. 240

[43] I Alekseev et al. Search for sterile neutrinos at the DANSS experiment. *Phys. Lett. B*, 787:56–63, 2018. doi: 10.1016/j.physletb.2018.10.038. 228

[44] V. I. Aleshin et al. A neutrino experiment at the Krasnoyarsk underground reactor. *Instrum. Exp. Tech.*, 51:499–505, 2008. doi: 10.1134/S0020441208040027. 40

[45] L Aliaga and others. Measurement of the neutrino mixing angle θ_{23} in nova. *Physical review letters*, 118(15):151802–151802, 2017. ISSN 1079-7114. 26

[46] W. W. M. Allison et al. Neutrino oscillation effects in Soudan-2 upward-stopping muons. *Phys. Rev. D*, 72:052005, 2005. doi: 10.1103/PhysRevD.72.052005. 24

[47] H. Almazán et al. Improved sterile neutrino constraints from the stereo experiment with 179 days of reactor-on data. *Phys. Rev. D*, 102:052002, Sep 2020. doi: 10.1103/PhysRevD.102.052002. URL `https://link.aps.org/doi/10.1103/PhysRevD.102.052002`. 36, 84, 162, 166, 178

[48] H. Almazán et al. Joint Measurement of the ^{235}U Antineutrino Spectrum by Prospect and Stereo. *Phys. Rev. Lett.*, 128(8):081802, 2022. doi: 10.1103/PhysRevLett.128.081802. 139, 164

[49] H. Almazán et al. STEREO neutrino spectrum of ^{235}U fission rejects sterile neutrino hypothesis. *Nature*, 613(7943):257–261, 2023. doi: 10.1038/s41586-022-05568-2. 40, 228, 237, 241, 244, 247, 249, 251, 252

[50] M. Altmann et al. Complete results for five years of GNO solar neutrino observations. *Phys. Lett. B*, 616:174–190, 2005. doi: 10.1016/j.physletb.2005.04.068. 22, 31, 187

[51] F. An and others. Neutrino physics with JUNO. *Journal of Physics G Nuclear Physics*, 43(3):030401, March 2016. doi: 10.1088/0954-3899/43/3/030401. 40, 236

[52] F. P. An et al. Observation of electron-antineutrino disappearance at daya bay. *Phys. Rev. Lett.*, 108:171803, Apr 2012. doi: 10.1103/PhysRevLett.108.171803. URL `https://link.aps.org/doi/10.1103/PhysRevLett.108.171803`. 58, 244

[53] F. P. An et al. The Detector System of The Daya Bay Reactor Neutrino Experiment. *Nucl. Instrum. Meth. A*, 811:133–161, 2016. doi: 10.1016/j.nima.2015.11.144. 39, 40, 162, 178

[54] F. P. An et al. *Nucl. Inst. Meth. A*, 940:230 – 242, 2019. 97

[55] F. P. An et al. Antineutrino Energy Spectrum Unfolding Based on the Daya Bay Measurement and Its Applications. *Chin. Phys. C*, 45:073001, 2021. doi: 10.1088/1674-1137/abfc38. URL `https://doi.org/10.1088/1674-1137/abfc38`. 163, 180, 183, 202, 238, 241, 246

[56] F. P. An et al. Joint Determination of Reactor Antineutrino Spectra from U235 and Pu239 Fission by Daya Bay and PROSPECT. *Phys. Rev. Lett.*, 128(8): 081801, 2022. doi: 10.1103/PhysRevLett.128.081801. 139, 164, 166

[57] F. P. An et al. Precision Measurement of Reactor Antineutrino Oscillation at Kilometer-Scale Baselines by Daya Bay. *Phys. Rev. Lett.*, 130(16):161802, 2023. doi: 10.1103/PhysRevLett.130.161802. 246

[58] Feng Peng An et al. Measurement of the Reactor Antineutrino Flux and Spectrum at Daya Bay. *Phys. Rev. Lett.*, 116(6):061801, 2016. doi: 10.1103/PhysRevLett.116.061801,10.1103/PhysRevLett.118.099902. [Erratum: Phys. Rev. Lett.118,no.9,099902(2017)]. 58

[59] Feng Peng An et al. Measurement of electron antineutrino oscillation based on 1230 days of operation of the Daya Bay experiment. *Phys. Rev. D*, 95(7): 072006, 2017. doi: 10.1103/PhysRevD.95.072006. 211

[60] F.P. An et al. Observation of electron-antineutrino disappearance at Daya Bay. *Phys. Rev. Lett.*, 108:171803, 2012. doi: 10.1103/PhysRevLett.108.171803. 39

[61] F.P. An et al. Improved measurement of the reactor antineutrino flux and spectrum at daya bay. *Chinese Physics C*, 41(1):013002, jan 2017. doi: 10.

1088/1674-1137/41/1/013002. URL https://doi.org/10.1088/1674-1137/41/1/013002. 178

[62] F.P. An et al. Evolution of the Reactor Antineutrino Flux and Spectrum at Daya Bay. *Phys. Rev. Lett.*, 118(25):251801, 2017. doi: 10.1103/PhysRevLett.118.251801. 189

[63] F.P. An et al. Improved Measurement of the Evolution of the Reactor Antineutrino Flux and Spectrum at Daya Bay. 2022. doi: 10.48550/ARXIV.2210.01068. URL https://arxiv.org/abs/2210.01068. 36

[64] F.P. et al. (Daya Bay Collaboration) An, S.B. et al. (RENO Collaboration) Kim, and Y. et al. (Double Chooz Collaboration) Abe. Combined analysis of reactor neutrino experiments daya bay, reno, and double chooz: Measurement of mixing angle θ_{13}. *Journal of High Energy Physics*, 2018(10):123, 2018. doi: 10.1007/JHEP10(2018)123. 240

[65] D. Jason Koskinen and. Atmospheric neutrino results from IceCube-DeepCore and plans for PINGU. *Journal of Physics: Conference Series.*, 888:012023, sep 2017. doi: 10.1088/1742-6596/888/1/012023. URL https://doi.org/10.1088/1742-6596/888/1/012023. 24

[66] N Tolich and. Final results from SNO. *Journal of Physics: Conference Series.*, 375(4):042049, jul 2012. doi: 10.1088/1742-6596/375/1/042049. URL https://doi.org/10.1088/1742-6596/375/1/042049. 23, 39

[67] M. Andriamirado and others. Prospect-ii physics opportunities, 2021. URL https://arxiv.org/abs/2107.03934. 236

[68] M. Andriamirado and others. Final measurement of the ^{235}U antineutrino energy spectrum with the prospect-i detector at hfir. *Phys. Rev. Lett.*, 131:021802, Jul 2023. doi: 10.1103/PhysRevLett.131.021802. URL https://link.aps.org/doi/10.1103/PhysRevLett.131.021802. 154, 160, 169, 179, 184

[69] M. Andriamirado et al. Limits on sub-gev dark matter from the prospect reactor antineutrino experiment. *Phys. Rev. D*, 104:012009, Jul 2021. doi: 10.1103/PhysRevD.104.012009. URL `https://link.aps.org/doi/10.1103/PhysRevD.104.012009`. 139

[70] M. Andriamirado et al. Improved short-baseline neutrino oscillation search and energy spectrum measurement with the prospect experiment at hfir. *Phys. Rev. D*, 103:032001, Feb 2021. doi: 10.1103/PhysRevD.103.032001. URL `https://link.aps.org/doi/10.1103/PhysRevD.103.032001`. 40, 53, 79, 83, 87, 92, 93, 96, 102, 103, 106, 107, 109, 115, 117, 118, 120, 121, 123, 125, 127, 129, 132, 134, 136, 137, 138, 139, 140, 160, 162, 164, 165, 178, 180, 183, 188, 190, 191, 224, 227

[71] M Andriamirado. et al. Prospect-ii physics opportunities. *Journal of Physics G: Nuclear and Particle Physics*, 49(7):070501, jun 2022. doi: 10.1088/1361-6471/ac48a4. URL `https://dx.doi.org/10.1088/1361-6471/ac48a4`. 183

[72] M. Apollonio et al. Limits on neutrino oscillations from the CHOOZ experiment. *Phys. Lett. B*, 466:415–430, 1999. doi: 10.1016/S0370-2693(99)01072-2. 39

[73] B. Armbruster et al. Upper limits for neutrino oscillations muon-anti-neutrino —> electron-anti-neutrino from muon decay at rest. *Phys. Rev. D*, 65:112001, 2002. doi: 10.1103/PhysRevD.65.112001. 27

[74] Ashenfelter et al. Measurement of the antineutrino spectrum from 235u fission at hfir with prospect. *Physical review letters*, 122(25):251801–251801, 2019. ISSN 1079-7114. 139, 164, 165, 180

[75] J. Ashenfelter and others. The PROSPECT Physics Program. *ArXiv e-prints*, December 2015. 85

[76] J. Ashenfelter and others. Background radiation measurements at high power research reactors. *Nuclear Instruments and Methods in Physics Research A*, 806:401–419, January 2016. doi: 10.1016/j.nima.2015.10.023. 51

[77] J. Ashenfelter and others. Lithium-loaded liquid scintillator production for the PROSPECT experiment. *Journal of Instrumentation*, 14(03):P03026–P03026, mar 2019. doi: 10.1088/1748-0221/14/03/p03026. URL `https://doi.org/10.1088/1748-0221/14/03/p03026`. 59, 61

[78] J. Ashenfelter, A. B. Balantekin, C. Baldenegro, H. R. Band, C. D. Bass, et al. The prospect reactor antineutrino experiment. *Nuclear Instruments and Methods in Physics Research, Section A: Accelerators, Spectrometers, Detectors and Associated Equipment*, 922:287–309, Apr 2019. ISSN 0168-9002. doi: 10.1016/j.nima.2018.12.079. 51, 54, 57, 60, 63, 64, 66, 68, 77, 79, 115

[79] J. Ashenfelter et al. Light Collection and Pulse-Shape Discrimination in Elongated Scintillator Cells for the PROSPECT Reactor Antineutrino Experiment. *JINST*, 10(11):P11004, 2015. doi: 10.1088/1748-0221/10/11/P11004. 75, 84

[80] J. Ashenfelter et al. Background Radiation Measurements at High Power Research Reactors. *Nucl. Instrum. Meth.*, A806:401–419, 2016. doi: 10.1016/j.nima.2015.10.023. 54

[81] J. Ashenfelter et al. Performance of a segmented ^{6}Li-loaded liquid scintillator detector for the PROSPECT experiment. *JINST*, 13(06):P06023, 2018. doi: 10.1088/1748-0221/13/06/P06023. 75, 84

[82] J. Ashenfelter et al. First search for short-baseline neutrino oscillations at HFIR with PROSPECT. *Phys. Rev. Lett.*, 121:251802, 2018. 139, 188, 190, 191, 227

[83] J. Ashenfelter et al. The radioactive source calibration system of the prospect reactor antineutrino detector. *Nuclear Instruments and Methods in Physics*

Research Section A: Accelerators, Spectrometers, Detectors and Associated Equipment, 944:162465, November 2019. ISSN 0168-9002. doi: 10.1016/j.nima.2019.162465. URL http://dx.doi.org/10.1016/j.nima.2019.162465. 67, 69, 70, 72, 73

[84] P Astier et al. Final NOMAD results on muon-neutrino —> tau-neutrino and electron-neutrino —> tau-neutrino oscillations including a new search for tau-neutrino appearance using hadronic tau decays. *Nucl. Phys. B*, 611:3–39, 2001. doi: 10.1016/S0550-3213(01)00339-X. 27

[85] P. Astier et al. Search for nu(mu) —> nu(e) oscillations in the NOMAD experiment. *Phys. Lett. B*, 570:19–31, 2003. doi: 10.1016/j.physletb.2003.07.029. 27

[86] A. Balantekin et al. *Phys. Rev. C*, 101:054605, 2020. 55

[87] V. Barger and K. Whisnant. The effects of neutrino oscillations with one mass scale on the atmospheric neutrino flux. *Physics Letters B*, 209(2): 365–372, 1988. ISSN 0370-2693. doi: https://doi.org/10.1016/0370-2693(88)90964-1. URL https://www.sciencedirect.com/science/article/pii/0370269388909641. 25

[88] V. V. Barinov et al. Search for electron-neutrino transitions to sterile states in the BEST experiment. *Phys. Rev. C*, 105(6):065502, 2022. doi: 10.1103/PhysRevC.105.065502. 188, 189, 192, 194, 228, 231

[89] Barry C. Barish. Atmospheric neutrinos in macro. *Nuclear Physics B - Proceedings Supplements*, 91(1):141–146, 2001. ISSN 0920-5632. doi: https://doi.org/10.1016/S0920-5632(00)00934-8. URL https://www.sciencedirect.com/science/article/pii/S0920563200009348. Neutrino 2000. 24

[90] R. Becker-Szendy et al. A Search for muon-neutrino oscillations with the IMB detector. *Phys. Rev. Lett.*, 69:1010–1013, 1992. doi: 10.1103/PhysRevLett.69.1010. 24

[91] F. Bergsma and others. A search for neutrino oscillations. *Zeitschrift für Physik C Particles and Fields*, 40(2):171–192, Jun 1988. ISSN 1431-5858. doi: 10.1007/BF01555880. URL `https://doi.org/10.1007/BF01555880`. 27

[92] H. Bethe and R. Peierls. The neutrino. *Nature*, 133(3362):532–532, Apr 1934. ISSN 0028-0836. doi: 10.1038/133532a0. 7

[93] Florian Beutler, Chris Blake, Matthew Colless, D. Heath Jones, Lister Staveley-Smith, Lachlan Campbell, Quentin Parker, Will Saunders, and Fred Watson. The 6dF Galaxy Survey: Baryon Acoustic Oscillations and the Local Hubble Constant. *Mon. Not. Roy. Astron. Soc.*, 416:3017–3032, 2011. doi: 10.1111/j.1365-2966.2011.19250.x. 236

[94] S. M. Bilenky. Bruno pontecorvo and neutrino oscillations. *Advances in High Energy Physics*, 2013:1–9, 2013. ISSN 1687-7357. doi: 10.1155/2013/873236. 15

[95] Samoil M. Bilenky and B. Pontecorvo. The Quark-Lepton Analogy and the Muonic Charge. *Yad. Fiz.*, 24:603–608, 1976. 16

[96] John B. Birks. *The Theory and practice of scintillation counting*. 1964. 98

[97] F. Boehm et al. Final results from the Palo Verde neutrino oscillation experiment. *Phys. Rev. D*, 64:112001, 2001. doi: 10.1103/PhysRevD.64.112001. 39

[98] Rene Brun and Fons Rademakers. ROOT - An Object Oriented Data Analysis Framework. *Nuclear Instrumentation Methods*, A389:81 – 86, 1997. doi: 10.1016/S0168-9002(97)00048-X. 82

[99] C. Buck et al. Investigating the spectral anomaly with different reactor antineutrino experiments. *Phys. Lett. B*, 765:159–162, 2017. ISSN 0370-2693. doi: https://doi.org/10.1016/j.physletb.2016.11.062. URL https://www.sciencedirect.com/science/article/pii/S0370269316307456. 180

[100] D. Casper and others. Measurement of atmospheric neutrino composition with the imb-3 detector. *Phys. Rev. Lett.*, 66:2561–2564, May 1991. doi: 10.1103/PhysRevLett.66.2561. URL https://link.aps.org/doi/10.1103/PhysRevLett.66.2561. 24

[101] G. Cheng and others. Dual baseline search for muon antineutrino disappearance at 0.1 $\mathrm{ev}^2 lt; \Delta m^2 lt; 100\ \mathrm{ev}^2$. *Phys. Rev. D*, 86:052009, Sep 2012. doi: 10.1103/PhysRevD.86.052009. URL https://link.aps.org/doi/10.1103/PhysRevD.86.052009. 27

[102] B. T. Cleveland, T. Daily, R. Jr. Davis, J. R. Distel, K. Lande, et al. Measurement of the solar electron neutrino flux with the homestake chlorine detector. *The Astrophysical Journal*, 496(1):505–526, Mar 1998. ISSN 0004-637X. doi: 10.1086/305343. 15

[103] MicroBooNE Collaboration. Search for an excess of electron neutrino interactions in microboone using multiple final state topologies. *Physical Review Letters*, 128(24):241801, 2022. doi: 10.1103/PhysRevLett.128.241801. URL https://doi.org/10.1103/PhysRevLett.128.241801. 238

[104] C L Cowan, Jr, F.B.f Kruse H.W. Reines, F.f Harrison, and A D McGuire. Detection of the free neutrino: A confirmation. *Science See Saiensu*, Vol: 124, 7 1956. doi: 10.1126/science.124.3212.103. URL https://www.osti.gov/biblio/4360254. 1, 7

[105] Glen Cowan, Kyle Cranmer, Eilam Gross, and Ofer Vitells. Asymptotic formulae for likelihood-based tests of new physics. *Eur. Phys. J. C*, 71:1554,

2011. doi: 10.1140/epjc/s10052-011-1554-0. [Erratum: Eur.Phys.J.C 73, 2501 (2013)]. 307

[106] G. Danby, J. Gaillard, K. Goulianos, L. M. Lederman, N. Mistry, M. Schwartz, and J. Steinberger. Observation of high-energy neutrino reactions and the existence of two kinds of neutrinos. *Physical Review Letters*, 9(1):36–44, 1962. doi: 10.1103/PhysRevLett.9.36. 8

[107] R. Davis. Solar neutrinos. ii. experimental. *Physical Review Letters*, 12(11): 303–305, Mar 1964. ISSN 0031-9007. doi: 10.1103/PhysRevLett.12.303. 15

[108] H. de Kerret, T. Abrahão, H. Almazan, J. C. dos Anjos, S. Appel, et al. Double chooz θ_{13} measurement via total neutron capture detection. *Nature Physics*, 16 (5):558–564, May 2020. ISSN 1745-2481. doi: 10.1038/s41567-020-0831-y. 47

[109] H. de Kerret et al. The Double Chooz antineutrino detectors. 1 2022. 39, 40, 162, 178

[110] J. Dorenbosch et al. Prompt Neutrino Production in 400-GeV Proton - Copper Interactions. *Z. Phys. C*, 40:497, 1988. doi: 10.1007/BF01560221. 27

[111] F. Dydak et al. A search for ν_μ oscillations in the δm^2 range $0.3 - 90\,\mathrm{eV}^2$. *Phys. Lett.*, B134:281, 1984. 27

[112] William T Eadie, Daniel Drijard, Frederick E James, Matts Roos, and Bernard Sadoulet. *Statistical methods in experimental physics; 1st ed.* North-Holland, Amsterdam, 1971. URL `https://cds.cern.ch/record/100342`. 309

[113] S. Eidelman and others. Review of particle physics. *Physics Letters B*, 592(1):1–5, 2004. ISSN 0370-2693. doi: https://doi.org/10.1016/j.physletb.2004.06.001. URL `https://www.sciencedirect.com/science/article/pii/S0370269304007579`. Review of Particle Physics. 22

[114] Shalom Eliezer and Arthur R. Swift. Experimental Consequences of electron Neutrino-Muon-neutrino Mixing in Neutrino Beams. *Nucl. Phys. B*, 105:45–51, 1976. doi: 10.1016/0550-3213(76)90059-6. 16

[115] C. D. Ellis and W. A. Wooster. The average energy of disintegration of radium e. *Proceedings of the Royal Society of London. Series A, Containing Papers of a Mathematical and Physical Character*, 117(776):109–123, Dec 1927. ISSN 0950-1207. doi: 10.1098/rspa.1927.0168. 5, 8, 13

[116] E. Eskut and others. New results from a search for $\rightarrow$ and e$\rightarrow$ oscillation. *Physics Letters B*, 497:8–22, 01 2001. doi: 10.1016/S0370-2693(00)01317-4. 27

[117] I. Esteban, M.C. Gonzalez-Garcia, M. Maltoni, T. Schwetz, and A. Zhou. Nufit global analysis of neutrino oscillation data: Status and implications. *Journal of High Energy Physics*, 2021(09):178, 2021. doi: 10.1007/JHEP09(2021)178. 240

[118] M. Estienne et al. Updated Summation Model: An Improved Agreement with the Daya Bay Antineutrino Fluxes. *Phys. Rev. Lett.*, 123(2):022502, 2019. doi: 10.1103/PhysRevLett.123.022502. 162, 185, 189

[119] M. Fallot et al. *Phys. Rev. Lett.*, 109:202504, 2012. 41

[120] Gary J. Feldman and Robert D. Cousins. Unified approach to the classical statistical analysis of small signals. *Phys. Rev. D*, 57:3873–3889, Apr 1998. doi: 10.1103/PhysRevD.57.3873. URL `https://link.aps.org/doi/10.1103/PhysRevD.57.3873`. 228, 308, 309, 310

[121] S. J. Freedman and others. Limits on neutrino oscillations from $\overline{\nu}_e$ appearance. *Phys. Rev. D*, 47:811–829, Feb 1993. doi: 10.1103/PhysRevD.47.811. URL `https://link.aps.org/doi/10.1103/PhysRevD.47.811`. 27

[122] H. Fritsch and P. Minkowski. Vectorlike weak currents, massive neutrinos, and neutrino beam oscillations. *Physics Letters B*, 62(1):72–76, 1976. ISSN

0370-2693. doi: https://doi.org/10.1016/0370-2693(76)90051-4. URL https://www.sciencedirect.com/science/article/pii/0370269376900514. 16

[123] Y. Fukuda and others. Evidence for oscillation of atmospheric neutrinos. *Physical review letters*, 81(8):1562–1567, 1998. ISSN 0031-9007. 24, 25

[124] M. García-León. Radioactivity: Decay law, definitions, and units. In *Radioactivity: Introduction and History*, pages 21–34. 2022. doi: 10.1007/978-3-031-09970-0_2. 42

[125] Y. Gebre et al. Prospects for Improved Understanding of Isotopic Reactor Antineutrino Fluxes. *Phys. Rev. D*, 97(1):013003, 2018. doi: 10.1103/PhysRevD.97.013003. 183

[126] Claudio Giganti. T2k results and perspectives. *Nuclear and particle physics proceedings*, 265-266:147–152, 2015. ISSN 2405-6014. 26

[127] C. Giunti and T. Lasserre. *Annual Review of Nuclear and Particle Science*, 69:163, 2019. 47, 187

[128] C. Giunti, Y.F. Li, C.A. Ternes, and Z. Xin. Reactor antineutrino anomaly in light of recent flux model refinements. *Physics Letters B*, 829:137054, 2022. ISSN 0370-2693. doi: https://doi.org/10.1016/j.physletb.2022.137054. URL https://www.sciencedirect.com/science/article/pii/S0370269322001885. 49, 189

[129] Carlo Giunti and Chung W. Kim. *Fundamentals of Neutrino Physics and Astrophysics*. 2007. ISBN 978-0-19-850871-7. 16, 21, 22, 24

[130] Gene H. Golub and Charles F. Van Loan. *Matrix Computations*. Johns Hopkins University Press, Baltimore, MD, 4th edition, 2013. ISBN 978-1421407944. Section on Cholesky Decomposition. 298

[131] M. Gonzalez-Garcia and M. Yokoyama. *Neutrino Masses, Mixing, and Oscillations*, chapter 14. Particle Data Group, Jun 2020. 12

[132] Maria Concepcion Gonzalez-Garcia, Michele Maltoni, and Thomas Schwetz. Nufit: Three-flavour global analyses of neutrino oscillation experiments. *Universe*, 7(12), 2021. ISSN 2218-1997. doi: 10.3390/universe7120459. URL `https://www.mdpi.com/2218-1997/7/12/459`. 30

[133] Z. D. Greenwood, W. R. Kropp, M. A. Mandelkern, S. Nakamura, E. L. Pasierb-Love, L. R. Price, F. Reines, S. P. Riley, H. W. Sobel, N. Baumann, and H. S. Gurr. Results of a two-position reactor neutrino-oscillation experiment. *Phys. Rev. D*, 53:6054–6064, Jun 1996. doi: 10.1103/PhysRevD.53.6054. URL `https://link.aps.org/doi/10.1103/PhysRevD.53.6054`. 40

[134] D.E. Groom et al. Review of Particle Physics. *Eur. Phys. J. C*, 15:1, 2000. doi: 10.1007/s100520000474. 28

[135] N. Haag, A. Gütlein, M. Hofmann, L. Oberauer, W. Potzel, et al. Experimental determination of the antineutrino spectrum of the fission products of ^{238}u. *Physical Review Letters*, 112(12):122501, Mar 2014. ISSN 0031-9007. doi: 10.1103/PhysRevLett.112.122501. 46

[136] Brennan Theresa Hackett. DANG and the Background Characterisation of HFIR for PROSPECT. Master's thesis, University of Surrey, 2017. 54

[137] D.R Hadley. The hyper-k experiment: Present and rd for the next decade. *Nuclear instruments methods in physics research. Section A, Accelerators, spectrometers, detectors and associated equipment*, 824:630–634, 2016. ISSN 0168-9002. 26

[138] Steffen Hagstotz, Pablo F. de Salas, Stefano Gariazzo, Sergio Pastor, Martina Gerbino, Massimiliano Lattanzi, Sunny Vagnozzi, and Katherine Freese. Bounds on light sterile neutrino mass and mixing from cosmology

and laboratory searches. *Phys. Rev. D*, 104:123524, Dec 2021. doi: 10.1103/PhysRevD.104.123524. URL https://link.aps.org/doi/10.1103/PhysRevD.104.123524. 238

[139] A. Hahn, K. Schreckenbach, W. Gelletly, F. von Feilitzsch, G. Colvin, et al. Antineutrino spectra from ^{241}pu and ^{239}pu thermal neutron fission products. *Physics Letters B*, 218(3):365–368, Feb 1989. ISSN 0370-2693. doi: 10.1016/0370-2693(89)91598-0. 44, 45

[140] T. J. Haines et al. Calculation of Atmospheric Neutrino Induced Backgrounds in a Nucleon Decay Search. *Phys. Rev. Lett.*, 57:1986–1989, 1986. doi: 10.1103/PhysRevLett.57.1986. 24

[141] Lawrence J. Hall and Hitoshi Murayama. Study of inclusive multiring events from atmospheric neutrinos. *Phys. Lett. B*, 436:323–330, 1998. doi: 10.1016/S0370-2693(98)00865-X. 24

[142] L. Hayen et al. First forbidden transitions in the reactor anomaly. *Phys. Rev. C*, 100(5):054323, 2019. doi: 10.1103/PhysRevC.100.054323. 162

[143] A. C. Hayes, J. L. Friar, G. T. Garvey, Duligur Ibeling, Gerard Jungman, T. Kawano, and Robert W. Mills. Possible origins and implications of the shoulder in reactor neutrino spectra. *Phys. Rev. D*, 92:033015, Aug 2015. doi: 10.1103/PhysRevD.92.033015. URL https://link.aps.org/doi/10.1103/PhysRevD.92.033015. 46

[144] Anna C. Hayes and Petr Vogel. Reactor neutrino spectra. *Annual Review of Nuclear and Particle Science*, 66(1):219–244, 2016. doi: 10.1146/annurev-nucl-102115-044826. URL https://doi.org/10.1146/annurev-nucl-102115-044826. 46, 50, 180

[145] Anna C. Hayes, Gerard Jungman, E.A. McCutchan, Alejandro A. Sonzogni, Gerry T. Garvey, and Xiaobao Wang. Analysis of the Daya Bay Reactor

Antineutrino Flux Changes with Fuel Burnup. *Phys. Rev. Lett.*, 120(2):022503, 2018. doi: 10.1103/PhysRevLett.120.022503. 189

[146] Blaine Alexander Heffron. Characterization of Reactor Background Radiation at HFIR for the PROSPECT Experiment. Master's thesis, University of Tennessee, 2017. 54

[147] K. Hidaka, M. Honda, and S. Midorikawa. Neutrino oscillations and the anomalous atmospheric neutrino flux. *Phys. Rev. Lett.*, 61:1537–1540, Oct 1988. doi: 10.1103/PhysRevLett.61.1537. URL `https://link.aps.org/doi/10.1103/PhysRevLett.61.1537`. 25

[148] P. W. Higgs. Broken symmetries and the masses of gauge bosons. *Physical Review Letters*, 13(16):508–509, 1964. doi: 10.1103/PhysRevLett.13.508. 15

[149] P. Huber. Determination of antineutrino spectra from nuclear reactors. *Physical Review C*, 84(2):024617, Aug 2011. ISSN 0556-2813. doi: 10.1103/PhysRevC.84.024617. 43, 45, 162, 163, 178, 241

[150] P. Huber. Reactor antineutrino fluxes: Status and challenges. *Nuclear Physics B*, 908:268–278, Jul 2016. ISSN 0550-3213. doi: 10.1016/j.nuclphysb.2016.04.012. 42, 43

[151] Patrick Huber. NEOS Data and the Origin of the 5 MeV Bump in the Reactor Antineutrino Spectrum. *Phys. Rev. Lett.*, 118(4):042502, 2017. doi: 10.1103/PhysRevLett.118.042502. 180

[152] J V Jelley. Cerenkov radiation and its applications. *British Journal of Applied Physics.*, 6(7):227–232, jul 1955. doi: 10.1088/0508-3443/6/7/301. URL `https://doi.org/10.1088/0508-3443/6/7/301`. 22

[153] Xiangpan Ji, Wenqiang Gu, Xin Qian, Hanyu Wei, and Chao Zhang. Combined neyman–pearson chi-square: An improved approximation to the poisson-likelihood chi-square. *Nuclear Instruments and Methods in Physics Research*

Section A: Accelerators, Spectrometers, Detectors and Associated Equipment, 961:163677, May 2020. ISSN 0168-9002. doi: 10.1016/j.nima.2020.163677. URL http://dx.doi.org/10.1016/j.nima.2020.163677. 201, 221, 305

[154] Y.J. Ko et al. Sterile Neutrino Search at the NEOS Experiment. *Phys. Rev. Lett.*, 118(12):121802, 2017. doi: 10.1103/PhysRevLett.118.121802. 40, 228, 237

[155] Makoto Kobayashi and Toshihide Maskawa. Cp violation in the renormalizable theory of weak interaction. *Progress of Theoretical Physics*, 49(2):652–657, 1973. doi: 10.1143/PTP.49.652. 11

[156] K. Kodama, N. Ushida, S. Kasuga, and et al. (DONUT Collaboration). Observation of tau neutrino interactions. *Physical Review Letters*, 87(4):041801, 2001. doi: 10.1103/PhysRevLett.87.041801. 9

[157] V. Kopeikin, M. Skorokhvatov, and O. Titov. Reevaluating reactor antineutrino spectra with new measurements of the ratio between ^{235}u and ^{239}pu β spectra. *Physical Review D*, 104(7), Oct 2021. ISSN 2470-0029. doi: 10.1103/PhysRevD.104.L071301. 45, 46, 185, 241

[158] V. I. Kopeikin, Yu. N. Panin, and A. A. Sabelnikov. Measurement of the Ratio of Cumulative Spectra of Beta Particles from ^{235}U and ^{239}Pu Fission Products for Solving Problems of Reactor-Antineutrino Physics. *Phys. Atom. Nucl.*, 84 (1):1–10, 2021. doi: 10.1134/S1063778821010129. 189

[159] M Koshiba. Observational neutrino astrophysics. *Physics Reports*, 220(5): 229–381, 1992. ISSN 0370-1573. doi: https://doi.org/10.1016/0370-1573(92)90083-C. URL https://www.sciencedirect.com/science/article/pii/037015739290083C. 22

[160] H. Kwon, F. Boehm, A. A. Hahn, H. E. Henrikson, J. L. Vuilleumier, J. F. Cavaignac, D. H. Koang, B. Vignon, F. v. Feilitzsch, and R. L. Mössbauer.

Search for neutrino oscillations at a fission reactor. *Phys. Rev. D*, 24:1097–1111, Sep 1981. doi: 10.1103/PhysRevD.24.1097. URL https://link.aps.org/doi/10.1103/PhysRevD.24.1097. 40

[161] Olga Kyzylova. *Characterization of Time-Varying Backgrounds in the PROSPECT Experiment*. PhD thesis, Drexel University, 2021. 113, 119

[162] Oak Ridge National Laboratory. High flux isotope reactor (hfir), 2024. URL https://neutrons.ornl.gov/hfir. Accessed: 2024-11-21. 51

[163] John G. Learned, Sandip Pakvasa, and Thomas J. Weiler. Neutrino mass and mixing implied by underground deficit of low energy muon-neutrino events. *Physics Letters B*, 207(1):79–85, 1988. ISSN 0370-2693. doi: https://doi.org/10.1016/0370-2693(88)90890-8. URL https://www.sciencedirect.com/science/article/pii/0370269388908908. 25

[164] Los Alamos National Laboratory. The reines-cowan experiments: Detecting the poltergeist. *Los Alamos Science*, (25), 1997. 7

[165] I. Machikhiliyan. The danss neutrino spectrometer: the results of reactor antineutrino studies. *Physics of particles and nuclei*, 53(2):546–551, 2022. ISSN 1063-7796. 237

[166] Andrzej Mackiewicz and Waldemar Ratajczak. Principal components analysis (pca). *Computers & Geosciences*, 19(3):303–342, 1993. doi: 10.1016/0098-3004(93)90090-R. 85

[167] K. B. M. Mahn and others. Dual baseline search for muon neutrino disappearance at 0.5 $\mathrm{ev}^2 lt; \Delta m^2 lt; 40$ ev^2. *Phys. Rev. D*, 85:032007, Feb 2012. doi: 10.1103/PhysRevD.85.032007. URL https://link.aps.org/doi/10.1103/PhysRevD.85.032007. 27

[168] Ziro Maki, Masami Nakagawa, and Shoichi Sakata. Remarks on the unified model of elementary particles. *Progress of theoretical physics*, 28(5):870–880, 1962. ISSN 0033-068X. 15, 16

[169] Kevin Scott McFarland et al. A Limit on ν_μ (anti-muon-neutrino) $\rightarrow \nu_\tau$ (anti-tau-neutrino) oscillations from a precision measurement of neutrino - nucleon neutral current interactions. *Phys. Rev. Lett.*, 75:3993–3996, 1995. doi: 10.1103/PhysRevLett.75.3993. 27

[170] G. Mention et al. The reactor antineutrino anomaly. *Physical Review D*, 83(7), 2011. doi: 10.1103/PhysRevD.83.073006. 29, 47, 48, 50, 187, 190

[171] D. G. Michael and others. Observation of muon neutrino disappearance with the minos detectors in the numi neutrino beam. *Phys. Rev. Lett.*, 97:191801, Nov 2006. doi: 10.1103/PhysRevLett.97.191801. URL `https://link.aps.org/doi/10.1103/PhysRevLett.97.191801`. 26

[172] Th. A. Mueller et al. Improved Predictions of Reactor Antineutrino Spectra. *Phys. Rev. C*, 83:054615, 2011. doi: 10.1103/PhysRevC.83.054615. 41, 45, 187

[173] T Nakaya. K2k results. *Nuclear physics. Section B, Proceedings supplement*, 143:96–103, 2005. ISSN 0920-5632. 26

[174] D. Naples et al. A High statistics search for neutrino(e) (anti-neutrino(e)) —> neutrino(tau) (anti-neutrino(tau)) oscillations. *Phys. Rev. D*, 59:031101, 1999. doi: 10.1103/PhysRevD.59.031101. 27

[175] J. Neyman. On the two different aspects of the representative method: the method of stratified sampling and the method of purposive selection. *Journal of the Royal Statistical Society*, 97(4):558–625, 1934. 294

[176] J. Neyman. Outline of a Theory of Statistical Estimation Based on the Classical Theory of Probability. *Philosophical Transactions of the Royal Society of*

London Series A, 236(767):333–380, August 1937. doi: 10.1098/rsta.1937.0005. 221, 308

[177] J. Neyman, E. S. Pearson, S. Kotz, and N. L. Johnson. On the problem of the most efficient tests of statistical hypotheses. In *Breakthroughs in Statistics: Foundations and Basic Theory*, pages 73–108. Springer New York, New York, NY, 1992. doi: 10.1007/978-1-4612-0919-5_6. URL https://doi.org/10.1007/978-1-4612-0919-5_6. 294, 297

[178] M. Andriamirado others. Final search for short-baseline neutrino oscillations with the prospect-i detector at hfir, 2024. URL https://arxiv.org/abs/2406.10408. 196, 219, 231, 244

[179] Yuichi Oyama. Results from kamiokande-ii experiment. *Nuclear Physics B - Proceedings Supplements*, 13:362–367, 1990. ISSN 0920-5632. doi: https://doi.org/10.1016/0920-5632(90)90087-B. URL https://www.sciencedirect.com/science/article/pii/092056329090087B. 23

[180] W. Pauli. Dear radioactive ladies and gentlemen. *Physics Today*, 31(9):23–28, Sep 1978. 5

[181] Lorenzo Périssé, Anthony Onillon, Xavier Mougeot, Matthieu Vivier, Thierry Lasserre, Alain Letourneau, David Lhuillier, and Guillaume Mention. Comprehensive revision of the summation method for the prediction of reactor $\overline{\nu}_e$ fluxes and spectra. *Phys. Rev. C*, 108:055501, Nov 2023. doi: 10.1103/PhysRevC.108.055501. URL https://link.aps.org/doi/10.1103/PhysRevC.108.055501. 189

[182] X. Qian, A. Tan, J. J. Ling, Y. Nakajima, and C. Zhang. The Gaussian CL_s method for searches of new physics. *Nucl. Instrum. Meth. A*, 827:63–78, 2016. doi: 10.1016/j.nima.2016.04.089. 227, 307

[183] Xin Qian and Jen-Chieh Peng. Physics with Reactor Neutrinos. *Rept. Prog. Phys.*, 82(3):036201, 2019. doi: 10.1088/1361-6633/aae881. 36

[184] F. Reines, M. F. Crouch, T. L. Jenkins, W. R. Kropp, H. S. Gurr, G. R. Smith, J. P. F. Sellschop, and B. Meyer. Evidence for high-energy cosmic-ray neutrino interactions. *Phys. Rev. Lett.*, 15:429–433, Aug 1965. doi: 10.1103/PhysRevLett.15.429. URL `https://link.aps.org/doi/10.1103/PhysRevLett.15.429`. 24

[185] Ashley J. Ross, Lado Samushia, Cullan Howlett, Will J. Percival, Angela Burden, and Marc Manera. The clustering of the SDSS DR7 main Galaxy sample - I. A 4 per cent distance measure at $z = 0.15$. *Mon. Not. Roy. Astron. Soc.*, 449:835–847, 2015. doi: 10.1093/mnras/stv154. 236

[186] Sheldon M. Ross. *A First Course in Probability*. Pearson, 9 edition, 2012. 221

[187] S. Schoppmann. Status of anomalies and sterile neutrino searches at nuclear reactors. *Universe*, 7(10):360, Sep 2021. ISSN 2218-1997. doi: 10.3390/universe7100360. 47

[188] K. Schreckenbach, G. Colvin, W. Gelletly, and F. von Feilitzsch. Determination of the antineutrino spectrum from ^{235}u thermal neutron fission products up to 9.5 mev. *Physics Letters B*, 160(4-5):325–330, Oct 1985. ISSN 0370-2693. doi: 10.1016/0370-2693(85)91337-1. 43, 44, 45

[189] S. H. Seo et al. Spectral Measurement of the Electron Antineutrino Oscillation Amplitude and Frequency using 500 Live Days of RENO Data. *Phys. Rev.*, D98 (1):012002, 2018. doi: 10.1103/PhysRevD.98.012002. 58

[190] A. P. Serebrov et al. Search for sterile neutrinos with the neutrino-4 experiment and measurement results. *Phys. Rev. D*, 104:032003, Aug 2021. doi: 10.1103/PhysRevD.104.032003. URL `https://link.aps.org/doi/10.1103/PhysRevD.104.032003`. 40, 84, 188, 189, 192, 204, 231

[191] A. A. Sonzogni, T. D. Johnson, and E. A. McCutchan. Nuclear structure insights into reactor antineutrino spectra. *Phys. Rev. C*, 91:011301, Jan 2015. doi: 10.1103/PhysRevC.91.011301. URL `https://link.aps.org/doi/10.1103/PhysRevC.91.011301`. 41

[192] I. E. Stockdale and others. Limits on muon-neutrino oscillations in the mass range $30lt;\Delta m^2lt;1000$ ev$^2/c^4$. *Phys. Rev. Lett.*, 52:1384–1388, Apr 1984. doi: 10.1103/PhysRevLett.52.1384. URL `https://link.aps.org/doi/10.1103/PhysRevLett.52.1384`. 27

[193] M Talebzadeh and others. Search for tau-neutrino interactions in the bebc beam dump experiment. *Nuclear physics. B*, 291:503–515, 1987. ISSN 0550-3213. 27

[194] M. Tanabashi et al. Review of Particle Physics. *Phys. Rev. D*, page 030001, 2018. 187

[195] W. Tang, X. Li, X. Qian, H. Wei, and C. Zhang. Data Unfolding with Wiener-SVD Method. *Journal of Instrumentation*, 12(10):P10002, Oct 2017. ISSN 1748-0221. doi: 10.1088/1748-0221/12/10/p10002. URL `http://dx.doi.org/10.1088/1748-0221/12/10/P10002`. 164, 173, 299

[196] The Nobel Prize. Fission chain reaction interactive learning. `https://educationalgames.nobelprize.org/educational/physics/energy/fission_2.html`, 2024. Accessed: 2024-11-21. 35

[197] Mark Thomson. *Modern Particle Physics*. Cambridge University Press, Cambridge, 2013. 10, 11

[198] N. Ushida and others. Limits to $\nu_\mu, \nu_e \to \nu_\tau$ oscillations and $\nu_\mu, \nu_e \to \tau^-$ direct coupling. *Phys. Rev. Lett.*, 57:2897–2900, Dec 1986. doi: 10.1103/PhysRevLett.57.2897. URL `https://link.aps.org/doi/10.1103/PhysRevLett.57.2897`. 27

[199] D. Vignaud. The gallex solar neutrino experiment. *Nuclear Physics B - Proceedings Supplements*, 60(3):20–29, 1998. ISSN 0920-5632. doi: https://doi.org/10.1016/S0920-5632(97)00498-2. URL `https://www.sciencedirect.com/science/article/pii/S0920563297004982`. 22

[200] Edoardo Vitagliano, Irene Tamborra, and Georg Raffelt. Grand Unified Neutrino Spectrum at Earth: Sources and Spectral Components. *Rev. Mod. Phys.*, 92:45006, 2020. doi: 10.1103/RevModPhys.92.045006. 21

[201] P. Vogel. *Phys. Rev. C*, 76:025504, 2007. 163

[202] P. Vogel and J. F. Beacom. Angular distribution of neutron inverse beta decay, $^{-}$ e + p → e + + n. *Physical review. D, Particles and fields*, 60(5), 1999. ISSN 0556-2821. 130

[203] Petr Vogel, Liangjian Wen, and Chao Zhang. Neutrino Oscillation Studies with Reactors. *Nature Commun.*, 6:6935, 2015. doi: 10.1038/ncomms7935. 38

[204] F. von Feilitzsch, A. Hahn, and K. Schreckenbach. Experimental beta-spectra from ^{239}pu and ^{235}u thermal neutron fission products and their correlated antineutrino spectra. *Physics Letters B*, 118(1-3):162–166, Dec 1982. ISSN 0370-2693. doi: 10.1016/0370-2693(82)90622-0. 41, 44, 45

[205] J.L Vuilleumier and others. New limits on oscillation parameters for electron antineutrinos. *Physics letters. B*, 114(4):298–302, 1982. ISSN 0370-2693. 40

[206] K. Way and E. P. Wigner. The rate of decay of fission products. *Phys. Rev.*, 73:1318–1330, Jun 1948. doi: 10.1103/PhysRev.73.1318. URL `https://link.aps.org/doi/10.1103/PhysRev.73.1318`. 34

[207] Wikipedia contributors. Table of nuclides. `https://en.wikipedia.org/wiki/Table_of_nuclides`, 2024. Accessed: 2024-11-21. 35

[208] F. L. Wilson. Fermi's theory of beta decay. *American Journal of Physics*, 36 (12):1150–1160, Dec 1968. ISSN 0002-9505. doi: 10.1119/1.1974382. 6

Appendix

Appendix A

Statistical Methods

A.1 Covariance matrix formalism

In hypothesis testing and parameter estimation, constraints on the parameters of interest are typically established by constructing confidence intervals. This process involves defining a test statistic, which is a function that depends on both the parameters of interest and the observed data. In the large statistics regime, where the data can be approximated by a Gaussian distribution, a commonly used test statistic for a set of N variables is given by

$$\chi^2(\boldsymbol{\theta}) = \sum_{i=1}^{N} \frac{\left[M_i(\boldsymbol{\theta}) - e_i(\boldsymbol{\theta}) - \sum_{j=1}^{K} \alpha_j s_{ji}(\boldsymbol{\theta})\right]^2}{\sigma_i^2} + \sum_{j=1}^{K} \alpha_j^2, \tag{A.1}$$

where M_i and e_i are the observed and expected counts for the i^{th} variable given the parameters $\boldsymbol{\theta}$, with an associated statistical uncertainty σ_i. The term s_{ji} represents the systematic uncertainty from the j^{th} source in the i^{th} bin, considering K sources of systematic uncertainty. The statistical uncertainty σ_i may depend on $\boldsymbol{\theta}$ depending on the specific formulation of the test statistic [175, 177]. The nuisance parameters α_j are adjusted along with $\boldsymbol{\theta}$ to minimize the test statistic, yielding $\chi^2(\boldsymbol{\theta})_{\text{min}}$. The best-fit parameters are then defined as $\boldsymbol{\theta}_{\text{min}} = \arg\min \chi^2(\boldsymbol{\theta})$.

Eq. A.1 could be represented in matrix form as

$$\begin{aligned}\chi^2 &= \left(\mathbf{u} - \mathbf{R}^{\mathrm{T}}\boldsymbol{\alpha}\right)^{\mathrm{T}}\left(\mathbf{u} - \mathbf{R}^{\mathrm{T}}\boldsymbol{\alpha}\right) + \boldsymbol{\alpha}^{\mathrm{T}}\boldsymbol{\alpha} \\ &= \mathbf{u}^{\mathrm{T}}\mathbf{u} - 2\boldsymbol{\alpha}^{\mathrm{T}}\mathbf{R}\mathbf{u} + \boldsymbol{\alpha}^{\mathrm{T}}\mathbf{R}\mathbf{R}^{\mathrm{T}}\boldsymbol{\alpha} + \boldsymbol{\alpha}^{\mathrm{T}}\boldsymbol{\alpha}\end{aligned} \tag{A.2}$$

where

$$\begin{aligned}u_i &\equiv \frac{M_i - e_i}{\sigma_i}, \text{with dimensions } N\text{x1} \\ \alpha_k &\equiv k^{th} \text{ fit parameter with dimensions } K\text{x1 and} \\ R_{ji} &\equiv \frac{s_{ji}}{\sigma_i}, \text{ with dimensions } K\text{x}N\end{aligned} \tag{A.3}$$

The minimum values of the nuisance parameters could be found analytically by taking the derivative with respect to $\boldsymbol{\alpha}$ and setting it equal to zero.

$$\begin{aligned}&\frac{\partial\chi^2}{\partial\boldsymbol{\alpha}} = 0 \\ &\mathbf{R}\mathbf{u} + \mathbf{R}\mathbf{R}^{\mathrm{T}}\boldsymbol{\alpha}_{\min} + \boldsymbol{\alpha}_{\min} = 0.\end{aligned} \tag{A.4}$$

Multiplying Eq A.4 on the left side with $\boldsymbol{\alpha}_{\min}$ gives

$$\boldsymbol{\alpha}_{\min}^{\mathrm{T}}\,\mathbf{R}\mathbf{u} + \boldsymbol{\alpha}_{\min}^{\mathrm{T}}\,\mathbf{R}\mathbf{R}^{\mathrm{T}}\boldsymbol{\alpha}_{\min} + \boldsymbol{\alpha}_{\min}^{\mathrm{T}}\,\boldsymbol{\alpha}_{\min} = 0 \tag{A.5}$$

Solving for $\boldsymbol{\alpha}_{\min}$ produces

$$\boldsymbol{\alpha}_{\min} = \mathbf{R}\left(\mathbf{R}^{\mathrm{T}}\mathbf{R} + \mathbf{I}_K\right)^{-1}\mathbf{u} \tag{A.6}$$

where $\mathbf{I}_K$ is the unit matrix in $K \times K$ dimensions. The existence of an inverse for the matrix $\left(\mathbf{I}_K + RR^T\right)$ follows from the assumption that the χ^2 of Eq. A.1 has a unique analytical minimum. As a result, if $\left(\mathbf{I}_K + RR^T\right)$ is invertible, then so must be $\left(\mathbf{I}_N + R^T R\right)$

$$\left(\mathbf{I}_N + R^T R\right)^{-1} = \mathbf{I}_N - R^T\left(\mathbf{I}_K + RR^T\right)^{-1}R \tag{A.7}$$

As a result, it can be shown that:

$$\begin{aligned}
&\left(\mathbf{I}_N + R^T R\right)\left[\mathbf{I}_N - R^T\left(\mathbf{I}_K + RR^T\right)^{-1} R\right] \\
&= \mathbf{I}_N + R^T R - \left(\mathbf{I}_N + R^T R\right) R^T\left(\mathbf{I}_K + RR^T\right)^{-1} R \\
&= \mathbf{I}_N + R^T R - \left(R^T + R^T RR^T\right)\left(\mathbf{I}_K + RR^T\right)^{-1} R \\
&= \mathbf{I}_N + R^T R - R^T\left(\mathbf{I}_K + RR^T\right)\left(\mathbf{I}_K + RR^T\right)^{-1} R \\
&= \mathbf{I}_N + R^T R - R^T R \\
&= \mathbf{I}_N
\end{aligned}$$

The equality of the left-inverse and the right-inverse follows from the symmetry of the matrix $\left(\mathbf{I}_N + R^T R\right)$. Having proved the existence of $\left(\mathbf{I}_N + R^T R\right)^{-1}$, $\alpha_{\min}$ can be redefined as follows:

$$\begin{aligned}
\alpha_{\min} &= \left(\mathbf{I}_K + RR^T\right)^{-1} R\left(\mathbf{I}_N + R^T R\right)\left(\mathbf{I}_N + R^T R\right)^{-1} u \\
&= \left(\mathbf{I}_K + RR^T\right)^{-1}\left(R + RR^T R\right)\left(\mathbf{I}_N + R^T R\right)^{-1} u \\
&= \left(\mathbf{I}_K + RR^T\right)^{-1}\left(\mathbf{I}_K + RR^T\right) R\left(\mathbf{I}_N + R^T R\right)^{-1} u \\
&= R\left(\mathbf{I}_N + R^T R\right)^{-1} u
\end{aligned} \tag{A.8}$$

Substituting Eq A.4 in Eq A.2 for $\boldsymbol{\alpha}$=$\boldsymbol{\alpha}_{\min}^{\mathrm{T}}$ gives

$$\chi^2_{\min} = \mathbf{u}^{\mathrm{T}}\mathbf{u} - \boldsymbol{\alpha}_{\min}^{\mathrm{T}}\mathbf{R}\mathbf{u}. \tag{A.9}$$

Substituting the value for $\boldsymbol{\alpha}_{\min}$ from Eq. A.8 in Eq. A.9 for $\chi^2_{\min}$ produces

$$\chi^2_{\min} = \mathbf{u}^{\mathrm{T}}\left(\mathbf{R}^{\mathrm{T}}\mathbf{R} + \mathbf{I}_N\right)^{-1}\mathbf{u} \tag{A.10}$$

Separating the matrix $\mathbf{u}$ into two parts:

$$\begin{aligned}
\Delta_i &\equiv M_i - e_i \\
S_{ij} &\equiv \sigma_i \delta_{ij},
\end{aligned} \tag{A.11}$$

the Eq. A.1 can be written as

$$\begin{aligned}\chi^2_{\text{min}} &= \boldsymbol{\Delta}^{\text{T}} \left(\mathbf{S}^{\text{T}} \left(\mathbf{R}^{\text{T}}\mathbf{R} + \mathbf{I}_N\right) \mathbf{S}\right)^{-1} \boldsymbol{\Delta} \\ &= \boldsymbol{\Delta}^{\text{T}} \mathbf{V}^{-1} \boldsymbol{\Delta}.\end{aligned} \tag{A.12}$$

where $\mathbf{V}$ is the resulting covariance matrix defined by:

$$\mathbf{V}_{ij} = \sigma_i^2 \delta_{ij} + \sum_l^K s_{li} s_{lj} \tag{A.13}$$

Using a covariance matrix provides the advantage of automatically including correlations between all bins through the non-diagonal elements. Because the covariance matrix inherently accounts for systematic variations, there is no need for explicit fitting over nuisance parameters, resulting in a significant reduction in computation time. This derivation followed closely from [177].

A.1.1 Covariance matrix generation

In the context of the PROSPECT experiment, Eq. A.13 can be reformulated to generate the covariance matrix for each systematic uncertainty as follows:

$$\mathbf{V} = \text{E}\left[(\mathbf{X} - \boldsymbol{\mu})(\mathbf{X} - \boldsymbol{\mu})^T\right] \tag{A.14}$$

Here, $\mathbf{X}$ represents a toy vector sampled from a nominal distribution $\boldsymbol{\mu}$, with fluctuations determined by the specific systematic uncertainty under consideration. Depending on the covariance matrix being constructed, these toy vectors were generated either by varying parameters in PG4-simulated distributions or by analytically modifying the HM-based spectrum passed through the full detector response. The values for each uncertainty were derived from a dedicated study of the respective effects. After applying this procedure to each systematic uncertainty, the total covariance matrix, defined as

$$\mathbf{V}_{tot} = \mathbf{V}_{stat} + \mathbf{V}_{sys}, \tag{A.15}$$

is constructed and serves as the main input in Eq. A.17.

A.1.2 Toy generation with covariance matrices

The previous section described the need to use toy distributions containing fluctuations based on a given uncertainty parameter to construct a covariance matrix for each systematic uncertainty. However, for various statistical methods employed in high-level analyses, such as constructing the Wiener filter (see Section A.2) for the spectral shape analysis or establishing confidence intervals in the search for sterile neutrino oscillations (see Section A.5), it is required to use toy datasets that incorporate the fluctuations arising from the full range of statistical and systematic uncertainties represented by the total covariance matrix $\mathbf{V}_{\text{tot}}$. This can be accomplished by means of the Cholesky decomposition [130].

Cholesky decomposition is a mathematical technique used to decompose a symmetric, positive-definite matrix into a product of a lower triangular matrix and its transpose. In the context of covariance matrices, which are by nature symmetric and positive semi-definite (and often positive definite in practice), $\mathbf{V}_{\text{tot}}$ can be Cholesky decomposed as

$$\mathbf{V}_{tot} = \mathbf{L}\mathbf{L}^T \tag{A.16}$$

where $\mathbf{L}$ is a lower triangular matrix, and $\mathbf{L}^T$ is its transpose (which is upper triangular) with

- $L_{ii} = \sqrt{V_{tot,ii} - \sum_{k=1}^{i-1} L_{ik}^2}$
- $L_{ij} = \frac{1}{L_{jj}} \left(V_{tot,ij} - \sum_{k=1}^{j-1} L_{ik} L_{jk} \right)$
- and $i < j$, $L_{ij} = 0$ since $\mathbf{L}$ is lower triangular.

A Cholesky decomposition is often used to generate samples from a multivariate normal distribution. Given the total covariance matrix $\mathbf{V}_tot$, correlated samples can be generated by applying $\mathbf{L}$ to a vector of independent standard normal variables $\mathbf{z}$. With this in mind and going back to Eq. A.16 it can be shown that a toy distribution generated this way incorporates all fluctuations described by the covariance matrix

$$\begin{aligned} \mathbf{V}_{tot} &= \mathbf{L}\mathbf{L}^{\mathrm{T}} \\ &= \mathbf{L}\mathrm{E}\left[\mathbf{z}\mathbf{z}^{T}\right]\mathbf{L}^{\mathrm{T}} \end{aligned} \tag{A.17}$$

In this equation, since the elements of $\mathbf{z}$ are uncorrelated random variables, we have $\mathrm{E}\left[\mathbf{z}\mathbf{z}^{\mathrm{T}}\right] = \mathbf{I}$. Given that expectation is a linear operator:

$$\begin{aligned} \mathbf{V}_{tot} &= \mathrm{E}\left[\mathbf{L}\mathbf{z}\mathbf{z}^{\mathrm{T}}\mathbf{L}^{\mathrm{T}}\right] \\ &= \mathrm{E}\left[(\mathbf{L}\mathbf{z})(\mathbf{L}\mathbf{z})^{\mathrm{T}}\right] \end{aligned} \tag{A.18}$$

confirming that the expectation value of $\mathbf{L}\mathbf{z}(\mathbf{L}\mathbf{z})^{\mathrm{T}}$ is the input covariance matrix. Referring back to the definition of the covariance matrix in Eq. A.14, and recognizing that Cholesky decomposition yields a unique result, Eq. A.18 demonstrates that $\mathbf{L}\mathbf{z} = \mathbf{X} - \boldsymbol{\mu}$ implying that

$$\mathbf{X} = \boldsymbol{\mu} + \mathbf{L}\mathbf{z} = \mathbf{X}_{\mathbf{tot}} \tag{A.19}$$

where $\mathbf{X}_{\mathbf{tot}}$ is a toy vector containing fluctuations from all statistical and systematic errors for a given analysis.

A.2 Wiener-SVD unfolding technique

The entire derivation of the Wiener-SVD filter presented in this section is derived from [195]. Data unfolding is a technique commonly used in high-energy physics (HEP) to estimate the true distribution of a physical quantity, such as an energy spectrum, from measurements affected by detector response and uncertainties (both

statistical and systematic). The challenge lies in that a simple inversion of the detector response matrix can result in an amplified contribution of low-statistics and high-noise bins, leading to unrealistic results.

The unfolding problem in HEP is typically formulated as the minimization of a χ^2 test function such as Eq. A.12. By replacing Δ in Eq. A.12 with $\Delta = m - r \cdot s$, where m is the vector of measured data, r is the response matrix that maps the true signal to the observed data, and s is the unknown vector representing the true signal, a χ^2 test statistic as a function of s can be defined as

$$\chi^2(s) = (\mathbf{m} - \mathbf{r} \cdot \mathbf{s})^T \cdot \mathbf{V}_{tot}^{-1} \cdot (\mathbf{m} - \mathbf{r} \cdot \mathbf{s}) \tag{A.20}$$

with V_{tot}^{-1} being the total covariance matrix for the analysis. Employing the Cholesky decomposition of V_{tot} explained in Section A.1.2 such that $V_{tot} = L^T \cdot L$, Eq. A.20 can be rewritten as

$$\chi^2(s) = (M - R \cdot s)^T \cdot (M - R \cdot s) = \sum_i \left(M_i - \sum_j R_{ij} \cdot s_j \right)^2 \tag{A.21}$$

with $M := L \cdot \mathbf{m}$ and $R := L \cdot \mathbf{r}$, and this process is commonly referred to as pre-scaling or pre-whitening. The primary goal is to estimate the true signal $\mathbf{s}$ from the measured data $\mathbf{m}$ while accounting for the detector's response and associated uncertainties. The solution after minimizing Eq. A.21 leads to the estimation $\hat{s}$ of the true signal s_{true}. This can be expressed as:

$$\hat{s} = (R^T R)^{-1} R^T M \tag{A.22}$$

which can, in turn be rewritten as

$$\hat{s} = (R^T R)^{-1} R^T (R \cdot s_{true} + N) \tag{A.23}$$

where N represents the noise introduced by statistical and systematic uncertainties associated with $\mathbf{m}$ and $\mathbf{r}$. Drawing a parallel to the discussion about toy generation using covariance matrices detailed in section A.1.2, it can be noted that

$$N = M - R \cdot s_{true} = L \cdot (\mathbf{m} - \mathbf{r} \cdot s_{true}) = L \cdot \mathbf{z} \tag{A.24}$$

implying that $\mathbf{z} = \mathbf{m} - \mathbf{r} \cdot s_{true}$.

Furthermore, to further reduce the impact of noise present in the pre-scaled response matrix R, R can be decomposed using Singular Value Decomposition (SVD):

$$R = U' \cdot D \cdot V'^{T} \tag{A.25}$$

where

- U' is an $m \times m$ orthogonal matrix.
- V' is an $n \times n$ orthogonal matrix.
- D is an $m \times n$ diagonal matrix containing the singular values of R d_i.

Incorporating Eq. A.2 into Eq. A.23 it yields

$$\begin{aligned} \hat{s} &= V' \cdot D^{-1} \cdot U'^{T} \cdot (R \cdot s_{true} + N) \\ &= V' \cdot D^{-1} \cdot (R_{U'} \cdot s_{true} + N_{U'}) \\ &= V' \cdot D^{-1} \cdot M_{U'} \end{aligned} \tag{A.26}$$

This last expression illustrates why a regularized unfolding procedure results in an unfolding signal with large fluctuations. Specifically, the presence of smearing in the matrix $\mathbf{r}$ or R causes the magnitude of the singular values d_i to decrease significantly as i increases. Beyond a certain point, the value of d_i may become extremely small, resulting in an exceedingly large value in the corresponding element of D^{-1}. In an ideal scenario with no noise N_U, these large diagonal elements are effectively canceled out by the small values in the signal $R \cdot s_{true}$, allowing for the unbiased recovery of

the signal after data unfolding. However, the situation changes drastically in the presence of noise N_U. Since this noise is greatly amplified when multiplied by D^{-1}, the unfolded results exhibit substantial fluctuations.

A.2.1 Traditional Regularization Approach

Regularization is typically used to address the noise amplification issue. Two common regularization methods in HEP are the Tikhonov regularization and the Bayesian unfolding methods:

Tikhonov Regularization:

This method introduces a penalty term into the chi-square function to regularize the solution by adding constraints on the strength or smoothness of the unfolded results. The regularization strength τ controls the trade-off between bias and variance. To zeroth order, the regularized unfolded spectrum is given by an expression of the form:

$$\hat{s} = V' \cdot F \cdot D^{-1} \cdot (R_{U'} \cdot s_{\text{true}} + N_{U'}) \tag{A.27}$$

where $F_{ii} = \frac{d_i^2}{d_i^2+\tau}$ is an $n \times n$ diagonal matrix favoring small values of the signal. The optimal value of τ is typically determined by scanning and minimizing a chosen metric, such as the sum of variance and bias. For small values of d_i, the corresponding noise components in N_U are now mitigated by the factor $\frac{d_i}{d_i^2+\tau}$ at a finite τ, rather than being amplified by $\frac{1}{d_i}$. This modification effectively reduces the large fluctuations in the unfolded results arising from noise N_U.

Bayesian Unfolding:

In Bayesian unfolding, the approach starts with an initial guess of the true signal. The estimate is iteratively refined based on the difference between the measured data and the prediction from the current guess. The process stops early to prevent

overfitting, which is a regularization mechanism. The Bayesian method is beneficial when positivity constraints (e.g., non-negative unfolded data) are essential.

A.2.2 Wiener-SVD Approach

The Wiener-SVD approach is introduced as a powerful alternative to traditional regularization methods. This method constructs a Wiener filter W that optimizes the signal-to-noise ratio directly in the space of the measurement $M_{U'}$, defined by the SVD transformation. The Wiener filter is constructed based on the following considerations:

- **Signal Expectation**: The filter takes into account the expected signal ($\overline{s}$), which is obtained from the transformation of the measured data. $\overline{s}$ is used instead of s_{true} since the true signal is often unknown.
- **Noise Characteristics**: It also incorporates knowledge about noise, ensuring that the filter maximizes the ratio of signal power to noise power in each effective frequency bin.

In the regularization methods described above, the functional form of $F_{ii} = d_i^2 / (d_i^2 + \tau)$ is independent of the signal shape. With the concept of the Wiener filter, we can construct W (replacing F in regularization) directly to optimize the signal-to-noise ratio. In general terms, the Wiener filter W is constructed as the ratio of the average expected signal to the average expected signal plus noise

$$W = \frac{\overline{R^2 \cdot \overline{s}^2}}{\overline{R^2 \cdot \overline{s}^2} + \overline{N^2}} \tag{A.28}$$

Making use of the SVD decomposition of R Eq. A.28 can be rewritten as

$$W_{ik} = \frac{d_i^2 \left(\sum_j {V'_{ij}}^T \overline{s}_j \right)^2}{d_i^2 \left(\sum_j {V'_{ij}}^T \overline{s}_j \right)^2 + 1} \tag{A.29}$$

where

- W_{ik} is the Wiener filter applied to the i-th singular value of the measured signal.
- d_i are the singular values from the SVD decomposition.
- $\overline{s}_j$ represents the components of the expected signal.

The key advantage of the Wiener-SVD approach lies in its ability to automatically adjust the level of filtering based on the signal-to-noise ratio in each signal bin. This results in a solution that effectively balances the trade-off between bias and variance without manually tuning a regularization parameter. The Wiener-SVD method is particularly well-suited for situations where prior knowledge about the signal and noise can be leveraged to improve the accuracy of the unfolded results. By incorporating this knowledge directly into constructing the Wiener filter, the method provides a more robust and efficient solution to the data unfolding problem. With this in mind, the final regularized spectrum becomes:

$$\hat{s} = A_W \cdot \left(R^T R\right)^{-1} \cdot R^T \cdot M \tag{A.30}$$

where A_W is the smearing matrix defined as $A_W = C^{-1} \cdot V_C \cdot W_C \cdot V_C^T \cdot C$ containing the effects of the regularization, with C being an additional matrix representing a measure of the average curvature of the expected signal, imposing a constraint on the smoothness of the signal. Furthermore, the term $\left(R^T R\right)^{-1} \cdot R^T$ removes the noise from directly applying the response matrix R to the measured signal M. In addition, since the unfolded results are a linear transformation of the measurement, the covariance matrix can also be unfolded as follows

$$\hat{s} = R_W \cdot \mathbf{m} \tag{A.31}$$

with

$$R_W = A_W \cdot \left(R^T R\right)^{-1} \cdot R^T \cdot L \tag{A.32}$$

Then, the covariance matrix of $\hat{s}$ can be deduced from the Cov (the covariance matrix of M) as

$$\mathrm{V}_{tot,\hat{s}} = R_{tot} \cdot \mathrm{V}_{\mathrm{tot}} \cdot R_{tot}^{T} \tag{A.33}$$

A.3 Combined Neyman-Pearson χ^2 test

An essential component of the final sterile neutrino analysis is using a new statistical method, the Combined Neyman-Pearson (CNP) approach [153], which helps reduce biases arising from bins with low statistics. Unlike previous analyses that employed uneven baseline binning to achieve equal statistics across all bins, the CNP method allows for uniform binning in both baseline and energy, thereby enhancing the robustness and consistency of the analysis.

For the relativized comparison between measured and predicted prompt spectra per baseline used in the oscillation analysis, the statistical covariance matrix is calculated as follows:

$$V_{\mathrm{stat}} = \sigma^2 \left(M_{l,e} - M_e \frac{P_{l,e}}{P_e} \right). \tag{A.34}$$

For the Neyman (Pearson) contribution, the statistical uncertainty is defined based on the measured (predicted) value $M_{l,e}(P_{l,e})$. Consequently, the statistical uncertainty in Eq. A.34 can be separated into the corresponding Neyman and Pearson contributions as:

$$\sigma^2_{\mathrm{Neyman}} \left(M_{l,e} - M_e \frac{P_{l,e}}{P_e} \right) = \sigma^2 \left(M_{l,e} \right) + \left(\frac{P_{l,e}}{P_e} \right)^2 \sigma^2 \left(M_e \right) - 2 \frac{P_{l,e}}{P_e} \mathrm{Cov} \left(M_{l,e}, M_e \right), \tag{A.35}$$

$$\sigma^2_{\text{Pearson}}\left(M_{l,e} - M_e\frac{P_{l,e}}{P_e}\right) = M_e^2\sigma^2\left(\frac{P_{l,e}}{P_e}\right)$$
$$\approx M_e^2\left(\left(\frac{P_{l,e}}{P_e}\right)^2\left[\left(\frac{\sigma\left(P_{l,e}\right)}{P_{l,e}}\right)^2 + \left(\frac{\sigma\left(P_e\right)}{P_e}\right)^2 - 2\frac{\text{Cov}\left(P_{l,e}, P_e\right)}{P_{l,e}P_e}\right]\right) \tag{A.36}$$

To calculate the covariance of two variables, where one is a subset of the other, $\text{Cov}\left(A_{l,e}, A_e\right)$, with $A = \{M, P\}$, new variables can be defined such that:

$$\begin{aligned} X &= A_{l,e}, \\ Y &= A_e, \\ Y &= X + Z, \end{aligned} \tag{A.37}$$

allowing $\text{Cov}\left(X, Y\right)$ to be expressed as:

$$\begin{aligned} \text{Cov}(X, Y) &= \text{Cov}(X, X + Z) \\ &= \text{Cov}(X, X) + \text{Cov}(X, Z) \\ &= \sigma^2(X). \end{aligned} \tag{A.38}$$

Substituting the result from Eq. A.38 into Eq. A.35 and Eq. A.36, the resulting uncertainty contributions from both Neyman and Pearson statistics for the relativized comparison are:

$$\begin{aligned} \sigma^2_{\text{Neyman}}\left(M_{l,e} - M_e\frac{P_{l,e}}{P_e}\right) &= (1-2k)\cdot\sigma^2\left(M_{l,e}\right) + k^2\cdot\sigma^2\left(M_e\right), \\ \sigma^2_{\text{Pearson}}\left(M_{l,e} - M_e\frac{P_{l,e}}{P_e}\right) &\approx M_e^2\cdot k^2\left(\left(\frac{\sigma\left(P_{l,e}\right)}{P_{l,e}}\right)^2 + \left(\frac{\sigma\left(P_e\right)}{P_e}\right)^2 - 2\frac{\sigma^2\left(P_{l,e}\right)}{P_{l,e}P_e}\right) \\ &= \frac{M_e^2}{P_e^2}\left[(1-2k)\sigma^2\left(P_{l,e}\right) + k^2\sigma^2\left(P_e\right)\right], \end{aligned} \tag{A.39}$$

where $k = P_{l,e}/P_e$. Based on these results, and within the CNP formalism, the final statistical covariance matrix is defined as a linear combination of the Neyman and Pearson χ^2 uncertainty contributions:

$$V_{\text{stat}} = \frac{1}{3}\left(V_{\text{Neyman}} + 2V_{\text{Pearson}}\right). \tag{A.40}$$

A.4 Gaussian CLs method

The Gaussian CL_s method [182] is employed when the Feldman-Cousins approach (see next section) is too computationally intensive due to the need to construct a large number of toy MC experiments. For this method, three quantities must be calculated for each ($\sin^2 2\theta_{14}$, Δm^2_{41}) pair:

$$\Delta T = \chi^2_{\text{min}}(x)_1 - \chi^2_{\text{min}}(x)_0, \tag{A.41}$$

$$\overline{\Delta T_0} = \chi^2_{\text{min}}(x_{\text{Asim},0})_1, \tag{A.42}$$

$$\overline{\Delta T_1} = -\chi^2_{\text{min}}(x_{\text{Asim},1})_0. \tag{A.43}$$

In these equations, the subscript 0 indicates that the χ^2 is calculated using predictions based on the null hypothesis (no oscillations). The subscript 1 indicates calculation under the assumption of the chosen Δm^2_{41}-$\sin^2 2\theta_{14}$ pair. x_{Asim} represents the Asimov dataset [105], either un-oscillated or oscillated (subscript 0 or 1). $\Delta\chi^2_{\text{min}}$ is the difference in χ^2 between the chosen ($\sin^2 2\theta_{14}$, Δm^2_{41}) pair and the pair that yields the lowest χ^2.

Once these quantities are known, confidence regions can be constructed using the approximation for the p-value:

$$\text{CL}_s = \frac{1-p_1}{1-p_0} \approx \frac{1+\text{Erf}\left(\frac{\overline{\Delta T_1}-\Delta T(x)}{\sqrt{8|\overline{\Delta T_1}|}}\right)}{1+\text{Erf}\left(\frac{\overline{\Delta T_0}-\Delta T(x)}{\sqrt{8|\overline{\Delta T_0}|}}\right)}. \tag{A.44}$$

A point can be considered approximately excluded at a given confidence level if CL_s is less than $1 - \alpha$, where α is the stated confidence level. For example, at a 90% confidence level, points with $CL_s < 0.1$ would be excluded. It should be noted that the use of the Gaussian CL_s method is valid only when the following three conditions are satisfied:

1. The nuisance parameter space is continuous under null and alternative hypotheses.

2. The dataset is large enough for the Gaussian approximation of the ΔT test to be valid.

3. The difference between the predictions of both hypotheses is small, which is typically true for modifications to the Standard Model.

If any of these conditions are not met, the Feldman-Cousins (FC) method should be used to calculate the exclusion region.

A.5 Feldman-Cousins method

To evaluate the statistical power of an oscillation experiment, it is crucial to understand how the measured statistics, such as propagation length and energy, relate to the goodness of fit for different theoretical parameters. An experiment typically measures a distribution of an observable x, which is then used to infer the likelihood of a theoretical parameter μ. Following Feldman and Cousins [120], the true parameter values are denoted with subscript t, while the measured values are represented by subscript 0. The goal is establishing confidence intervals for the theoretical parameters μ_t based on the observed distribution x_0.

This approach uses classical statistics for discrete distributions, as developed by Neyman [176], and applies an ordering principle based on likelihood ratios proposed

by Feldman and Cousins [120]. This method transitions smoothly between an upper limit and a two-sided confidence interval, avoiding undercoverage.

Neyman's confidence intervals are defined by:

$$P(\mu \in [\mu_1, \mu_2]) = \alpha, \tag{A.45}$$

where x is a function of μ, a set of theoretical parameters. The Bayesian approach, in contrast, estimates the probability of μ_t given a measurement x_0:

$$P(\mu_t|x_0) = \mathcal{L}(x_0|\mu_t)\frac{P(\mu_t)}{P(x_0)}, \tag{A.46}$$

where $\mathcal{L}$ is the likelihood function, and P represents probability densities. In neutrino oscillation experiments, selecting an appropriate prior $P(\mu_t)$ is difficult due to the unbounded nature of the squared-mass difference parameters. Thus, classical confidence intervals are generally preferred.

In Neyman's construction, α is the fraction of experiments with a fixed unknown μ_t that result in a measured μ_0 within the interval $[\mu_1, \mu_2]$. A parameter μ is covered if $P(\mu \in [\mu_1, \mu_2]) = \alpha$; undercovered if $P(\mu \in [\mu_1, \mu_2]) < \alpha$; and overcovered if $P(\mu \in [\mu_1, \mu_2]) > \alpha$. Overcoverage is conservative but can prevent rejecting false hypotheses, while undercoverage means the intervals do not meet the claimed confidence level. To construct confidence intervals, the confidence belt method [112] selects a range $[x_1, x_2]$ for a given μ such that:

$$P(x \in [x_1, x_2]|\mu) = \alpha. \tag{A.47}$$

An upper limit is defined by:

$$P(x < x_1|\mu) = 1 - \alpha, \tag{A.48}$$

and a central interval by:

$$P(x < x_1|\mu) = P(x > x_2|\mu) = \frac{1-\alpha}{2}. \tag{A.49}$$

Feldman and Cousins [120] proposed ordering intervals based on likelihood ratios to avoid undercoverage. For a given μ, identify μ_{best} that maximizes $P(x|\mu)$ and compute:

$$R = \frac{P(x|\mu)}{P(x|\mu_{\text{best}})}. \tag{A.50}$$

sum $P(x|\mu)$ in descending order of R until the desired confidence level is reached. This procedure, known as the Feldman-Cousins (FC) method, is repeated for each μ.

A.5.1 Example: Determining the Mixing Angle in a Neutrino Oscillation Experiment

Background

Neutrino oscillation experiments aim to measure the parameters governing the oscillation of neutrinos between different flavors (e.g., electron neutrinos, ν_e, muon neutrinos, ν_μ, and tau neutrinos, ν_τ). These oscillations are described by parameters such as the mixing angles (θ_{12}, θ_{13}, θ_{23}) and the squared mass differences between the neutrino mass eigenstates (Δm^2_{21}, Δm^2_{31}).

A typical experiment detects a certain number of neutrinos of a specific flavor (e.g., ν_μ) at a distance from the source. The number of detected neutrinos is compared to the expected number in the absence of oscillations to determine the values of the oscillation parameters.

Problem

Suppose a neutrino oscillation experiment measures the disappearance of muon neutrinos as they travel from a source to a detector. The probability $P(\nu_\mu \to \nu_\mu)$

that a muon neutrino remains a muon neutrino after traveling a distance L through a vacuum is given by:

$$P(\nu_\mu \to \nu_\mu) = 1 - \sin^2(2\theta) \sin^2\left(\frac{1.27\Delta m^2 L}{E}\right),$$

where:

- θ is the mixing angle.
- Δm^2 is the squared mass difference between the two neutrino mass eigenstates (in eV^2).
- L is the distance traveled by the neutrinos (in kilometers).
- E is the neutrino energy (in GeV).

The experiment detects N muon neutrinos at the detector, and the goal is to use this measurement to estimate the mixing angle θ and establish a confidence interval.

Applying the Feldman-Cousins Method

1. **Define the Likelihood Function:**

   Let N_{obs} be the observed number of muon neutrinos and $N_{\text{exp}}(\theta, \Delta m^2)$ be the expected number of neutrinos in the detector for a given set of oscillation parameters θ and Δm^2. The expected number N_{exp} can be modeled as:

   $$N_{\text{exp}}(\theta, \Delta m^2) = N_0 \cdot P(\nu_\mu \to \nu_\mu),$$

   where N_0 is the number of neutrinos expected without oscillation.

   The likelihood of observing N_{obs} given the expected number is Poisson-distributed:

   $$\mathcal{L}(N_{\text{obs}} \mid \theta, \Delta m^2) = \frac{(N_{\text{exp}}(\theta, \Delta m^2))^{N_{\text{obs}}} e^{-N_{\text{exp}}(\theta, \Delta m^2)}}{N_{\text{obs}}!}.$$

2. **Construct the Confidence Intervals:**

   To construct a confidence interval for the parameter θ, the Feldman-Cousins method ranks possible outcomes (in this case, the values of θ) based on the likelihood ratio:

$$R(\theta) = \frac{\mathcal{L}(N_{\text{obs}} \mid \theta, \Delta m^2)}{\mathcal{L}(N_{\text{obs}} \mid \theta_{\text{best}}, \Delta m^2)},$$

   where θ_{best} is the value of θ that maximizes the likelihood for the observed data N_{obs}.

   Then, the confidence interval is constructed by including values of θ in descending order of $R(\theta)$ until the cumulative probability reaches the desired confidence level (e.g., 90%).

3. **Determine the Critical Region:**

   By Monte Carlo simulation, generate many sets of pseudo-experiments for various hypothetical true values of θ and Δm^2. Calculate the distribution of $R(\theta)$ for each true value. The critical region is determined by finding the outcomes corresponding to the desired confidence level.

4. **Extract the Confidence Interval:**

   Based on the observed number of events N_{obs} and the calculated likelihood ratios, determine the range of θ values that fall within the critical region. This range constitutes the confidence interval for θ at the chosen confidence level.

Vita

Diego Venegas Vargas was born on March 30, 1997, in Tunja, Boyacá, Colombia. He is the son of Fabio Gomez Sierra and Gloria Vargas Avendaño and has one sibling, Melissa Venegas Vargas. Diego started playing tennis at seven and, at twelve, began training with Hugo Escobar Riveros, who played a key role in his athletic and professional growth. This mentorship earned him a collegiate athletic scholarship in the United States, where he studied Physics after graduating from Colegio Salesiano Maldonado in December 2013.

In 2014, he moved to Pittsburgh, PA, where Mario Fratangelo and Jose Mieres supported his transition to the U.S. In 2019, he earned a B.Sc. in Physics from Ohio Wesleyan University, specializing in experimental nuclear physics under Robert Haring-Kaye. While at Ohio Wesleyan, he played on the tennis team coached by Robert Postma.

During his undergraduate years, Diego participated in summer research at Ohio Wesleyan in 2018 and at Oak Ridge National Laboratory (ORNL) in 2019. His ORNL work, supervised by Alfredo Galindo-Uribarri, led to his Ph.D. studies at the University of Tennessee, Knoxville, starting in the fall of 2019. Diego completed his Ph.D. in December 2024, focusing on reactor antineutrino physics with the PROSPECT experiment. After graduation, Diego will join Johns Hopkins University as a Miller postdoctoral fellow under the supervision of Danielle Norcini.